Modeling Earth as an exoplanet in reflected and polarized light

Giulia Roccetti

München 2025

Modeling Earth as an exoplanet in reflected and polarized light

Giulia Roccetti

Dissertation
der Fakultät für Physik
der Ludwig-Maximilians-Universität
München

vorgelegt von
Giulia Roccetti
aus Rom, Italien

München, den 02. Juni 2025

Erstgutachter: Prof. Dr. Barbara Ercolano
Zweitgutachter: Prof. Dr. Leonardo Testi
Tag der mündlichen Prüfung: 14. Juli 2025

"And once the storm is over you won't remember how you made it through, how you managed to survive. You won't even be sure, in fact, whether the storm is really over. But one thing is certain. When you come out of the storm you won't be the same person who walked in. That's what the storm is all about."

Haruki Murakami

This work was carried out at the European Southern Observatory (ESO) in Garching bei München under the supervision of Dr. Michael Sterzik (ESO) and Dr. Claudia Emde (LMU). The committee members for the doctoral defense were Professors Katia Parodi, Barbara Ercolano, Leonardo Testi, and Til Birnstiel.

Contents

List of Publications

First author publications

- **HAMSTER: Hyperspectral Albedo Maps dataset with high Spatial and TEmporal Resolution**
  Giulia Roccetti, Luca Bugliaro, Felix Gödde, Claudia Emde, Ulrich Hamann, Mihail Manev, Michael Sterzik and Cedric Wehrum
  Atmospheric Measurement Techniques, Volume 17, p. 6025-6046 (2024)

- **Planet Earth in reflected and polarized light. I. Three-dimensional radiative transfer simulations of realistic surface-atmosphere systems**
  Giulia Roccetti, Claudia Emde, Michael F. Sterzik, Mihail Manev, Julia V. Seidel and Stefano Bagnulo
  Astronomy & Astrophysics, Volume 697, A170 (2025)

- **Planet Earth in reflected and polarized light. II. Refining contrast estimates for rocky exoplanets with ELT and HWO**
  Giulia Roccetti, Michael Sterzik, Julia V. Seidel, Claudia Emde, Mihail Manev and Stefano Bagnulo
  Astronomy & Astrophysics, Volume 700, A62 (2025)

- **Planet Earth in reflected and polarized light. III. Modeling and analysis of a decade-long catalog of Earthshine observations**
  Giulia Roccetti, Michael Sterzik, Claudia Emde, Mihail Manev, Stefano Bagnulo and Julia V. Seidel
  Astronomy & Astrophysics, Volume 702, A262 (2025)

Co-authored publications

- **HD 110067 c has an aligned orbit - Measuring the Rossiter–McLaughlin effect inside a resonant multi-planet system with ESPRESSO**
  Jiri Zak, Henri M. J. Boffin, Elyar Sedaghati, Andrea Bocchieri, Quentin Changeat, Akihiko Fukui, Artie Hatzes, Todd Hillwig, Kamil Hornoch, Dominika Itrich, Valentin D. Ivanov, David Jones, Petr Kabath, Yugo Kawai, Lorenzo V. Mugnai, Felipe Murgas, Norio Narita, Enric Pallé, Enzo Pascale, Petr Pravec, Seth Redfield, **Giulia Roccetti**, Markus Roth, Jiri Srba, Qiushi Tian, Angelos Tsiaras, Diego Turrini and J. P. Vignes
  Astronomy & Astrophysics, Volume 687, L2 (2024)

- **Vertical structure of an exoplanet's atmospheric jet stream**
  Julia V. Seidel, Bibiana Prinoth, Lorenzo Pino, Leonardo A. dos Santos, Hritam

List of Abbreviations

1D: One-Dimensional
3D: Three-Dimensional
3D CG: Three-Dimensional Cloud Generator
3MI: Multi-Viewing, Multi-Channel, Multi-Polarisation Imager
AIRS: Atmospheric Infrared Sounder
ALIS: Absorption Lines Importance Sampling
ANDES: ArmazoNes high Dispersion Echelle Spectrograph
AO: Adaptive Optics
ARIEL: Atmospheric Remote-sensing Infrared Exoplanet Large-survey
ARTS: Atmospheric Radiative Transfer Simulator
ASTER: Advanced Spaceborne Thermal Emission and Reflection Radiometer
BBSO: Big Bear Solar Observatory
BPDF: Bidirectional Polarization Distribution Function
BRDF: Bidirectional Reflectance Distribution Function
CALIPSO: Cloud-Aerosol Lidar and Infrared Pathfinder Satellite Observation
CCD: Charge-Coupled Device
CCN: Cloud Condensation Nuclei
CDF: Cumulative Distribution Function
CGLS: Copernicus Global Land Service
CIE: International Commission on Illumination
CLM5: Community Land Model version 5
CMG: Climate Modeling Grid
CMIP3: Coupled Model Intercomparison Project Phase 3
CRIRES+: Cryogenic High-Resolution InfraRed Echelle Spectrograph
DDIS: Detector Directional Importance Sampling
DOM: Discrete Ordinate Method
DOY: Day Of the Year
DSCOVR: Deep Space Climate Observatory
EarthCARE: Earth Clouds, Aerosol and Radiation Explorer
ECMWF: European Centre for Medium-range Weather Forecasts
ECOSTRESS: ECOsystem Spaceborne Thermal Radiometer Experiment on Space Station
ELT: Extremely Large Telescope
EMIT: Earth Surface Mineral Dust Source Investigation
EPIC: Earth Polychromatic Imaging Camera
EPOXI: Extrasolar Planet Observation and Characterization (EPOCh) and Deep Impact eXtended Investigation (DIXI)
ERA5: ECMWF ReAnalysis fifth-generation product
ERA Interim: ECMWF ReAnalysis Interim product
ESA: European Space Agency

ESM: Earth System Model
ESO: European Southern Observatory
EXP-RAN: Exponential-Random overlap
FORS2: FOcal Reducer and low dispersion Spectrograph 2
GCM: General Circulation Model
GLASS: Global LAnd Surface Satellite
GSV: General Spectral Vector
HAMSTER: Hyperspectral Albedo Maps dataset with high Spatial and TEmporal Resolution
HARMONI: High Angular Resolution Monolithic Optical and Near-infrared Integral field spectrograph
HEY: Hong, Emde, Yang parametrization
HiRISE: High-Resolution Imaging and Spectroscopy of Exoplanets
HST: Hubble Space Telescope
HWO: Habitable Worlds Observatory
HZ: Habitable Zone
IFS: Integrated Forecast System
ICRAF-ISRIC: International Centre for Research in Agroforestry (ICRAF) and the International Soil Reference and Information Centre (ISRIC)
IPCC: Intergovernmental Panel on Climate Change
IR: InfraRed
ISCCP: International Satellite Cloud Climatology Project
ISS: International Space Station
IWC: Ice Water Content
JWST: James Webb Space Telescope
KDE: Kernel Density Estimation
LCROSS: Lunar CRater Observation and Sensing Satellite
LE: Local Estimate
LER: Lambertian Equivalent Reflectivity
LIFE: Large Interferometer For Exoplanets
LSA SAF: Land Surface Analysis Satellite Application Facility
LUCAS: Land Use/Cover Area frame statistical Survey
LWC: Liquid Water Content
MAIAC: Multi-Angle Implementation of Atmospheric Correction
MAX-RAN: Maximum-Random overlap
MCMC: Monte Carlo Markov Chain
MCRT: Monte Carlo Radiative Transfer
MGS/TES: Mars Global Surveyor Thermal Emission Spectrometer
MIR: Mid-InfraRed
MLT: Magnetic Local Time
MODIS: Moderate Resolution Imaging Spectroradiometer
MSG: Meteosat Second Generation (satellite)
MYSTIC: Monte Carlo code for the phYSically correct Tracing of photons In Cloudy

atmosphere
NASA: National Aeronautics and Space Administration
NDVI: Normalized Difference Vegetation Index
NIMS: Near-Infrared Mapping Spectrometer
NIR: Near-InfraRed
OLCI: Ocean and Land Colour Instrument
p-T profile: Pressure-Temperature profile
PACE: Plankton, Aerosol, Cloud, ocean Ecosystem mission
PAR: Photosynthetically Active Radiation
PCA: Principal Component Analysis
PCS: Planetary Camera and Spectrograph
PDF: Probability Density Function
PDVI: Polarized Difference Vegetation Index
PLATO: PLAnetary Transits and Oscillations of stars
POLDER: POLarization and Directionality of the Earth's Reflectances
PSG: Planetary Spectrum Generator
REPTRAN: Representative Wavelengths Absorption Parameterization
RISTRETTO: high-Resolution Integral-field Spectrograph for the Tomography of Resolved Exoplanets Through Timely Observations
RGB: Red Green Blue
RMSE: Root Mean Square Error
RT: Radiative Transfer
SEVIRI: Spinning Enhanced Visible and Infrared Imager
SNR: Signal-to-Noise Ratio
SPHERE: Spectro-Polarimetric High-contrast Exoplanet REsearch
SSI: Solid-State Imaging system
SVD: Singular Value Decomposition
THE: Terra Hunting Experiment
TOA: Top Of Atmosphere
TROPOMI: TROPOspheric Monitoring Instrument
UTC: Coordinated Universal Time
UV: UltraViolet
VIS: Visible
VLT: Very Large Telescope
VRE: Vegetation Red Edge
VROOM: Variance Reduction Optimal Options Methods
VRMs: Variance Reduction Methods
VSTAR: Versatile Software for Transfer of Atmospheric Radiation
YGLCT: Yearly Global Land Cover Types
ZIMPOL: Zurich IMaging POLarimeter

List of Figures

List of Tables

Abstract

The next generation of ground- and space-based observatories will enable the detailed characterization of rocky exoplanets within the habitable zones of their host stars. With improved sensitivity, these facilities allow us to observe Earth-like planets and study their reflected light, which provides valuable information about planetary albedo, a result of the interplay between surface and atmospheric properties. For the first time, we will be able to assess the habitability of nearby non-transiting rocky exoplanets, such as Proxima b, and explore whether they might retain liquid water on their surfaces.

Observing Earth as if it were an exoplanet offers crucial insights into how we assess exoplanetary habitability. Earthshine, the sunlight reflected from Earth onto the darker portion of the visible Moon, provides an opportunity to study Earth in a way that closely mirrors how exoplanets are observed in reflected light. Unlike satellite observations, Earthshine captures the complex scattering and reflection geometries encountered when observing exoplanets.

In this thesis, I model Earth as an exoplanet using advanced 3D Monte Carlo radiative transfer codes in the visible and near-infrared spectral ranges. My approach builds on codes originally developed for Earth's remote sensing, using 3D atmospheres and 2D surface albedo maps. By combining state-of-the-art knowledge from Earth observations and reanalysis product, I generate spatially unresolved spectra and phase curves of Earth. I address two notorious challenges: the accurate representation of surface properties and the complex behavior of clouds.

Earth's surface albedo is highly variable across space and time, with also wavelength-dependent features like the Vegetation Red Edge (VRE), a peak in vegetation reflectivity around 700 nm caused by chlorophyll absorption. Satellite data provides detailed albedo maps at only a few wavelengths in the visible and near-infrared, limiting our ability to fully simulate these features. To extend this data, I employ a Principal Component Analysis (PCA) algorithm to generate hyperspectral albedo maps, greatly improving surface representation.

Clouds pose an even greater challenge due to their complexity. Standard models using cloud properties from satellite observations and weather forecasts significantly overestimate the planet's global reflectivity, an issue also seen in climate models. To address this, I develop a 3D cloud generator algorithm that creates finer-grid cloud patterns, representing their patchy nature. This approach allows for a more precise representation of Earth's clouds and their influence on reflectivity, enhancing our ability to model Earth as an exoplanet.

I validate my model, particularly its treatment of clouds and surface albedo, using a decade-long dataset of Earthshine observations that encompass a variety of planetary geometries and cloud conditions, for both intensity and polarization. Polarization offers deeper insights into the planet's physical properties and has the advantage of not requiring atmospheric correction. I successfully validate the surface and clouds models in both intensity and polarized light, creating a robust framework capable of accurately representing Earth as an exoplanet. My model is far superior to previous descriptions in the literature because it

matches both the continuum features and the absorption lines of Earthshine observations in a way that has never been achieved by earlier attempts.
This work also proposes an optimal strategy for detecting liquid water on exoplanets. Ocean glint, observable at high phase angles through phase curve variability or water lines, is best detected via polarization, which is highly sensitive to ocean surfaces. Polarization also reveals liquid water in clouds by identifying rainbows at smaller phase angles, offering detailed insights into cloud droplet properties. Combining polarization with traditional spectroscopy enhances the precision of exoplanet habitability assessments. This study paves the way for future instruments on observatories like the Extremely Large Telescope (ELT) and upcoming space missions such as the Habitable Worlds Observatory (HWO). Additionally, the advanced modeling developed here contributes to both exoplanet science and climate research.

Zusammenfassung

Die nächste Generation boden- und weltraumgestützter Observatorien wird die detaillierte Charakterisierung felsiger Exoplaneten innerhalb der habitablen Zonen ihrer Wirtssterne ermöglichen. Mit verbesserter Sensibilität erlauben uns diese Einrichtungen, erdähnliche Planeten zu beobachten und ihr reflektiertes Licht zu analysieren, das wertvolle Informationen über die planetare Albedo liefert – ein Ergebnis des Zusammenspiels zwischen Oberflächen- und Atmosphäreneigenschaften. Zum ersten Mal werden wir die Habitabilität nahegelegener nicht-transitierender felsiger Exoplaneten, wie Proxima b, untersuchen und untersuchen können, ob sich flüssiges Wasser auf ihren Oberflächen befinden könnte.
Die Beobachtung der Erde, als wäre sie ein Exoplanet, liefert entscheidende Erkenntnisse darüber, wie wir die Habitabilität von Exoplaneten beurteilen. Erdschein, das von der Erde auf den dunkleren Teil des sichtbaren Mondes reflektierte Sonnenlicht, bietet die Möglichkeit, die Erde auf eine Weise zu untersuchen, die der Beobachtung von Exoplaneten im reflektierten Licht ähnelt. Im Gegensatz zu Satellitenbeobachtungen fängt das Erdlicht die komplexen Streu- und Reflexionsgeometrien ein, die bei der Beobachtung von Exoplaneten auftreten.
In dieser Dissertation modelliere ich die Erde als Exoplaneten mithilfe fortschrittlicher 3D-Monte-Carlo-Strahlungstransfermodelle im sichtbaren und nahinfraroten Spektralbereich. Mein Ansatz baut auf Codes auf, die ursprünglich für die Fernerkundung der Erde entwickelt wurden, unter Verwendung von 3D-Atmosphären und 2D-Oberflächenalbedokarten. Durch die Kombination modernster Erkenntnisse aus Erdbeobachtungen und Reanalyseprodukten erstelle ich räumlich unaufgelöste Spektren und Phasenkurven der Erde. Ich spreche zwei berüchtigte Herausforderungen an: die genaue Darstellung der Oberflächeneigenschaften und das komplexe Verhalten von Wolken.
Die Oberflächenalbedo der Erde variiert stark über Raum und Zeit und weist auch wellenlängenabhängige Merkmale wie das "Vegetation Red Edge" (VRE) auf, ein Reflexionsmaximum der Vegetation um 700 nm, verursacht durch Chlorophyllabsorption. Satellitendaten liefern nur für einige wenige Wellenlängen im sichtbaren und nahinfraroten Bereich detaillierte Albedokarten, was unsere Fähigkeit zur vollständigen Simulation dieser Merkmale einschränkt. Um diese Daten zu erweitern, verwende ich einen Hauptkomponentenanalyse-Algorithmus (PCA), um hyperspektrale Albedokarten zu generieren und so die Oberflächendarstellung erheblich zu verbessern.
Wolken stellen eine noch größere Herausforderung dar, da sie extrem komplex sind. Standardmodelle, die Wolkeneigenschaften aus Satellitenbeobachtungen und Wettervorhersagen verwenden, überschätzen die globale Reflektivität des Planeten erheblich – ein Problem, das auch in Klimamodellen auftritt. Um dem entgegenzuwirken, entwickle ich einen 3D-Wolkengenerator-Algorithmus, der feinere Gittermuster von Wolken erstellt und so ihre inhomogene Natur repräsentiert. Dieser Ansatz ermöglicht eine präzisere Darstellung der Wolken der Erde und ihres Einflusses auf die Reflektivität, wodurch unsere Fähigkeit zur Modellierung der Erde als Exoplaneten verbessert wird.
Ich validiere mein Modell, insbesondere dessen Behandlung von Wolken und Oberflächenal-

bedo, anhand eines zehn Jahre umfassenden Datensatzes Erdscheinbeobachtungen, der eine Vielzahl planetarer Geometrien und Wolkenbedingungen in Intensität und Polarisation umfasst. Polarisation bietet tiefere Einblicke in die physikalischen Eigenschaften des Planeten und hat den Vorteil, dass keine atmosphärische Korrektur erforderlich ist. Ich validiere die Oberflächen- und Wolkenmodelle sowohl in Intensität als auch in polarisiertem Licht erfolgreich und schaffe damit ein robustes Rahmenwerk, das die Erde als Exoplaneten genau repräsentiert. Mein Modell ist den bisherigen Beschreibungen in der Literatur weit überlegen, da es sowohl die kontinuierlichen Merkmale als auch die Absorptionslinien der Erdscheinbeobachtungen in einer Weise abbildet, die frühere Modelle nicht erreicht haben. Diese Arbeit schlägt zudem eine optimale Strategie zur Detektion von flüssigem Wasser auf Exoplaneten vor. Spiegelung an der Ozeanoberfläche, die bei hohen Phasenwinkeln durch Variabilität in der Phasenkurve oder Wasserlinien beobachtbar ist, lässt sich am besten durch Polarisation nachweisen, da diese besonders empfindlich darauf reagiert. Polarisation offenbart auch flüssiges Wasser in Wolken, da sie das Regenbogensignal bei kleineren Phasenwinkeln verstärkt und dadurch Informationen über die Eigenschaften von Wolkentröpfchen liefert. Die Kombination von Polarisation mit traditioneller Spektroskopie erhöht die Präzision bei der Bewertung der Habitabilität von Exoplaneten. Diese Studie ebnet den Weg für zukünftige Instrumente an Observatorien wie dem Extremely Large Telescope (ELT) und kommenden Weltraummissionen wie dem Habitable Worlds Observatory (HWO). Darüber hinaus trägt die hier entwickelte fortschrittliche Modellierung sowohl zur Exoplanetenforschung als auch zur Klimaforschung bei.

Sommario

La prossima generazione di telescopi terrestri e spaziali consentirà una caratterizzazione senza precedenti dei pianeti rocciosi situati nella zona abitabile delle proprie stelle. Grazie a una sensibilità strumentale significativamente aumentata, tali osservatori permetteranno di individuare e analizzare pianeti simili alla Terra attraverso lo studio della luce riflessa, che fornisce informazioni essenziali sull'albedo planetario, determinato dall'interazione tra le proprietà superficiali e atmosferiche del pianeta. Per la prima volta sarà quindi possibile valutare l'abitabilità di pianeti rocciosi non transitanti nelle vicinanze del Sistema Solare, come Proxima b, e indagare la possibilità che essi mantengano acqua liquida sulla loro superficie.
Osservare la Terra come se fosse un esopianeta offre un approccio unico per comprendere e perfezionare i metodi di valutazione dell'abitabilità degli esopianeti. Il fenomeno dell'Earthshine (o luce cinerea), ovvero la luce solare riflessa dalla Terra verso la porzione scura della Luna visibile, rappresenta un'analogia diretta con le osservazioni degli esopianeti in luce riflessa. A differenza delle misurazioni effettuate dai satelliti, l'Earthshine consente di studiare geometrie di scattering e riflessione analoghe a quelle che si riscontrano nelle osservazioni delle atmosfere planetarie.
In questa tesi la Terra viene simulata come un esopianeta mediante avanzati codici tridimensionali di trasferimento radiativo Monte Carlo, operanti nel visibile e nel vicino infrarosso. L'approccio adottato si basa su codici originariamente sviluppati per il telerilevamento terrestre, che utilizzano atmosfere tridimensionali e mappe bidimensionali dell'albedo superficiale. Combinando conoscenze dettagliate derivanti da osservazioni satellitari e prodotti di rianalisi, vengono generati spettri e curve di fase spazialmente non risolti della Terra. L'analisi affronta due sfide principali: la rappresentazione accurata delle proprietà superficiali e la descrizione dell'impatto delle nubi.
L'albedo superficiale terrestre presenta una notevole variabilità spaziale e temporale, oltre a caratteristiche spettrali dipendenti dalla lunghezza d'onda, come il Vegetation Red Edge (VRE), un picco nella riflettività della vegetazione attorno ai 700 nm dovuto all'assorbimento della clorofilla. I dati satellitari disponibili forniscono mappe dettagliate dell'albedo solo per un numero limitato di lunghezze d'onda nel visibile e nel vicino infrarosso, non rendendo possibile la riproduzione di tali caratteristiche. A tal fine, è stato sviluppato un algoritmo basato sull'Analisi delle Componenti Principali (PCA) per la generazione di mappe iperspettrali di albedo, che migliorano in modo significativo la rappresentazione della superficie terrestre.
Le nubi costituiscono un'ulteriore sfida, a causa della loro intrinseca complessità. I modelli convenzionali, basati su proprietà nuvolose derivate da osservazioni satellitari e previsioni meteorologiche, tendono a sovrastimare la riflettività globale del pianeta, un problema ricorrente anche nei modelli climatici. Per superare tale limitazione, è stato sviluppato un "3D Cloud Generator" capace di riprodurre le strutture interne delle nuvole e la loro natura disomogenea. Questo approccio consente una rappresentazione più realistica della copertura nuvolosa terrestre e del suo impatto sulla riflettività, migliorando sensibilmente

la modellizzazione della Terra come esopianeta.
Il modello è stato validato, in particolare per quanto riguarda il trattamento dell'albedo superficiale e delle nubi, utilizzando un catalogo di osservazioni di Earthshine raccolte nell'arco di un decennio, comprendenti diverse geometrie e condizioni atmosferiche, sia in intensità che in polarizzazione. La polarizzazione, che fornisce informazioni dettagliate sulle proprietà fisiche del pianeta e non richiede correzioni atmosferiche, si è dimostrata uno strumento particolarmente efficace. I risultati ottenuti mostrano un'eccellente corrispondenza tra modelli e osservazioni, sia in intensità sia in luce polarizzata, offrendo un quadro coerente e robusto per la rappresentazione della Terra come esopianeta. Il modello sviluppato si distingue nettamente rispetto agli approcci precedenti, poiché riproduce con elevata accuratezza sia le caratteristiche del continuo sia le linee di assorbimento osservate nell'Earthshine.
Infine, questo lavoro propone una strategia ottimale per il rilevamento dell'acqua liquida sugli esopianeti. Il glint oceanico, osservabile a grandi angoli di fase attraverso la variabilità delle curve di fase o delle linee dell'acqua, risulta più facilmente identificabile mediante misure in polarizzazione, particolarmente sensibili alle superfici oceaniche. La polarizzazione consente inoltre di riconoscere la presenza di acqua liquida nelle nubi attraverso la rivelazione di arcobaleni a piccoli angoli di fase, fornendo preziose informazioni sulle proprietà microfisiche delle particelle delle nubi. La combinazione di osservazioni polarimetriche e spettroscopiche tradizionali incrementa in modo significativo la precisione nella valutazione dell'abitabilità del pianeta.
Questo studio apre la strada a future osservazioni con strumenti di nuova generazione su telescopi come l'Extremely Large Telescope (ELT) e su missioni spaziali di prossima generazione, quali l'Habitable Worlds Observatory (HWO). Inoltre, il modello avanzato sviluppato in questa ricerca rappresenta un contributo rilevante non solo per la scienza degli esopianeti, ma anche per lo studio e la comprensione del clima terrestre.

1

Introduction

In our daily lives, we rarely stop to appreciate just how extraordinary our planet truly is. We often take for granted the delicate balance of conditions that has made the Earth the habitable world we know today. Earth is a rocky planet, unique in hosting vast oceans of liquid water that cover over 70% of its surface. The remaining 30% consists of continents that span an astonishing diversity of landscapes and climates, from tropical rainforests to arid deserts, from boreal forests to polar glaciers.

On a clear day, if we look up, we see a blue sky stretching above us. This seemingly simple view is the result of Rayleigh scattering, a phenomenon made possible by the composition of our atmosphere, primarily nitrogen (N_2) and oxygen (O_2). The presence of abundant O_2 itself is a profound clue: it is a direct by-product of life, and its continuous replenishment hints at the presence of active biological processes sustaining it over geological timescales. Often, when we gaze upward, we see clouds, which are masses of liquid and ice water suspended in the atmosphere. Clouds are part of a dynamic water cycle, which plays a fundamental role in the regulation of Earth's climate. Clouds are not only complex features to interpret in atmospheric studies; they also serve as strong indicators of the presence of liquid water on Earth's surface. Moreover, they are key regulators of the planet's energy balance, influencing both the reflection of incoming solar radiation and the trapping of outgoing infrared radiation.

We watch the Sun rise and set, a reminder that Earth orbits a G-type star within the so-called "habitable zone (HZ)" (Kasting et al., 1993), where conditions allow for liquid water to exist. Our planet benefits from a protective magnetic field, a large stabilizing Moon, and active plate tectonics, all key ingredients in the complex recipe that makes life possible.

This brings us to a fundamental and enduring question: how unique is our planet? This question has captivated human curiosity since the dawn of civilization. Are we alone in the universe? Thanks to remarkable technological advances over the past centuries, we now

know that Earth is indeed unique, at least within our Solar System. While a wide variety of environments exist on the terrestrial planets and the moons of the giant planets of the Solar System, none exhibits the complex and stable conditions found on Earth today.
Venus, often referred to as Earth's twin, hosts a hostile environment where surface temperatures and pressures are extreme. It likely experienced a runaway greenhouse effect in the early stages of its evolution, driven by carbon dioxide (CO_2) feedback (Ingersoll, 1969; Kasting, 1988; Leconte et al., 2013). Mars, too, appears today as a cold, arid desert. It likely hosted surface water during the first billion years of its history (Poulet et al., 2005). However, the early loss of its global magnetic field left the atmosphere vulnerable to erosion by the solar wind. Over time, this process stripped away much of the Martian atmosphere, leading to a dramatic climatic shift (Jakosky et al., 2018).
Exploration efforts have also turned toward the icy moons of Jupiter and Saturn, where subsurface oceans are believed to exist beneath thick layers of ice (e.g., Khurana et al. 1998; Porco et al. 2006). If life ever originated and still exists in these hidden oceans, it would likely be profoundly different from the life we know on Earth.
Despite the profound transformations Earth has undergone over its 4.5-billion-year history, life emerged remarkably early. Evidence suggests that microbial life may have originated as early as 3.7 billion years ago (Nutman et al., 2016), during a time when Earth's atmosphere and surface conditions were dramatically different from those we observe today. The young planet was a far more hostile environment, characterized by intense volcanic activity, a lack of O_2, and frequent asteroid impacts, yet somehow, life found a way to take hold (e.g., Harrison 2009).
For much of Earth's early history, life remained simple and unicellular (Knoll, 2015). It was not until nearly 3 billion years later that more complex, multicellular organisms began to appear (e.g., Bozdag et al. 2024). The transition from simple to complex life was neither rapid nor straightforward; it was shaped by a series of environmental shifts and evolutionary innovations. One pivotal event was the Great Oxidation Event, around 2.4 billion years ago, when photosynthetic microorganisms began releasing large amounts of O_2 into the atmosphere (Hohmann-Marriott & Blankenship, 2011). This transformation laid the ground for aerobic respiration and, eventually, the rise of more complex eukaryotic life. Multicellularity, sexual reproduction, and eventually the Cambrian explosion around 540 million years ago marked the emergence of a remarkable diversity of complex organisms (Hohmann-Marriott & Blankenship, 2011). From that point on, life on Earth entered an era of increasing complexity, leading to the rich biosphere we observe today.
The extensive body of knowledge accumulated about Earth's history, evolution, and the physical and chemical laws that govern its transformation now finds a broader context in the discovery, and increasingly, the characterization, of a vast and diverse population of exoplanets. Since the groundbreaking detection of the first exoplanet orbiting a main-sequence star in 1995 (Mayor & Queloz, 1995), it has become clear that planetary systems beyond our own exhibit an extraordinary range of configurations. Many of these newly discovered planets fall into categories that have no direct analog in our Solar System (e.g., Fulton et al., 2017; Christiansen et al., 2023), challenging and expanding our understanding of planetary formation and evolution.

Thanks to the rapid development of both ground-based and space-based telescopes, we are now able to begin characterizing the atmospheres of exoplanets (Charbonneau et al., 2002) and, in some cases, such as for airless bodies, even infer aspects of their surface composition (e.g., Kreidberg & Loeb, 2016; Zieba et al., 2023). As the volume and quality of observational data increase, advanced modeling frameworks are becoming essential for interpreting the signatures of exoplanet atmospheres. These models are built upon the same physical and chemical principles that underpin Earth system models, which have been refined over decades through continuous validation with real-time observations of our planet.

However, modeling exoplanets introduces a fundamentally different challenge: we must explore a much broader and less constrained parameter space. Physical and chemical conditions on these distant worlds can differ significantly from those on Earth, requiring adaptations to conventional modeling strategies. Unlike Earth system models (ESMs), which are tightly constrained by direct observations, exoplanet models must often operate with limited or indirect data, demanding a careful balance between complexity and computational feasibility.

From an astrophysical perspective, placing Earth in a broader cosmic context allows us to explore whether our planet is truly unique. At the same time, however, Earth is undergoing a period of rapid climate change driven by anthropogenic greenhouse gas emissions (Intergovernmental Panel on Climate Change (IPCC), 2023). While the search for and characterization of terrestrial-size exoplanets focuses on understanding the atmospheres, clouds, and potential surface conditions of these distant worlds, this scientific endeavor also offers a unique opportunity: to study planets that may be similar to Earth in terms of size, mass, and stellar irradiation, yet have evolved under entirely different conditions. This comparative approach not only helps us understand the diversity of planetary climates, but also enables us to reflect on Earth's own trajectory, both its geological past and its possible future.

By improving our understanding of Earth's fundamental physical properties and embedding them within a broader planetary context, we can refine and expand modeling frameworks used to study our planet. This, in turn, may reduce uncertainties in projections of Earth's future climate scenarios. In a broader context, these insights contribute to our understanding of the processes that govern planetary habitability and climate stability. They help understanding how close Earth may be to a runaway greenhouse scenario (Leconte et al., 2013), and they clarify the physical and chemical conditions required to form and sustain surface oceans. By comparing Earth with its planetary neighbors, like Venus and Mars, and extending that perspective to exoplanets, we can better grasp the delicate balance of factors that make a planet not only habitable, but also capable of maintaining habitable conditions over geological timescales. These are not merely theoretical explorations, they are fundamental to advancing both planetary science and climate research.

1.1 Earth as an exoplanet

Earth is the only benchmark we have in the search for habitable planets beyond our Solar System. While habitable exoplanets may not exactly resemble Earth, they are likely to share some common features, such as surface inhomogeneities, oceans, clouds, and biosignatures in their atmospheres. Over its 4.5-billion-year history, Earth's atmosphere and surface environment have undergone significant changes. However, for modern Earth, a wealth of data has been collected through Earth-orbiting satellites and spacecraft for Solar System exploration and ground-based observatories (Robinson & Reinhard, 2018). These datasets allow us to view Earth as if it were an exoplanet, helping us understand how signs of habitability and life might appear from afar.
Studying Earth in this context provides a critical foundation for developing tools and strategies for exoplanet characterization. By examining our planet's globally averaged signals and its disk-integrated light, we gain valuable insights into what remotely detectable indicators of habitability might look like. This "Pale Blue Dot" perspective, where Earth is reduced to a single unresolved pixel, is a unique testbed for refining retrieval techniques for interpreting the limited data we will obtain from rocky exoplanets and identifying ideal measurement strategies for upcoming missions. These observations also help us define the observational thresholds required to detect the presence of liquid water, assess the surface-atmosphere conditions, and potentially infer biological activity on exoplanets.
The viewing geometry becomes critical when observing the Earth as a spatially unresolved exoplanet. In disk-integrated observations, the complex three-dimensional variability of the planet is collapsed into a single pixel. The reflectance from different regions depends on the viewing geometry: for instance, areas near the limb or terminator contribute less flux due to lower illumination and geometric foreshortening. Specular reflection features like the ocean glint are also highly geometry-dependent. Additionally, disk-integrated observations result in a blending of cloudy and cloud-free regions, land and ocean pixels, and the overall photometric and spectral features are affected by latitudinal temperature gradients.
Following Robinson & Reinhard (2018), there are three main approaches for acquiring observations of the Earth as a spatially unresolved exoplanet:

- spacecraft photometric and spectroscopic observations taken from afar;
- spatially averaged high spatial resolution satellite observations;
- Earthshine observations.

These observational approaches are complementary and have been guiding the development of radiative transfer models, retrieval techniques, and observational strategies for identifying habitable exoplanets and searching for life beyond our Solar System.

1.1.1 Spacecraft observations

Sagan et al. (1993) conducted the first controlled experiment to assess evidence of life on

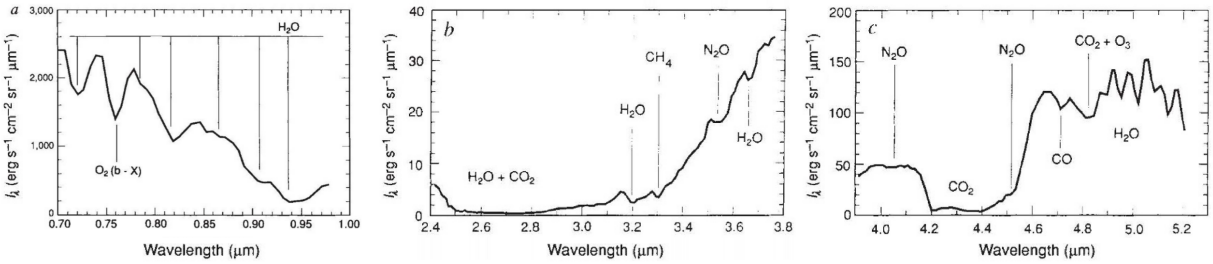

Figure 1.1: Long-wavelength VIS and NIR spectra of Earth over the Pacific Ocean, observed by the Galileo NIMS instrument during a flyby. The spectra reveal prominent features from H_2O, the O_2-A band, CO_2, as well as traces of N_2O, O_3 and CH_4. Figure adapted from Sagan et al. (1993).

Earth using first principles during one of the flybys of the Galileo spacecraft mission (Johnson et al., 1992). During this flyby, spatially resolved imagery and spectra revealed key features of Earth as seen from space. The Near-Infrared Mapping Spectrometer (NIMS) onboard the Galileo spacecraft detected condensed water over Antarctica through radiometric measurements, gas-phase water across the entire planet, and an albedo at 1 μm consistent with surface liquid water. This was further supported by the observation of specular reflection, indicating the presence of large, macroscopically smooth, and homogeneous areas, evidence for liquid water on an oceanic scale.
In Fig. 1.1, the NIMS visible (VIS) and near-infrared (NIR) spectra show a strong O_2-A band feature, along with the presence of several greenhouse gases such as CO_2, nitrous oxide (N_2O), ozone (O_3), and methane (CH_4). These features provide insight into the surface equilibrium temperature, suggesting it is above the freezing point of water. In particular, CH_4 is found at an abundance far from chemical equilibrium in such an O_2-rich atmosphere, an imbalance likely produced only by biological processes. The biological origin of O_2 is further supported by the detection of a sharp absorption edge near 0.7 μm, observed by the solid-state imaging system (SSI) camera over regions of South America. This sharp increase, known as the Vegetation Red Edge (VRE), is caused by chlorophyll pigments, which must be widespread in order to sustain the observed levels of atmospheric O_2. This experiment resulted in the first use of a spacecraft for Solar System exploration to gather insight into Earth's atmospheric and surface conditions and to assess key indicators of life. Historically, spacecraft observations have been the most direct method for mimicking observations of Earth-like exoplanets. In particular, observations taken from Lagrange points or interplanetary trajectories offer the best analogs for the full-disk, spatially unresolved views expected for exoplanet characterization. However, such Earth observations from spacecraft have been limited and largely opportunistic. Most were acquired during planetary flybys by missions not specifically designed for Earth observations, resulting in sparse and inconsistent temporal coverage. In some cases, the data remain unpublished or were collected primarily for outreach purposes rather than scientific analysis (Robinson & Reinhard, 2018).

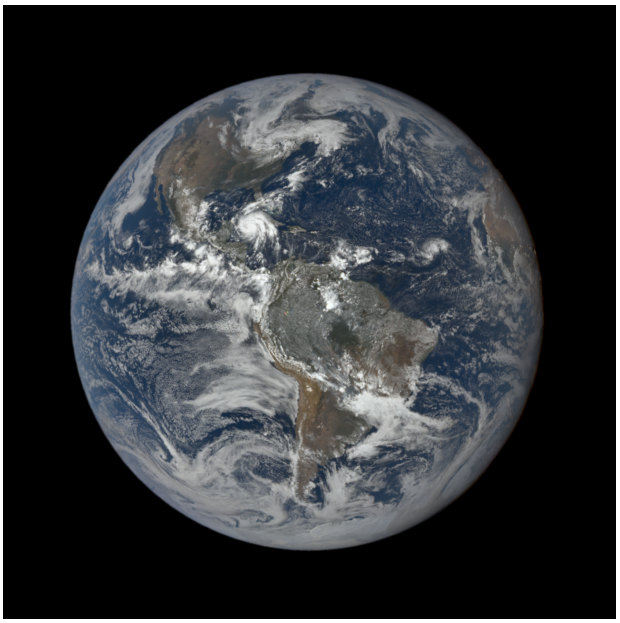

Figure 1.2: DSCOVR/EPIC natural color image of Earth on September 26$^{\text{th}}$ 2022. The natural color images are produced using the bands of the EPIC instrument within the human visual range and adjusted to simulate what a conventional camera would reproduce. Image credits: NASA/DSCOVR.

Notable exceptions include data from the Galileo spacecraft flyby (Sagan et al., 1993; Drossart et al., 1993), and the Mars Global Surveyor's Thermal Emission Spectrometer (MGS/TES), which acquired thermal infrared (IR) spectra that revealed features related to clouds, water vapor (H_2O), and surface materials (Christensen & Pearl, 1997). The EPOXI mission, which repurposed the Deep Impact spacecraft, obtained multi-wavelength time-series observations (from VIS to NIR) that tracked changes in Earth's brightness and spectra as the planet rotated (Cowan et al., 2011). These observations revealed surface features (e.g., land vs. ocean), cloud patterns and coverage, atmospheric composition (Cowan et al., 2011; Fujii et al., 2011; Robinson et al., 2011), and even the VRE signature (Livengood et al., 2011; Robinson et al., 2011). Similarly, the Lunar CRater Observation and Sensing Satellite (LCROSS) acquired VIS and NIR spectra that helped detect the presence and strength of ocean glint and O_3 absorption as functions of phase angle (Robinson et al., 2014).

A major advancement came with the launch of the Deep Space Climate Observatory (DSCOVR) in 2015. Stationed at the Earth–Sun L1 point, its Earth Polychromatic Imaging Camera (EPIC) continuously monitors the sunlit side of Earth in ten narrowband channels spanning the ultraviolet (UV) to VIS spectrum (Marshak et al., 2018). Fig. 1.2 shows a DSCOVR/EPIC image of September 26$^{\text{th}}$ 2022 showing the American continent, the Atlantic and Pacific oceans, and cloud fields present. While EPIC observes Earth at a near-zero phase angle, unlike the wider phase angles expected for exoplanet targets, it provides an unprecedented dataset for studying global reflectance and atmospheric vari-

ability. DSCOVR time-series data have been used to retrieve surface properties from disk-integrated observations, demonstrating that it is possible to separate surface and atmospheric contributions (e.g., Fan et al., 2019; Gu et al., 2021). Moreover, DSCOVR images and spectra were used by Kofman et al. (2024) to validate the Planetary Spectrum Generator (PSG; Villanueva et al., 2018).
Despite these efforts, significant observational gaps remain. There is a notable lack of disk-integrated measurements at large phase angles (beyond quadrature), which are essential for detecting features like specular reflection from ocean glint. High-resolution thermal IR spectra are also scarce, and no dataset offers continuous monitoring beyond 24-hour timescales. Furthermore, most VIS-wavelength observations are limited to broadband photometry, with spectroscopy below 1 μm still poorly represented.

1.1.2 Satellite observations

Another intuitive approach to creating a dataset of Earth observed as seen from afar is to leverage the extensive data collected by satellites, which provide broad temporal, spatial, and spectral coverage. Since the mid-20th century, low Earth orbit satellites have continuously monitored our planet, enabling studies of Earth's daily, seasonal, and annual variability. However, most satellite observations only capture small portions of the Earth at any given time, making the integration of multiple datasets into a coherent, disk-integrated view a non-trivial task. High spatial resolution satellite radiance measurements can be stitched together to simulate a global perspective, as pioneered by Hearty et al. (2009). However, this method is limited by temporal gaps in the datasets and cannot reproduce true snapshots of Earth due to evolving weather patterns and constraints imposed by satellite viewing geometries. Most satellite instruments acquire data at limited phase angles, typically around nadir (i.e., directly downward), and combining observations requires assumptions about how emission and solar incident angles influence the measured radiance.
As an alternative, Manalo-Smith et al. (1998) developed satellite-derived scene models that account for the viewing-geometry-dependent brightness of different surface types under varying cloud cover conditions. These models incorporate bidirectional reflectance distribution functions (BRDFs), but they are generally spectrally coarse and only provide broadband reflectivity estimates.
Mettler et al. (2020) analyzed thermal IR Earth observations from the Moderate Resolution Imaging Spectroradiometer (MODIS), using 15 years of data for five different surface types and locations. Due to the sun-synchronous orbit of the satellite, each target location was observed twice per month. They highlighted the crucial role of viewing geometry in thermal emission measurements, which varies depending on the dominant surface type, and demonstrated how seasonal variations, linked to planetary obliquity, can be extracted from time-resolved thermal emission spectra. Later, Mettler et al. (2023) extended this work using Atmospheric Infrared Sounder (AIRS, Chahine et al., 2006) data to derive disk-integrated mid-infrared (MID) thermal emission spectra for various Earth viewing geometries. They found that the strength of absorption features from gases such as N_2O,

CO_2, CH_4, and O_3 depends strongly on both the season and the observation geometry.

1.1.3 Earthshine observations

Earthshine is the sunlight scattered by Earth's atmosphere and surface and reflected onto the dark portion of the visible Moon, which is illuminated by Earth but not by the Sun. Earthshine has a long history of revealing key details about our planet. In Earthshine observations, Earth's phase as seen from the Moon is complementary to that of the Moon as seen from Earth; this means Earth appears nearly full when the Moon is a thin crescent. Figure 1.3 shows a schematic of the photon paths involved in Earthshine observations from a ground-based observatory. However, Earthshine cannot be used to measure Earth's thermal emission due to the Moon's own IR glow.

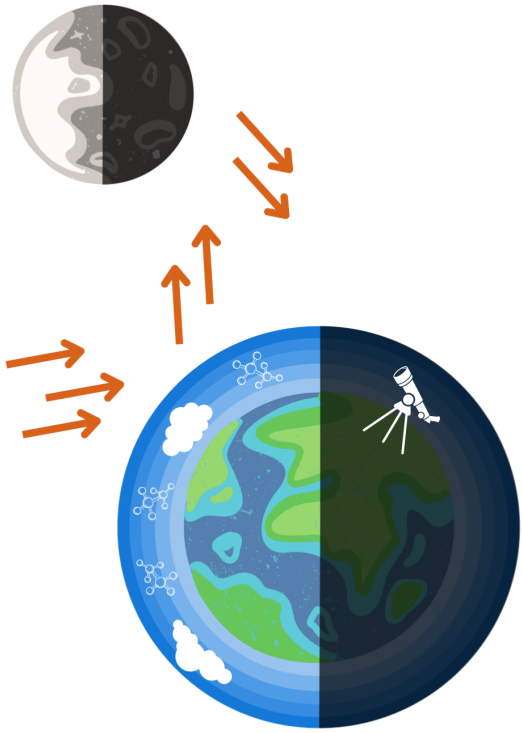

Figure 1.3: Schematic sketch of the photon path in Earthshine observations. Part of the sunlight is reflected off Earth's atmosphere and surface toward the Moon. Some of these photons are then reflected by the Moon and can be collected by a telescope pointed at the darker portion of the visible Moon. Effectively, in this configuration, the Moon resembles a diffuse reflector.

History of Earthshine

Between 1506 and 1509, Leonardo da Vinci wrote in his first notebook the following passage, as reported by Molaro (2017):

> ...some have believed that the Moon has some light of its own, but this opinion is false, for they have based it upon that glimmer visible in the middle between the horns of the new Moon...this brightness at such a time being derived from our ocean and the other inland seas, for they are at that time illuminated by the Sun, which is then on the point of setting, in such a way that the sea then performs the same office for the dark side of the Moon as the Moon when at full does for us when the Sun is set.

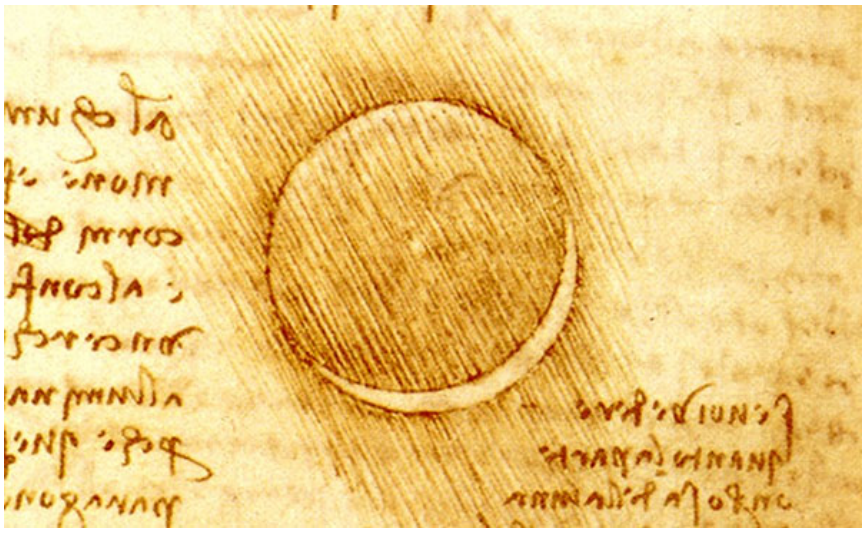

Figure 1.4: Leonardo Da Vinci drawing of the Earthshine phenomena in his Codex Leicester, written in the first decade of the 16th century. Image credit: Cove Studio.

Leonardo had already realized that during the crescent phase, the glow on the darker portion of the Moon was due to sunlight being reflected from the Earth onto the Moon. He originally thought that this glow was primarily produced by Earth's seas, as he thought them to reflect sunlight more efficiently than land. In his Codex Leicester, written around the same years, he drew this phenomenon and wrote the same explanation (see Fig. 1.4). Around a century later, Galileo noticed the same phenomenon, which he described in his *Sidereus Nuncius*:

> A certain faint light is also seen to mark out the periphery of the dark part which faces away from the Sun, separating this from the darker background of the aether.

Galileo's interpretation on the origin of this "Secunda Lunae Claritas" (secondary moonlight) was given in the *Dialogue Concerning the Two Chief World Systems*, from the mouth

of Salviati, the Galilean, that we write here as reported in Tucci (2022):

> To get back to our original discussion, I state that the sixth agreement between the Moon and the Earth is that just as the Moon supplies us with the light we lack from the Sun a great part of the time, and by reflection of its rays makes the nights fairly bright, so the Earth repays it by reflecting the solar rays when the Moon most needs them, giving a very strong illumination —as much greater than what the Moon gives us, it would seem to me, as the surface of the Earth is greater than that of the Moon

To Galileo, Earthshine was one of the arguments against the Ptolemaic and Aristotelic systems, given that it pointed to a similarity between the Earth and the Moon. Neither celestial body possessed light on its own, but both reflected it to each other. Moreover, according to Aristotelian philosophy, any light from Earth could not travel further than the sub-lunar world, while this observation seemed to contradict it. While nowadays this argument is often overlooked, in favour of the other arguments presented in the "Dialogue", it nonetheless caused great discussion among Galileo's contemporaries (Molaro, 2017).
In more recent times, Danjon (1928) conducted the first multi-year broadband measurements of Earthshine and made several important discoveries. First, he observed a significant difference between the color index of Earthshine and that of direct sunlight. He attributed this difference to atmospheric and surface effects on Earth, which alter the spectral properties of incoming sunlight and are subsequently revealed in the light reflected by the Moon.
Danjon (1928) also noted that Earthshine is highly variable, more so than for any other planet in the Solar System, and classified this variability into two categories. The first, which he termed "accidental" variability, encompasses random and short-term fluctuations primarily due to cloud cover, which increases Earth's albedo. However, cloud variability alone could not explain the second category: seasonal variability. To account for this, Danjon pointed to surface features that change cyclically over the year, such as snow cover and vegetation. In his conclusion, Danjon highlighted Earthshine as the only means available at the time to monitor global meteorological and climatological conditions, a role that, in the modern era, has been largely assumed by satellite observations:

> It is certain, moreover, that a cause capable of so profoundly modifying the energy exchanges of the atmosphere plays an important role in climatology. This latter consideration justifies the efforts made to better understand the astronomical phenomenon, which appears secondary, to which this thesis is devoted.

A few years later, Dubois (1947) repeated Earthshine observations and concluded that, since Earth reflects more light in the blue than in the red part of the spectrum, it would appear blue when viewed from space. Dubois also noted that the variability of Earth's albedo would make it one of the most interesting celestial bodies to observe from afar, compared to the other planets in the Solar System.

1.1.4 Modern Earthshine

In the modern era, Goode et al. (2001) performed regular Earthshine observations from the Big Bear Solar Observatory (BBSO) to quantify Earth's reflectance. They showed that an accuracy better than 1% could be achieved with their improved observational strategy, and that large variations, on the order of 5%, were due to changing weather patterns. This approach offers an alternative method for estimating Earth's albedo compared to satellite observations, which view only a small fraction of the planet at a time and require many observations to be combined. The advantage of Earthshine is that the coverage is instantaneous and hemispheric in scale. Goode et al. (2001) found an average terrestrial albedo of 0.297, which is consistent with simulations. However, the seasonal variation observed in the Earthshine data is twice as large as that predicted by the simulations. This revival of Earthshine observations has proven complementary to satellite-based monitoring of Earth's albedo, providing valuable data for long-term assessments of cloud cover and aerosols in studies of climate variability.

Woolf et al. (2002) obtained the first Earthshine spectrum, as shown in Fig. 1.5, moving beyond photometric observations, and recognized the potential of Earthshine as a benchmark for assessing the disk-integrated properties of Earth as seen from the perspective of a distant exoplanet. For instance, Arnold et al. (2002); Seager et al. (2005) demonstrated the variability of the VRE in the 600–800 nm range, revealing up to 10% increases in reflectivity under favorable conditions. However, Montañés-Rodríguez et al. (2006) found no significant VRE detection on a cloudy night, underlining the impact of cloud cover in masking surface features.

Earthshine offers the unique advantage of providing disk-integrated, hemispheric views of Earth's reflectivity, capturing variability on daily, seasonal, and decadal timescales (Goode et al., 2001; Pallé et al., 2003, 2004, 2009a, 2016). These long-term monitoring efforts demonstrated that Earth's apparent albedo exhibits interannual variability primarily driven by changes in global cloud cover and large-scale climate patterns. This was demostrated by Pallé et al. (2004), reporting a pronounced decrease in Earth's reflectance from the mid-1980s to around 2000, followed by a partial recovery in the early 2000s, suggesting a connection between cloud dynamics and the global energy budget. Additionally, Pallé et al. (2009a) found that albedo changes observed through Earthshine measurements were consistent with satellite-based observations and confirmed these variations, which are linked to changes in cloud properties. More recently, Pallé et al. (2016) identified two modest decadal-scale cycles in Earth's albedo but found no significant net change over the 1998–2014 period, emphasizing the complexity and quasi-cyclical nature of Earth's reflectance variability rather than a long-term trend.

In the NIR (0.7–2.4 μm), Turnbull et al. (2006) identified several molecular absorption bands associated with biological activity and geophysical processes. Robinson & Reinhard (2018), building on data from Pallé et al. (2003), analyzed Earth's phase-dependent apparent albedo, finding it varies significantly with phase angle: exhibiting weak backscattering at small angles, Lambertian behavior at intermediate phases, and strong forward scattering at large angles, unlike an ideal Lambert sphere, which would show constant albedo

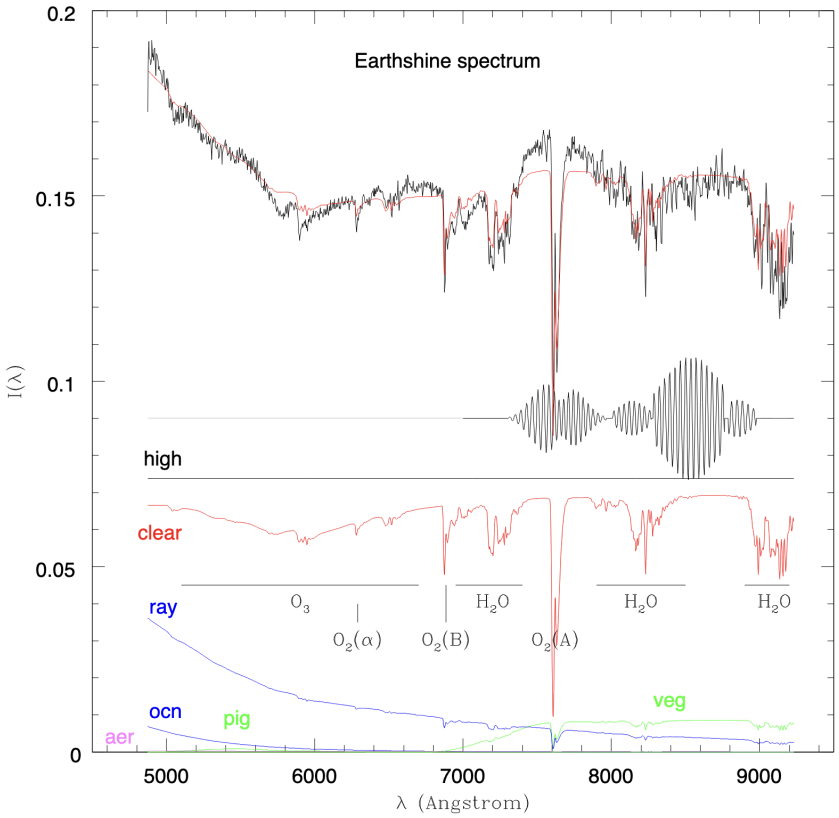

Figure 1.5: The first Earthshine spectrum, shown in black, was obtained by Woolf et al. (2002) and is presented in arbitrary units. The red curve represents the model spectrum, which is a composite of seven fitted component spectra displayed below the main plot. These components include high clouds (high), clear sky (clear), Rayleigh scattering (Ray), vegetation (veg), ocean (ocn), aerosols (are), and pigmented phytoplankton (pig). For more details on the model, see Chapter 2.4. Image credit: Woolf et al. (2002).

regardless of phase.

Earthshine techniques have also been innovatively applied to transmission spectroscopy during lunar eclipses. In these events, sunlight passing through Earth's atmosphere is reflected off the Moon and can be spectrally analyzed. Using this approach, Pallé et al. (2009b) detected biosignature gases such as O_2 and N_2, as well as pressure-broadened absorption features and ionized calcium lines. However, García Muñoz et al. (2012) later showed that atmospheric refraction limits such observations to altitudes above ∼10 km, preventing access to surface and tropospheric layers.

While Earthshine remains a valuable benchmark for disk-integrated Earth spectra and phase curves, it faces limitations: ground-based observations cannot continuously monitor Earth's full diurnal cycle and are subject to calibration challenges, often providing only scaled reflectance values.

1.1.5 Earthshine in polarization

One avenue to solve the calibration issue in Earthshine observations is to perform them using polarization, as the fractional polarization is largely unaffected by the transmission through Earth's atmosphere, and depolarization levels due to the lunar depolarization might be corrected accounting for the lunar albedo in the region of the observations. The first spectropolarimetric Earthshine observations were obtained by Sterzik et al. (2012), comparing two different Earth's sceneries: one with the illuminated side over the Pacific ocean, and one with a mixture of land and the Atlantic ocean surfaces (as shown in Fig. 1.6). Comparing the two spectra, they inferred the VRE, and detected such as variations in global cloud cover, the partial coverage of Earth's surface by oceans. Independent Earthshine measurements from Takahashi et al. (2013) and Bazzon et al. (2013), showing strong consistency with the initial polarization spectra from Sterzik et al. (2012).
Miles-Páez et al. (2014) expanded the wavelength range of polarimetric observations into the NIR, revealing sensitivity to molecular absorption features. Further progress came from Sterzik et al. (2019), who presented 33 new spectra spanning a range of phase angles, allowing the construction of Earth's polarized phase curves across various VIS and NIR bands. Extending this phase angle coverage, Sterzik et al. (2020) focused on small phase angles (30°–40°) to detect the cloudbow, a feature analogous to the secondary rainbow (see Chapter 2.3.2), arising from the microphysical properties of cloud droplets. This marked the first disk-integrated detection of Earth's cloudbow, which was used to retrieve the refractive index, size, and shape of cloud particles.
The use of polarization in planetary studies has a long history, dating back to the pioneering work of Hansen & Hovenier (1974). Their analysis of the polarization phase curve of Venus, and in particular of the cloudbow feature (peaking at around 20°) demonstrated that Venus' clouds consist of spherical droplets of sulfuric acid with typical radii of about 1 μm. This represented the first remote determination of the microphysical composition of an extraterrestrial atmosphere.
More recently, Takahashi et al. (2021) conducted NIR polarimetry of lunar Earthshine over 32 nights, revealing a clear positive correlation between the degree of polarization and the fraction of Earth's surface covered by oceans.

1.1.6 How to observe Earthshine

Earthshine observations are carried out by pointing ground-based telescopes at the Moon's dark, Earth-illuminated portion. Because this signal is faint compared to the sunlit crescent, astronomers use long exposure times and sensitive instruments while carefully masking or subtracting the bright lunar crescent to isolate the Earthshine component. Corrections for atmospheric interference, variations in lunar surface reflectivity, and scattered light are essential to obtain reliable measurements.
Polarimetric Earthshine observations by Sterzik et al. (2012, 2019, 2020) were performed using the FORS2 instrument (Appenzeller et al., 1998) on the Very Large Telescope (VLT). The telescope was aimed at the Moon's dark limb, with the FORS2 detector oriented east-

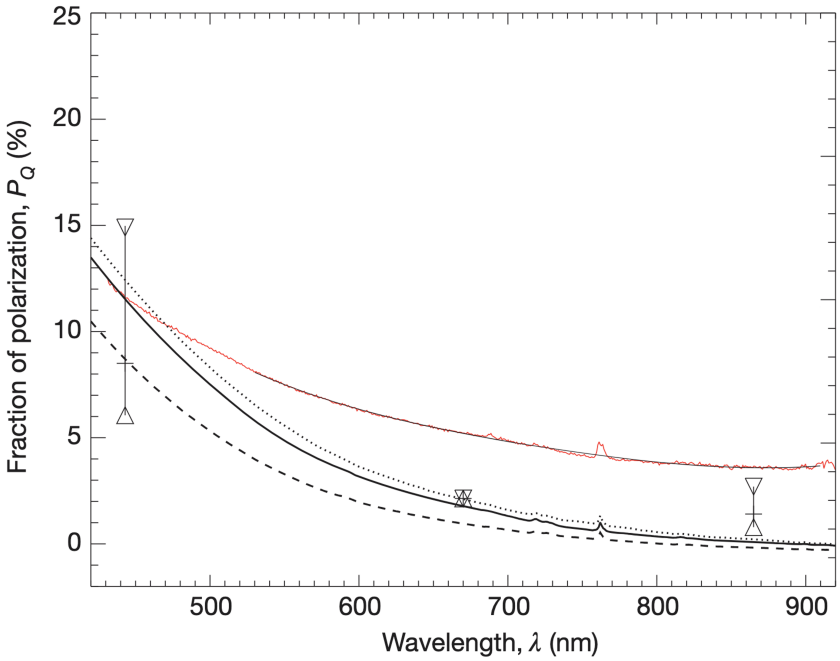

Figure 1.6: Observed fractional polarization (red lines) as a function of wavelength, compared with model spectra (black lines) for validation. Figure adapted from Sterzik et al. (2012).

west along the lunar edge. The first CCD chip contained five 22″ slitlets positioned across the lunar surface, while the second chip, separated by a 4″ gap, held four additional slitlets aimed at the sky for simultaneous background subtraction. The lunar limb was consistently aligned with the gap between the two detector chips to optimize signal isolation. Polarization measurements employed the beam-swapping technique (Bagnulo et al., 2009), a method that minimizes instrumental systematics in dual-beam polarimetry. This involved taking exposures at 16 different retarder waveplate angles, from 0° to 337.5°, in 22.5° increments. A full description of the data acquisition, preprocessing steps such as flat-fielding and sky subtraction, and additional calibration procedures is presented in Sterzik et al. (2019).

1.2 Atmospheric physics and Earth remote sensing

Understanding and simulating planetary atmospheres, especially those of exoplanets, requires a solid grasp of thermodynamics, radiative transfer, fluid dynamics, and atmospheric chemistry. In this section, I will provide a brief overview of fundamental concepts related to the vertical structure of atmospheres, the nature of clouds, the role of aerosols and surface albedo, and their implications for climate. Additionally, I will introduce key Earth observational satellite data and reanalysis datasets relevant to this thesis. The theoretical

framework of this section was inspired by Wallace & Hobbs (2006).

1.2.1 Atmospheric vertical profiles

The atmosphere is a spherical envelope of gas surrounding a planet's surface. Under a first approximation, we can consider it to be spherically symmetric and focus on its vertical structure. A static atmosphere can be assumed to be in hydrostatic equilibrium, meaning that the gravitational force pulling the atmosphere down towards the surface is exactly balanced by a pressure gradient force pushing upward:

$$\frac{dP}{dz} = -\rho g, \tag{1.1}$$

where P is the pressure, ρ the density, g the gravitational acceleration and z the height. By assuming that the gas composing the atmosphere obeys the ideal gas law, this differential equation can be solved, leading to an exponentially decaying vertical pressure profile:

$$P(z) = P_0 e^{-z/H}, \tag{1.2}$$

where P_0 is the pressure at the surface and H is the scale height of the atmosphere, which is approximately 7 km for Earth.

This derivation assumes an isothermal atmosphere, which is, of course, a crude simplification. Therefore, this exponential law should not be interpreted as exact but rather as a general indication that both pressure and density decrease approximately exponentially with altitude.

Fig. 1.7 shows the U.S. Standard Atmosphere model (United States Committee on Extension to the Standard Atmosphere, 1976), developed in 1976, which provides canonical vertical profiles for pressure, density, temperature, and the mixing ratios of various gases. As shown in the left panel, pressure indeed follows an exponential decay (note the logarithmic scale in the x-axis). The density profiles of the individual molecular constituents, however, vary, as shown in the central panel of Fig. 1.7. Some gases, such as O_2 and CO_2, maintain constant mixing ratios throughout much of the atmosphere due to turbulent mixing. Others exhibit strong vertical gradients resulting from specific atmospheric processes and chemical properties. For example, H_2O is concentrated near the surface, where it enters the atmosphere via evaporation from oceans and moist land. Most of it condenses into clouds by the tropopause, where temperatures drop sharply. In contrast, O_3 is concentrated around 30 km altitude, where it plays a critical role in shaping the vertical temperature structure.

The temperature profile, shown in the right panel of Fig. 1.7, reveals a layered structure that cannot be explained solely by distance from the surface or outer space. Instead, it highlights the importance of absorption processes. In particular, the absorption of UV radiation by O_3 significantly heats the stratosphere, creating a temperature maximum near 50 km. This temperature inversion is a clear illustration of the intricate coupling between radiation and matter in the atmosphere.

Understanding the physical and chemical processes that shape atmospheric profiles is essential for accurately modeling both Earth's atmosphere and those of exoplanets.

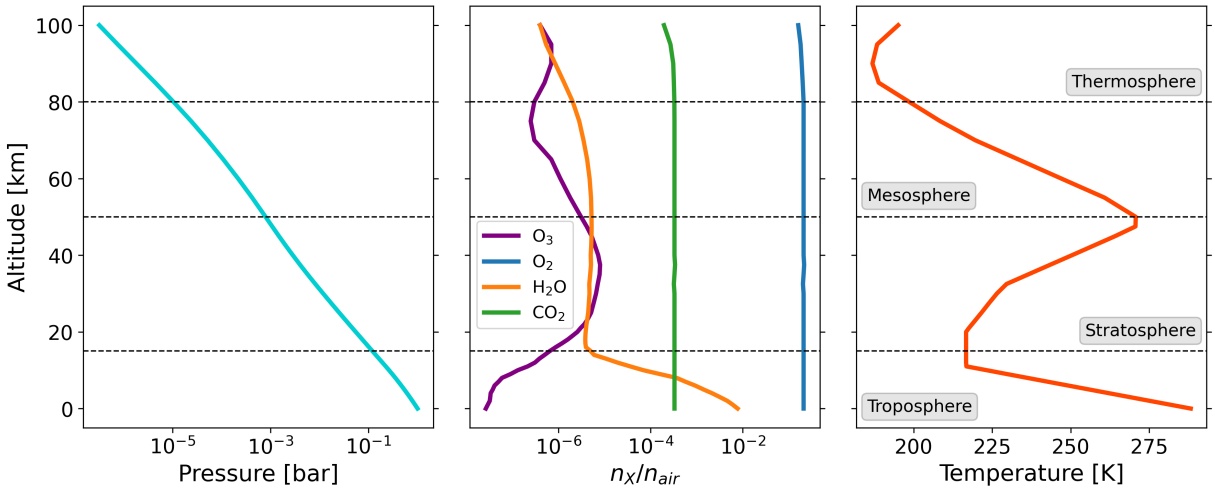

Figure 1.7: U.S. Standard Atmosphere model, showing the vertical profiles of pressure (left panel), mixing ratios of some atmospheric gases (central panel) and temperature (right panel).

1.2.2 Surface albedo

The surface of a planet plays a critical role in its radiative energy budget. Its effect is characterized by its albedo, the fraction of incident solar radiation that is reflected back into space without being absorbed by the surface. It is formally defined as

$$a = \frac{F_\uparrow}{F_\downarrow}, \tag{1.3}$$

where $F_\uparrow$ is the reflected solar flux and $F_\downarrow$ is the incident solar flux at the surface. The albedo typically ranges from 0, for a perfect absorber, to 1, a perfect reflector, and can vary significantly depending on surface type, conditions and geometry.
Moreover, albedo is a wavelength-dependent quantity. Ice and snow exhibit high reflectance in the VIS spectrum, while they absorb more radiation in the IR. On the other hand, vegetation absorbs VIS light while strongly reflects the NIR photons. This spectral behavior is used in remote sensing to characterize vegetation health using the Normalized Difference Vegetation Index (NDVI). The spectral-dependent albedo is defined simply as:

$$a(\lambda) = \frac{F_\uparrow(\lambda)}{F_\downarrow(\lambda)}. \tag{1.4}$$

In addition to its spatial and spectral variability, surface albedo can also vary temporally, especially as part of climate feedback mechanisms. One prominent example is the ice-albedo feedback: an initial increase in temperature causes the melting of highly reflective snow and ice, revealing darker surfaces underneath. These absorb more solar radiation, leading to further warming and additional melting, in a positive feedback loop which amplifies warming, particularly in polar regions.

On a global scale, planetary albedo incorporates both surface and atmospheric effects and measures the ratio of reflected to incident stellar radiation. From a simple planetary energy balance:

$$\frac{1}{4}(1 - A)F_{\odot} = \sigma T^4, \tag{1.5}$$

where A is the planetary albedo, $F_{\odot}$ is the solar flux at the top of the atmosphere (TOA) ($\sim$1361 W m^{-2}), σ is the Stefan–Boltzmann constant, and T is the planet's effective emission temperature. For Earth, with an observed $A \approx 0.3$, the blackbody temperature is approximately 255 K.
The strong nonlinear dependence of outgoing radiation on temperature (via the T^4 term) underlines the climate sensitivity to albedo. In the absence of feedback, a modest reduction in albedo by just 0.01 could increase roughly 1 K in Earth's equilibrium temperature (Goode et al., 2001). Such sensitivity highlights the pivotal role of albedo in regulating planetary climates.

Remote sensing of surface albedo

Surface albedo spatial, temporal, and spectral variability is continuously monitored through satellite observations, providing global, high-resolution datasets across multiple spectral bands. Instruments such as the MODIS aboard NASA's Terra and Aqua satellites, and the Ocean and Land Colour Instrument (OLCI) aboard the Sentinel-3 satellite, deliver long-term, consistent time series used to validate climate models and to study land surface changes. Notably, the MODIS MCD43D42–48 data products used in this thesis, offer daily measurements of surface albedo at a spatial resolution of 0.05° in both latitude and longitude.
However, satellites measure only radiances at the TOA, while the quantity of interest is the surface albedo. Retrieving surface albedo from TOA radiance involves inverting the radiative transfer processes that shaped the observed signal. This retrieval process is inherently degenerate, as multiple atmospheric and surface conditions can produce similar radiance signatures. To address this challenge, sophisticated atmospheric correction algorithms are employed to account for atmospheric effects, mask out clouds, and accurately model surface reflection. One such method is the MAIAC (Multi-Angle Implementation of Atmospheric Correction) algorithm used in processing MODIS data (Lyapustin et al., 2018).

1.2.3 Clouds

When water vapor in the atmosphere condenses under the right conditions, it can form clouds. Clouds are among the most influential components of the atmosphere, significantly affecting radiative transfer and the Earth's energy balance. This section provides a brief overview of the physical processes involved in cloud formation, distinguishes between liquid and ice water clouds, describes their optical properties, and outlines how clouds are represented in reanalysis products.

Cloud formation

The formation of clouds is primarily governed by the condensation of water vapor. The critical pressure at which water condenses is known as the saturation vapour pressure, and it can be determined using the Clausius–Clapeyron relation:

$$\frac{de_s}{dT} = \frac{L_v e_s}{R_v T^2}, \tag{1.6}$$

where e_s is the saturation water pressure, T the temperature, R_v the gas constant of water vapor and L_v the specific latent heat of water evaporation.
When the ambient vapour pressure exceeds the saturation vapour pressure, condensation begins. However, this condition alone is not sufficient for cloud formation, as droplet formation requires energy, potentially more than what is released during condensation. The energy balance governing droplet growth is expressed as

$$\Delta E = 4\pi R^2 \sigma - \frac{4}{3}\pi R^3 n k_B T \ln\left(\frac{e}{e_s}\right), \tag{1.7}$$

where σ is the energy per unit area required to increase the droplet size (which is also equal to the surface tension), R is the radius of the droplet (assumed to be spherical), n is the number density of water molecules, k_B is the Boltzmann constant, and e is the water vapor pressure.
The evolution of ΔE as a function of droplet radius is shown in Fig. 1.8, for two regimes. In the subsaturated regime, $\ln(e/e_s) < 0$ and $\Delta E > 0$ for all radii. Hence, droplet growth is energetically unfavourable, and it will instead immediately evaporate. In the supersaturated regime, $\ln(e/e_s) > 0$, and there is a critical radius r above which ΔE decreases, making droplet growth energetically favourable. For pure water droplets with initial radii

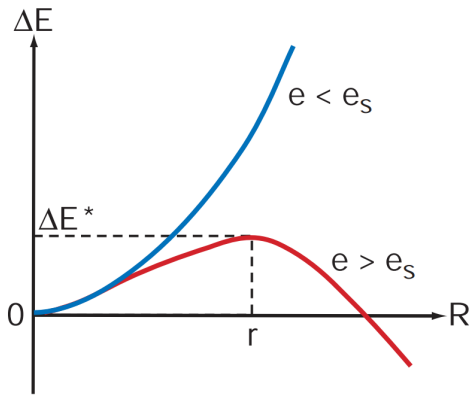

Figure 1.8: Energy required to grow a water droplet as a function of its initial radius for subsaturated and supersaturated conditions. In the supersaturated regime, growth becomes energetically favourable above a critical radius r. Figure from Wallace & Hobbs (2006).

around $R \sim 0.01\ \mu m$, the supersaturation required to overcome the energy barrier is $e/e_s \sim 12\%$. Moreover, to even build that initial seed of $R \sim 0.01\ \mu m$, the level of supersaturation required can be as large as several hundred percent (Rogers, 1989). However, typical atmospheric supersaturations caused by adiabatic lifting are only a few percent. Therefore, cloud formation in natural conditions typically requires larger particles to act as initial condensation sites. These cloud condensation nuclei (CCN) have a typical radius of $\sim 0.3\ \mu m$, at which the supersaturation needed is 0.4%, a value commonly reached in the atmosphere.

Liquid and ice water clouds

Clouds can consist of liquid water droplets, ice crystals, or a mixture of both. Unlike liquid water clouds, ice clouds can form via homogeneous nucleation, which does not require the presence of CCN. However, ice formation can also occur via heterogeneous nucleation, where water vapor condenses onto freezing nuclei at higher temperatures than those required for homogeneous nucleation. Given the different temperatures needed to form ice clouds compared to water clouds, they usually form at higher altitudes than liquid water clouds.
Another key difference lies in the typical particle sizes. Liquid water clouds are composed of droplets with radii on the order of $\sim$10 μm, whereas ice crystals tend to be significantly larger, with characteristic sizes around 50 μm. The parametrization of the liquid and ice cloud droplet size is detailed in ECMWF (2024).

Optical properties of clouds

To understand how much radiation is blocked by clouds, we need to estimate their optical thickness. A key quantity in this context is the liquid water content (LWC), defined as the amount of liquid water per unit volume within a cloud. Assuming the cloud consists of spherical droplets distributed according to a size distribution $n(r)$, we can compute the number concentration of droplets per unit volume by integrating over all radii

$$N_d = \int_0^\infty n(r)dr. \tag{1.8}$$

The LWC is then defined by multiplying the density of liquid water ρ_w by the expected value of the droplet volume (Petty, 2004)

$$\mathrm{LWC} = \rho_w \cdot \frac{4}{3}\pi \int_0^\infty r^3 n(r)dr = \frac{4}{3}\pi N_d r_{\mathrm{eff}}^3 \rho_w, \tag{1.9}$$

where r_{eff} is the effective radius, representing the radius that all droplets would have if they were identical and produced the same total volume as the actual distribution.
The cloud's extinction coefficient β can similarly be expressed as the expected value of the droplet cross-sectional area, multiplied by an extinction efficiency Q_{ext}:

$$\beta = \int_0^\infty Q_{\mathrm{ext}} \cdot \pi r^2 n(r)dr = Q_{\mathrm{ext}} \cdot N_d \pi r_{\mathrm{eff}} = \frac{3Q_{\mathrm{ext}}\mathrm{LWC}}{4\rho_w r_{\mathrm{eff}}}, \tag{1.10}$$

where we used the effective radius to approximate the average droplet area and substituted Eq. 1.9. For VIS wavelengths, which are much smaller than typical droplet sizes, it is common to assume $Q_{\text{ext}} \simeq 2$ (Petty, 2004).
The optical thickness τ_c of the cloud layer can then be computed by integrating the extinction coefficient vertically

$$\tau_c = \int_{z_{\text{base}}}^{z_{\text{top}}} \beta(z) dz = \frac{3 \text{ LWC } \Delta z}{2 \ r_{\text{eff}} \ \rho_w}, \tag{1.11}$$

where we assumed that both LWC and the effective radius are constant along the vertical direction.
Measuring the reflected light from a satellite, it is possible to simultaneously derive both τ_c and r_{eff}, and thus derive the LWC of the cloud. This method, first introduced by Nakajima & King (1990), uses two spectral bands: one in a wavelength region where cloud water is effectively transparent, making the reflectance primarily dependent on τ_c, and another in a region where cloud droplets absorb more strongly, making the reflectance sensitive to r_{eff}. By comparing reflectance at these two wavelengths, both parameters can be inferred.

The ERA5 reanalysis product

The highly dynamic nature of clouds in Earth's atmosphere poses a challenge for continuous monitoring through satellite observations alone. A more comprehensive approach combines observations with numerical modeling. The most widely used dataset for cloud properties is the ERA5 reanalysis product from the European Centre for Medium-Range Weather Forecasts (ECMWF). Reanalysis combines data from various sources, including satellites, ground-based meteorological stations, and ocean buoys, with numerical weather prediction models that are continuously updated through data assimilation techniques. The ERA5 reanalysis product offers hourly data on variables such as LWC, ice water content (IWC), cloud cover, temperature, and wind speed at 37 pressure levels and a resolution of 0.25° in latitude and longitude, from 1940 to the present day.
These datasets have been used throughout this thesis to provide the input cloud fields for radiative transfer simulations of Earth as an exoplanet. Hersbach et al. (2020) discusses the details of the ERA5 reanalysis procedure.

1.2.4 Aerosols

Aerosols are solid or liquid particles suspended in the atmosphere, with sizes ranging from less than 1 μm to several hundred micrometres. Their sources can be broadly classified into three main categories:

- Biological aerosols, which include bacteria, algae, sea salt, and smoke from forest fires. Many of these, especially particles around 0.1 μm in size, serve as ideal CCN.
- Geological aerosols, such as mineral dust from deserts and particulate matter from volcanic eruptions.

- Anthropogenic aerosols, which originate from human activities like fossil fuel combustion, industrial processes, and agriculture.

The size distribution of aerosols follows roughly a power law

$$\frac{dN}{d\log(R)} \propto R^{-3}, \tag{1.12}$$

which implies that small particles take up most of the number concentration of aerosols. Aerosols play two main roles in the atmosphere. First of all they can be CCN for cloud formation, thus regulating the amount of clouds that are formed in the atmosphere. Second, they are chemically active and can act as catalysts in atmospheric reactions. A key example is their role in the heterogeneous catalysis of O_3 depletion, a process particularly sensitive to anthropogenic aerosols.
From an observational perspective, aerosols are studied using satellite remote sensing, aircraft campaigns, and ground-based measurements. However, retrieving aerosol properties remains challenging, particularly when attempting to distinguish aerosol layers from thin clouds, especially over bright surfaces like snow or deserts. The development of polarimetric and multi-angle sensors is expected to enhance aerosol retrieval algorithms, improving their representation in numerical models and reanalysis datasets.

1.2.5 Relevance to the climate system

All the components described above (clouds, surfaces, and aerosols) play direct or indirect roles in regulating Earth's climate. Their contributions are quantified through radiative forcing terms in Earth's energy budget. A positive radiative forcing increases the amount of thermal energy retained in the atmosphere, leading to warming, while a negative radiative forcing reduces atmospheric energy and leads to cooling. Below, we briefly review the radiative forcing effects of these components:

- **Clouds** can exert both positive and negative radiative forcing effects. They reflect incoming solar radiation back to space, contributing to cooling, but also trap outgoing longwave radiation from the surface, enhancing the greenhouse effect. According to Intergovernmental Panel on Climate Change (IPCC) (2023), the net global effect of clouds is a positive radiative forcing. However, clouds remain the most uncertain component in climate models due to the challenges of accurately representing their climatological impact.

- **Surfaces** influence radiative forcing primarily through their albedo. A well-known positive feedback mechanism is the ice-albedo feedback, discussed in Sec. 1.2.2, where melting ice reduces surface reflectivity, leading to further warming. On the other hand, anthropogenic land use, such as deforestation, often replaces dark forested areas with brighter, more reflective surfaces, reducing absorbed solar radiation and resulting in a slightly negative radiative forcing. This is illustrated in Fig. 1.9.

Conversely, the deposition of dark aerosols on snow and ice surfaces reduces their albedo and contributes a positive radiative forcing.

- **Aerosols** influence climate both directly and indirectly. Directly, they interact with radiation by scattering and reflecting incoming solar energy, thereby contributing to cooling. Indirectly, aerosols act as CCN, as first described by Twomey (1974). When the number of CCNs increases while the amount of available H_2O remains constant, cloud droplets become more numerous but smaller. Smaller droplets reflect solar radiation more efficiently and have reduced interaction with thermal radiation, allowing more heat to escape to space. Consequently, both the direct and indirect effects of aerosols contribute to negative radiative forcing.

Figure 1.9 summarizes the effective radiative forcing associated with various atmospheric constituents, including surface albedo and aerosols. Greenhouses gases such as CO_2 and CH_4, however, present a net positive radiative forcing that vastly outweighs their negative contributions.

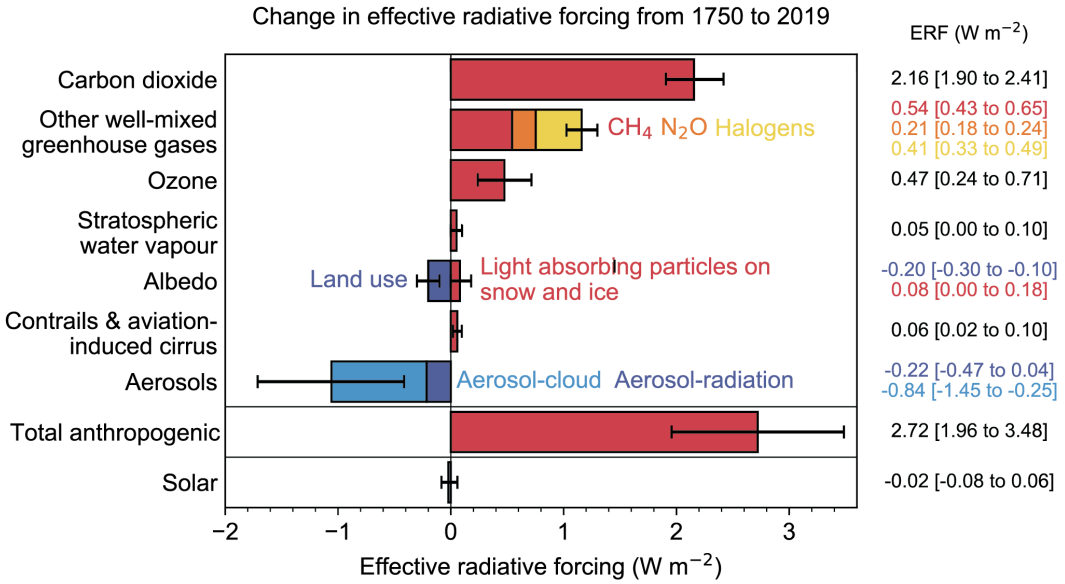

Figure 1.9: Contributions to radiative forcing of different atmospheric components. Both surface albedo and aerosols have a net negative impact, while atmospheric trace gases exhibit mostly positive forcings. Figure from Intergovernmental Panel on Climate Change (IPCC) (2023)

These examples show how atmospheric processes impact climate in complex and interconnected ways, often involving feedback loops. For this reason, the study of climate dynamics heavily relies on numerical simulations using ESMs. These models solve the Navier–Stokes equations to simulate atmospheric and oceanic circulation across the globe, compute radiative transfer and energy exchange between the atmosphere and the underlying surface,

and include representations of atmospheric chemistry, land surface processes, and other key components. ESMs are designed to be computationally efficient, enabling simulation of Earth's climate system over multi-decadal to centennial timescales.

1.3 Characterizing exoplanet atmospheres

Since the discovery of the first exoplanet orbiting a main-sequence star (51 Pegasi b) in 1995 by Mayor & Queloz (1995), the field of exoplanet science has rapidly expanded. To date, over 5 900 exoplanets have been confirmed, displaying a remarkable diversity in mass, radius, composition, and orbital configuration[1]. The majority of these exoplanets have been detected using the transit method, whereby a planet passes in front of its host star as seen from Earth, causing a periodic dimming in the observed stellar brightness. During a transit, a small fraction of the starlight passes through the planet's atmosphere before reaching the observer. This light is selectively absorbed and scattered by atmospheric molecules, imprinting spectral features that allow to probe the planet's atmospheric composition. This technique, known as transmission spectroscopy, was first demonstrated by Charbonneau et al. (2002) through the detection of sodium in the atmosphere of HD 209458 b.
Transmission spectroscopy is particularly effective for large, close-in exoplanets such as Hot Jupiters and Ultra-Hot Jupiters, where the high atmospheric scale heights and favorable star–planet radius ratios result in strong signals. The method has enabled the detection of key atmospheric constituents, including H_2O, Na, K, and CO, as well as insights into the presence of clouds and hazes (Brogi & Line, 2019). Ground-based observations using high-resolution spectroscopy have opened new windows into exoplanet atmospheres, allowing astronomers to resolve individual atomic lines (e.g., Wyttenbach et al., 2015; Allart et al., 2017; Prinoth et al., 2024a) and study atmospheric dynamics through Doppler shifts. This includes measuring wind speeds (Ehrenreich et al., 2020; Seidel et al., 2021), detecting atmospheric rotation, and even mapping the three-dimensional structure of jet streams in certain Hot Jupiters (Seidel et al., 2025). Additionally, the use of cross-correlation techniques has been instrumental in detecting molecules like CO and H_2O (Snellen et al., 2010), even when their features are buried in noisy data. Space-based observatories such as the Hubble Space Telescope (HST) and more recently the James Webb Space Telescope (JWST) have further advanced the field. These instruments have not only confirmed the presence of clouds and hazes in numerous exoplanet atmospheres (e.g., Gao et al., 2023) but also uncovered subtle phenomena like the glory effect (Demangeon et al., 2024), potentially linked to cloud microphysics and atmospheric scattering.
Despite its power, transmission spectroscopy has inherent limitations. It requires a transiting planet, which restricts the accessible sample. Additionally, it probes only the terminator region (the day–night boundary), limiting latitudinal and longitudinal coverage. The method is also sensitive to stellar heterogeneity, such as starspots and faculae, which can contaminate or bias spectral interpretations, especially important in the context of rocky

[1] `https://exoplanetarchive.ipac.caltech.edu`, accessed on June 2nd, 2025.

exoplanet observations around M-dwarfs.
An alternative and complementary technique is the observation of thermal emission from exoplanets (e.g., Pino et al., 2020), particularly through the use of phase curves (e.g., Stevenson et al., 2017; Sing et al., 2024; Dang et al., 2025). As a planet orbits its host star, different portions of its dayside and nightside become VI from Earth. By tracking the system's brightness over time, it is possible to infer the planet's thermal structure, heat redistribution efficiency, and composition. Thermal emission occurs primarily in the IR and is sensitive to the atmospheric pressure–temperature (p–T) profile. Molecular species such as H_2O, CO_2, CH_4, and NH_3 can be detected as absorption or emission features in the emergent spectrum. This technique does not require the planet to transit and has been effectively applied using both space-based with Spitzer (Stevenson et al., 2017) and JWST (Sing et al., 2024)) and, in the future, ground-based IR instruments such as HiRISE (e.g., Denis et al., 2025). Furthermore, directly imaged exoplanets, typically young and massive gas giants at wide separations, emit significant thermal radiation due to residual heat from their formation. These objects can be characterized through thermal emission spectroscopy, offering insight into the atmospheric properties of non-transiting exoplanets and complementing studies of older, cooler worlds (e.g., Lagrange, 2014; Chauvin, 2024).

1.3.1 Reflected light

A promising but yet-to-be-fully realized technique for characterizing exoplanet atmospheres is the observation of reflected light by detecting the fraction of stellar radiation that is reflected by an exoplanet's atmosphere or surface back toward the observer. Although direct detections of reflected light from exoplanets remain extremely challenging due to the high contrast and small angular separation between the star and the planet, upper limits and tentative detections have been reported for several targets (e.g., τ Boo, 51 Peg b) (Charbonneau et al., 1999; Martins et al., 2015).
Reflected light observations are conceptually analogous to Earth remote sensing techniques, albeit with the critical difference that exoplanets are observed as spatially unresolved point sources, effectively as a single pixel. This results in disk-integrated spectra, capturing globally averaged atmospheric and surface properties. One of the primary quantities accessible via this method is the planet's geometric albedo, which depends on a complex interplay of atmospheric composition, surface reflectivity, and cloud properties (Marley et al., 1999). By measuring the planet's albedo as a function of wavelength and phase angle, it is possible to infer the presence of scattering and absorbing species, as well as surface features. For instance, Rayleigh scattering manifests as a blue spectral slope, while molecular absorption bands from species such as O_2, H_2O, and CH_4 appear in the VIS and NIR. Furthermore, wavelength-dependent features like the VRE or phase angle-dependent features like the ocean glint may become detectable in favorable cases, particularly for rocky exoplanets orbiting nearby stars (e.g., Seager et al., 2005; Robinson et al., 2010). Fig. 1.10 illustrates the accessible scattering features and indicates the phase angles at which they can be observed, as explained in Vaughan et al. (2023).
Complementary to intensity-based reflected light observations is the measurement of the

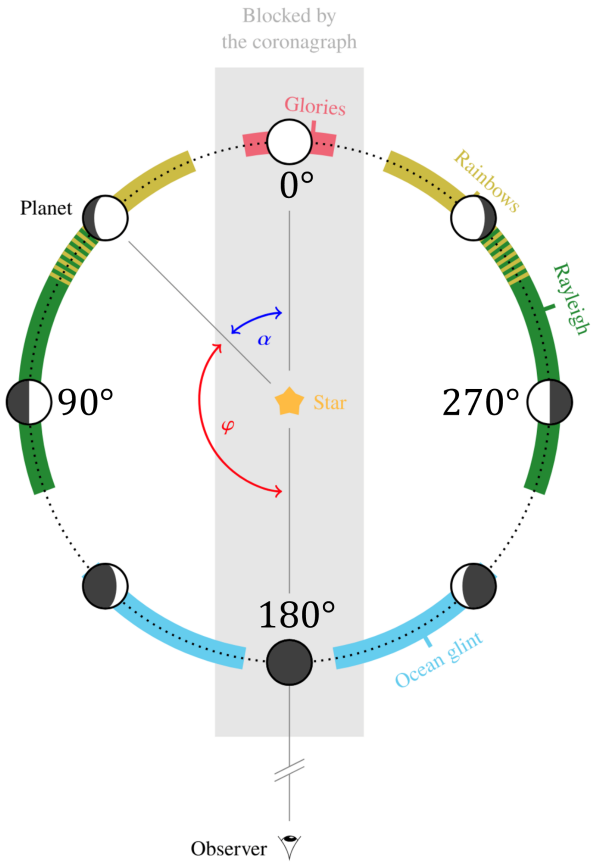

Figure 1.10: Schematic illustration of an exoplanet observed at different phase angles, α, and the scattering features accessible along its phase curve. Figure adapted from Vaughan et al. (2023), which demonstrates how a potential coronagraph for HWO might obscure observations at small and large phase angles.

degree of linear polarization. Light that is scattered by molecules, aerosols, or cloud particles in an exoplanet's atmosphere becomes linearly polarized, as well as light that reflects off certain types of planetary surfaces. The degree and angle of polarization vary with phase angle and wavelength and can enhance the detectability of specific planetary features. For instance, polarization can improve sensitivity to ocean glint at crescent phases, or reveal the cloudbow feature, which is an indicator of liquid water clouds (Stam, 2008; Karalidi et al., 2012; Emde et al., 2017; Trees & Stam, 2022).
Future telescopes and instruments, both on the ground and in space, are expected to make reflected light observations a viable pathway to exoplanet characterization. Notably, the Extremely Large Telescope (ELT) with instruments such as ANDES (Pallé et al., 2025) and PCS (Kasper et al., 2021), and proposed space-based missions like the Habitable Worlds Observatory (HWO) (National Academies of Sciences & Medicine, 2021), aim to directly image and spectrally characterize a range of exoplanets in reflected light, including potentially habitable Earth-sized planets in the solar neighborhood (Quanz et al., 2022).

In particular, this technique may enable the first atmospheric studies of Proxima b, the closest known exoplanet to Earth, which does not transit its host star. Reflected light spectroscopy and polarimetry could allow us to probe its lower atmosphere and surface conditions, potentially reaching down to the troposphere, the region where clouds form and where habitability-relevant processes occur. Among all current atmospheric characterization techniques, reflected light remains the only method directly sensitive to surface features, making it a unique approach for the future study of rocky exoplanets. However, despite its scientific potential, reflected light characterization remains technically demanding. The contrast ratio between star and planet in reflected light can be as low as 10^{-9} for an Earth-analog orbiting a Sun-like star (Pallé et al., 2025). This imposes stringent requirements on instrumental stability, starlight suppression, and calibration precision. However, the use of polarimetry can significantly enhance signal detection, as stellar light is typically unpolarized (Cotton et al., 2017) while the planetary signal is polarized, improving the contrast between the star and the planet and enhancing signal detections.

1.3.2 Atmospheric retrieval of exoplanets

To extract the physical and chemical properties of exoplanet atmospheres from observational data, we employ a technique known as atmospheric retrieval. This process involves comparing observations (e.g., transmission, emission, or reflected light spectra) to theoretical models of planetary atmospheres across a wide parameter space. The goal is to identify the range of atmospheric compositions and structures that are consistent with the observed data (Madhusudhan, 2019; Line et al., 2013). Atmospheric retrieval relies on the use of simplified but flexible atmospheric models that can be evaluated rapidly. These models test hypotheses about the atmospheric p-T structure, molecular abundances, cloud properties, and surface or planetary parameters. Unlike detailed general circulation models (GCMs) used for Earth or Solar System planets, retrieval models are typically one-dimensional and assume global averages. This is due to the limited information content in exoplanet spectra, which are generally disk-integrated and low in spectral resolution and signal-to-noise ratio (SNR). At the core of retrieval methods lies a Bayesian inference framework, which estimates the posterior probability distribution of the model parameters given the data (Trotta, 2008). This is expressed using Bayes' theorem:

$$P(\theta|D) = \frac{P(D|\theta)\,P(\theta)}{P(D)}. \tag{1.13}$$

Here, $P(\theta|D)$ is the posterior probability distribution of the parameters θ given the data D, $P(D|\theta)$ is the likelihood, representing how well the model matches the observations for a given set of parameters, $P(\theta)$ is the prior, encoding any assumptions or constraints on the parameters, and $P(D)$ is the evidence, a normalization constant in this context. The forward model is used to simulate the planetary spectrum given a set of atmospheric parameters. A retrieval algorithm, often employing techniques such as Monte Carlo Markov Chain (MCMC) or nested sampling, explores the parameter space to construct the full posterior distribution. The result of this process is not just a single "best-fit" model (i.e., the

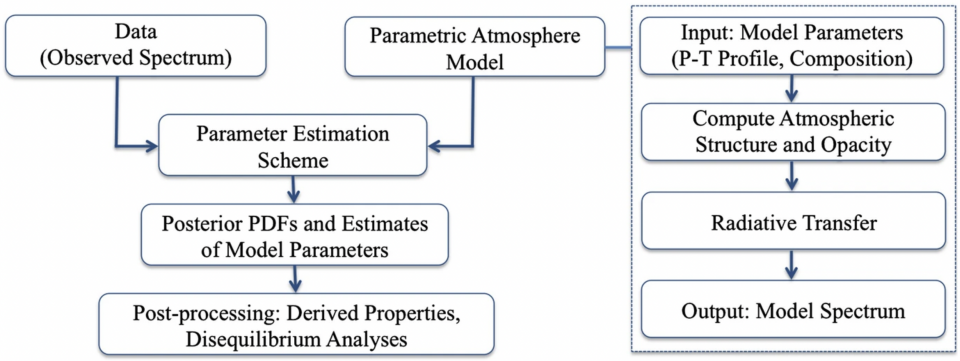

Figure 1.11: In an atmospheric retrieval code an observed spectrum is compared to a parametric model using statistical inference to estimate key atmospheric properties such as the p-T profile, molecular abundances, and cloud/haze properties. Retrieval methods produce posterior probability distributions for these parameters, enabling further inference of derived quantities like elemental abundance ratios. Figure from Madhusudhan (2018).

one with maximum likelihood), but a statistically robust characterization of the allowed parameter ranges, including uncertainties and degeneracies. The best-fit model refers to the set of parameters that maximizes the likelihood function and provides an intuitive comparison to the data, but may not represent the full complexity or uncertainty in the solution space. For scientific interpretation, the marginalized posterior distributions and credible intervals are typically more informative than the single best-fit solution.
Atmospheric retrieval has become a standard approach for analyzing transmission spectroscopy data, particularly for hot Jupiters where molecular and atomic features (e.g., H_2O, CO, Na) are prominent and relatively easier to detect in both space-based (e.g., Barstow et al., 2020; Welbanks et al., 2019) and ground-based observations (e.g., Seidel et al., 2020a; Gibson et al., 2020). More recently, efforts have been made to extend retrieval techniques to thermal emission spectra and reflected light observations (Lupu et al., 2016; Susemiehl et al., 2023). The latter introduces additional complexities, such as the impact of clouds, surface reflectance, and phase-dependent geometry, requiring further methodological advances. Despite they are broadly use to interpret exoplanet atmophere observations, retrieval models come with several limitations. Because they must evaluate the forward model many thousands of times, they rely on computationally efficient approximations, such as 1D atmospheres, equilibrium chemistry, and parametric p-T profiles. Additionally, there are often degeneracies between different parameters (e.g., between cloud opacity and molecular abundances) that limit the uniqueness of the inferred solutions. As observational precision increases with missions like JWST and future direct imaging telescopes, atmospheric retrieval methods will need to evolve to include more physical realism, such as 3D structures, disequilibrium chemistry, and scattering effects.

1.3.3 Habitability and biosignatures

An exoplanet is said to lie within the habitable zone (HZ) of its host star when its orbital distance allows for the presence of liquid water on its surface, assuming Earth-like atmospheric pressure (Kasting et al., 1993; Kopparapu et al., 2013). The concept of the HZ is not a strict boundary, but rather a range that depends on stellar luminosity, planetary atmosphere, and geophysical factors such as volcanism and tectonic recycling. While the presence of liquid water is a necessary condition for life as we know it, it is by no means sufficient. Thus, the HZ merely serves as a first-order filter in the search for potentially habitable worlds. The detection of a biosignature, a molecule or phenomenon that provides scientific evidence of past or present life, is a central objective in exoplanet science. On Earth, examples of atmospheric biosignatures include O_2, O_3, CH_4, and N_2O, which are produced in large quantities by biological processes and maintained far from thermodynamic equilibrium (Des Marais et al., 2002; Meadows et al., 2018). A classic example is the coexistence of O_2 and CH_4, which under abiotic conditions would rapidly react and disappear from the atmosphere. This simultaneous presence signals a strong disequilibrium that on Earth is maintained by life. However, caution must be exercised in interpreting these biosignatures, as several gases once proposed as biosignatures can also be generated through abiotic processes. For example, CH_4 can arise from serpentinization in hydrothermal systems, and phosphine (PH_3) may form in reducing atmospheres without biological activity (Sousa-Silva et al., 2020). Likewise, O_2 itself can be produced abiotically through photodissociation of water followed by hydrogen escape, particularly around M-dwarf stars (Luger & Barnes, 2015). These false positives show the importance of considering planetary context and complementary spectral features.
Geophysical processes such as volcanic outgassing, mantle redox state, and tectonics play a crucial role in setting the baseline composition of an atmosphere (Noack et al., 2017). These factors determine the outgassing rates of CO_2, SO_2, and H_2O, all of which shape the planet's climate and influence the detectability and stability of potential biosignatures. Additionally, photochemistry can significantly modify atmospheric compositions, potentially destroying or creating biosignature-like molecules in ways that depend on stellar UV flux, temperature, and atmospheric composition (Harman et al., 2018). In this context, the next generation of observatories will revolutionize our capacity to assess the habitability of exoplanets. From the ground, instruments like ANDES and PCS at the ELT will deliver high-resolution spectra that may constrain molecular signatures in reflected light. In space, future missions such as the HWO (National Academies of Sciences & Medicine, 2021) and LIFE (Quanz et al., 2022) are designed to directly image and spectrally characterize Earth-sized planets in the HZ of nearby stars.

1.4 Scope of this Thesis

In this thesis, I approach the study of Earth through the lens of an exoplanet observer. To do this, I employ advanced radiative transfer models, commonly used in Earth remote

sensing, to simulate how Earth would appear as a distant, spatially unresolved point of light. I use a large catalog of Earthshine observations, which capture sunlight reflected by Earth and then scattered off the darker portion of the visible Moon, to derive disk-integrated spectra representative of Earth's appearance as an exoplanet. By simulating these Earthshine datasets, I aim to develop a robust and validated model that can inform the physical requirements for accurately interpreting exoplanet observations.
This thesis is guided by the following central questions:

- Q1: Exoplanet models involve a vast number of parameters and are computationally expensive. How many, and which, parameters are truly necessary to include in order to reliably compare models with observations? Using Earth as a benchmark, can we identify the threshold between oversimplification and unnecessary complexity? This is closely related to Einstein's dictum: "Everything should be made as simple as possible, but not simpler."

- Q2: What insights can be gained from studying Earthshine observations? Specifically, can polarimetric measurements enhance our ability to distinguish key planetary characteristics such as surface types, cloud cover, or biosignatures?

- Q3: How does an exoplanet model of Earth compare to traditional Earth system models? Can this independent approach provide novel validation tools or even lead to improvements in how we model and understand Earth's own energy balance?

2

Radiative transfer: theory and simulations

2.1 Introduction to radiative transfer

Radiative transfer (RT) is the study of the interaction between electromagnetic radiation and matter. It is a topic that lies at the core of both astrophysical and atmospheric sciences, providing the foundation for interpreting the spectra of distant stars and galaxies and modeling the energy balance in planetary atmospheres. RT describes how solar and terrestrial radiations propagate through the atmosphere, accounting for processes such as absorption, scattering, and emission by gases, aerosols, clouds, and the surface.
A fundamental understanding of RT is essential for this thesis, as it underpins the modeling of Earth as an exoplanet and the interpretation of disk-integrated observations, such as Earthshine. This chapter introduces the theoretical framework of the RT equation, explains its physical significance, and outlines the main numerical methods used to solve it. The content of this Section is based on the treatments presented in Liou (2002) and Marshak & Davis (2005). In deriving the RT equation, we adopt the plane-parallel atmosphere approximation, where variations in radiance and atmospheric properties are assumed to occur only in the vertical direction.

2.1.1 Interaction between radiation and the atmosphere

The fundamental quantity used to describe the transport of radiaiton in the atmosphere is the spectral radiance $I_\lambda(\mathbf{r}, \theta, \phi, t)$, which depends on spatial position $\mathbf{r}$, propagation direction (θ, ϕ) and time t. The subscript λ denotes its wavelength dependence. The explicit dependence on position and time is often omitted for simplicity. Spectral radiance represents the energy per unit time, area, solid angle, and wavelength and is expressed

in units of $\mathrm{W\,m^{-2}\,sr^{-1}\,\mu m^{-1}}$. By integrating radiance over the solid angle, we obtain the spectral irradiance $E_\lambda(\mathbf{r}, t)$, in units of $\mathrm{W\,m^{-2}\,\mu m^{-1}}$, which represents the total energy incident on a surface per unit area and wavelength.
As radiation travels through the atmosphere, it interacts with its constituents (i.e., gases, aerosols, and cloud particles), undergoing several key processes, typically grouped into four main categories:

- Transmission, where photons pass through the medium without any interaction;
- Absorption, in which photons are absorbed by particles or molecules when their energy matches the energy difference between two quantized states;
- Scattering, where photons are redirected by particles or molecules;
- Emission, which occurs when matter emits radiation, adding new energy to the radiation field.

Absorption and scattering play a significant role in the VIS and IR spectral regions. For example, H_2O, CO_2, and O_3 exhibit strong absorption features in the IR. At shorter wavelengths, absorption by O_3 is the more dominant process. Understanding these processes is important for interpreting how radiation propagates through the atmosphere and retrieving atmospheric and surface properties from satellite and ground-based observations.

2.1.2 Absorption

If a photon traveling through the atmosphere has an energy (or, equivalently, a wavelength) that matches the energy difference between two quantized states of a molecule, it can be absorbed, causing the molecule to transition to a higher energy level. This absorption process is governed by the molecular structure and composition, as well as the energy of the incoming radiation. The amount of absorption varies significantly depending on both these factors.
When a radiance I_λ passes through a layer of absorbing material with infinitesimal path length ds, the differential loss due to absorption is described by the following extinction law as

$$dI_\lambda = -\kappa_\lambda \rho I_\lambda ds, \tag{2.1}$$

where ρ is the density of the medium and κ_λ is the wavelength-dependent mass extinction coefficient.
In the approximation of a plane-parallel atmosphere, we replace the differential displacement ds with the vertical differential

$$dz = ds \cdot \cos(\theta) = ds \cdot \mu, \tag{2.2}$$

where $\mu = \cos(\theta)$ is the cosine of the zenith angle of the radiation path.
To simplify the RT equation, we introduce the concept of optical depth (or optical thick-

ness), defined as the line integral of the extinction coefficient along the vertical path:

$$\tau(z) = \int_0^z \kappa_\lambda \rho(z')dz', \tag{2.3}$$

from which we can derive its differential simply as

$$d\tau = \kappa_\lambda \rho dz. \tag{2.4}$$

Substituting this into the extinction law, we obtain the absorption term of the RT equation:

$$\mu \left(\frac{dI_\lambda}{d\tau} \right)_{\text{abs}} = -I_\lambda. \tag{2.5}$$

This first-order linear differential equation can be solved analytically, yielding the Beer–Bouguer– Lambert law:

$$I_\lambda(\tau) = I_\lambda(0)e^{-\tau/\mu}. \tag{2.6}$$

This solution reveals the physical meaning of the optical depth: it quantifies the exponential attenuation of radiation as it propagates through an absorbing medium.

2.1.3 Emission

Emission is the inverse process of absorption. The energy previously absorbed by matter is released in the form of photons. The amount and the spectral distribution of the emission depend primarily on the temperature of the material. The simplest model of an emitter is the black body, whose emission is described by Planck's radiation law:

$$B_\lambda(T) = \frac{2hc^2}{\lambda^5} \frac{1}{e^{\frac{hc}{\lambda k_B T}} - 1}, \tag{2.7}$$

where B_λ is the spectral radiance emitted at wavelength λ, T is the temperature of the black body, h is Planck's constant, c is the speed of light in vacuum, and k_B is Boltzmann's constant.
In the atmosphere, the two principal sources of electromagnetic radiation are:

- the Sun, which emits primarily in the UV, VIS, and NIR parts of the spectrum;
- the Earth's atmosphere system itself, which emits thermal (IR) radiation.

Both black body radiances are shown in Fig. 2.1. The two curves span a broad spectral range, from approximately 0.1 μm to 100 μm. Solar radiation, often called shortwave radiation, dominates at wavelengths shorter than about 4 μm. In contrast, radiation emitted by the Earth and its atmosphere (longwave radiation) prevails in the thermal IR region, typically between 4 and 100 μm. Because of their vastly different surface temperatures, the peaks of their respective emission curves lie at different wavelengths, around 0.5 μm for the Sun and 10.1 μm for the Earth. The clear spectral distinction between solar and

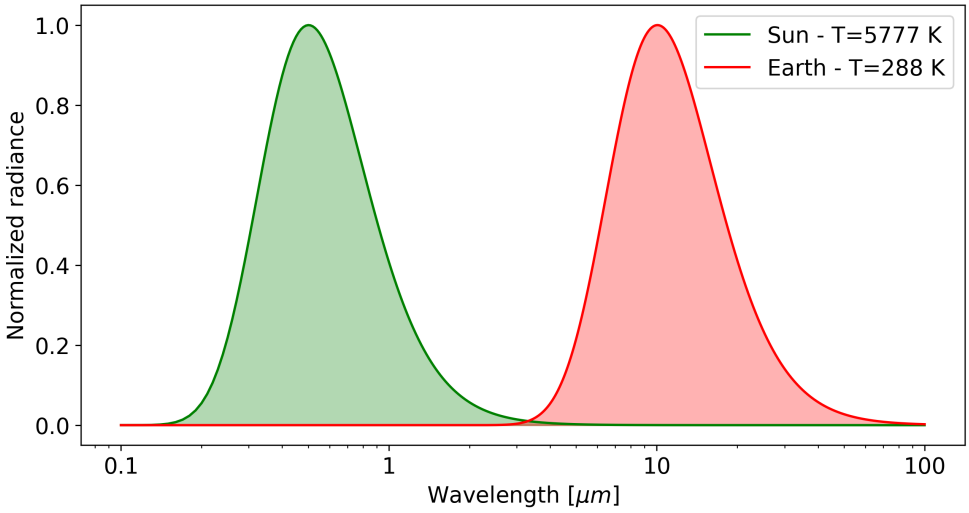

Figure 2.1: Normalized radiances of the Sun and the Earth, modeled as two black bodies with temperatures of $T_\odot = 5777\,K$ and $T_\oplus = 288\,K$, respectively.

terrestrial emission simplifies remote sensing, as the dominant radiation source is usually unambiguous at most wavelengths.
In the RT equation, thermal emission is introduced via Planck's law. The emission term is proportional to the Planck function and modulated by the absorption properties of the medium:

$$\mu \left(\frac{dI_\lambda}{d\tau} \right)_{\text{emiss}} = (1 - \tilde{\omega}) B[T(\tau)], \tag{2.8}$$

where the black body radiation depends on the optical depth through the temperature of the medium. The factor $(1 - \tilde{\omega})$ accounts for the fact that only the absorbing part of the medium contributes to thermal emission. In a scattering-dominated regime, instead, no radiation is absorbed, and thus no radiation can be reemitted as thermal radiation. The single scattering albedo $\tilde{\omega}$ is defined as

$$\tilde{\omega} = \frac{\sigma_\lambda}{\sigma_\lambda + \kappa_\lambda}, \tag{2.9}$$

where σ_λ and κ_λ are, respectively, the scattering and absorption coefficients. The single scattering albedo $\tilde{\omega}$ characterizes the dominance of scattering over extinction:

- $\tilde{\omega} = 0$ for purely absorbing medium, without any scattering;
- $\tilde{\omega} = 1$ for purely scattering medium, with no absorption and thus no emission.

Thus, in a scattering-dominated regime, thermal emission vanishes because there is negligible absorption to power it.

2.1.4 Scattering

In addition to being absorbed or emitted, photons can also be redirected upon interaction with molecules or particles in the atmosphere. In the RT equation, this process, scattering, has a dual effect: it removes radiance from the direction of interest by deflecting photons away, and it adds radiance by redirecting photons into the direction of interest from other paths. The extent of scattering, and more importantly, its angular distribution, depends on the wavelength of the radiation and its relation to the size of the scattering particles. The relative size of a scattering particle is described by the size parameter

$$x = \frac{2\pi r}{\lambda}, \tag{2.10}$$

where r is the physical radius of the particle. Depending on the value of x, different scattering regimes apply:

- **Rayleigh scattering:** Occurs when particles are much smaller than the wavelength of the incident radiation ($x \ll 1$). The scattering intensity varies as λ^{-4}, making shorter wavelengths (e.g., blue light) scatter much more efficiently than longer wavelengths (e.g., red light). This is the process responsible for the blue color of the sky. Rayleigh scattering is nearly symmetric in the forward and backward directions, as illustrated in the left panel of Fig. 2.2.

- **Mie scattering:** Applies when the particle size is comparable to the wavelength ($x \sim 1$), as is typical for cloud droplets in the VIS and IR. Mie scattering is generally anisotropic, with a strong preference for the forward direction (see the central panel of Fig. 2.2).

- **Geometric optics:** When particles are much larger than the wavelength ($x \gg 1$), scattering can be approximated using geometric optics, where photons behave like rays that reflect and refract according to Snell's law and Fresnel's equations. This regime is commonly used to describe the interaction of visible light with raindrops. An example is shown in the right panel of Fig. 2.2.

The scattering patterns illustrated in Fig. 2.2 were generated using the phase curves presented in Liou (2002, Fig. 3.13). These curves correspond to cloud droplets ($\sim 10\ \mu m$), aerosols ($\sim 1\ \mu m$), and molecules ($\sim 10^{-4}\ \mu m$) illuminated by visible light with a wavelength of approximately $\sim 0.5\ \mu m$. As such, they represent the three scattering regimes discussed above: geometric optics, Mie scattering, and Rayleigh scattering, respectively. The fundamental function to describe the scattering properties of a medium is the scattering phase function $P(\mu, \phi; \mu', \phi')$, which describes the conditional probability of scattering into the new direction (μ, ϕ), coming from the initial direction (μ', ϕ'). The phase function is incorporated in the RT equation in two terms. The first one weights the intensity coming from all directions in a layer of the atmosphere by the phase function to compute how

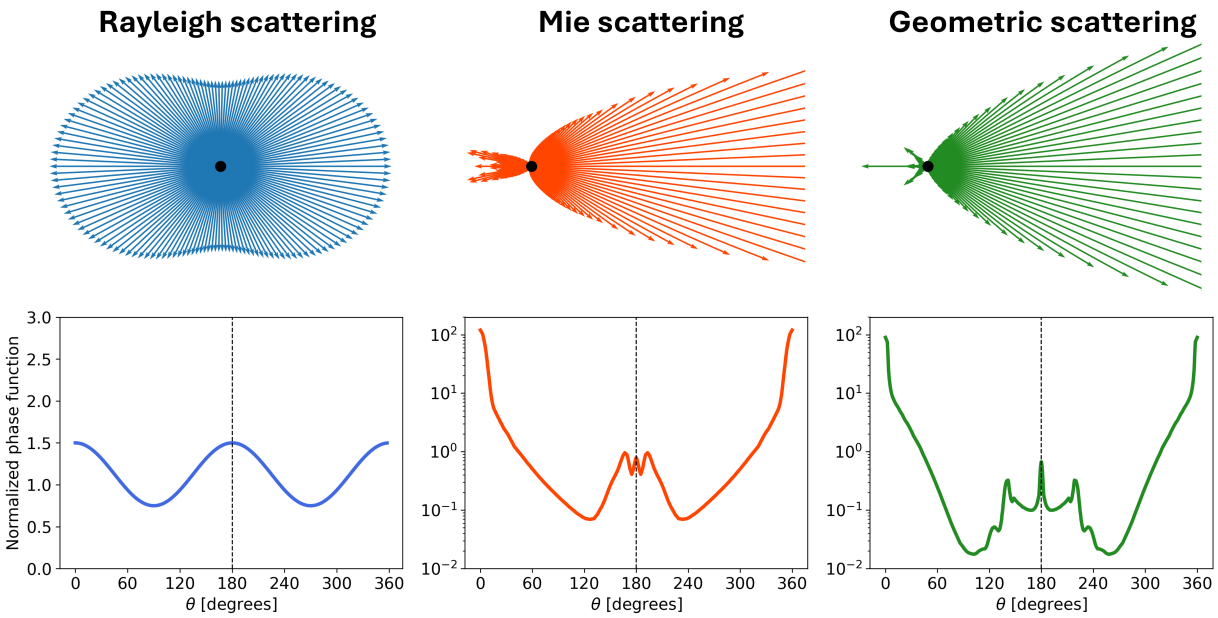

Figure 2.2: Top row: scattering patterns for the Rayleigh, Mie, and Geometric optics scattering regimes. The black dot shows the position of the scattering particle. Bottom row: phase functions used to generate the scattering patterns above. The phase functions are taken from Fig. 3.13 of Liou (2002).

much of that intensity will be scattered in a specific direction of propagation:

$$\mu \left(\frac{dI_\lambda(\mu, \phi)}{d\tau} \right)_{\text{scat}} = \frac{\tilde{\omega}}{4\pi} \int_0^{2\pi} \int_{-1}^{1} I_\lambda(\tau, \mu', \phi') P(\mu, \phi; \mu', \phi') d\mu' d\phi', \tag{2.11}$$

where 4π is introduced as a normalization term, and the $\tilde{\omega}$ signifies the strength of scattering. The second term weights how much of the unscattered starlight, which enters the atmosphere at an angle (μ_0, ϕ_0), is scattered into the direction (μ, ϕ). Additionally, this term must be attenuated by an extinction term proportional to $e^{-\tau/\mu_0}$ as

$$\mu \left(\frac{dI_\lambda(\mu, \phi)}{d\tau} \right)_{\text{scat}} = \frac{\tilde{\omega}}{4\pi} F_\odot e^{-\tau/\mu_0} P(\mu, \phi; \mu_0, \phi_0) = S e^{-\tau/\mu_0} P(\mu, \phi; \mu_0, \phi_0), \tag{2.12}$$

where $F_\odot$ is the incident sunlight, and, in the second equivalence, we defined a source term S incorporating the terms

$$S = \frac{\tilde{\omega} F_\odot}{4\pi}. \tag{2.13}$$

A notable example of a scattering phase function is the one describing Rayleigh scattering:

$$P(\mu) = \frac{3}{4}(1 + \mu^2). \tag{2.14}$$

As shown in Fig. 2.2, this phase function is symmetric with respect to the forward ($\mu = 1$) and backward ($\mu = -1$) directions.

2.1.5 The radiative transfer equation

By combining all the components derived in the previous sections, we arrive at the RT equation, which governs the evolution of radiance as it propagates through a medium. This equation incorporates the effects of absorption, emission, and scattering, and serves as a fundamental tool in atmospheric sciences, astrophysics, and remote sensing:

$$\begin{aligned}\mu\frac{dI_\lambda(\tau,\mu,\phi)}{d\tau} = &- I_\lambda + \frac{\tilde{\omega}}{4\pi}\int_0^{2\pi}\int_{-1}^{1} I_\lambda(\tau,\mu',\phi')P(\mu,\phi;\mu',\phi')d\mu' d\phi' + \\ &+ Se^{-\tau/\mu_0}P(\mu,\phi;\mu_0,\phi_0) + (1-\tilde{\omega})B[T(\tau)].\end{aligned} \tag{2.15}$$

The RT equation contains sink terms representing extinction, either by absorption or out-scattering, and source terms accounting for in-scattering, incoming stellar radiation, and thermal emission, modelled using the Planck function $B[T(\tau)]$.
As an integro-differential equation, where the radiance in a given direction depends on contributions from all other directions, the RT equation cannot be solved analytically without substantial approximations. Consequently, a variety of numerical methods have been developed to obtain its solutions. The following Section 2.2 presents both one-dimensional (1D) and three-dimensional (3D) numerical methods used to solve the RT equation.

2.1.6 Surface reflection

While the RT equation describes the propagation of radiance from the TOA down to the surface, it is also necessary to model the interaction of radiation with the surface itself. Part of the incident radiation is absorbed by the surface, while the remainder is reflected back into the atmosphere. The albedo a quantifies the fraction of incident radiation that is reflected, whereas the bidirectional reflectance distribution function (BRDF) characterizes the angular distribution of this reflected radiation.
Analogous to the phase function P used to describe scattering, the BRDF is a function of both the incoming direction (μ', ϕ') and the outgoing direction (μ, ϕ), and it describes the probability that light arriving from one direction is reflected into another. The simplest example of BRDF is the Lambertian reflectance, which assumes that the surface reflects radiation isotropically:

$$\mathrm{BRDF}(\mu,\phi;\mu',\phi')_{\mathrm{Lamb}} = \frac{a}{\pi}, \tag{2.16}$$

where a is the albedo of the surface and the π factor is included to ensure energy conservation.

2.2 Numerical methods for radiative transfer

2.2.1 One-dimensional solvers

In this Section, I will briefly review some of the most widely used 1D numerical methods for solving the RT equation. Some methods adopt a more direct approach, discretizing

the angular domain and numerically solving the resulting system of differential equations. Others employ more indirect techniques, such as the doubling-adding method and Monte Carlo simulations. I will outline the fundamental principles behind each of these methods and highlight their respective areas of application.

Discrete ordinate method

The discrete ordinate method (DOM) is one of the most straightforward approaches for numerically solving the RT equation. It was first introduced by Chandrasekhar (1950) and then applied by Liou (1973) to cloudy atmospheres.
To illustrate the method, we consider a simplified scenario assuming azimuthal symmetry, isotropic scattering, and no atmospheric emission. More advanced implementations drop these assumptions to model more general cases.
Under these conditions, the RT equation becomes

$$\mu \frac{dI(\tau,\mu)}{d\tau} = -I(\tau,\mu) + \frac{\tilde{\omega}}{2}\int_{-1}^{1} I(\tau,\mu')d\mu' + Se^{-\tau/\mu_0}. \tag{2.17}$$

Having assumed isotropic scattering, the phase function simplifies to $P(\mu;\mu') = 1$, eliminating directional dependence in the scattering term.
To solve this equation numerically, we discretize the continuous angular direction μ into $2n$ directions μ_i and use the Gauss-Legendre quadrature formula to discretize the integral:

$$\mu_i \frac{dI_i(\tau)}{d\tau} = -I_i(\tau) + \frac{\tilde{\omega}}{2}\sum_{j=-n}^{n} a_j I_j + Se^{-\tau/\mu_0}, \tag{2.18}$$

where the a_j coefficients are the quadrature weights.
This system of equations forms a set of coupled, non-homogeneous first-order differential equations. It is typically solved by combining the general solution of the corresponding homogeneous system with a particular solution of the inhomogeneous system.
Although this example assumes isotropic scattering, DOM is also capable of handling anisotropic scattering accurately, with increasing precision as more angular directions are included, at the cost of greater computational complexity. The method is especially useful when the full radiation field, including the angular distribution at each atmospheric level, is required.

Two-stream approximation

The two-stream approximation method (Toon et al., 1989) is a simplified and computationally efficient variant of the DOM. It assumes radiation propagates in only two directions: upward and downward. We denote the corresponding radiances by $I^{\uparrow}$ and $I^{\downarrow}$ respectively. The sum in Eq 2.18 reduces to only two elements, and for the special case of $n = 1$, the

quadrature weights simplify to $a_1 = a_{-1} = 1$. The system in Eq. 2.18 reduces to:

$$\begin{aligned} \mu_1 \frac{dI^{\uparrow}}{d\tau} &= -I^{\uparrow} - \frac{\tilde{\omega}}{2}(I^{\uparrow} + I^{\downarrow}) - Se^{-\tau/\mu_0} \\ -\mu_1 \frac{dI^{\downarrow}}{d\tau} &= -I^{\downarrow} - \frac{\tilde{\omega}}{2}(I^{\uparrow} + I^{\downarrow}) - Se^{-\tau/\mu_0}. \end{aligned} \tag{2.19}$$

The next step is to define two new radiances, the sum and the difference between the upward and downward radiances: $M = I^{\uparrow} + I^{\downarrow}$ and $N = I^{\uparrow} - I^{\downarrow}$. Summing and subtracting the two equations above, we obtain

$$\begin{aligned} \mu_1 \frac{dM}{d\tau} &= N \\ \mu_1 \frac{dN}{d\tau} &= -(1 + \tilde{\omega})M - 2Se^{-\tau/\mu_0}. \end{aligned} \tag{2.20}$$

Differentiating these equations with respect to τ and substituting back, we arrive at two decoupled second-order differential equations:

$$\begin{aligned} \frac{d^2M}{d\tau^2} &= -\frac{1 + \tilde{\omega}}{\mu_1^2} M - \frac{2S}{\mu_1^2} e^{-\tau/\mu_0} \\ \frac{d^2N}{d\tau^2} &= -\frac{1 + \tilde{\omega}}{\mu_1^2} N + \frac{2S}{\mu_1 \mu_0} e^{-\tau/\mu_0} \end{aligned} \tag{2.21}$$

These equations can be solved efficiently and then inverted to retrieve $I^{\uparrow}$ and $I^{\downarrow}$.
While very simple and dependent on the approximation of only two streams, this method is still very valuable due to its fast evaluation of a solution to the RT equation. In particular, it is highly relevant for GCMs, where computational efficiency is a significant factor.

Doubling-adding method

Compared to previous methods, the doubling-adding method approaches the RT equation from a fundamentally different perspective. First introduced by Hansen & Travis (1974) for the study of sunlight propagation through clouds, this method does not discretize the angular space to solve differential equations, as in the DOM. Instead, it constructs the solution by working with the integral properties of thin atmospheric layers.
The vertical structure of the atmosphere is divided into very thin, horizontally homogeneous layers (typically with optical thickness $\Delta\tau < 10^{-8}$). For each of these thin layers, the reflectance R and transmittance T functions are computed based on the single-scattering approximation, using the phase function P and the single-scattering albedo $\tilde{\omega}$:

$$R(\mu, \phi; \mu_0, \phi_0) = \frac{\tilde{\omega}\Delta\tau}{4\mu\mu_0} P(\mu\phi; -\mu_0, \phi_0) \tag{2.22}$$

$$T(\mu, \phi; \mu_0, \phi_0) = \frac{\tilde{\omega}\Delta\tau}{4\mu\mu_0} P(-\mu\phi; -\mu_0, \phi_0). \tag{2.23}$$

To obtain the radiative properties of thicker layers, the method applies two recursive operations: doubling, which combines two identical layers to simulate a thicker one, and adding, which merges different layers. Through repeated application of these steps, the method builds up the full atmospheric column to a desired optical depth or all the way to the surface.
The doubling-adding method is particularly effective for atmospheres that are stratified and horizontally homogeneous. It naturally accounts for multiple scattering by combining multiple single-scattering R and T and is especially useful in optically thick regimes, such as cloudy layers.

Monte Carlo methods

The last method presented in this short review is Monte Carlo Radiative Transfer (MCRT). Instead of tackling the RT equation directly, the MCRT method relies on a probabilistic reinterpretation of the physical processes described by the RT equation. While many different reviews exist of the Monte Carlo method, we refer mainly to Mayer (2009) and Noebauer & Sim (2019). As an illustrative example, we consider the simplest atmospheric process: photon absorption.
From the Beer-Bouguer-Lambert law, we can determine that the probability of survival of photons travelling in the atmosphere is

$$p(\tau) = \frac{\#\text{ of photons survived after } \tau}{\#\text{ of initial photons at } \tau = 0} = \frac{I(\tau)}{I(0)} = e^{-\tau}. \tag{2.24}$$

In this sense, we can reinterpret the optical thickness as a measure of the probability of absorption for a photon traveling through the atmosphere.
From the probability density function $p(\tau)$ we can compute the corresponding cumulative density function (CDF) as

$$C(\tau) = \int_0^\tau e^{-\tau'} d\tau' = 1 - e^{-\tau}. \tag{2.25}$$

In an MCRT simulation, the trajectories of photons launched from the TOA are simulated using random number generators. Specifically, a random number $\xi \in (0, 1)$ is drawn and used to sample from the CDF using inverse transform sampling. This is then used to sample the CDF by inverse sampling:

$$\xi = 1 - e^{\tau} \quad \rightarrow \quad \tau = -\ln(1 - \xi). \tag{2.26}$$

This sampled optical depth is then converted into a physical distance traveled by the photon using the definition of optical depth. Assuming a constant extinction coefficient $\kappa_\lambda \rho$ along the path, the relation becomes

$$s = \frac{\tau}{\kappa_\lambda \rho}. \tag{2.27}$$

After traveling this distance s, the photon is considered absorbed by the atmosphere and is removed from the simulation. Other processes, such as emission, scattering, and surface interactions, can similarly be described probabilistically and incorporated into the MCRT framework.
By simulating a large number of photons (typically $N \sim 10^6$), the cumulative distribution function is sampled more accurately, resulting in a more precise simulation of radiative processes. The error in an MCRT simulation scales as $\sigma \sim 1/\sqrt{N}$, meaning that a high number of photon packets is needed to keep statistical noise low.
Despite its computational cost, MCRT has several advantages over the other methods discussed in this Section. It is highly flexible, can be naturally generalized to complex geometries and to 3D domains, and even include polarization effects (Marchuk et al., 1980). However, due to its high computational cost, it is not suitable for GCMs, which require fast and lightweight algorithms. Instead, MCRT is typically used for remote sensing retrievals, benchmarking, and simulations involving complex atmospheric scenes, such as clouds and surface interactions. For example, MCRT methods have been employed to simulate radiances for satellite missions like EarthCARE and PACE, where accurate treatment of 3D radiative effects is critical.

2.2.2 The three-dimensional solver MYSTIC

1D models are widely used due to their simplicity and computational efficiency, but the plane-parallel approximation they rely on can be too restrictive for some real-world scenarios. Atmospheric features such as broken clouds, complex terrain, urban structures, and shadowing effects introduce spatial heterogeneities that cannot be captured by 1D models but significantly influence the radiance distribution through the atmosphere. To accurately represent these effects, 3D RT models are required.
Solving the RT equation in 3D is substantially more complex than in 1D, as it demands resolving both spatial and angular variability in all directions. In this thesis, I employed MYSTIC, the Monte Carlo code for the phYSically correct Tracing of photons In Cloudy atmospheres (Mayer, 2009; Emde et al., 2010), to simulate Earth as an exoplanet. MYSTIC is part of the libRadtran software package (Mayer & Kylling, 2005a; Emde et al., 2016) and is a comprehensive 3D Monte Carlo RT code capable of handling clouds, aerosols, polarization, surface inhomogeneities, and complex atmospheric composition.
To address the otherwise prohibitive computational demands of 3D Monte Carlo simulations, MYSTIC incorporates a variety of techniques to reduce statistical noise and enable simulations at high spectral resolution, making it a powerful tool for detailed atmospheric modeling.

Photon weight

In our simplified description of MCRT, we initially stated that when a photon is absorbed, it is removed from the simulation. While conceptually straightforward, this approach is computationally inefficient, as it requires launching a new photon each time one is

absorbed. Instead, what MYSTIC does is to assign to each photon a weight w, initialized to 1 and multiplied, after each scattering event, by a factor $e^{-\tau}$ (Mayer, 2009). In this way, absorption is treated probabilistically, and the photon continues to propagate, carrying a diminishing weight that reflects its survival probability. To compute, for example, the radiance reaching the surface, the weights of all photons that arrive there are averaged:

$$I_{\text{surf}} = I_0 \mu_0 \cdot \frac{1}{N} \sum_{i=1}^{N_s} w_i, \tag{2.28}$$

where I_0 is the radiance at the TOA, μ_0 the incoming angle, N the total number of photons and N_s the number of photons that reach the surface (some may still be reflected back into space, even if they are not absorbed completely by the atmosphere).
Using photon weights rather than simply counting photon arrivals makes the MCRT approach much more computationally efficient. Furthermore, it allows for radiance and flux calculations at any altitude and in any region by averaging the weights of photons passing through or interacting with a given location. This enables flexible and accurate diagnostics across the entire domain of the simulation.

Local estimate

Since MCRT is often used in remote sensing retrievals, the primary interest is typically in analyzing radiation traveling in a specific direction, such as toward a detector. However, due to the stochastic nature of scattering events, it is unlikely for a photon to travel precisely in the desired direction. As a result, a very large number of photon paths would be required to obtain a sufficient signal from photons that reach the detector by chance. A straightforward way to overcome this limitation is by applying the so-called local estimate (LE) method (Marshak & Davis, 2005).
At each scattering event, we compute the probability that the photon would have scattered in the direction of the detector, denoted μ_{LE}, and assign a corresponding LE weight w_{LE} as

$$w_{\text{LE},i} = w_{i-1} p(\mu_{\text{LE}}) e^{-\tau_{\text{LE}}}, \tag{2.29}$$

where w_{i-1} is the photon weight after the previous scattering, $p(\mu_{\text{LE}})$ is the value of the scattering phase function in the direction of the detector, and τ_{LE} is the extinction between the scattering point and the detector. The geometry of the LE method is shown in Fig. 2.3.
When the photon exits the computational domain, its total contribution to the detector radiance via LE is computed as the sum of all LE weights over the photon's path:

$$w_{\text{LE}} = \sum_{i=1}^{n} w_{\text{LE},i}, \tag{2.30}$$

where n is the number of scattering events.
This method ensures that every photon contributes to the radiance in the detector's direction, not just those that happen to be scattered along that path. As a result, it greatly improves statistical efficiency in directional radiance estimates.

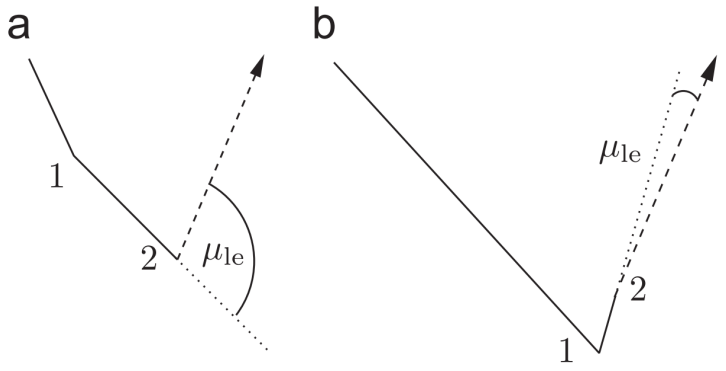

Figure 2.3: Two examples of LE in the case of double scattering. In panel (a), the first scattering moves the photon away from the detector, and thus p_{LE} at the second scattering is small and will contribute with a small LE. In panel (b), instead, the photon gets scattered in the direction of the detector, and thus p_{LE} will produce a spike in radiance. Figure from Buras & Mayer (2011a).

Variance reduction methods

Although the LE method is highly effective for computing radiances in specific directions in MCRT simulations, it has a significant drawback when applied to particles with strongly forward-peaked phase functions, such as cloud droplets and ice crystals. A photon that is scattered, by chance, directly toward the detector will contribute a large LE, since $p(\mu \sim 1)$ is several orders of magnitude higher than in other directions (see the right panel in Fig. 2.3). This results in sharp spikes in the radiance estimates, hindering the convergence behavior expected from an MCRT simulation and increasing statistical noise.
To address this numerical artifact, various variance reduction methods (VRMs) have been developed. In MYSTIC, a suite of VRMs is implemented within a framework called VROOM (Variance Reduction Optimal Options Methods), which applies each method in the most suitable way depending on the context (Buras & Mayer, 2011b). Somewhat counterintuitively, rather than preventing spikes, these VRMs aim to increase their number while reducing their individual weight. This strategy makes the spikes less pronounced and improves convergence. Here, we focus on one such method: detector directional importance sampling (DDIS).
DDIS works by artificially increasing the likelihood of photons being scattered toward the detector before the actual scattering direction is sampled. More precisely, for each scattering event, the direction is sampled from a modified phase function:

$$p^{\dagger}(\mu) = (1 - \epsilon_{\text{DDIS}}) \cdot p(\mu) + \epsilon_{\text{DDIS}} \cdot p_{\text{DDIS}}(\mu'), \tag{2.31}$$

where μ' is the direction toward the detector, ϵ_{DISS} and p_{DISS} are a tunable mixing parameter and an artificial phase function, respectively. Typical choices are $\epsilon_{\text{DISS}} \sim 0.1$ and $p_{\text{DISS}} = C \cdot \max_i (p_i(\mu))$, with C a normalization factor and the p_i representing all the phase functions in the simulation (for all water and ice clouds, aerosols, etc.).

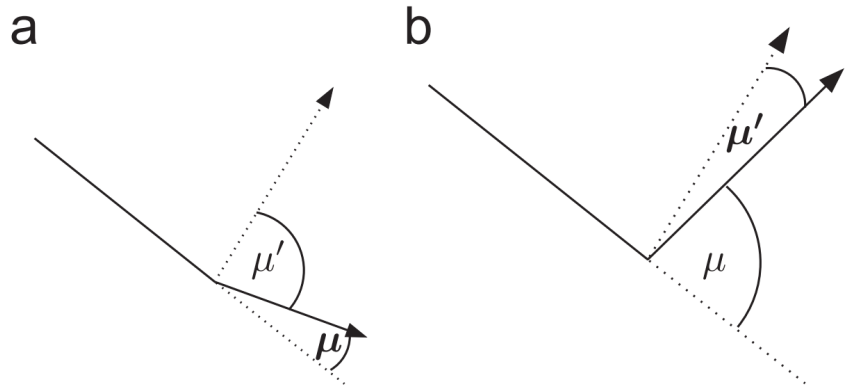

Figure 2.4: Illustration of how DDIS works. With probability $(1 - \epsilon_{\mathrm{DDIS}})$, the photon is scattered naturally and follows the path in the left panel. With probability ϵ_{DDIS}, instead, the photon is first turned towards the detector and then scattered, as shown in the right panel. Figure from Buras & Mayer (2011a).

This equation can be interpreted in the following way: with probability $(1 - \epsilon_{\mathrm{DISS}})$, the photon is scattered according to the original phase function $p(\mu)$, following the natural scattering behavior (left panel of Fig. 2.4). With probability ϵ_{DISS}, instead, the photon is first turned towards the detector, and then scattered on a random direction μ' sampled from the p_{DISS} phase function (right panel of Fig. 2.4). Since the direction μ' chosen from $p_{\mathrm{DISS}}(\mu)$ is unlikely to have been selected from the original phase function $p(\mu)$, we typically have $p(\mu) \ll p_{\mathrm{DISS}}(\mu')$. Naturally, this directional bias introduces a potential error in the radiance calculation. To preserve the physical accuracy and ensure an unbiased result, the photon weight must be adjusted:

$$w_i = \frac{p(\mu)}{p^{\dagger}(\mu)}. \tag{2.32}$$

Since $p(\mu) \ll p^{\dagger}(\mu)$ during a DISS step, the photon's weight is significantly reduced, even though it is more likely to contribute to the detector. This balancing mechanism reduces variance while maintaining the statistical correctness of the simulation.

Absorption lines importance sampling

In a traditional MCRT simulation, obtaining the wavelength-dependent reflectance $I(\lambda)$ requires running a separate simulation for each wavelength bin. This approach becomes computationally prohibitive for high-resolution applications, such as resolving molecular absorption lines. To address this issue, MYSTIC employs the absorption lines importance sampling (ALIS) method (Emde et al., 2011). The idea is simple, yet effective. Only a single simulation is needed, at a reference wavelength λ_0, which is used to trace the photon trajectories. However, within this single simulation, each photon is assigned wavelength-dependent absorption weights $w_{\mathrm{abs}}(\lambda)$ which are updated according to the ab-

sorption optical depth at each wavelength:

$$w_{\text{abs}}(\lambda) = e^{-\tau_{\text{abs}}(\lambda)}. \tag{2.33}$$

Coupling this with the LE method, which can also be treated spectrally, we obtain a final wavelength-dependent radiance of a single photon j as

$$I_j(\lambda) = \sum_{i=1}^{n} w_{\text{abs},i} \cdot w_{\text{LE},i}, \tag{2.34}$$

where n is the number of scattering events along the photon path. To improve the accuracy of the ALIS method, the scattering weights can also be adjusted to reflect their spectral dependence, in contrast to the fixed scattering used in monochromatic simulations. However, because the photon paths are still traced only at the reference wavelength λ_0, the spectral range must remain sufficiently narrow around λ_0 to ensure that the approximation remains valid.

Backward MCRT

A final enhancement to the standard MCRT approach is the use of backward photon tracing. When the goal is to compute the radiance at a detector with a small area relative to the entire computational domain, it becomes highly inefficient to simulate a large number of photons from the TOA, since only a small fraction will reach the detector by chance. To

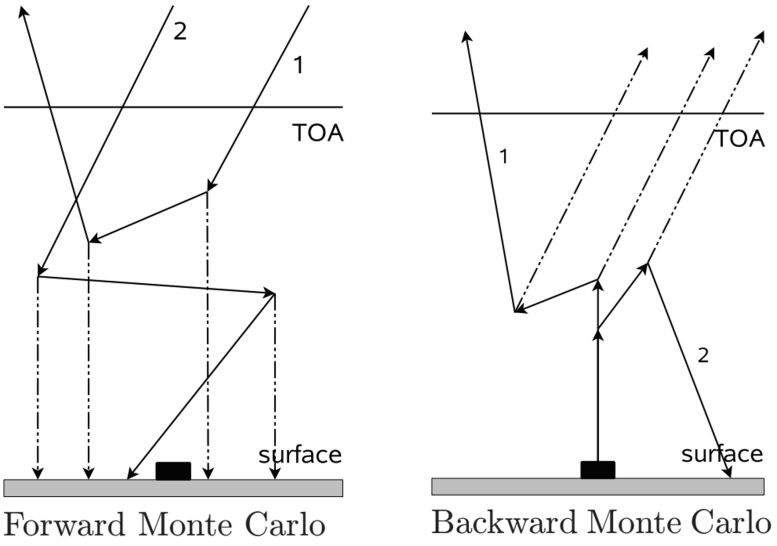

Figure 2.5: Difference between forward and backward MCRT. In the forward case, photons hit the detector only rarely, while in the backward case, they all start from the detector and their contribution to the incoming radiation is computed with LE at each scattering event. Figure adapted from Mayer (2009).

address this, backward tracing leverages the reciprocity principle of photon paths, which states that the trajectory of light is reversible (Veach, 1998). Guided by this principle, photons are launched from the detector, rather than from the TOA. During the simulation, the LE method is used to evaluate the contribution of each backward-traced photon toward the original solar direction μ_0. The difference between the forward and backward MCRT is shown in Fig. 2.5. This approach significantly improves computational efficiency by focusing on photon paths that contribute to the radiance at the detector. As a result, the number of photons required to achieve a given SNR at the detector is drastically reduced, making backward MCRT an ideal choice for simulating small detectors or narrow fields of view.

2.3 Polarization

Although invisible to the human eye, polarization is a fundamental property of electromagnetic waves. Variations in the amplitude and phase of the electric and magnetic field components define the polarization state of light, which encodes valuable information about the interactions the light has undergone after entering the atmosphere. While incoming stellar radiation is typically unpolarized, it can acquire various polarization states through scattering by molecules and aerosols, as well as through surface reflection.
To account for these effects, the scalar RT equation can be extended to its vectorial form, which describes not only the evolution of intensity but of the full Stokes vector $\mathbf{S} = [I, Q, U, V]$. This formalism enables a comprehensive treatment of polarization in RT modeling.
In this Section, I will first introduce the fundamental concepts of polarization, followed by a discussion of the main sources and sinks of polarization in Earth's atmosphere.

2.3.1 Stokes vector

Electromagnetic radiation can be described by two transverse waves travelling along the z-axis:

$$\begin{aligned} E_L &= a_L e^{-i(kz-\omega t+\delta_L)} \\ E_R &= a_R e^{-i(kz-\omega t+\delta_R)}, \end{aligned} \tag{2.35}$$

where the subscript L and R refer to the waves oscillating parallel and perpendicular to a chosen reference plane, a is the amplitude of the waves, $k = 2\pi/\lambda$ is the wavenumber, ω is the angular frequency, and δ represents the phase. A more convenient way to describe the polarization state of the electromagnetic wave is through the Stokes parameters:

$$\begin{aligned} I &= E_L E_L^* + E_R E_R^* = a_L^2 + a_R^2 \\ Q &= E_L E_L^* - E_R E_R^* = a_L^2 - a_R^2 \\ U &= E_L E_R^* + E_R E_L^* = 2 a_L a_R \cos\delta \\ V &= -i(E_L E_R^* - E_R E_L^*) = 2 a_L a_R \sin\delta \end{aligned} \tag{2.36}$$

where $\delta = \delta_R - \delta_L$ is the phase difference between the two waves.
These parameters can be interpreted in the following way.

- If either $a_L = 0$ or $a_R = 0$, the electromagnetic wave will be oscillating only along a single direction, and thus the wave will be linearly polarized.
- If $a_L = a_R \neq 0$, the wave will be either linearly polarized at $\pm 45°$, or circularly polarized, depending on the phase difference between the two waves. If the waves are in phase, meaning $\delta = 0°$, the resulting wave will be diagonally polarized, while if they are out of phase, $\delta = \pm 90°$, and the polarization will be circular.

Accordingly, the Stokes parameters Q, U and V describe:

- Q: Linear polarization along and perpendicular to the reference plane.
- U: Linear polarization at $\pm 45°$ to the reference plane.
- V: Circular polarization.

A geometrical visualization of this interpretation of the Stokes parameter is shown in Fig. 2.6. From the Stokes parameter, we can define a degree of polarization P as

$$P = \frac{\sqrt{Q^2 + U^2 + V^2}}{I}, \tag{2.37}$$

which quantifies the amount of polarization in a given Stokes vector $\mathbf{S} = [I, Q, U, V]$.

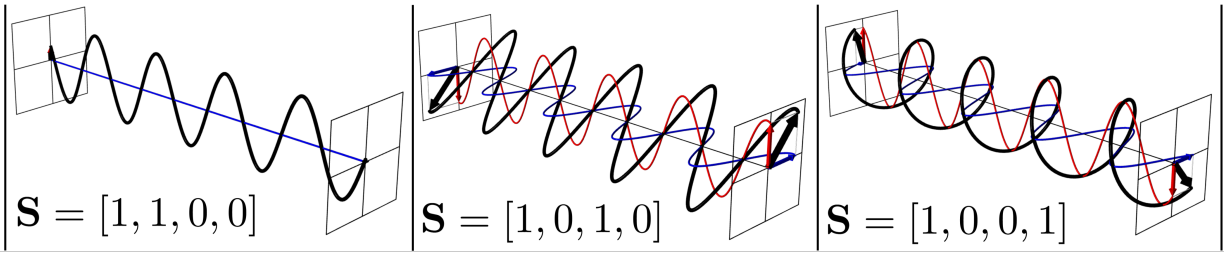

Figure 2.6: Visualization of the physical meaning of the Stokes parameters. The different polarization states arise from amplitude or phase differences between the electric and magnetic waves. This visualization was made using the online tool available at https://emanim.szialab.org.

2.3.2 Atmospheric processes

The sunlight that reaches the top of the Earth's atmosphere is almost completely unpolarized. However, processes within the atmosphere can both polarize and depolarize radiation. In this Section, we will show some examples of such processes, like scattering and surface reflection.

Scattering

When an incoming Stokes vector $\mathbf{S_0}$ is scattered, it undergoes the following transformation:

$$\mathbf{S} = \mathbf{P}(\theta)\mathbf{S_0}, \tag{2.38}$$

where the matrix $\mathbf{P}(\theta)$ is the scattering matrix, or Mueller matrix, which characterizes the effect of scattering at an angle θ on the polarization state of the light. The component $\mathbf{P}_{11}$ corresponds to the scalar phase function introduced earlier in Section 2.1.4. For Rayleigh scattering, which describes the scattering by small particles such as atmospheric molecules, the appropriate Mueller matrix is given by Chandrasekhar (1950); Brown (2014):

$$\mathbf{P}(\theta) = \frac{3}{4}\begin{pmatrix} 1+\cos^2\theta & -\sin^2\theta & 0 & 0 \\ -\sin^2\theta & 1+\cos^2\theta & 0 & 0 \\ 0 & 0 & 2\cos\theta & 0 \\ 0 & 0 & 0 & 2\cos\theta \end{pmatrix} \tag{2.39}$$

In Rayleigh scattering, the electric dipole oscillates within a defined scattering plane, determined by the incident and scattered directions. If the light is scattered in the plane, it retains its original polarization state (or remains unpolarized), but if it is scattered perpendicular to the plane, it becomes linearly polarized.
This behavior can be illustrated by applying the Mueller matrix to an unpolarized incident beam, represented by the Stokes vector $\mathbf{S_0} = [I_0, 0, 0, 0]^T$:

$$\mathbf{S} = \mathbf{P}(\theta)\begin{bmatrix} I_0 \\ 0 \\ 0 \\ 0 \end{bmatrix} = \frac{3}{4}I_0\begin{bmatrix} 1+\cos^2\theta \\ -\sin^2\theta \\ 0 \\ 0 \end{bmatrix} \tag{2.40}$$

This scattered light is now partially linearly polarized. The degree of polarization P is given by

$$P = \frac{\sin^2(\theta)}{1+\cos^2\theta}. \tag{2.41}$$

This expression confirms that the polarization is maximal (i.e., $P = 1$) when $\theta = 90°$, and vanishes (i.e., $P = 0$) when $\theta = 0°$, as expected from physical intuition. Fig. 2.7 shows the degree of polarization in the sky for three different Sun altitude angles. As expected, the polarization increases when looking away from the direction towards the Sun.
While a single scattering event can polarize initially unpolarized light, multiple scattering events tend to depolarize it. In such cases, the Stokes vector is repeatedly transformed by a sequence of Mueller matrices corresponding to various scattering angles θ_1, θ_2, ..., θ_{N_s}, for N_s scattering events. Since these scattering directions are generally random, the cumulative effect of multiple scatterings averages out polarization signatures, leading to a progressive reduction in the degree of polarization.

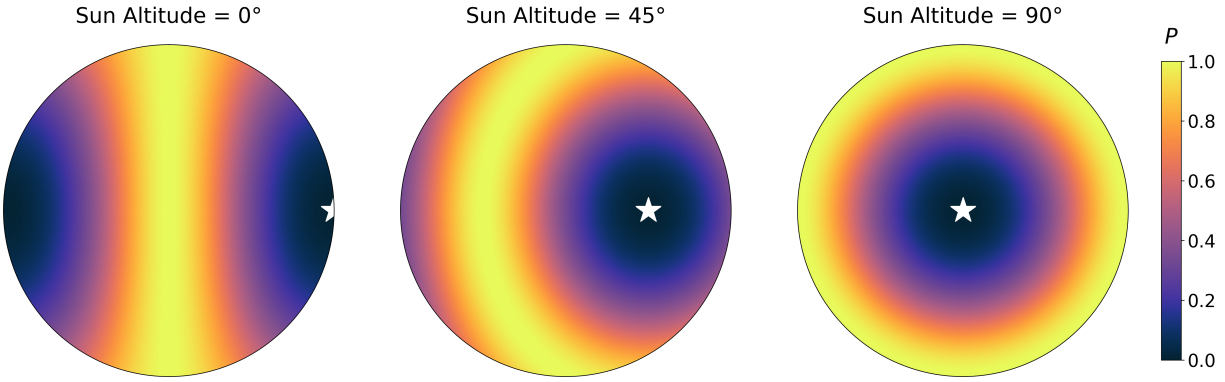

Figure 2.7: Sky polarization for three different Sun altitude angles. $P = 0$ when looking directly towards the Sun, and it increases until reaching its maximum when the angle between the observed direction and the Sun is 90°.

Surface reflection

Another important mechanism by which light can change its polarization state is surface reflection. When an electromagnetic wave encounters the boundary between two media with different refractive indices n_1 and n_2, the components of the electric field parallel and perpendicular to the plane of incidence are reflected with different efficiencies. These differences in reflectance are described by the Fresnel equations:

$$R_\perp = \frac{(n_1 \cos\theta_i - n_2 \cos\theta_t)^2}{(n_1 \cos\theta_i + n_2 \cos\theta_t)^2} \quad R_\parallel = \frac{(n_2 \cos\theta_i - n_1 \cos\theta_t)^2}{(n_2 \cos\theta_i + n_1 \cos\theta_t)^2}, \tag{2.42}$$

where θ_i is the angle of incidence and θ_t is the angle of transmission (or refraction). By using Snell's law, we can relate the angles of incidence and transmission with the refractive indices of the two media:

$$n_1 \sin\theta_i = n_2 \sin\theta_t. \tag{2.43}$$

Using this relation, the Fresnel equations can also be expressed in terms of the angles:

$$R_\perp = \frac{\sin^2(\theta_i - \theta_t)}{\sin^2(\theta_i + \theta_t)} \quad R_\parallel = \frac{\tan^2(\theta_i - \theta_t)}{\tan^2(\theta_i + \theta_t)}. \tag{2.44}$$

A particularly important angle in reflection is the Brewster angle θ_B, defined as the angle of incidence for which the reflected light is entirely polarized perpendicular to the plane of incidence. At this angle, the reflected component parallel to the plane vanishes, i.e., $R_\parallel = 0$, and the transmitted and reflected rays are orthogonal ($\theta_B + \theta_t = \pi/2$). From Snell's law, the Brewster angle can be written as

$$\theta_B = \arctan\left(\frac{n_2}{n_1}\right). \tag{2.45}$$

To understand the impact of reflection on the polarization state of light, we can express the Fresnel reflection behavior in terms of a Mueller matrix (Collett, 1971):

$$\mathbf{P} = \frac{1}{2}\begin{pmatrix} R_\perp + R_\parallel & R_\perp - R_\parallel & 0 & 0 \\ R_\perp - R_\parallel & R_\perp + R_\parallel & 0 & 0 \\ 0 & 0 & 2\sqrt{R_\perp R_\parallel} & 0 \\ 0 & 0 & 0 & 2\sqrt{R_\perp R_\parallel} \end{pmatrix} \tag{2.46}$$

When this matrix is applied to an unpolarized incident Stokes vector $\mathbf{S_0} = [I_0, 0, 0, 0]^T$, the reflected Stokes vector becomes:

$$\mathbf{S} = \mathbf{P}\mathbf{S_0} = \frac{1}{2} I_0 \begin{pmatrix} R_\perp + R_\parallel \\ R_\perp - R_\parallel \\ 0 \\ 0 \end{pmatrix} \tag{2.47}$$

The resulting degree of polarization P of the reflected light is then

$$P = \frac{|R_\perp - R_\parallel|}{R_\perp + R_\parallel}. \tag{2.48}$$

At the Brewster angle, where $R_\parallel = 0$, this simplifies to $P = 1$, indicating complete linear polarization. For an air–water interface, where $n_{\text{air}} \simeq 1.0$ and $n_{\text{water}} \simeq 1.33$, the Brewster angle is approximately:

$$\theta_B \simeq \arctan\left(\frac{1.33}{1.0}\right) \simeq 53^\circ. \tag{2.49}$$

A striking example of surface-induced polarization is the ocean glint, the bright, mirror-like reflection of sunlight off the ocean surface, often visible in satellite imagery. The left panel of Fig. 2.8 shows a photograph taken from the International Space Station (ISS) of the ocean glint partially covered by clouds. Ocean glint occurs when the angle of observation from a satellite matches the angle of solar incidence, satisfying the condition for specular reflection. In this geometric configuration, the sea surface reflects sunlight directly into the telescope's field of view, producing a localized, highly illuminated region.

Beyond being bright, ocean glint can also be strongly polarized, especially when the reflection occurs near the Brewster angle. When glint occurs at or near this angle, the degree of polarization measured by the satellite can reach values as high as 80% to 90%, depending on observational circumstances. The central and right panels of Fig. 2.8 show a true color and a polarization images obtained from MYSTIC simulations of a cloudless ocean planet at a phase angle of $\alpha = 120^\circ$, close to double the Brewster angle for air-water interface.

While the polarized signal is clear in a cloudless simulation, multiple scattering in clouds can strongly reduce the observed degree of polarization. While ocean glint can strongly polarize light, many terrestrial surfaces tend to have the opposite effect, depolarizing the incoming radiation. This depolarization primarily arises from multiple scattering events within the material, surface roughness, and the heterogeneous composition of natural surfaces such as soil or vegetation, all of which can disrupt the coherence of the incoming

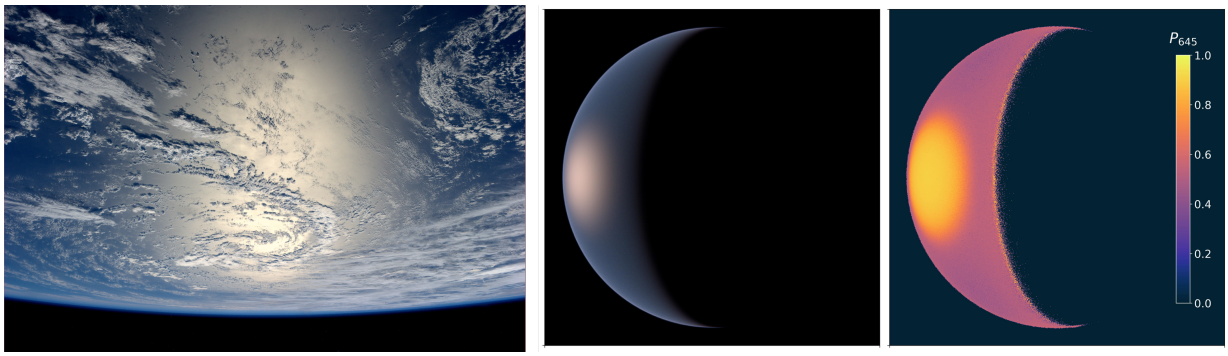

Figure 2.8: Left panel: ISS view of the ocean glint (Credits: ESA/NASA). Central and right panels: true color and polarization images from MYSTIC simulations of a cloudless ocean planet at a phase angle of $\alpha = 120°$. The polarization was measured at the wavelength $\lambda = 645$ nm.

polarization state. These effects can be analyzed using Mueller matrix formalism or summarized through scalar depolarization metrics. However, unlike the analytically tractable case of Fresnel reflection, depolarization behavior over complex surfaces is typically determined empirically through polarimetric measurements (Breon & Maignan, 2017).
So far, we have not examined the directional behavior of reflected polarized light in detail. While perfectly smooth surfaces follow the classical law of reflection, where the angle of incidence equals the angle of reflection ($\theta_i = \theta_r$), real-world surfaces are often rough or complex and require more sophisticated models. In Section 2.1.6, we introduced the BRDF as a way to characterize how light is reflected as a function of both incident and outgoing directions. This concept can be generalized to account for polarization, leading to the polarized BRDF, also known as pBRDF or bidirectional polarization distribution function (BPDF).
A BPDF is a function that combines the directional dependence of a BRDF with the polarization-transforming capabilities of a Mueller matrix. Formally, it is represented as a 4×4 matrix-valued function, where each matrix element $P_{ij}(\mu, \phi; \mu', \phi')$ depends on both the incoming (μ, ϕ) and outgoing (μ', ϕ') directions. The BPDF acts on an incident Stokes vector $\mathbf{S_0}$ to produce a reflected Stokes vector $\mathbf{S}$, accounting for changes in both direction and polarization:

$$S_j(\mu', \phi') = \sum_{i=1}^{4} P_{ij}(\mu, \phi; \mu'\phi') S_{0,i}(\mu, \phi). \tag{2.50}$$

In this formulation, the element P_{ij} describes how the i-th component of the incident Stokes vector contributes to the j-th component of the reflected Stokes vector. This framework allows for modeling complex surface reflection behaviors, including depolarization and anisotropic scattering, commonly observed in natural surfaces like soil, vegetation, snow, and ocean waves.

Rainbows and cloudbows

Rainbows represent the final polarization mechanism discussed here in the context of atmospheric optics. To understand why rainbows produce polarized light, we must first revisit the optical processes responsible for their formation. When sunlight enters a spherical water droplet suspended in the atmosphere, it undergoes a sequence of refractions and internal reflections. The light is first refracted upon entering the droplet from the surrounding air. It then reflects off the internal boundary of the droplet a number of times, denoted by k, and finally refracts again as it exits the droplet toward the observer.
For a rainbow to be observed, a large number of incident rays must emerge from the droplet within a narrow angular range. This focusing effect occurs for a specific angle of incidence, given by (Adam, 2002):

$$\cos\theta_i = \sqrt{\frac{n_{\text{water}}^2 - 1}{k(k+2)}}. \tag{2.51}$$

Here, k indicates the order of the rainbow. For the primary rainbow ($k = 1$) and for a water droplet ($n_{\text{water}} \simeq 1.33$), this yields an incidence angle of $\theta_i \simeq 59.4°$. Using Snell's law, the corresponding refraction angle inside the droplet is:

$$\theta_t = \arcsin\left(\frac{n_{\text{air}}}{n_{\text{water}}}\sin(\theta_i)\right) \simeq 40.2°. \tag{2.52}$$

This angle also serves as the angle of incidence for the internal reflection. The Brewster angle for internal reflection from water to air is given by

$$\theta_B = \arctan\left(\frac{n_{\text{air}}}{n_{\text{water}}}\right) \simeq 36.9°. \tag{2.53}$$

Note that in this case, the light is incident from water into air, which is the reverse of the geometry considered in the case of surface reflection. Comparing this Brewster angle to the internal reflection angle associated with rainbow formation, we find they are relatively close, only a few degrees apart. This proximity results in significant linear polarization of the light during internal reflection. The light then retains its polarization as it exits the droplet and can be detected by an external observer.
Rainbows are produced by fixed geometric conditions that are largely independent of droplet size, which typically exceeds $> 100\ \mu m$. In contrast, cloudbows occur in clouds composed of much smaller droplets (on the order of $\sim 10\ \mu m$), where the scattering is best described by Mie theory rather than geometric optics. In this regime, the polarization signal, particularly its angular dependence and magnitude, is highly sensitive to the droplet size. This makes cloudbow polarization a valuable tool for retrieving microphysical properties of clouds. Satellite measurements of polarized cloudbow features can be compared with theoretical Mie simulations to accurately retrieve droplet size, an essential parameter for understanding cloud formation processes and improving climate models (Bréon & Goloub, 1998). Fig. 2.9 shows a measurement of polarized light from Pörtge et al. (2023), which was used to retrieve the droplet size of clouds. In their observations, polarization significantly enhances the signal from the cloudbow, a feature that remains nearly invisible when considering intensity alone.

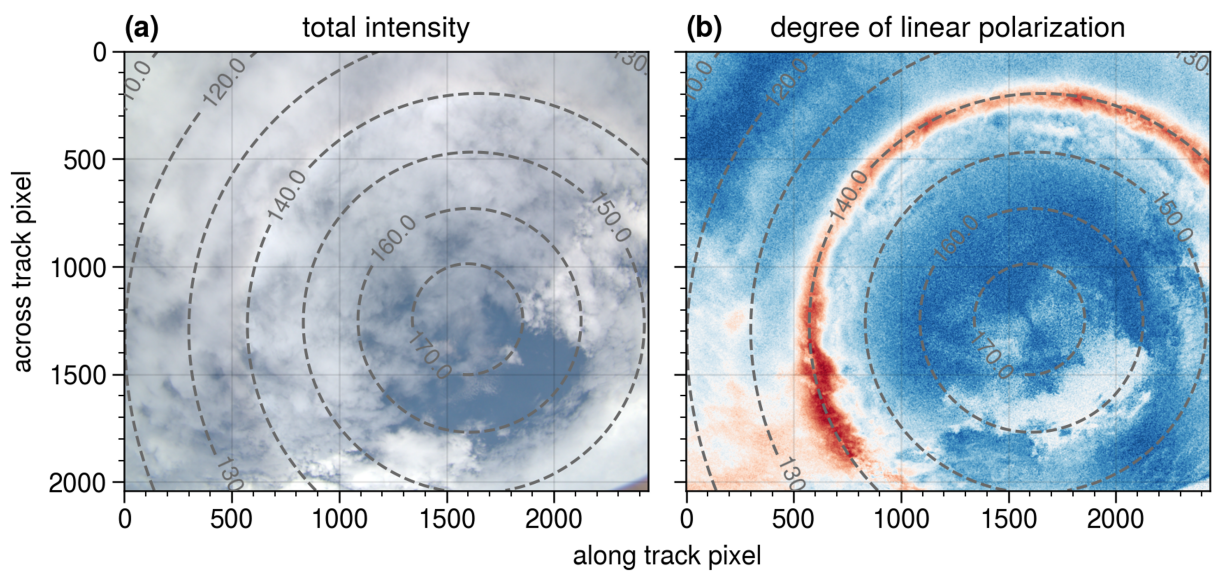

Figure 2.9: Observation of linear polarization from a cloudbow, adapted from Pörtge et al. (2023). Polarization measurements were used to retrieve the size of cloud droplets. The cloudbow feature is nearly undetectable in intensity alone but is strongly enhanced in polarization.

2.3.3 Polarization in simulations

The inclusion of polarization in RT models introduces an additional layer of complexity and realism, particularly in the treatment of scattering and reflection. Unlike models that consider only intensity, polarized RT accounts for the vector nature of electromagnetic waves. This allows the simulation of polarization changes resulting from scattering processes, non-spherical particles, and surface reflection effects.

The MCRT code MYSTIC, introduced in Section 2.2.2, is one of the most advanced and widely used models capable of simulating polarized RT in fully 3D domains. MYSTIC solves the full Stokes-vector RT equation in both plane-parallel and 3D geometries, making it especially valuable for modeling polarized radiances in complex atmospheric scenarios (Emde et al., 2010).

In MYSTIC, polarization is incorporated by tracking the Stokes vector of each photon packet and applying Mueller matrices at scattering events. Precomputed Mueller matrices for various particles, such as non-spherical ice crystals, allow for accurate modeling of polarized satellite observations, including those from instruments like POLDER and 3MI.

The capability to simulate polarization enables MYSTIC to support retrievals of aerosol size distributions, as well as cloud droplet shapes and sizes. Moreover, compared to methods such as the DOM, Monte Carlo simulations are particularly well-suited for polarization studies, as they do not significantly increase the computational cost relative to intensity-only simulations.

2.4 How to simulate the Earth as an exoplanet

Simulating the radiative signatures of spatially unresolved exoplanets requires a RT model that accurately captures the physical complexity of planetary atmospheres in disk-integrated observations. Various modeling approaches have been developed to replicate the spacecraft, satellite, and Earthshine observations of Earth as an exoplanet discussed in Section 1.1. Once these models are validated against observational datasets, they enable the extension of studies on the Earth seen as an exoplanet across wavelengths and spectral resolutions that are currently lacking in different observational methods. These models are essential for preparing the next generation of telescopes, which will primarily focus on characterizing Earth-like exoplanets.

One-dimensional models

1D models can be used as a first simplification to simulate the Earth as an exoplanet. These models only consider the vertical atmospheric profile and omit horizontal latitudinal and longitudinal variations, reducing their computational time.
Traub & Jucks (2002) developed the first of such models, which was later used by Woolf et al. (2002) and Turnbull et al. (2006) to simulate Earthshine spectra. This model spanned from the UV to the thermal IR and synthesized disk-integrated spectra by linearly combining nine individual components into a box model approximated by four parallel streams. All the reflected light simulations assumed a fixed solar zenith angle (60°) in a plane-parallel atmosphere. Their models takes into account the optical depth of the standard atmospheric species (such as H_2O and O_2), the optical depth of the stratospheric O_3, Rayleigh scattering, aerosol scattering, the reflectivity of high altitude clouds, reflectivity of the ocean surface (without specular reflection), the reflectivity of the ocean pigment, the reflectivity of the vegetated land due to chlorophyll, and the reflectivity of the low altitude clouds and other surface components. This model focuses on the net resulting spectrum due to the different components (see Fig. 1.5), and Woolf et al. (2002) found that the two dominant components needed to match the Earthshine spectra are the high altitude clouds and the clear atmosphere spectrum of H_2O, O_2, and O_3. The next largest process contributing to the signal was Rayleigh scattering from molecules.
Montañés-Rodríguez et al. (2006) made a substantial improvement in the modeling of Earthshine intensity spectra using a multilevel multiple scattering RT model in 1D for the calculation of the line-by-line atmospheric emission/transmission spectra in planetary atmosphere (Kratz et al., 2005; Martin-Torres & Mlynczak, 2005). This model showed excellent agreement in replicating the observed spectra, largely due to the improved handling of scattering processes. They also developed a new approach for the cloud and surface representation. Using global cloud maps from the international satellite cloud climatology project (ISCCP) (Schiffer & Rossow, 1983), they calculate a global mean percentage of clouds and surface types by applying solar and lunar geometry-based weighting to generate disk-averaged reflectance.
Kaltenegger et al. (2007) later adapted the Traub & Jucks (2002) and Des Marais et al.

(2002) framework to study Earth's spectral evolution over geological time, evolving the tropospheric abundances of five key gases from Kasting (2004): CO_2, CH_4, O_2, O_3, and NO_2, with cloud cover assumed to not change appreciably over time. They show that atmospheric features on Earth-like exoplanets change considerably over their evolution from a CO_2 rich atmosphere to a CO_2/CH_4 rich Earth to a present-day atmosphere. Rugheimer & Kaltenegger (2018) further extended these geological evolution spectra to Earth-like planets orbiting F-G-K-M stars and to interpret data from space missions such as EPOXI Rugheimer et al. (2013).

Three-dimensional models

3D models of Earth, viewed as an exoplanet, compute the planet's reflected light by integrating the radiance over the visible hemisphere. This is achieved by summing the spatially resolved specific intensity, weighted by the projected area of each surface element as seen from the observer's viewpoint. Following Robinson & Reinhard (2018), the disk-integrated flux density $F_\lambda(\hat{o}, \hat{s})$ is expressed as

$$F_\lambda(\hat{o}, \hat{s}) = \frac{R_\oplus^2}{d^2} \int_{2\pi} I_\lambda(\hat{n}, \hat{o}, \hat{s})(\hat{n} \cdot \hat{o})\, d\omega, \tag{2.54}$$

where $R_\oplus$ is Earth's radius, d is the observer's distance, I_λ is the location-dependent intensity, $\hat{n}$ is the surface normal vector, and $\hat{o}$ and $\hat{s}$ are unit vectors pointing toward the observer and the Sun, respectively.

The simplest 3D models specify the reflectivity of each surface patch on the disk as a function of the viewing geometry. This is typically done using empirical BRDFs (Manalo-Smith et al., 1998), and can produce either broadband (e.g., Pallé et al., 2003, 2008; Williams & Gaidos, 2008) or spectrally resolved simulations (Ford et al., 2001). Fujii et al. (2011) developed a more comprehensive modeling framework that includes atmospheric Rayleigh scattering and wavelength-dependent BRDFs for various surface and atmospheric components.

More advanced and realistic 3D tools solve the plane-parallel, multiple-scattering RT equation to generate radiance maps. These models accurately account for atmospheric absorption as well as cloud and gas scattering effects (Tinetti et al., 2006a; Fujii et al., 2011; Robinson et al., 2011; Feng et al., 2018). In addition to spatial coverage data, they require cloud optical properties for detailed simulations, often sourced from Earth science datasets such as ISCCP.

More recently, Kofman et al. (2024) employed the fully 3D RT code PSG (Planetary Spectrum Generator, Villanueva et al., 2018) to model DSCOVR images, incorporating the appropriate incident and emission angles. Their approach includes 3D atmospheric models for both liquid and ice water clouds, vertical mixing profiles, and surface coverage derived from monthly satellite observations. Clouds and aerosols are treated using multiple scattering, with optical properties calculated via Mie theory.

Full Stokes models for polarization

As introduced in Chapter 2.3, linear polarization inherently provides greater diagnostic power than intensity-only simulations and observations. Stam (2008) developed the first model to simulate the disk-integrated fraction of polarized light reflected by an Earth-like exoplanet. Using an adding-doubling solver, the model computes RT through a locally plane-parallel planetary atmosphere, followed by a disk-integration algorithm that integrates the reflected flux vector over the illuminated and visible portion of the planetary disk, accounting for the incident angle of stellar radiation. Inputs to the model include the optical thickness of each atmospheric layer, single scattering albedo, scattering matrix, and the composition of molecules and cloud particles. The surface is treated as a homogeneous, flat layer with a defined reflection matrix, either a Lambertian vegetation surface that fully depolarizes light or a black ocean surface including specular reflection, though without waves. Stam (2008) demonstrated that polarization is sensitive to atmospheric parameters in ways that intensity-only observations are not, such as in determining cloud altitudes from the continuum near the O_2-A band and estimating O_2 mixing ratios. However, the Stam (2008) model only handles horizontally homogeneous planets. It was also applied to fit the Earthshine polarization spectra in Sterzik et al. (2012), but failed to reproduce the spectral slope and continuum level.
Karalidi & Stam (2012) extended the doubling-adding method of Stam (2008) to include inhomogeneous planetary surfaces and clouds. Subsequently, Karalidi et al. (2012) conducted an in-depth investigation into the cloudbow polarization feature as a means of detecting liquid water clouds in Earth-like exoplanet atmospheres.
The first application of a Monte Carlo method to jointly model intensity and linear polarization in exoplanetary atmospheres was introduced by García Muñoz (2015). Later, Emde et al. (2017) applied a different MCRT code, MYSTIC, to investigate how clouds, aerosols, and sunglint influence polarimetric signals. Their model supports fully 3D atmospheric configurations, incorporating 3D distributions of cloud and aerosol particles, and includes surface reflection modeled either as a two-dimensional Lambertian surface or as a global ocean represented using a BPDF to account for specular reflection. Their results showed that reflected sunlight from ocean surfaces in the sunglint region leads to the highest polarization enhancements at large phase angles. However, the Emde et al. (2017) model was unable to reproduce the Earthshine polarization spectra reported by Sterzik et al. (2012), particularly with respect to the spectral slope.
More recent work by Trees & Stam (2022) built upon the Stam (2008) adding-doubling model, introducing a Fresnel ocean model that accounts for wind-ruffled waves, foam, and wave shadowing. Their results suggest that a liquid ocean may be detectable via spectropolarimetry at a single phase angle; notably, the glint introduces a trough, rather than a peak, in the polarization spectrum near the 950 nm H_2O absorption band. Additionally, Gordon et al. (2023) attempted to reproduce the VIS and NIR Earthshine polarization measurements by Miles-Páez et al. (2014) using two modeling frameworks: the Stam (2008) doubling-adding model and the VSTAR model (Versatile Software for Transfer of Atmospheric Radiation; Kopparla et al., 2018). Both models failed to match the observations

accurately, showing polarization discrepancies of several percent. These discrepancies were primarily attributed to the oversimplified treatment of the ocean as a black, non-reflective surface and the omission of the polarization contribution from ocean glint. Building on this work, Goodis Gordon et al. (2025) extended their modeling framework to simulate Earth-like planets across various geological epochs, demonstrating that polarized light offers improved sensitivity to atmospheric features such as clouds and hazes compared to flux-only observations.

While significant progress has been made in modeling polarization from Earth-like planets with increasing realism, no current model successfully reproduces the Earthshine polarization spectra. This limitation forms the starting point of this thesis, which aims to identify and improve the physical representations needed to benchmark Earth as an exoplanet using polarized Earthshine observations.

3

HAMSTER: Hyperspectral Albedo Maps dataset with high Spatial and TEmporal Resolution

Published as
Roccetti et al., 2024, Atmospheric Measurement Techniques, Volume 17, n. 20, pp. 6025-6046

Full authors list:
Giulia Roccetti; Luca Bugliaro; Felix Gödde; Claudia Emde; Mihail Manev; Michael Sterzik and Cedric Werhum.

Surface albedo is an important parameter in radiative-transfer simulations of the Earth's system, as it is fundamental for correctly calculating the energy budget of the planet. The Moderate Resolution Imaging Spectroradiometer (MODIS) instruments on NASA's Terra and Aqua satellites continuously monitor daily and yearly changes in reflection at the planetary surface. The MODIS Surface Reflectance Black-Sky Albedo dataset (version 6.1 of MCD43D) provides detailed albedo maps for seven spectral bands in the visible and near-infrared range. These albedo maps allow us to classify different Lambertian surface types and their seasonal and yearly variability and change, albeit only into seven spectral bands. However, a complete set of albedo maps covering the entire wavelength range is required to simulate radiance spectra, and correctly retrieve atmospheric and cloud properties from remote sensing observations of the Earth. We use a principal component analysis (PCA) regression algorithm to generate hyperspectral albedo maps of the Earth. By combining different datasets containing laboratory measurements of hyperspectral reflectance for various dry soils, vegetation surfaces, and mixtures of both, we reconstruct albedo maps across the entire wavelength range from 400 to 2500 nm. The PCA method is trained with a 10-year average of MODIS data for each day of the year. We obtain hyperspectral albedo maps with a spatial resolution of 0.05° in latitude and longitude, a spectral resolution of 10 nm, and a temporal resolution of 1 d (day). Using the hyperspectral albedo maps, we estimate the spectral profiles of different land surfaces, such as forests, deserts, cities and icy surfaces, and study their seasonal variability. These albedo maps will enable us to refine calculations of the Earth's energy budget and its seasonal variability and improve climate simulations.

3.1 Introduction

The surface albedo of the planet plays a crucial role within the climate system, governing the proportion of reflected solar light relative to incoming solar radiation at the surface. This holds significant importance as it effectively regulates the Earth's surface energy budget (Liang et al., 2010; He et al., 2014). The role of albedo extends to climate regulation, with snow and ice albedo feedback exerting a significant influence on climate change dynamics. Snow and ice possess much higher reflectivity compared to the surfaces they overlay. As temperatures rise, the diminishing extent of snow and ice cover leads to a decline in the planet's albedo. Consequently, this intensifies surface warming through a positive feedback mechanism.

Land surface albedo displays remarkable variability, both spatially and temporally. Notable fluctuations in surface albedo coincide with changes in land cover and surface conditions, including factors like vegetation (Loarie et al., 2011; Lyons et al., 2008), snow (He et al., 2013), soil moisture (Govaerts & Lattanzio, 2008; Zhu et al., 2011), and urban development (Offerle et al., 2005). In addition, soil and vegetation surfaces show different reflectance behaviours as a function of wavelength and are usually not incorporated into Earth system models (ESMs).

In the last decades, the advancement of satellite remote sensing techniques has enabled more accurate monitoring of the Earth's surface, enhancing radiative transfer and climate models. This progress allows for the continuous acquisition of extensive land surface observation data. However, climate models still struggle to capture temporal and spatial variations in albedo. In particular, global and regional climate models often require albedo products with an absolute accuracy of 0.02–0.03 (Sellers et al., 1995; He et al., 2014). Zhang et al. (2010) compared Moderate Resolution Imaging Spectroradiometer (MODIS) albedo products with model results from the Coupled Model Intercomparison Project Phase 3 (CMIP3) from 2000 to 2008, revealing discrepancies in globally averaged albedo of up to 0.06. In addition, validation of different satellite land surface products, such as MODIS (Schaaf et al., 2002), the Global LAnd Surface Satellite (GLASS; Liu et al., 2013; Qu et al., 2014), and the Copernicus Global Land Service (CGLS; Buchhorn et al., 2020), shows absolute global differences of up to 0.02–0.06, with the largest variations occasionally exceeding 0.1 (Shao et al., 2021).

The divergence among different albedo products is not the only source of uncertainty in the radiative-transfer calculations of ESMs. Most ESMs use a two-stream approach for the land component, where soil albedo has fixed values in two spectral broadband regions: the photosynthetically active radiation (PAR) band (400–700 nm) and the near-infrared (NIR) band (700–2500 nm). However, broadband radiative-transfer schemes show strong spectral discontinuities at 700 nm (Braghiere et al., 2023). This divergence in surface reflectance propagates into other radiative-partitioning terms, such as absorptance and transmittance at the top of the atmosphere (TOA).

More generally, in cloud-free simulations over land, the dominant factor impacting TOA visible (VIS) and near-infrared radiance is surface reflection (Vidot & Borbás, 2014). Var-

ied surface optical properties exhibit distinct spectral signatures contingent on the type of surface. Furthermore, within the VIS–NIR range, surface optical properties showcase a robust geometrical reliance that changes in accordance with solar and satellite directions. To elucidate the spectral reliance of the surface, an assumption of Lambertian behaviour can be made, implying isotropic luminance regardless of the viewer's angle. The albedo quantifies the proportion of reflected light under the assumption of isotropic radiation reflection.

Polar-orbiting satellites, such as NASA's Terra and Aqua satellites, provide global albedo maps, which are vital for the spectral, temporal, and spatial assessment of global albedo. The MODIS instrument aboard NASA's Terra and Aqua satellites offers coverage of the Earth's surface every 1 to 2 d, enhancing our understanding of terrestrial, oceanic, and atmospheric processes. In the VIS–NIR range, MODIS features seven spectral bands that deliver data on land surface characteristics. However, radiative-transfer simulations demand precise radiance calculations across all wavelengths, which necessitates hyperspectral albedo maps. For example, retrievals of cloud pressure thickness using the O_2 A band (760–770 nm) require precise albedo estimates in this spectral region (Li & Yang, 2024). Such comprehensive data are lacking due to the impracticality of obtaining albedo maps from satellites for every wavelength. As a result, various assumptions are incorporated into radiative-transfer codes to overcome this lack of information. MODIS albedo measurements are derived simultaneously from the bidirectional reflectance distribution function (BRDF), depicting radiation discrepancies resulting from the scattering (anisotropy) of individual pixels. This methodology relies on multi-date, atmospherically corrected, and cloud-cleared input data obtained over 16 d intervals. The spatial resolution is set at 30 arcsec in latitude and longitude (equivalent to 1 km at the Equator) using the Climate Modeling Grid (CMG). To derive climatological averages, the MODIS MCD43D42-48 albedo datasets are averaged over a 10-year period in steps of 1 d, and albedo maps are built for each day.

In this work, we introduce a novel methodology for creating hyperspectral albedo maps based on the seven representative bands of the MODIS instrument. Using a principal component analysis (PCA) regression approach, we combine different soil, rock, and vegetation datasets representative of different parts around the world, as well as maps illustrating Lambertian surface albedo from version 6.1 of the MCD43D product (Schaaf & Wang, 2021), derived from the Terra and Aqua satellites. These maps cover the seven bandpasses relevant for land surface albedos. Employing a PCA algorithm, as previously done in Vidot & Borbás (2014) and Jiang & Fang (2019), enables us to reduce the problem's high dimensionality and generate new albedo maps by interpolating between the measured bandpasses.

These hyperspectral albedo maps of Lambertian surfaces hold significance with respect to various climate and radiative-transfer models of the Earth's system. Using an ESM with coupled atmosphere–land simulations, Braghiere et al. (2023) demonstrated the impact of making simplistic assumptions on albedo maps using only two broadband values, which were compared to hyperspectral albedo maps. They combined the soil colour scheme from the Community Land Model version 5 (CLM5) (Lawrence et al., 2019) with eigenvectors calculated using a general-spectral-vector (GSV) decomposition algorithm (Jiang & Fang,

2019) to build hyperspectral soil reflectance maps and assess the impact of these maps on ESMs. Unlike our dataset of hyperspectral albedo maps, their approach is not based on satellite measurements, meaning it is less accurate and overlooks the seasonal and temporal variability in surface reflectance. However, it holds significance when assessing the impact of hyperspectral treatment of Lambertian albedo on ESMs. Braghiere et al. (2023) estimated a divergence in radiative forcing of $3.55\,\mathrm{W\,m^{-2}}$, which impacts net solar flux at the TOA ($>3.3\,\mathrm{W\,m^{-2}}$), cloudiness, rainfall, surface temperature, and latent heat fluxes. Braghiere et al. (2023) also highlight the impact of implementing hyperspectral albedo maps on regional models, where differences in latent heat can be higher than $5\,\mathrm{W\,m^{-2}}$, demonstrating implications for regional climate variability and the prediction of extreme events.
In the near future, the launch of new satellite missions, such as NASA's Earth Surface Mineral Dust Source Investigation (EMIT) mission, will allow us to obtain hyperspectral soil and vegetation data and benchmark the accuracy of model-generated hyperspectral maps.

3.2 Data and Methods

3.2.1 MODIS surface albedo climatology

NASA's MODIS instruments (Salomonson et al., 1989) aboard the Terra and Aqua satellites (launched in 1999 and 2002, respectively) observe the Earth in 36 spectral bands. Two channels (centred at 645 and 858 nm; see Table 3.1) have a spatial resolution of 250 m, and five channels (centred at 469, 555, 1240, 1640, and 2130 nm), including three in the shortwave-infrared range, have a spatial resolution of 500 m. All other channels have a resolution of 1 km.

Band	Central λ (nm)	Bandwidth (nm)
1	645	620–670
2	858	841–876
3	469	459–479
4	555	545–565
5	1240	1230–1250
6	1640	1628–1652
7	2130	2105–2155

Table 3.1: Spectral bands of MODIS in the VIS–NIR range that provide information about land surface. For each band, we specify the central wavelength and the bandwidth.

The science dataset (version 6.1 of MCD43D; Schaaf & Wang, 2021) is a combined Aqua–Terra MODIS Level-3 (L3) surface reflectance product and provides daily global estimates

of directional–hemispherical surface reflectance (black-sky albedo) and bihemispherical surface reflectance (white-sky albedo) for the seven MODIS bands mentioned above, as well as for three spectral broadband intervals (visible (300–700 nm), near-infrared (700–5000 nm), and shortwave (300–5000 nm)), exhibiting a spatial resolution of 30 arcsec in latitude and longitude (corresponding to roughly 1000 m at the Equator). Cloud-free MODIS observations are collected over 16 d and corrected for atmospheric gases and aerosols to derive surface albedo for land pixels (waterbodies are not considered). Data are temporally weighted relative to the ninth day of the retrieval period, and this day appears in the filename. Each surface reflectance pixel contains the best possible measurement from the period, selected on the basis of high observation coverage, low view angles, an absence of clouds or cloud shadow, and aerosol loading. Usually, due to the sun-synchronous orbits of the Terra and Aqua satellites (with equatorial crossing times at 10:30 and 13:30 MLT (magnetic local time), respectively), only pixels with a local solar noon zenith angle of up to approximately 80° are provided with an albedo value.
The MODIS land surface products have been validated against in situ measurements and other satellite-based land surface albedo. Globally, the MODIS product is less accurate with respect to high solar zenith angles (Sánchez-Zapero et al., 2023).
We compile a black-sky-albedo climatology for the seven MODIS spectral bands, starting with the MCD43D42-48 products. We average the available daily MODIS product data over a 10-year period, from 2013 to 2022, in steps of 1 d, starting on 1 January – i.e. from the first day of the year (DOY 1) to DOY 365. This results in 365 climatologically averaged albedo maps per spectral band, each with a spatial resolution of 30 arcsec in latitude and longitude. The aim is to create a complete surface albedo climatology map for all grid boxes that are illuminated by the Sun, i.e. up to a local solar noon zenith angle of 90°. Pixels that are in the dark throughout the entire DOY (i.e. where the Sun is always below the horizon) are left unfilled. For the computation of the climatology, we proceed in the following way:

1. First, we select the MCD43D42-48 albedo retrievals with an albedo quality between 0 and 3 (see Table 3.2) and compute the mean value of the surface albedo for each grid box over 10 years for a given DOY. After this averaging procedure, some pixels remain unfilled due to factors such as cloudiness and constraints on the local solar noon zenith angle (mentioned above).

2. Thus, for each DOY, we fill in the missing values with the mean of the albedo calculated for DOY-n and DOY+n (temporal averages obtained in step 1), where $n \in [1, 40]$. The mean value with the smallest n value, i.e. the value that is closest in time, is the one that is used.

3. For some DOYs close to solstices and for local solar noon zenith angles between 80 and 90°, a range of 40 d is not sufficient for providing filled values that correspond to both the future and the past. It might be, for example, that a value is available close in the future; however, to have a corresponding value in the past, we would

have to look further than 40 d. The reason why, in the previous step, we require values for both the past and the future is to balance out seasonal changes and avoid sharp transitions near the solstices. In such cases, we first search for the closest filled values that correspond to both the past and the future, even if the two intervals are different or if one of them is larger than 40 d. Then, we average the values of albedo over a 10 d interval around the selected future and past available days. Instead of simply assigning the mean of these averages to the actual DOY, we perform a linear interpolation to give more weight to the values closer in time to the actual DOY.

4. In a fourth step, remaining missing values for a given DOY are replaced with the spatial average for the same DOY over an area of $m \times m$ grid boxes around each missing value, where $m \in [3, 5, 7, 9]$. The mean value with the smallest m value, i.e. the value corresponding to the smallest surrounding area, is the one that is used.

5. Further remaining missing values are replaced with the mean surface albedo calculated across longitudes within 2° latitude bands for the same DOY.

6. If missing values still exist at this stage for given grid boxes and given DOYs, the mean value calculated across all DOYs during the 10 years under consideration is used to replace them.

7. Finally, since the MCD43D product only retrieves land properties, we compute an albedo value for the ocean pixels in each of the seven MODIS bands using the "deep-ocean" spectrum from the old ECOSTRESS library of the US Geological Survey (USGS) database (Baldridge et al., 2009; Meerdink et al., 2019). To this end, incoming solar spectral irradiance (Kurucz, 1992) is first convolved with the spectral response function of the given MODIS channels. Then, under the assumption of no atmosphere, reflected spectral irradiance at the surface is computed upon multiplication with the spectral ocean albedo and integrated over the wavelength. This value is finally divided by the integral of the incoming spectral irradiance, computed above, to obtain the band albedo values for the ocean. These values are used everywhere for global waterbodies and at all times. Of course, we are aware that water surfaces are better characterised using a BRDF in order to account for specular reflection (Cox & Munk, 1954a,b; Nakajima, 1983).

MODIS also provides data for coastal regions covering some ocean pixels. These pixels were filled in the climatology, as described in steps 1–6, and were not replaced with ocean pixels in step 7. Some of these coastal pixels also exhibit sea ice, which remains included in the climatology. The percentages of missing land pixels filled after each step of the climatology are shown in Fig. 3.1. The percentages are calculated as the average values across all DOYs. In step 3, most of the remaining missing pixels with a local solar noon zenith angle between 80 and 90° are filled. These pixels only receive nearly parallel incoming solar radiation, and thus their impact on radiative-transfer calculations is limited. On the other hand, our methodology allows us to estimate these pixels with high local solar noon zenith angles,

Flag value	Description
0	Best quality (full BRDF inversions)
1	Good quality (full BRDF inversions)
2	Magnitude inversion (number of observations ≥ 7)
3	Magnitude inversion (number of observations ≥ 2 and < 7)
255	Fill value

Table 3.2: Descriptions of the MCD43D albedo quality flags.

which are usually also highly reflective in the visible wavelengths.
This climatology serves as the starting point for building the hyperspectral albedo maps, where average ice and snow cover values are automatically included. Our MODIS black-sky-albedo climatology from the years 2013 to 2022 is available at https://opendata.physik.lmu.de/pt52a-nhm92. For each pixel, we provide a flag indicating at which step the albedo value was filled. The spatial resolution is the same as that of the MCD43D product (30 arcsec).

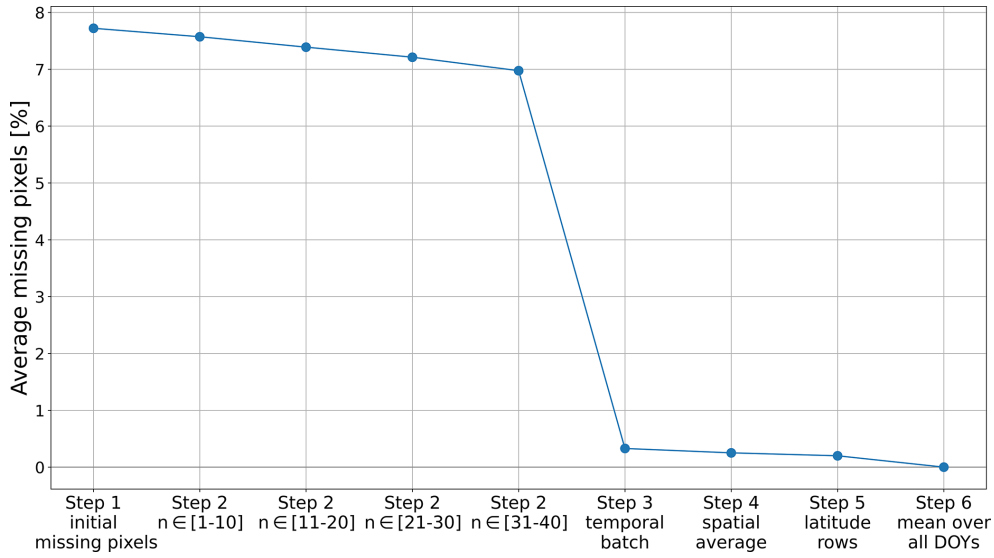

Figure 3.1: Percentage of land missing pixels as an average over all DOYs. We indicate the remaining percentage of missing values after each step of the climatology process.

3.2.2 Soil and vegetation spectra

To create hyperspectral albedo maps for each DOY, we use laboratory and in situ hyperspectral measurements of different soils, rocks, and vegetation surfaces. Jiang & Fang (2019) developed hyperspectral soil reflectance eigenvectors to improve canopy radiative

transfer. Studying the impacts of different regional datasets, they found that, compared to regional datasets, there was an increase in accuracy and robustness when including a global sample coverage of different soil and vegetation spectra.
Following this prescription, we select three dry-soil and vegetation datasets that cover different countries and different surface materials:

1. First, we select the ECOSTRESS library (Baldridge et al., 2009; Meerdink et al., 2019), which includes 1023 surface spectra from the United States. Among these, 487 are vegetation spectra, 62 are nonphotosynthetic-vegetation spectra, 381 are rock spectra, 40 are soil spectra, 45 are humanmade-material spectra (referred to as "man-made materials" in the ECOSTRESS library), and 8 are water ice and snow spectra.

2. Second, we select the ICRAF–ISRIC dataset (ICRAF-ISRIC, 2021), which is a global dataset with 4440 spectra for different soils from 58 different countries (including Africa, Asia, Europe, North America, and South America).

3. Third, we use the LUCAS (Land Use and Coverage Area frame Survey) dataset (Orgiazzi et al., 2018), which contains 21 782 different soil spectra from 28 European Union countries, from which we select the 30° viewing angle. As shown by Shepherd et al. (2003), LUCAS spectra are problematic between 400 and 500 nm, where they exhibit negative values. Following Jiang & Fang (2019), we use the multiple-linear-regression algorithm from scikit-learn (`sklearn.linear_model.LinearRegression`) (Pedregosa et al., 2011), trained on the ICRAF–ISRIC dataset, to reconstruct the LUCAS spectra in the 400–500 nm spectral range.

All the datasets cover the 400–2500 nm spectral range, albeit with different spectral resolutions. The LUCAS dataset has a spectral resolution of 0.5 nm, while the ICRAF–ISRIC and ECOSTRESS datasets have a spectral resolution of 10 nm. We interpolate the least-resolved datasets to obtain a resolution of 1 nm for all spectra. Among the waterbodies in the ECOSTRESS library, there are three different snow spectra: coarse granular snow, medium granular snow, and fine snow. In addition, there are spectra for frost and ice, sea foam, seawater, and tap water. Together, these form the eight water ice and snow spectra in the ECOSTRESS library.
In total, we use 26 635 dry-soil, vegetation, snow, and ice spectra from 82 different countries as input to extract the principal components. In Fig. 3.2, we show some representative soil and vegetation spectra from the ECOSTRESS library. One limitation of our approach is that vegetation spectra are only present in the ECOSTRESS library, which is a local dataset from the United States. However, to our knowledge, this is the only available dataset with tree, shrub, and grass spectra, which are fundamental for the purpose of this study. Jiang & Fang (2019) also study the influence of humid soils on the PCA regression algorithm. They find that the effect of soil moisture is non-linear, causing a general reduction in reflectance due to a total internal reflection effect of the water surface. This effect is more prominent in the near-infrared range (1100–2500 nm). They conclude that

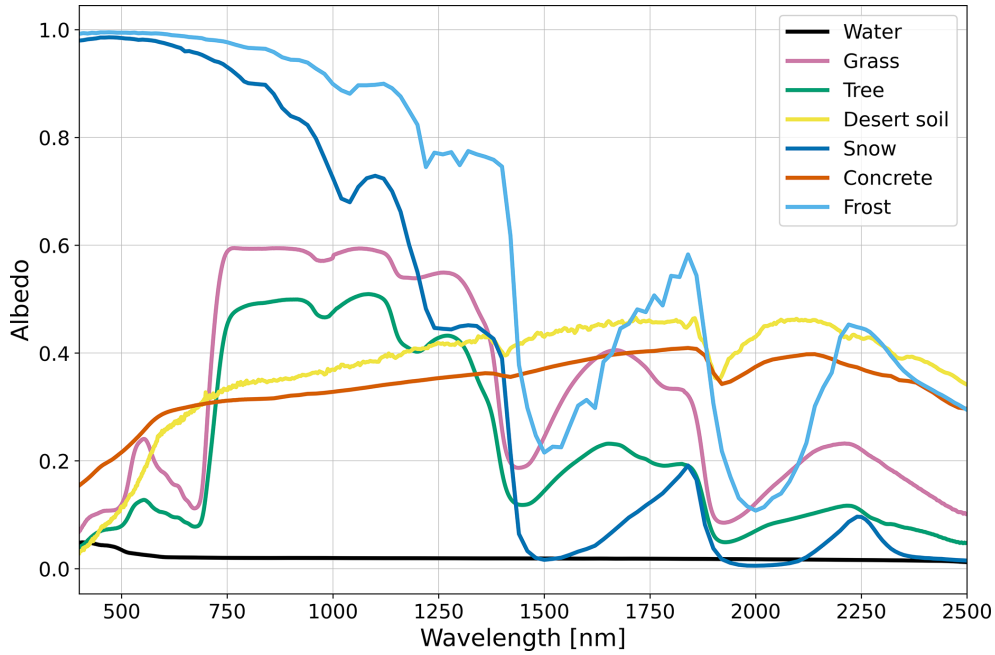

Figure 3.2: Albedo spectral signatures of typical soils, vegetation, and waterbodies from the ECOSTRESS library.

treating dry and humid soils separately leads to a more applicable soil reflectance model. A comprehensive, global database of humid soils is currently not available in the literature, and the inclusion of humid soils is beyond the scope of our work.

3.2.3 Principal component analysis

The vector of the MODIS albedo data (Sect. 3.2.1) for the seven wavelengths ($\vec{R}$) can generally be decomposed as

$$\vec{R} = \vec{c}\mathbf{U}, \tag{3.1}$$

where $\vec{R} = (r_1, ..., r_n)$ is the albedo vector, with n representing the number of wavelengths; $\vec{c} = (c_1, ..., c_m)$ is the coefficient vector, with m representing the number of surface spectra; and $\mathbf{U}$ is an $m \times n$ matrix containing the laboratory spectra of different soil and vegetation types. In order to calculate the hyperspectral albedo maps, we first need to compute the coefficient vector ($\vec{c}$) at every pixel by inverting Eq. (3.1). Since $\mathbf{U}$ is not a square matrix, the correct inverse equation is

$$\vec{c} = \vec{R}\mathbf{U}^T(\mathbf{U}\mathbf{U}^T)^{-1}. \tag{3.2}$$

From the MODIS dataset, $\vec{R}$ is available only for seven spectral bands (see Table 3.1); however, the goal of this work is to fill the spectral gaps between the bands and reconstruct a full VIS–NIR spectrum with a fine spectral resolution. Computing Eq. (3.2), which has a dimensionality of $m = 26\,635$, is too computationally expensive. In order to reduce the dimensionality of this problem, we follow Vidot & Borbás (2014) and apply a principal

component analysis (PCA) algorithm, which is an unsupervised machine learning algorithm, and extract the principal components from the matrix $\mathbf{U}$.
We need seven principal components (or eigenvectors) to solve our problem. As done by Vidot & Borbás (2014), we generate six principal components and use a constant value for a seventh one as this approach has been tested and shown to improve performance. The other six principal components are generated from the three dry datasets described in the previous section. Since these datasets account for different surface types (with vegetation spectra only given in the ECOSTRESS dataset) and come in different quantities, we cannot directly merge the spectra of the three datasets. Thus, we balance the number of spectra from the different datasets clustering them using a k-means algorithm (`sklearn.cluster.KMeans`; Pedregosa et al. (2011)), as done in Liu et al. (2023). In this way, we obtain 100 representative soil spectra for the ICRAF–ISRIC dataset, 100 for the LUCAS dataset, and 128 for the ECOSTRESS dataset; these include 40 vegetation spectra, 10 nonphotosynthetic-vegetation spectra, 40 soil spectra, 20 rock spectra, 10 humanmade-material spectra, and 8 waterbody spectra. The waterbody spectra, which include spectra for snow of different granular sizes, frost, deep oceans, coastal oceans, and tap water, were not reduced in dimensionality. Without accounting for this difference in number, the vegetation and water surfaces present in the ECOSTRESS dataset would be outweighed by the number of soil spectra from the other datasets, resulting in a considerably lower algorithm performance.
We use the `scikitlearn.decomposition.PCA` implementation of PCA, which follows singular value decomposition (SVD) of the data, as shown in Halko et al. (2011). From this process, we end up with the matrix $\tilde{\mathbf{U}}_\lambda$, which has the same spectral resolution as the laboratory spectra, where λ represents the hyperspectral nature of this matrix. To combine it with the albedo data vector $\vec{R}$, which is only available for the seven MODIS bands, we need to convolve the full matrix $\tilde{\mathbf{U}}_\lambda$ using the average satellite response function of the Terra and Aqua satellites for each band. This convolution is necessary to correctly estimate the measured albedo for the central wavelength of each band, which is crucial for generating hyperspectral albedo maps with the PCA.
The result of the convolution is a square matrix $\tilde{\mathbf{U}}$ for the seven MODIS wavelengths available from satellite data. Since $\tilde{\mathbf{U}}$ is a square matrix, we can simply calculate

$$\vec{c} = \vec{R}\tilde{\mathbf{U}}^{-1}. \tag{3.3}$$

In this way, we have seven equations for seven coefficients, allowing us to estimate the coefficient vector $\vec{c}$. Once $\vec{c}$ is known, it is possible to calculate the albedo maps across all selected wavelengths using

$$\vec{R}_\lambda = \vec{c}\tilde{\mathbf{U}}_\lambda, \tag{3.4}$$

where the subscript λ indicates the hyperspectral nature of the elements. The same process is applied to all the pixels in the map to generate a final albedo map with a spatial resolution of 0.05° in latitude and longitude, and it is applied across all the different days of the year, considering the Earth's seasonal variability.
Vidot & Borbás (2014) created BRDF maps using a PCA algorithm for their radiative-transfer code. They used the ASTER library (now called ECOSTRESS library) – which,

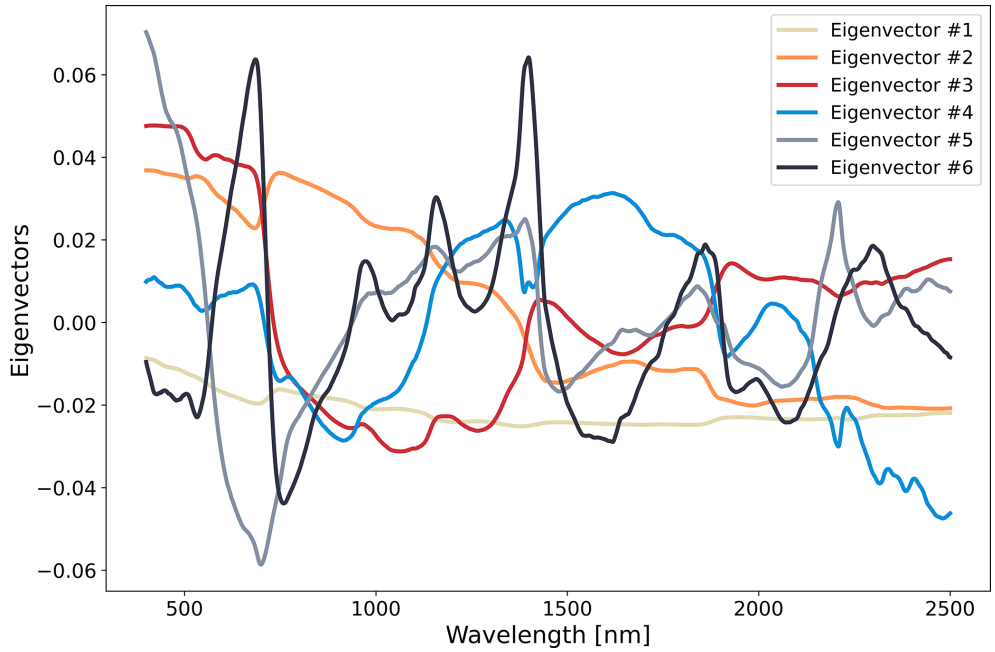

Figure 3.3: Eigenvectors generated by the PCA using the LUCAS, ICRAF–ISRIC, and ECOSTRESS datasets. These eigenvectors are used to build the hyperspectral albedo maps. They are plotted in order of importance, as determined by the PCA.

at the time, contained far fewer soil and vegetation spectra – to create average maps in order to include the hyperspectral reflectivity of soils in their radiative-transfer simulations. Jiang & Fang (2019) demonstrated that increasing the sample size of different soils from various countries helps to validate several datasets against each other. Without using satellite data to create the maps of the Earth's albedo, Jiang & Fang (2019) calculated eigenvectors using an SVD algorithm to study the hyperspectral properties of canopy trees in radiative-transfer simulations, including small, local datasets of humid soils. For the scope of this work, it is not possible to directly use the three eigenvectors generated by Jiang & Fang (2019) as we regress the hyperspectral albedo maps from the seven MODIS bands; thus, seven eigenvectors are needed.

As a result of the method explained above, we obtain a hyperspectral climatology of black-sky surface albedo over the entire globe, covering a wavelength range from 400 to 2500 nm in steps of 10 nm. While the interpolation is performed at a 1 nm resolution for the hyperspectral albedo maps, the final Hyperspectral Albedo Maps dataset with high Spatial and TEmporal Resolution (HAMSTER) has a spectral resolution of 10 nm to reduce the size of the single maps. We also reduce the spatial resolution of the hyperspectral albedo maps from the MCD43D 30 arcsec resolution to a resolution of 180 arcsec, which corresponds to 0.05° in latitude and longitude, again due to size constraints. HAMSTER can be generated at the same spatial resolution as the MODIS MCD43D product and at a spectral resolution down to 1 nm, and hyperspectral albedo maps with higher spatial and spectral resolutions are available upon request. The temporal resolution of the hyperspectral climatology is 1 d, and

it incorporates information contained in the MODIS climatology and extends it to wavelengths that were not available before. HAMSTER is available at its finer spatial resolution (0.05° in latitude and longitude) at https://opendata.physik.lmu.de/04zd8-7et52, while a version with a coarser spatial resolution, more suitable for global applications, is available at https://doi.org/10.5281/zenodo.11459410.

3.3 Validation

As a first test, we use the hyperspectral albedo maps to reconstruct the MODIS channels' black-sky-albedo climatology. We multiply the hyperspectral maps by the satellite's spectral response function, and we estimate the root-mean-square error (RMSE) for all seven channels. For all MODIS channels (see Table 3.1), the RMSE is less than 0.0003. This confirms that the computed hyperspectral albedo maps are able to reconstruct the original MODIS climatology with great accuracy.
To validate the PCA-retrieved maps (HAMSTER), we compare them with the land surface albedo product of the Spinning Enhanced Visible and Infrared Imager (SEVIRI) instrument aboard the geostationary Meteosat Second Generation (MSG) satellite (Schmetz et al., 2002). SEVIRI has three channels in the VIS–NIR range, which are reported in Table 3.3. As the MSG satellite is geostationary, we cannot compare the entire world map; instead, we can only compare the Earth's "disc", which includes Africa, parts of Europe, South America, and the Middle East. SEVIRI channels have spectral response functions that are broader than those of the analogous MODIS bands and are centred at slightly different wavelengths; thus, we convolved the hyperspectral maps to account for this. In particular, the SEVIRI channel centred at 810 nm touches the vegetation "ramp" that starts from 700 nm and is expected to show higher albedo values than the first SEVIRI channel.

Band	Central λ (nm)	Bandwidth (nm)
1	635	600–680
2	810	775–850
3	1640	1550–1750

Table 3.3: Spectral bands of SEVIRI in the VIS–NIR range that provide information about land surface. For each band, we specify the central wavelength and the bandwidth.

The SEVIRI land surface albedo product, MDAL (Geiger et al., 2008; Juncu et al., 2022; product identifier no. LSA-101), is offered daily by the Land Surface Analysis Satellite Application Facility (LSA SAF) on the native SEVIRI grid. It has a spatial resolution of 3 km at the sub-satellite point and is similar to the MODIS-based MCD43D product, against which it has been evaluated (Carrer et al., 2010). Both bihemispherical (white-sky) and directional–hemispherical (black-sky) albedo are available for the MCD43D product.

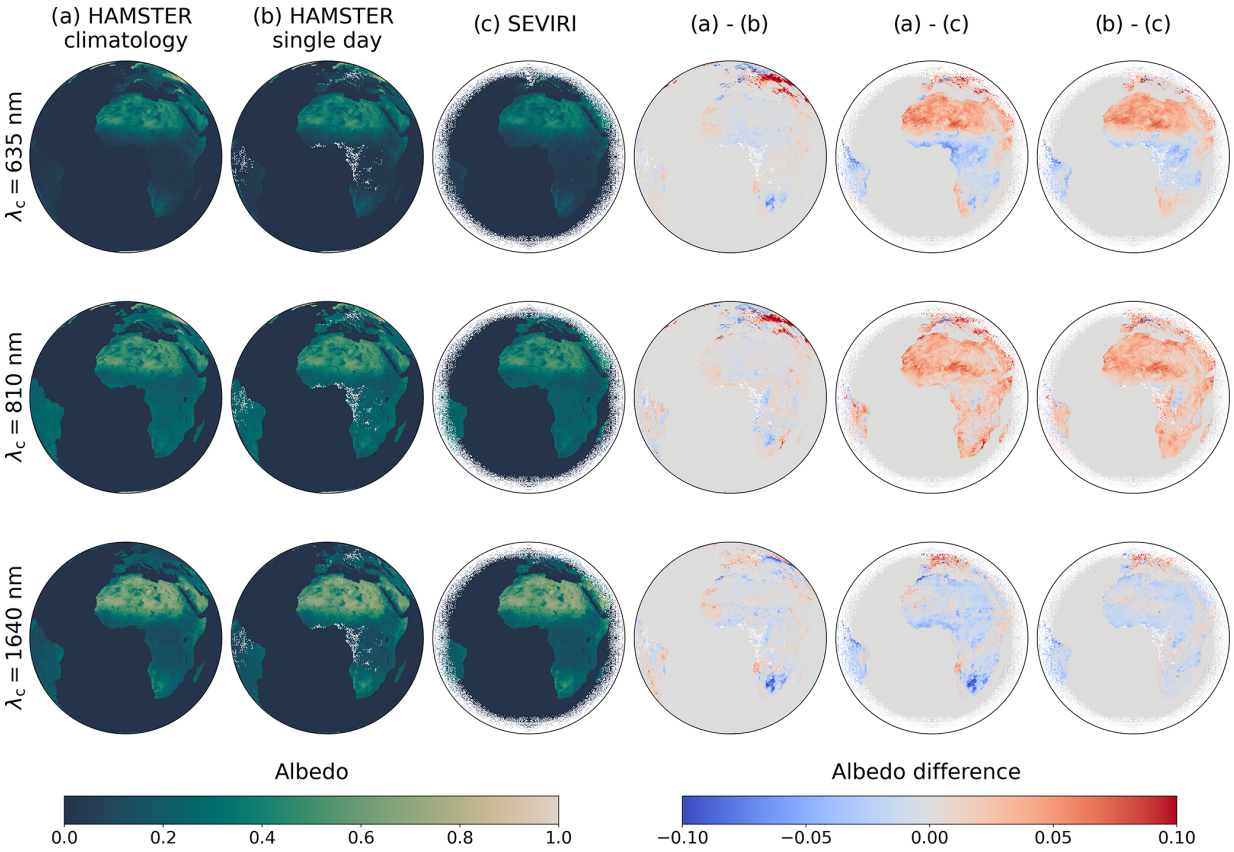

Figure 3.4: Comparison between the HAMSTER climatology, the single-day HAMSTER reconstruction, and SEVIRI in late boreal winter (5 March 2016 (DOY 65)) for the three SEVIRI VIS–NIR channels. The first three columns show the albedo values for **(a)** the HAMSTER climatology and **(b)** the single-day HAMSTER reconstruction, both of which are integrated over each SEVIRI channel, as well as **(c)** the SEVIRI albedo product. In the last three columns, we display the albedo differences between the three different albedo products or reconstructions, ranging from −0.10 to 0.10.

To enable comparisons with the HAMSTER hyperspectral albedo maps constructed from MODIS, we reprojected the SEVIRI data to the MCD43D grid, downscaling the data to a 0.05° resolution in latitude and longitude to allow for a consistent comparison. We selected two different days in 2016: one in late boreal winter (5 March (DOY 65)) and one in mid-boreal summer (30 July (DOY 209)) to compare surface reflectivity during two different vegetation stages, considering possible snow cover in winter and no snow in summer over northern Europe. The results are shown in Figs. 3.4 and 3.5.
We compare the three solar satellite channels offered by SEVIRI with the reconstructed channels from the HAMSTER climatology and the single-day HAMSTER reconstruction (first three columns in Figs. 3.4 and 3.5). SEVIRI channel 3 has the same central wavelength ($\lambda_c = 1640\,\text{nm}$) as MODIS band 6, allowing for an almost direct comparison between MODIS and SEVIRI land surface products. However, the hyperspectral nature of the re-

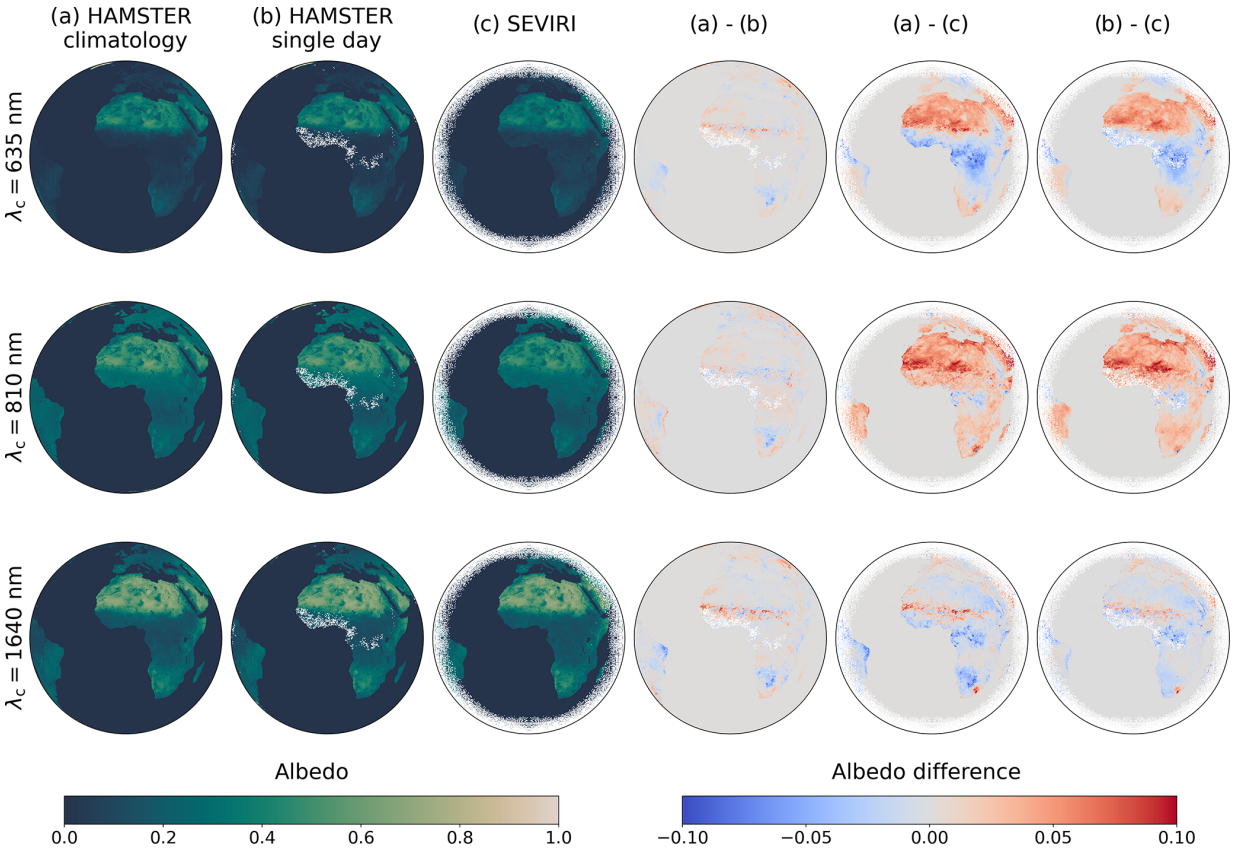

Figure 3.5: Comparison between the HAMSTER climatology, the single-day HAMSTER reconstruction, and SEVIRI in boreal summer (30 July 2016 (DOY 209)) for the three SEVIRI VIS–NIR channels. The first three columns show the albedo values for **(a)** the HAMSTER climatology and **(b)** the single-day HAMSTER reconstruction, both of which are integrated over each SEVIRI channel, as well as **(c)** the SEVIRI albedo product. In the last three columns, we display the albedo differences between the three different albedo products or reconstructions, ranging from −0.10 to 0.10.

trieved HAMSTER maps is still used to convolve around the 1640 nm MODIS band. The same applies to SEVIRI channel 1 and MODIS band 1, for which there is only 10 nm of difference in the central wavelength. On the other hand, SEVIRI channel 2 ($\lambda_c = 810$ nm) is outside any MODIS band. This last case allows us to make a comparison between the reconstructed albedo maps and the SEVIRI measurements, rather than comparing the land surface products of the two instruments.

In addition, in Figs. 3.4 and 3.5, we also assess the difference between the HAMSTER climatological average (first column) and a single-day HAMSTER reconstruction (second column), without accounting for the 10-year average of the climatology. White pixels in the single-day HAMSTER reconstruction correspond to pixels without albedo values from the MODIS MCD43D product. The climatological average shows fewer features, particularly over Europe, which might be due to fluctuations occurring on a single day, while the single-

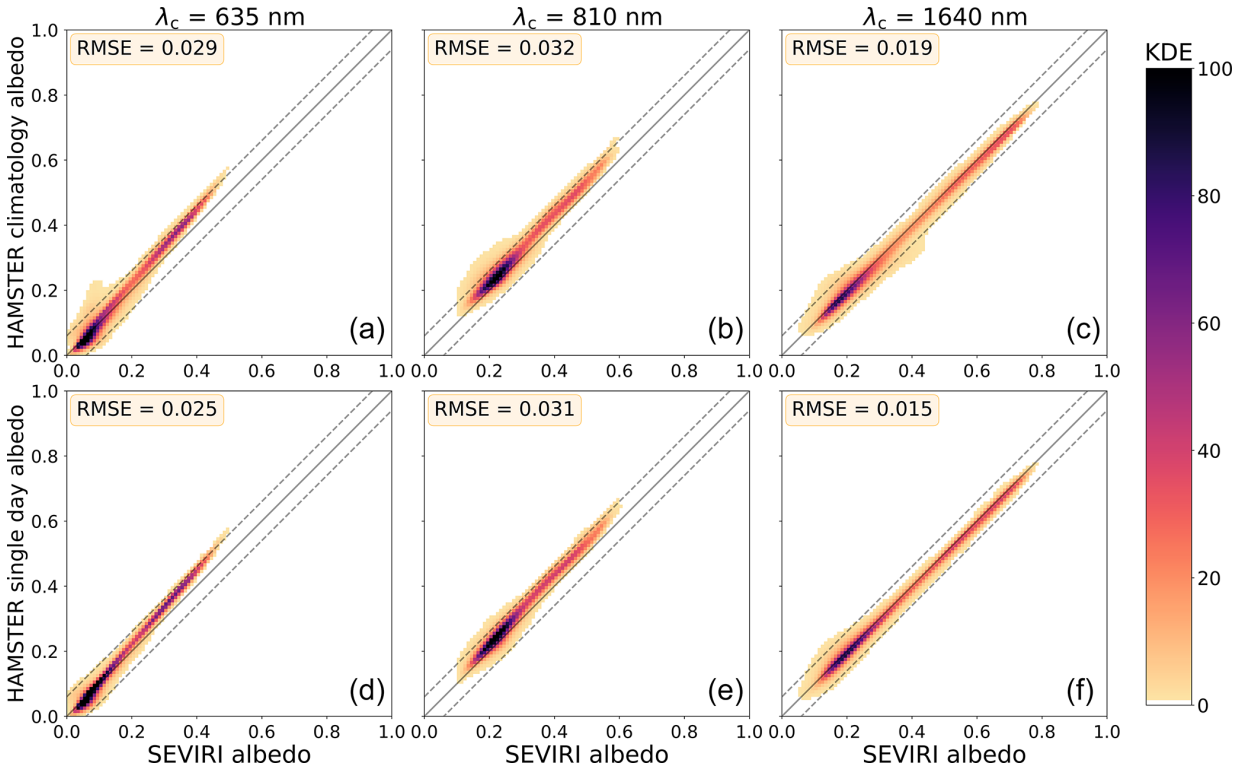

Figure 3.6: Kernel density estimation (KDE) between the HAMSTER climatology, the single-day HAMSTER reconstruction, and SEVIRI albedo data for 5 March 2016 (DOY 65) across the three central wavelengths of the SEVIRI channels (shown in different columns). Panels **(a)**, **(b)**, and **(c)** display hyperspectral albedo maps based on the HAMSTER climatology, while panels **(d)**, **(e)**, and **(f)** illustrate the single-day reconstruction. The solid line represents a perfect linear fit, while the dashed lines show a linear fit with an offset of 0.06.

day HAMSTER reconstruction shows a larger dependence on seasonality. The effect of the climatology is shown in the fourth column, where we plot the albedo difference between the HAMSTER climatology and the single-day HAMSTER reconstruction. In Fig. 3.4, we clearly see discrepancies of around 0.10 in the first two channels, while SEVIRI channel 3 shows lower albedo values over southern Africa for the HAMSTER climatology. Fewer differences are found for DOY 209 (in boreal summer; Fig. 3.5). To conclude, the last two columns of Figs. 3.4 and 3.5 display the differences between HAMSTER (i.e. the climatology and single-day reconstruction) integrated over the SEVIRI channels and the SEVIRI land surface product. We notice an overestimation of approximately 0.05 in the reconstructed HAMSTER hyperspectral albedo maps for the first two channels across the Sahara, while vegetated areas across Africa and parts of Europe and South America show either a negative discrepancy (SEVIRI channel 1) or a positive discrepancy (SEVIRI channel 2) compared to the SEVIRI measurements, with the discrepancies being of a similar magnitude. On the other hand, SEVIRI channel 3 ($\lambda_c = 1640\,\text{nm}$) is mostly underestimated

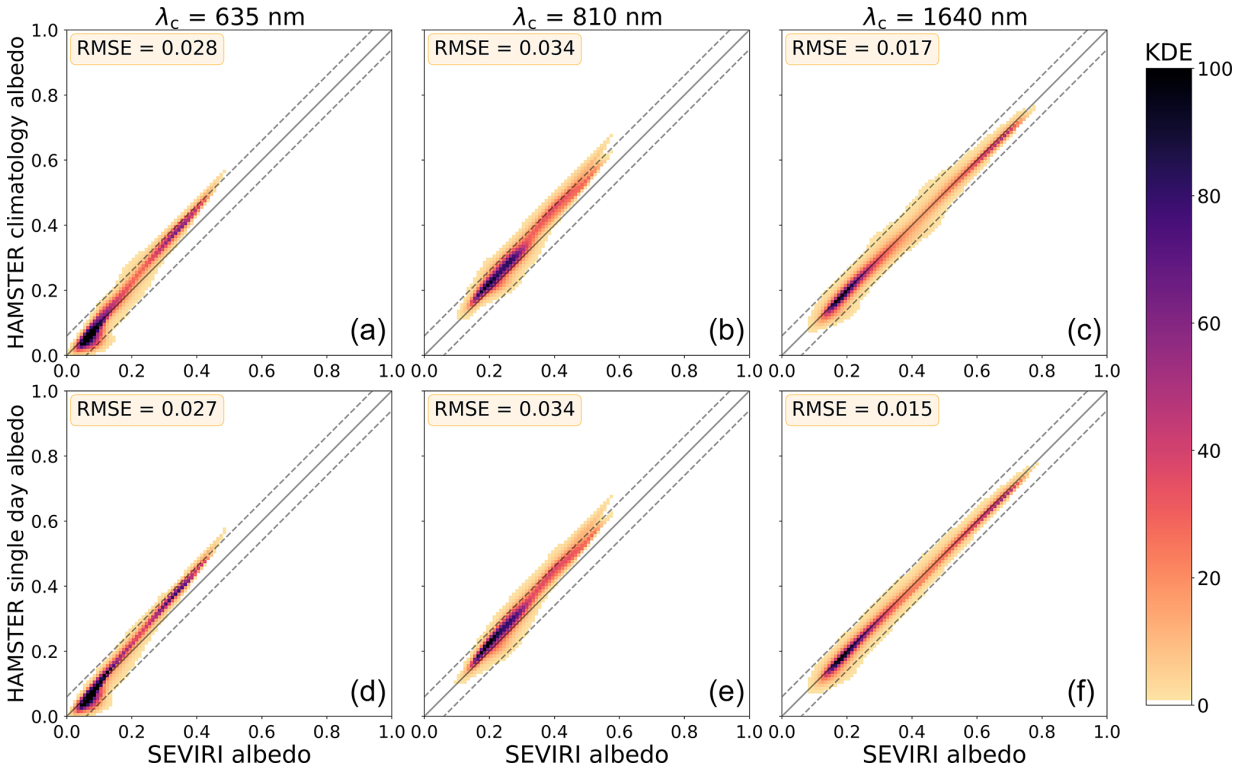

Figure 3.7: Kernel density estimation (KDE) between the HAMSTER climatology, the single-day HAMSTER reconstruction, and SEVIRI albedo data for 30 July 2016 (DOY 209) across the three central wavelengths of the SEVIRI channels (shown in different columns). Panels **(a)**, **(b)**, and **(c)** display hyperspectral albedo maps based on the HAMSTER climatology, while panels **(d)**, **(e)**, and **(f)** illustrate the single-day reconstruction. The solid line represents a perfect linear fit, while the dashed lines show a linear fit with an offset of 0.06.

by HAMSTER, with a smaller albedo difference compared to the other two channels. Since HAMSTER is based on the MODIS land surface product, our results are in accordance with the discrepancies found by Shao et al. (2021), which point towards differences of up to 0.06 between various land surface products. Though we describe the different offsets arising from this comparison, we can conclude that the reconstructed maps are consistent with the discrepancies arising from different satellite data products with respect to their validation.

In Figs. 3.6 and 3.7, we show probability density functions (PDFs) calculated using kernel density estimation (KDE), a Gaussian-kernel-based probability density method (Scott, 1992), to compare HAMSTER (i.e. the HAMSTER climatology and single-day HAMSTER reconstruction) with the SEVIRI land surface products for the two DOYs selected. For each comparison, we estimate the RMSE and represent the discrepancies between the different albedo products using KDE.

We notice that the RMSE is always very small, consistent with intrinsic differences be-

tween different retrievals of the albedo products. For both DOYs, the RMSE is larger for SEVIRI channel 2 (centred at $\lambda_c = 810\,\text{nm}$), which is the SEVIRI channel furthest from any MODIS channel. We also notice that comparing with hyperspectral maps built from single-day albedos consistently shows a slightly smaller RMSE since the climatology can only reproduce the climatological vegetation state and snow coverage pattern for a specific DOY.
In addition, we also calculate the RMSE between the HAMSTER climatology and all three SEVIRI channels for each day in 2016 (Fig. 3.8). We can conclude that the two DOYs selected for a more in-depth analysis (DOY 65 and DOY 209) are representative of the general trend. We notice that the comparison with SEVIRI channel 2 results in a larger RMSE, as expected, as this channel is outside the MODIS bands. However, the performance of the hyperspectral albedo maps is still in agreement with the discrepancies among different albedo products.

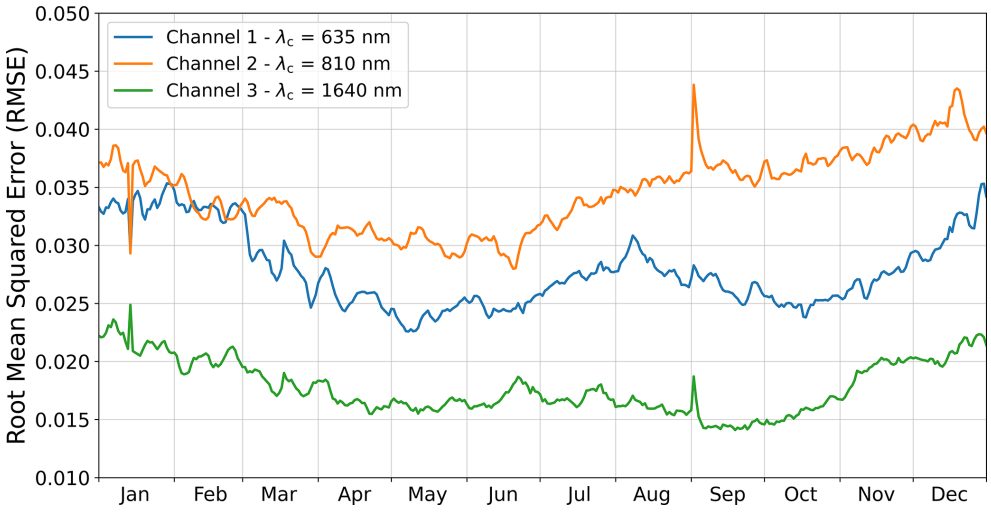

Figure 3.8: Root-mean-square error (RMSE) of the comparison between the HAMSTER climatology and all three SEVIRI channels. The comparison is performed for each day in 2016.

As a last test, we compare the hyperspectral albedo maps with the TROPOspheric Monitoring Instrument (TROPOMI) Lambertian-equivalent reflectivity (LER) product, which is available at `https://www.temis.nl/surface/albedo/tropomi_ler.php` (last access: 10 January 2024) (Tilstra et al., 2021, 2024). The TROPOMI LER product (with a sub-satellite pixel size of $0.125° \times 0.125°$) is remarkably different from the MODIS MCD43D product as it provides separate surface albedo values for snow and ice-free conditions and snow and ice conditions. The snow and ice conditions are also averaged over a month, which does not allow for a direct comparison with MODIS, which provides daily snow coverages. Due to the high reflectivity of snow and ice in the visible wavelengths, the large discrepancy between the two products does not result from the PCA-retrieved albedo but from the products' different approaches used to assess snow coverage. On the other hand,

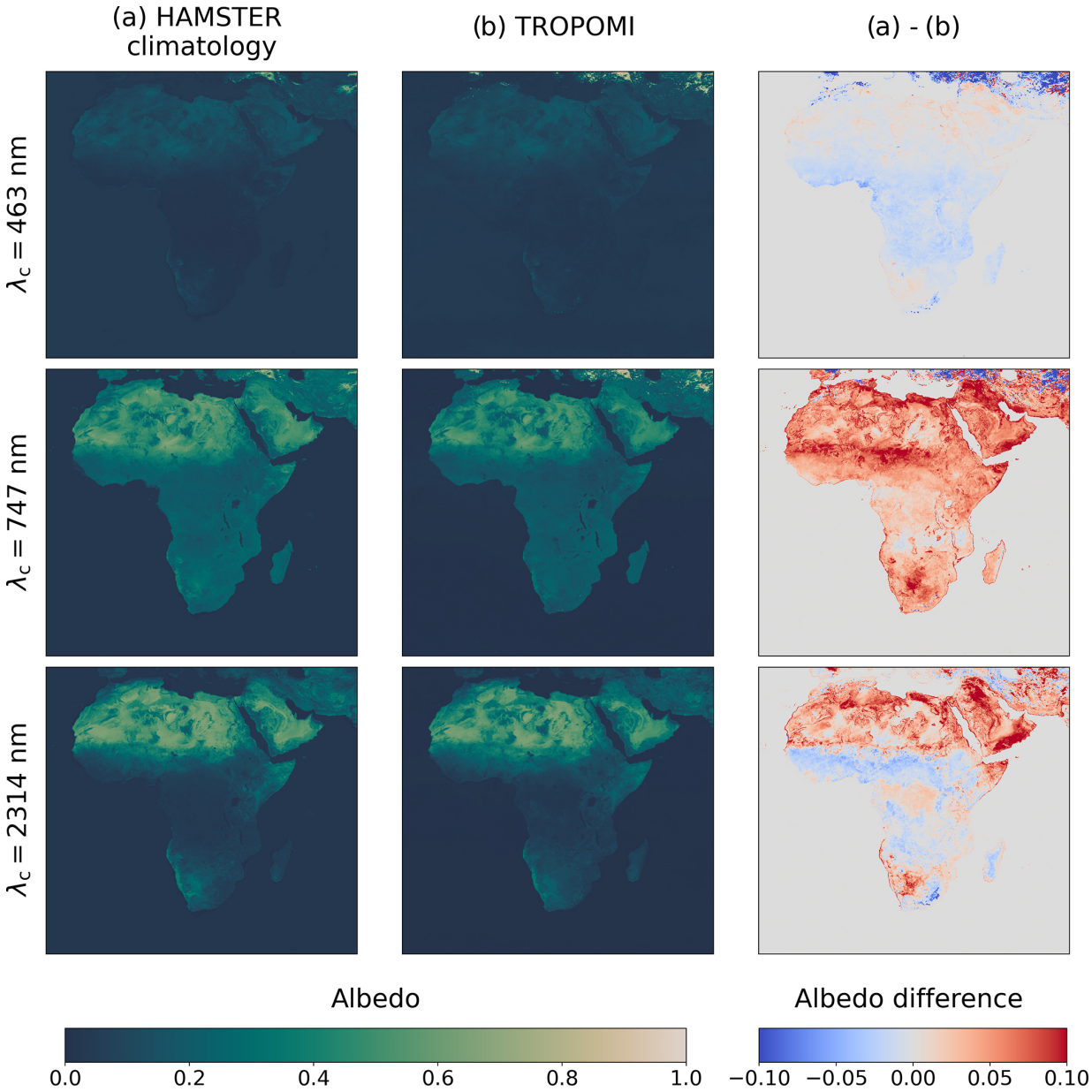

Figure 3.9: Comparison between the HAMSTER climatology **(a)** and TROPOMI **(b)** in late boreal winter (month of March) for three selected wavelengths within the TROPOMI VIS–NIR channels. Panels **(a–b)** show the albedo difference between the HAMSTER climatology and the TROPOMI LER albedo product.

TROPOMI bands are very narrow (just 1 nm), and they provide many channels in the "vegetation red edge" (VRE) ramp. For this reason, we validate our hyperspectral albedo maps using the TROPOMI product exclusively for the African continent and the Middle East since these regions exhibit the least snow coverage, allowing for a direct and consistent comparison of land surface albedo between the two products. In this way, we avoid

comparisons with snow and ice products which are not fully consistent. Due to the narrow satellite bands of TROPOMI, it was not necessary to convolve its satellite response function, and we estimated the RMSE between the TROPOMI LER product and our HAMSTER hyperspectral albedo maps (at a spectral resolution of 1 nm). The results are shown in Table 3.4.

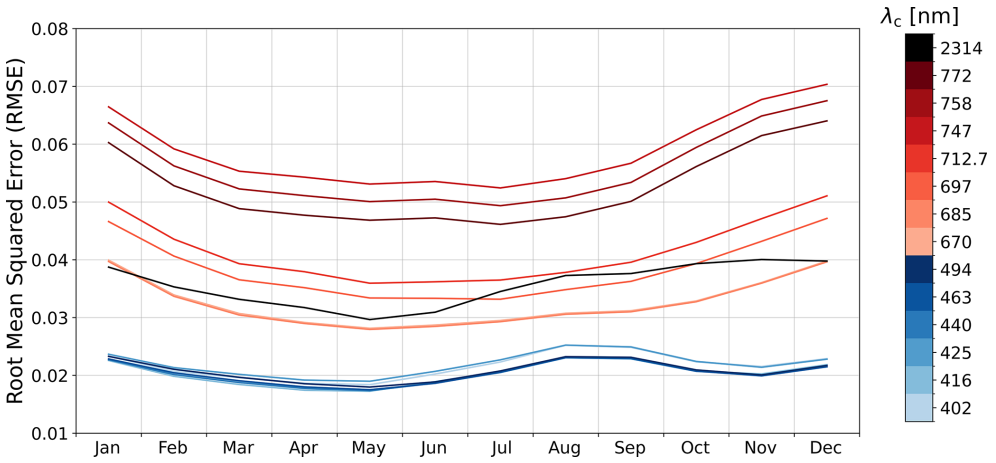

Figure 3.10: Root-mean-square error (RMSE) of the comparison between the HAMSTER climatology and all TROPOMI channels. The comparison is performed for each month.

The RMSE is comparable to what we find for SEVIRI and reflects known discrepancies among different surface albedo products. It remains relatively small in the TROPOMI bands between 670 and 772 nm, within the VRE domain and far from the MODIS bands. This confirms the good performance of the hyperspectral albedo maps, even when they are far from the MODIS bands from which they were retrieved. In Fig. 3.9, we select three TROPOMI bands and compare the albedo values over Africa between the HAMSTER climatology (first column) and the TROPOMI albedo product (second column). We select the TROPOMI monthly product for the month of March (average from 2018 to 2023), and we compare it with the average of the HAMSTER climatology from DOY 61 to DOY 91 (corresponding to all days in March). In the third column, we again plot the albedo difference between the two products. For $\lambda_c = 463$ nm, we notice very good agreement, with discrepancies of around 0.019 over Africa. For $\lambda_c = 747$ nm, within the VRE domain, the discrepancies are larger, with HAMSTER generally overestimating albedo compared to TROPOMI, resulting in differences of up to 0.10 but an overall RMSE of 0.055. We also compared the two products with a band in the far NIR range ($\lambda_c = 2314$ nm) and found that HAMSTER overestimates dry and desert areas and underestimates vegetated regions. Also, in this last band, albedo products show differences of up to 0.10, particularly over deserts, but have a small RMSE (0.033). As with SEVIRI, we also validate the HAMSTER climatology against TROPOMI for each month, estimating the RMSE for each TROPOMI band. Since TROPOMI offers monthly albedo products, we used the monthly averages of the HAMSTER climatology over Africa and the Middle East to perform the comparison. In Fig. 3.10, we show the monthly validation results. For TROPOMI bands

λ (nm)	402	416	425	440	463	494	670	685	697	712	747	758	772	2314
RMSE	0.019	0.018	0.020	0.019	0.019	0.020	0.031	0.030	0.037	0.039	0.055	0.052	0.049	0.033

Table 3.4: Spectral bands of the TROPOMI LER product in the VIS–NIR range, along with the RMSEs of the comparisons with HAMSTER hyperspectral albedo maps of Africa.

between 400 and 500 nm, the RMSE is always very small (around 0.02). Moving into the VRE domain (from 700 to 800 nm), the RMSE ranges from 0.05 to 0.07, which is still comparable with discrepancies among different albedo products. For the NIR TROPOMI band ($\lambda_c = 2314$ nm), the RMSE is around 0.03–0.04 for all months.

3.4 Results

In this section, we present the two main results of this paper: the MODIS black-sky-surface-albedo climatology for the seven bands and, building on that, the extended Hyperspectral Albedo Maps dataset with high Spatial and TEmporal Resolution (HAMSTER).

3.4.1 MODIS climatology dataset

As described in Sect. 3.2.1, we derived a 10-year climatology of surface albedo for different DOYs as a starting point for generating the hyperspectral albedo maps. This climatological average, with a temporal resolution of 1 d, allows for the study of temporal variability in the albedo of the planet, as shown in Fig. 3.11. Since albedo values are not available for every pixel of the Earth's surface throughout the year due to missing solar illumination during winter, we study the temporal evolution of the mean global albedo between 67° N and 67° S. At these latitudes, we consistently have an estimate of the albedo for every single pixel across all DOYs. As a consequence, we exclude the Arctic and Antarctica regions, as well as other high-latitude land surfaces in the Northern Hemisphere, from the mean altitude estimation. For this reason, the mean albedo value should be interpreted not as a global estimate for the Earth but rather as an indicator of its temporal variation.
In Fig. 3.11, we notice that the mean albedo is higher in the NIR bands, following the VRE peaks. At 858 nm, which peaks right after the VRE, we notice the largest albedo value for the planet, followed by 1240 nm. Continuing into the NIR range, with 1640 and 2130 nm, the albedo values decrease. In contrast, in the VIS range, there is very little variation in albedo among the three bands. The VIS bands show a clear seasonal trend due to the melting of ice and snow in the Northern Hemisphere, followed by the subsequent blossoming of vegetation. Thus, the Earth's albedo peaks in late boreal winter in the VIS range and then decreases in boreal summer. This large-variability trend can be interpreted in terms of seasonal differences in snow coverage, and it mainly follows the variability in the Northern Hemisphere, which hosts almost 80 % of the Earth's land. However, in the NIR bands, other features observed around late boreal spring and autumn are due to the blossoming of flowers and the reddening of leaves, which decrease the general reflectivity

of green leaves. In Fig. 3.12, we study the spatial variability in albedo throughout the year

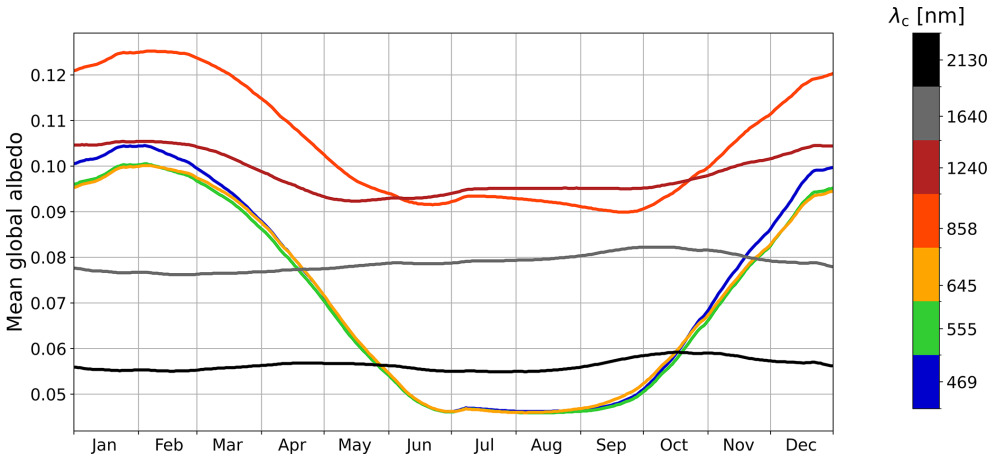

Figure 3.11: Yearly cycle of the black-sky-albedo data from the MODIS climatology, covering 67° N to 67° S. The different curves represent the different MODIS channels, indicated by their central wavelengths.

at a particular wavelength for the entire 10-year climatological average. Here, we select MODIS band 1, centred at 645 nm. In particular, we plot the difference between the maximum and minimum albedo values for the entire year, regardless of when the maximum and minimum are reached. For instance, the maximum reflectivity over high latitudes in the Northern Hemisphere is reached during boreal summer, while along the coast of Antarctica, it happens during austral summer due to ice melting. It is important to note that the MCD43D product does not contain sea surface albedo or sea ice albedo. However, coastal regions exhibit albedo values and are subject to large seasonal differences.
Moreover, since albedo data are not available during boreal winter (summer) for the Northern (Southern) Hemisphere, the difference between the maximum and minimum albedo for high-latitude regions (north and south of 67°) is calculated over a shorter time period corresponding to the data coverage of the region.
By illustrating this reflectivity variation for every pixel, the map in Fig. 3.12 highlights regions with the largest variations. In particular, Arctic and Antarctic regions exhibit high reflectivity variations due to snow, ice, and sea ice melting in coastal regions, as clearly visible in the map. Mainland Greenland also shows more variability than mainland Antarctica, possibly pointing towards the melting of Greenland's glaciers during boreal summer. Deserts all over the world, such as the Sahara and Australian deserts, show the least variability, remaining almost constant throughout the year. Also, tropical rainforests, such as the Amazon rainforest, do not exhibit significant seasonal variability. In contrast, temperate and boreal forests show pronounced variation due to differences in snow cover between the winter and summer months.

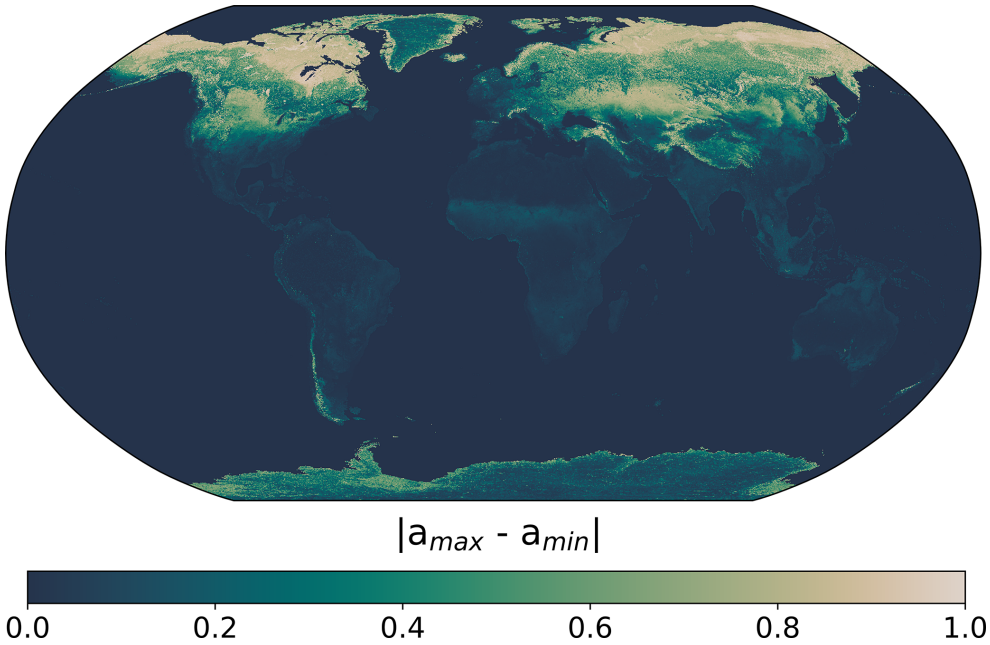

Figure 3.12: Spatial variation in the MODIS climatology, showing the difference between the maximum and minimum albedo ($a_{\max}$ and $a_{\min}$, respectively) for each pixel throughout the year.

3.4.2 Hyperspectral albedo maps

Using MODIS climatology data, we build hyperspectral albedo maps with a PCA regression algorithm, as described in Sect. 3.2.3. The hyperspectral albedo maps allow us to combine the spectral features of different soils, vegetation, and water surfaces with the high spatial and temporal resolution of the MODIS climatology data. This has many possible applications, ranging from implementation in climate models (as demonstrated by Braghiere et al. (2023)) to the improvement of remote sensing retrieval frameworks. The new hyperspectral albedo maps have been implemented in the radiative-transfer software package `libRadtran` (`http://www.libradtran.org/doku.php`, last access: 12 December 2023; Mayer & Kylling, 2005a; Emde et al., 2016).

As a first application, we use these hyperspectral maps to calculate the mean global albedo value around the equinoxes. In this way, we ensure that almost all pixels are filled with an albedo value, allowing us to assess a mean albedo value for the entire globe as a function of wavelength (see Fig. 3.13). The main difference between the spring and autumn equinoxes pertains to snow coverage over the Northern Hemisphere, which increases reflectivity during the boreal-spring equinox. This mostly affects the VIS wavelengths, following the typical albedo profile of snow and frost (see Fig. 3.2). From these hyperspectral albedo maps, we found that the mean global albedo is around 0.21 in the VIS range during March and around 0.17 in autumn, whereas it decreases to below 0.10 in the NIR range. The dots in Fig. 3.13 represent the average over the MODIS channels, without taking into account

the hyperspectral albedo maps.

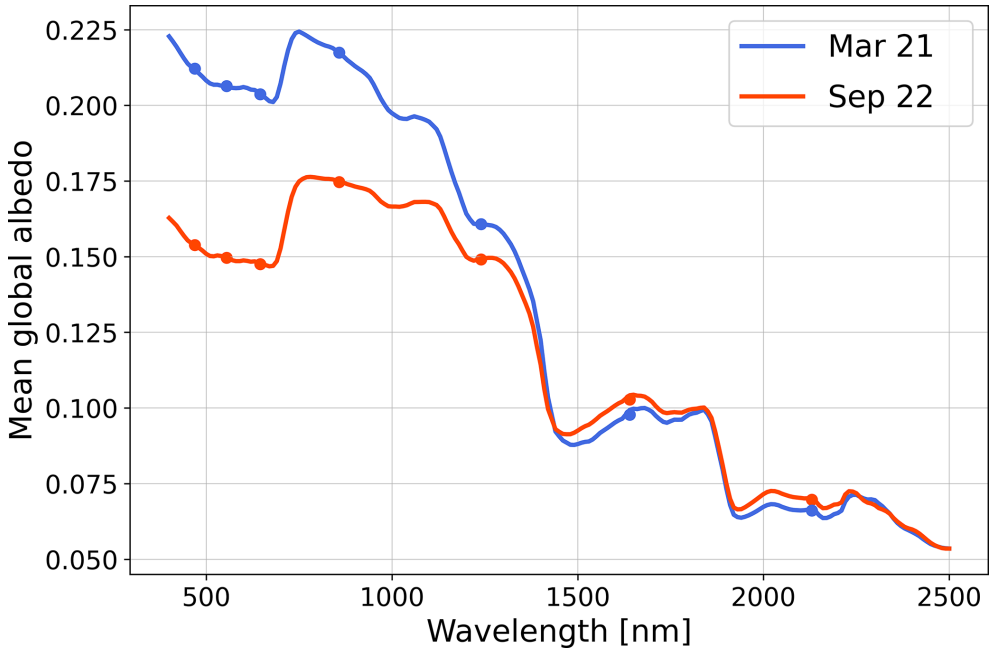

Figure 3.13: Mean global albedo as a function of wavelength across the entire globe. We select the two DOYs closest to the equinoxes, when almost all pixels are filled with albedo values. The seven dots represent the albedo values of the seven MODIS bands, while the curves are derived from the average of all pixels in the HAMSTER hyperspectral albedo maps for a given wavelength.

In addition, we apply the hyperspectral maps to study the VRE, which shows a steep increase in the reflectivity of vegetation due to chlorophyll, as shown in Fig. 3.13 at around 700 nm. In Fig. 3.14, we show the progression of vegetation reflectivity from 700 to 850 nm (with steps of 50 nm) for DOY 65 (5 March). We notice a substantial increase in albedo for all kinds of forests, from tropical to boreal, with the largest increase occurring between 700 and 750 nm, as expected for the VRE. This comparison is only possible when using albedo maps that account for the hyperspectral dimension. Using only the MODIS wavelengths would result in missing the entire VRE transition because the closest bands are only at 645 and 858 nm. Lastly, we study the spectral profile of different regions around the world, accounting for their seasonal variability. We select different examples of rainforests, boreal forests, deserts, urban areas, and ice-covered regions, as shown in Fig. 3.15. Using pixels from within the boundaries of the areas highlighted in Fig. 3.15, we average the spectra of all pixels in the regions in order to obtain an average spectrum that is representative of the entire region. The averages are calculated separately for the four seasons. The first comparison pertains to forest spectra (dark green regions in Fig. 3.15). We selected three different rainforests (the Amazon, Borneo, and Congo rainforests), two different boreal forests (located in Canada and Russia), and a savanna region in Kenya and Tanzania. The selection of these different areas was made by maximising land area with similar properties

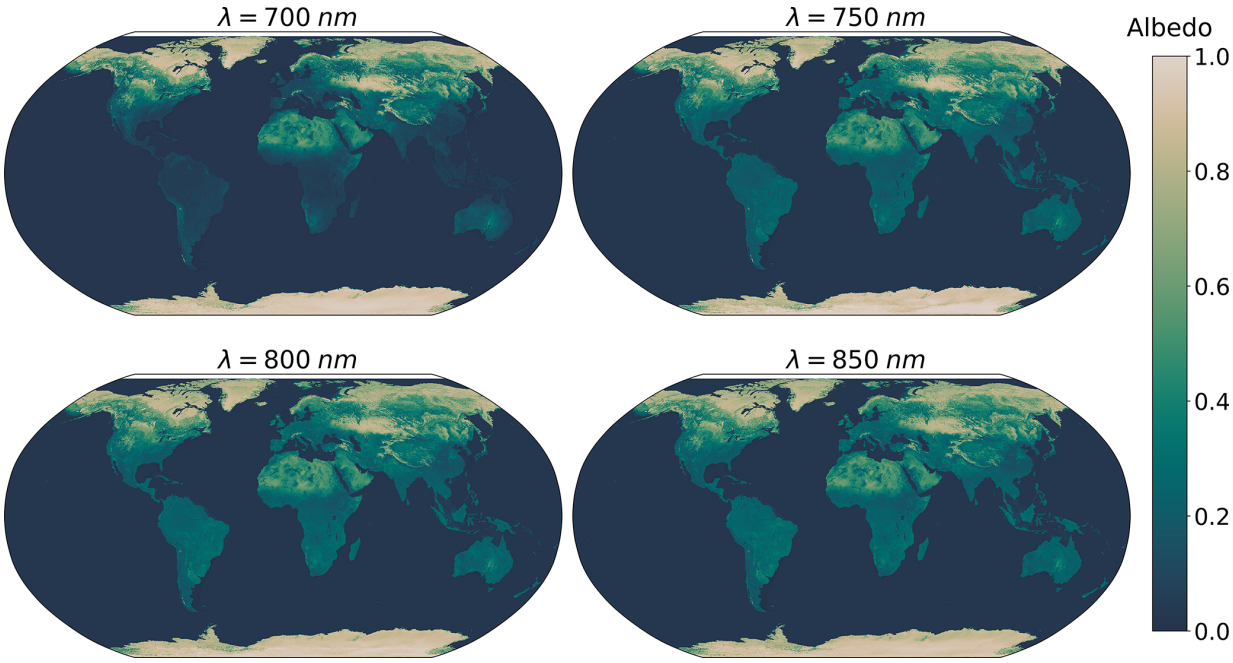

Figure 3.14: Spectral evolution of surface albedo for 5 March (DOY 65). From λ =700 nm to λ =850 nm, there is a steep increase in albedo over forests, attributed to the VRE.

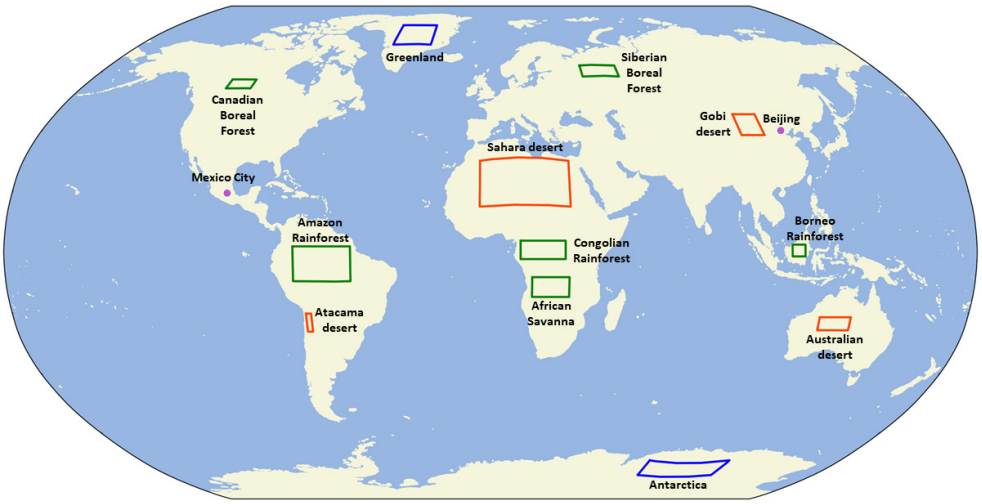

Figure 3.15: Regions of the world investigated in this study. The green boxes represent the forests, the orange boxes represent the deserts, the blue boxes represent the ice sheets, and the purple circles represent the cities.

while avoiding mixtures of urbanised soils and different land types within the regions. Figure 3.16 shows a comparison between spectra of different forests. We notice a similar trend among all kinds of forests, characterised by similar spectral features. In particular, all forests show three jumps in reflectivity of decreasing amplitude. The main difference

between tropical rainforests and boreal forests resides, as expected, in their seasonal variability. Tropical rainforests exhibit almost no seasonal change as they are very similar to each other. On the other hand, boreal forests experience an important decrease in reflectivity from boreal winter to boreal summer. This is due to the melting of snow in boreal forests, which also happens on different timescales. There are also some small differences within tropical rainforests. The Borneo rainforest shows the least seasonal variation, while the Congo rainforest shows the lowest reflectivity.
The final spectra are always combinations of different soils and vegetation, and the small differences we find are due to variations in tree, soil, and ground types, as well as varying tree coverage across the different forests. If we compare the obtained spectra with the spectral signatures shown in Fig. 3.2, we find overall agreement between their main spectral features, but our final spectra are modulated by the combination of many different soils and are averaged over seasons and different pixels. We extend the comparison to desert areas (orange regions in Fig. 3.15). We select the Sahara, the Australian desert, the Gobi Desert, and the Atacama Desert to extract spectral properties from the hyperspectral albedo maps. Figure 3.17 shows the comparison among different arid regions. We find that the reflectivity profiles of deserts can greatly vary depending on the mineralogy and composition of different soils and sands. In addition, as discussed in Fig. 3.12, the Sahara and Australian desert do not display any significant seasonal changes. This is not the case for the Gobi Desert, which shows enhanced reflectivity in the winter months due to partial snow coverage.
In general, deserts exhibit a common spectral shape, with a steep increase in reflectivity up to 750 nm, similar spectral features until the NIR range is reached, and a more or less steep decrease in reflectivity around 2150 nm. Compared to forests, different desert areas show larger discrepancies among themselves.
The same methodology is applied to study the Greenland and Antarctic ice sheets (blue areas in Fig. 3.15). We select two regions which are always snow-covered to study their spectral features and seasonal patterns (see Fig. 3.18). As expected for fully snow-covered surfaces, their reflectivity is very high, reaching a value of almost 1 in the VIS range, and it then decreases in the NIR range. During the winter in Greenland and Antarctica, not all the pixels were always available; thus, we averaged fewer pixels across fewer days to estimate their winter seasonal spectra. In Fig. 3.2, we see that snow and frost show different reflectivity patterns, particularly in the NIR range. This may explain the spread in the NIR spectra of both Antarctica and Greenland. This should be considered alongside the formation of clear, liquid-water lakes on the surface of glaciers during the melting season, which lowers the total reflectivity of the surface. For Greenland and Antarctica, we find similar behaviours in the NIR range, with winter seasons exhibiting higher reflectivity than summer seasons. We also notice that in the VIS range, there is almost no seasonal spectral variability over Antarctica, whereas Greenland shows two distinct trends between boreal autumn and winter and boreal spring and summer. To conclude, we also extracted spectral profiles for two different urban areas: the urban areas of Beijing and Mexico City. Among the 45 humanmade spectral materials from the ECOSTRESS library, there are general construction materials, road materials, roofing materials, and reflectance targets.

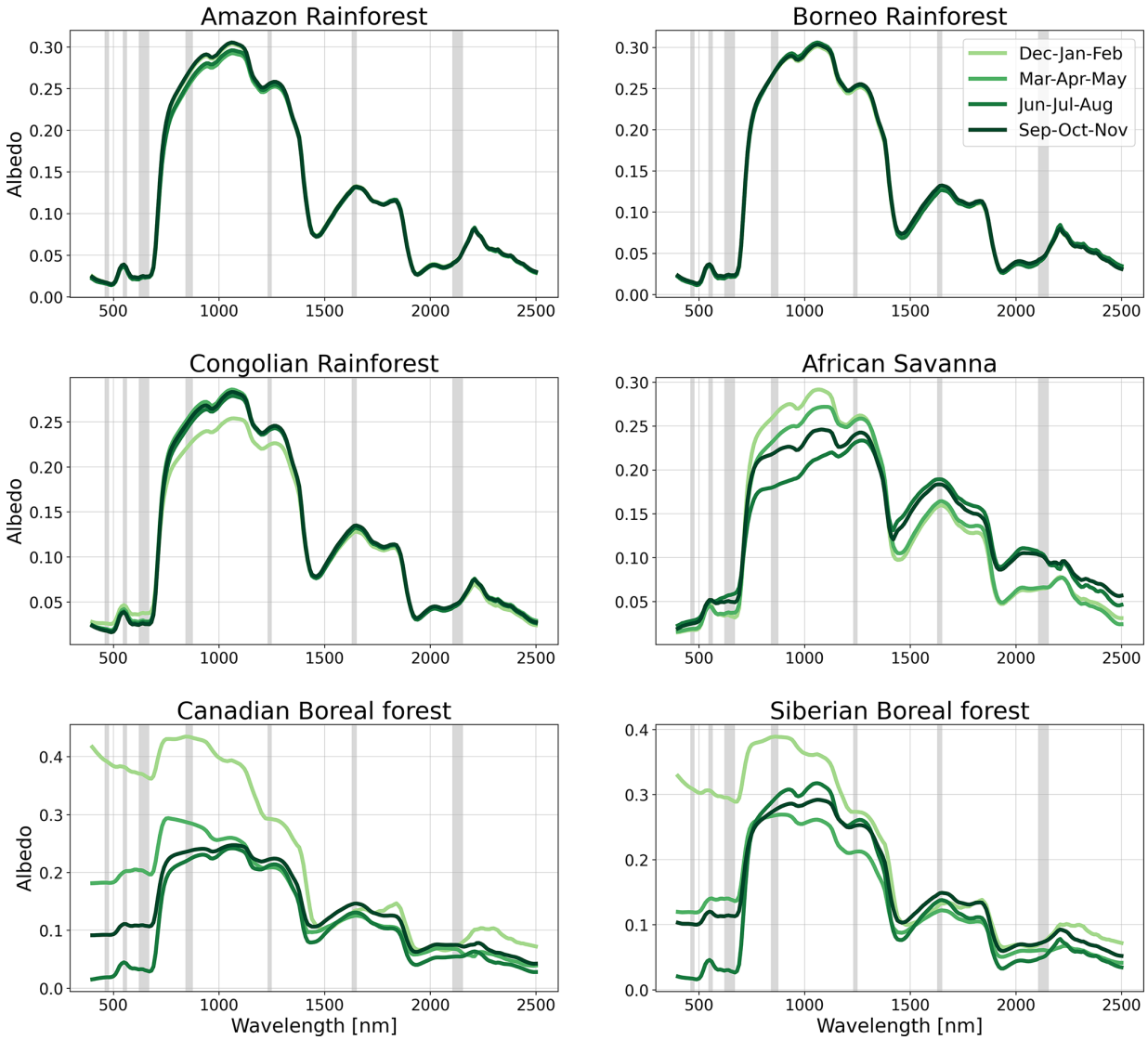

Figure 3.16: Spectra of different forests around the world, obtained by averaging the spectra over all pixels in the corresponding regions using the hyperspectral albedo maps. Seasonal variability is shown by averaging the spectra over 3-month periods, with different colours indicating different periods. Grey bands represent the MODIS bandwidths.

Urban areas are treated as a linear combination of different components, such as human-made materials, vegetation, and soils, and the PCA handles these components similarly to how it handles all other soil and vegetation spectra. MODIS albedo performance over cities has not been quantitatively assessed, and MODIS might underestimate surface reflectivity (Coddington et al., 2008); thus, city spectra should be used with caution. Figure 3.19 shows that Beijing has larger seasonal variability than Mexico City. In general, the spectra of the two cities look different but share some common spectral features. Urban areas show a lower albedo than the other regions investigated, indicating the use of asphalt and

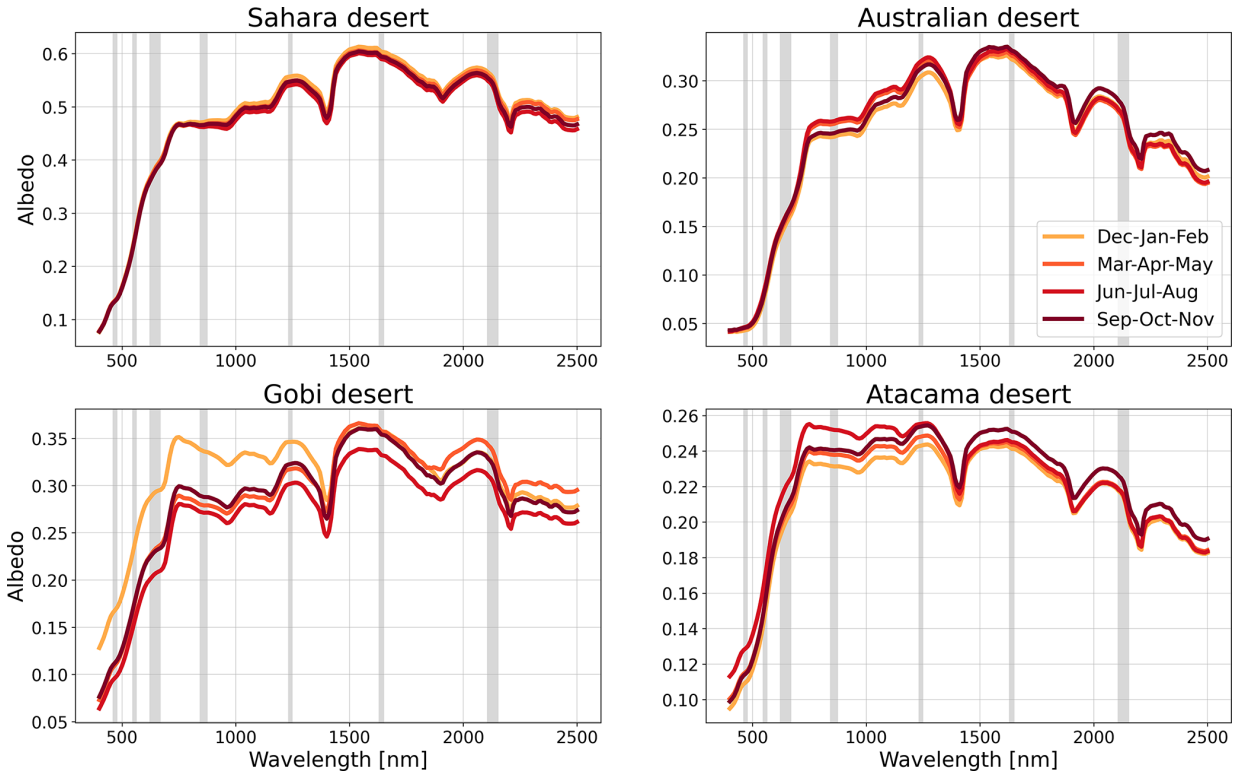

Figure 3.17: Spectra of different deserts around the world, obtained by averaging the spectra over different pixels from the hyperspectral albedo maps. Seasonal variability is shown by averaging the spectra over 3-month periods, with different colours indicating different periods. Grey bands represent the MODIS bandwidths.

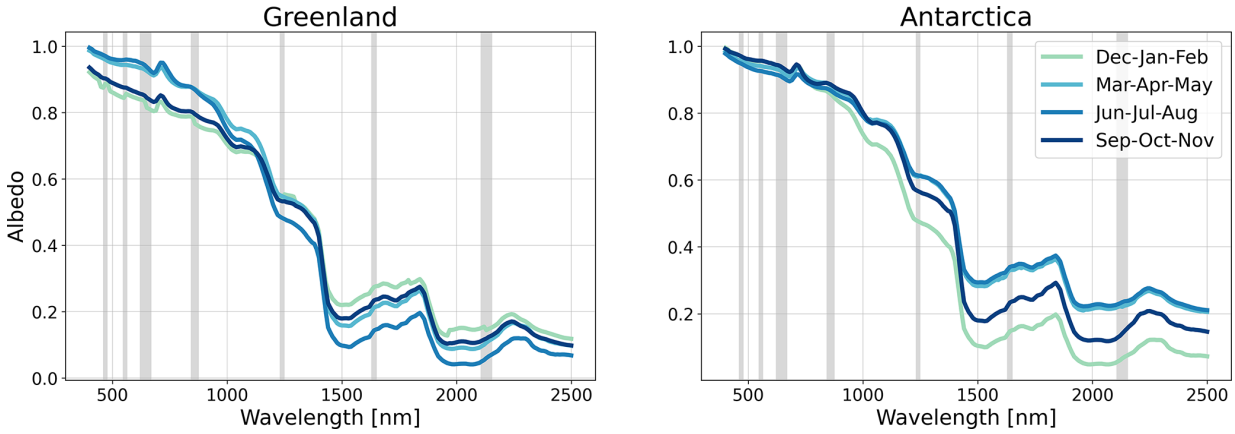

Figure 3.18: Spectra of different ice surfaces around the world, obtained by averaging the spectra over different pixels from the hyperspectral albedo maps. Seasonal variability is shown by averaging the spectra over 3-month periods, with different colours indicating different periods. Grey bands represent the MODIS bandwidths.

concrete spectra in the PCA, and their general spectral shape appears different from that of all other regions. The steep increase in the VIS range might be due to vegetation, while other features in the NIR range come from humanmade materials and different soils present in the training dataset. As expected, the peak reflectivity for urbanised areas is low.

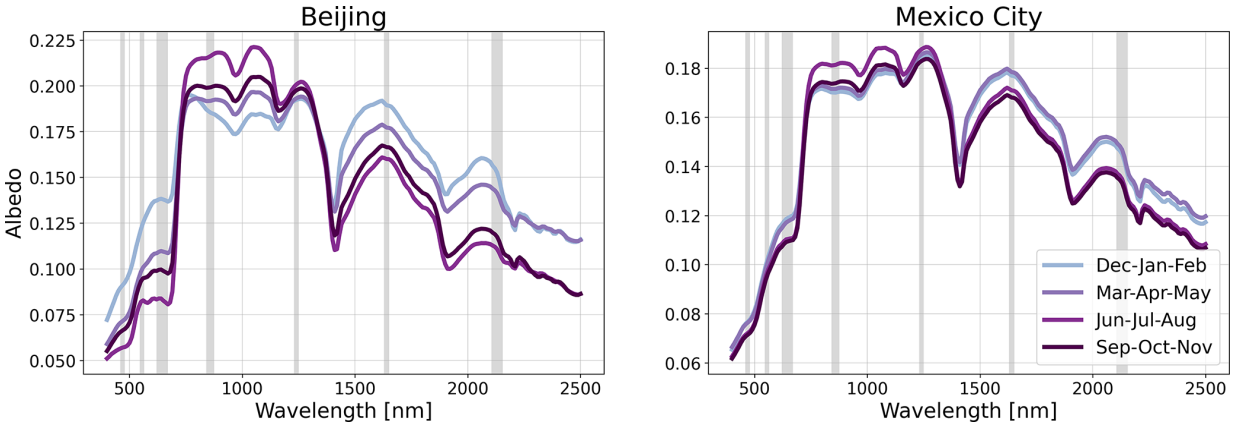

Figure 3.19: Spectra of two different cities (Beijing and Mexico City), obtained by averaging the spectra over different pixels from the hyperspectral albedo maps. Seasonal variability is shown by averaging the spectra over 3-month periods, with different colours indicating different periods. Grey bands represent the MODIS bandwidths.

In general, when extracting the spectra of different surface types, we found good agreement among the typical spectral features of soils and vegetation expected to dominate the different surface types. For instance, different kinds of forests all have a typical shape due to the VRE. However, the spectra of various land types contain much more information than the single spectrum of a tree or a particular soil, and we can clearly see that they constitute a linear combination of different spectra within the sample, with each set of spectra having varying weights. In fact, forests are a combination of trees with a typical spectral shape, modulated by different soil reflectivities. As a result, the retrieved albedo of an entire forest is noticeably lower than that of single trees in the dataset. This is in agreement with Jiang & Fang (2019), who generated different spectra for canopy-tree radiative-transfer simulations and studied the influence of soils on the total reflectivity of vegetated areas. While typical vegetated features are always present in the spectrum, they are modulated by the properties of the background soil.

3.5 Conclusion

In this work, we create hyperspectral albedo maps to study the wavelength-dependent characteristics of the black-sky albedo of the Earth's surface. We select spectra of various soils, vegetation, snow, waterbodies, and humanmade materials from three different datasets: the ECOSTRESS library, which includes spectra of soils, vegetation, humanmade materials, snow, and waterbodies; the LUCAS dataset, which contains spectra of different

soils from many countries around the world; and the ICRAF–ISRIC dataset, a catalogue of thousands of soil spectra from European Union countries. In total, we end up with 26 635 spectra of different soils and vegetation from 82 countries.
Due to the huge dimensionality of the final training dataset, we use a PCA regression algorithm to extract the principal components of the dataset. These principal components serve as eigenvectors to recover the albedo reflectivity of different pixels across the Earth, starting with the MODIS land surface product. Specifically, MODIS measures land surface properties across seven different bands in the VIS–NIR wavelength range. These seven MODIS bands are used as the starting point for building the hyperspectral albedo maps. Using PCA, we extract six principal components, following Vidot & Borbás (2014), and, with the addition of a seventh constant eigenvector, we combine these components with the seven bands of MODIS data, for which the albedo values of all single pixels are known. From this computation, it is possible to extract the spectral albedo value for the entire wavelength range, pixel by pixel.
To generate climatological hyperspectral albedo maps, we use the 1 d land surface product from the MODIS MCD43D product, and we average the data for each DOY from 2013 to 2022. This allows us to obtain a climatological average of global surface properties, fill in missing pixels that might be cloudy for a particular year, and disentangle pixels from yearly variability patterns. As a final outcome, we obtain the Hyperspectral Albedo Maps dataset with high Spatial and TEmporal Resolution (HAMSTER) with

- a spectral resolution of 10 nm, ranging from 400 to 2500 nm;
- a spatial resolution of 0.05° in latitude and longitude;
- a temporal resolution of 1 d, averaged over the time period from 2013 to 2022.

As demonstrated by Vidot & Borbás (2014) and Jiang & Fang (2019), PCA and SVD algorithms are powerful tools for combining large samples of soil and vegetation spectra and reconstructing the albedo profiles of different areas around the world. In addition to generating hyperspectral albedo maps through PCA, as demonstrated in Vidot & Borbás (2014), we also follow advice from Jiang & Fang (2019) by training the PCA with a much larger dataset, accounting for different countries around the world. In addition, our hyperspectral albedo maps cover all 365 DOYs, making it possible to retain all seasonal-variability patterns present in MODIS data.
Our MODIS climatological maps and hyperspectral albedo maps are validated against SEVIRI and TROPOMI land surface products. To perform this comparison, we adapt the SEVIRI dataset to the MODIS projection, and we find that there is good agreement between the MODIS climatology and the HAMSTER hyperspectral maps with SEVIRI observations, with discrepancies of up to 0.06, which is a typical order of magnitude for land surface product comparisons (Zhang et al., 2010; Shao et al., 2021). Similar results are found in the comparison with TROPOMI.
The MODIS climatological dataset already displays interesting temporal and spatial patterns. Thanks to its high spatial and temporal resolution, we can study the Earth's tem-

poral variability across different wavelengths and display the maximal albedo difference for each pixel, highlighting regions with high temporal variability. The mean spectral albedo of the planet peaks at wavelengths longer than those corresponding to the VRE and shows larger variability at the VIS wavelengths than at the NIR ones, with seasonal variations between snow-covered high-latitude regions in the Northern Hemisphere displaying an increase in surface albedo in boreal winter.
We combine information from the temporal and spatial resolution of the MODIS climatology data with the ability to spectrally extend the information about different regions to create typical spectra of different land surface types. We identify the following:

- Forests, as expected, exhibit typical vegetation-induced spectral features, such as the VRE. Tropical rainforests do not undergo much seasonal change, while boreal forests have increased reflectivity in winter due to partial snow cover. Savanna regions experience a drying of the land after the end of the summer, which flattens the typical vegetation-induced spectral features.

- Deserts show almost no seasonal variability, except for those with occasional snow coverage. Depending on the properties, colour, and mineralogical composition of the soils, as well as the presence of sand, the overall reflectivity of the desert can greatly vary.

- Ice- and snow-covered surfaces, such as the Greenland and Antarctic ice sheets, reflect almost entirely in the VIS range, with a steep decrease in the NIR range. During summer months, their albedo is slightly lower than during late winter or spring due to the melting of surface ice, which creates lakes on top of icy surfaces.

- Urbanised areas, such as Beijing and Mexico City, reflect a combination of many different spectra for humanmade materials, soil, and vegetation, and their spectral shape contains features from all of them. The total reflectivity of a city is less than 20 %.

These hyperspectral albedo maps can be used for many different applications, from improving climate models to enhancing remote sensing of the Earth, correctly simulating the disc-integrated spectra of the Earth (Emde et al., 2017), and correctly modelling earthshine observations (Sterzik et al., 2012, 2019). Only by using the full spectral variations in land surfaces can we correctly establish the Earth's energy budget. Braghiere et al. (2023) studied the impact of using only two broadband albedo values, as done in ESMs, versus using hyperspectral albedo maps. They found that while general radiative forcing is noticeably lower than that from a doubling of CO_2, omitting the hyperspectral nature of the Earth's surface causes deviations in many climatological patterns, such as precipitation and surface temperature, particularly across regional scales.

Data availability

The HAMSTER dataset is available at its finer spatial resolution (0.05° in latitude and longitude) at https://opendata.physik.lmu.de/04zd8-7et52. A lighter version of HAMSTER at a coarser spatial resolution (0.25° in latitude and longitude), useful for global applications (e.g. in ESM simulations), is available on Zenodo at https://doi.org/10.5281/zenodo.11459410. The MODIS climatology used as the initial step to generate HAMSTER from the MODIS MCD43D product can be found at https://opendata.physik.lmu.de/pt52a-nhm92. Finer spatial and spectral resolutions of the dataset (up to 30 arcsec and 1 nm, respectively) are available upon request from the corresponding author.

Video supplement

A video supplement for this work is available at https://doi.org/10.5446/66248, where we show the spectral and spatial evolution of HAMSTER for four different DOYs.

Author contribution

GR designed the research. GR, LB, and UH performed the MODIS climatology analysis. GR and FG trained the PCA using the soil and vegetation spectra. GR performed the analysis and made the plots. GR, CE, MFS, and MM interpreted the results. GR wrote the draft. All of the authors contributed to improving the paper. CW and CE implemented the dataset in `libRadtran`.

Competing interests

The contact author has declared that none of the authors has any competing interests.

Disclaimer

Publisher's note: Copernicus Publications remains neutral with regard to jurisdictional claims made in the text, published maps, institutional affiliations, or any other geographical representation in this paper. While Copernicus Publications makes every effort to include appropriate place names, the final responsibility lies with the authors.

Acknowledgements

The authors thank NASA for providing the MODIS Terra–Aqua "BRDF/Albedo Black-Sky Albedo Daily L3 Global 30 ArcSec CMG" MCD43D42-48 datasets for bands 1–7, whose albedo maps we used in this work. We also acknowledge EUMETSAT for providing the SEVIRI dataset and the ESA for providing the TROPOMI dataset. In addition, we acknowledge the ECOSTRESS, LUCAS, and ICRAF–ISRIC libraries, whose surface spectra we used in the PCA training.

Review statement

This paper was edited by Alexander Kokhanovsky and reviewed by Luis Ackermann and one anonymous referee.

4

Planet Earth in reflected and polarized light. I. Three-dimensional radiative transfer simulations of realistic surface-atmosphere systems

Published as
Roccetti et al., 2025a, Astronomy & Astrophysics, Volume 697, A170

Full authors list:
Giulia Roccetti; Claudia Emde; Michael F. Sterzik; Mihail Manev; Julia V. Seidel and Stefano Bagnulo.

Future ground- and space-based telescopes will enable the characterization of rocky exoplanets in reflected light, allowing for the observation of their albedo, which depends on surface, cloud, and atmospheric properties. Identifying key atmospheric, cloud, and surface features is essential for assessing the potential habitability of these exoplanets. We present reference spectra and phase curves for a spatially unresolved Earth-like exoplanet in reflected and polarized light, highlighting how wavelength-dependent and phase-angle-dependent reflectance reveals key planetary properties. Performing simulations with the 3D Monte Carlo radiative transfer code MYSTIC, we improve surface and cloud modeling by introducing validated wavelength-dependent albedo maps of Earth's seasonal and spectral features, as well as a novel treatment of subgrid cloud variability and inhomogeneities based on reanalysis data from ERA5. Our models incorporate high-resolution 3D cloud structures, demonstrating that subgrid cloud variability significantly affects both intensity and polarization. It reduces total reflectance and increases phase curve variability, especially at large phase angles where ocean glint dominates. Additionally, we show that neglecting realistic wavelength-dependent albedo maps leads to a significant overestimation of the vegetation red edge feature in reflected light spectra. Comparing an ocean planet to an Earth-like planet with seasonal cloud variability, we find that polarization is far more sensitive than intensity alone to identify the two scenarios. Moreover, polarization captures richer information on surface properties, making it a critical tool for breaking degeneracies in retrieval frameworks. We present detailed model simulations that provide a ground-truth reference for observing Earth as an exoplanet and that serve as critical benchmarks for developing observational strategies and retrieval frameworks for future telescopes targeting small rocky exoplanets. Furthermore, this study informs model requirements and establishes a framework to optimize strategies for characterizing rocky exoplanets,

emphasizing the pivotal role of polarization in breaking retrieval degeneracies across different models.

4.1 Introduction

The next generation of ground-based and space-based observatories will attempt to characterize rocky exoplanets in the habitable zones (Kasting et al., 1993) of nearby stars. Reflected light observations offer a powerful method for studying these planets by analyzing starlight that is either reflected off their surfaces or scattered in their atmospheres. Although current reflected light measurements can only provide upper limits (Charbonneau et al., 1999; Hoeijmakers et al., 2018; Spring et al., 2022), future instruments such as the ArmazoNes high Dispersion Echelle Spectrograph (ANDES; Pallé et al., 2025) and the Planetary Camera and Spectrograph (PCS; Kasper et al., 2021) on the Extremely Large Telescope (ELT), along with the proposed Habitable Worlds Observatory (HWO; National Academies of Sciences & Medicine, 2021), will enable the detection of reflected light from rocky exoplanets.

Reflected light is sensitive to planetary albedo, which is influenced by surface features such as ocean glint (Robinson et al., 2011; Livengood et al., 2011; Robinson et al., 2014; Lustig-Yaeger et al., 2018; Emde et al., 2017; Ryan & Robinson, 2022; Trees & Stam, 2022; Vaughan et al., 2023) and the vegetation red edge (VRE; Arnold et al., 2002; Woolf et al., 2002; Seager et al., 2005; Tinetti et al., 2006b; Fujii et al., 2011; Kawahara & Fujii, 2010; Wang & He, 2021) as well as atmospheric properties like clouds (Kaltenegger et al., 2007; Kitzmann et al., 2011; Damiano & Hu, 2020; Lin & Kaltenegger, 2020; Mukherjee et al., 2021; Pallé et al., 2025). These clouds, although they pose challenges in other techniques, enhance the potential of a positive detection in reflected light by increasing the planet's overall reflectance.

Observing Earth as an exoplanet provides an essential benchmark for future rocky planet studies. Techniques such as spacecraft observations, disk-integrated spectra from satellites, and Earthshine observations offer crucial insights into how Earth-like planets might appear in reflected light (Robinson & Reinhard, 2018). Contrary to satellite observations, Earthshine replicates the complex scattering and reflection geometry of how rocky exoplanets will be observed in reflected light. In recent years, Earthshine observations have been performed in intensity Goode et al. (2001); Woolf et al. (2002); Pallé et al. (2003); Tinetti et al. (2006a); Pallé et al. (2008, 2016) and in polarization (Sterzik et al., 2012; Takahashi et al., 2013; Bazzon et al., 2013; Miles-Páez et al., 2014; Sterzik et al., 2019, 2020; Takahashi et al., 2021). For ground-based observations, spectropolarimetry is particularly beneficial in distinguishing between telluric contamination, caused by Earth's own atmospheric transmission, and the actual reflected light from Earth. In standard spectroscopic observations, telluric lines overlap with the reflected light signals that we aim to detect, making it challenging to isolate the true reflected light features. Polarization filters out telluric lines, which remain largely unaffected by polarization, while retaining the polarized signal from the target.

The biggest challenge in observing rocky exoplanets in the habitable zone is the huge contrast between the stellar and planetary flux. Since F-, G-, and K-type stars emit nearly unpolarized light (Cotton et al., 2017), polarization serves as a valuable tool for distinguish-

ing planetary signals from stellar radiation. Incoming stellar light gets partially linearly polarized when reflected due to scattering in the atmosphere or to surface reflections. Polarization has the potential to aid in the detection of exoplanets, and it also provides crucial insights into surface properties, enabling the differentiation between land and ocean surfaces.

Advanced radiative transfer models enable realistic simulations of Earth as an exoplanet, considering both intensity and polarization. Stam (2008) developed the first of such models using an adding-doubling approach that assesses the influence of the phase angle (i.e., the angle between the star, the planet, and the observer) and the wavelength dependence on the degree of linear polarization of various homogeneous planets. Karalidi & Stam (2012) extended the model to simulate inhomogeneous planets by dividing the planet into small pixels with homogeneous characteristics, and found that results differ significantly when compared with horizontally homogeneous exoplanets. This highlights how horizontal inhomogeneities leave distinct traces in flux and polarization signals. A more realistic setup for comparison with Earthshine observations was developed by Emde et al. (2017), using a 3D Monte Carlo radiative transfer code that accounts for the treatment of fully inhomogeneous spherical geometry, in contrast to plane-parallel independent column models. The ability to simulate a realistic Earth-like exoplanet was of fundamental importance in assessing the influence of water and ice clouds, aerosols, and ocean glint on the polarization spectra of Earthshine and in constraining several biomarkers of our planet. In particular, Emde et al. (2017) demonstrated that light reflected by the ocean surface in the ocean glint region causes the highest increase in polarization. Trees & Stam (2019) further improved the adding-doubling algorithm from Stam (2008) by incorporating a more realistic treatment of the ocean surface, including Fresnel reflecting waves and scattering within the water body.

Notably, the ocean glint feature enhances intensity and contributes strongly to linear polarization in both the planetary spectrum and the phase curve. The color change of the polarized flux appears to uniquely identify an ocean surface, independent of surface pressure or cloud fraction. This feature may serve as a key indicator of surface water. Model simulations by Trees & Stam (2022) predict that an ocean on the surface of an exoplanet might already be detectable through spectropolarimetric measurement at a single phase angle: the glint leaves a dip instead of a peak in the polarization spectrum across the H_2O-gas absorption band around 950 nm. Additionally, using polarized rather than unpolarized reflectance makes it possible to exclude false-positive detections, which might be generated by reflecting dry surfaces or ice caps (Cowan et al., 2012). However, multiple scattering by clouds and aerosols can depolarize the signal and increase the total flux, complicating interpretations (Hansen, 1971; Emde et al., 2017).

Polarization also plays a significant role in detecting liquid water clouds, as demonstrated by the presence of the polarized cloudbow feature (Karalidi et al., 2012). Even partial ice cloud cover does not completely obscure this signal. Observationally, Sterzik et al. (2020) derived from spectropolarimetric Earthshine observations that clouds on Earth are made up of liquid water, inferring their particle size from the cloudbow feature as a demonstration of this technique for Earth-like exoplanets. This shows that spectropolarimetry can

identify the composition of clouds.
In this first paper in the series, we present an updated modeling framework based on the Monte Carlo code for the phYsically correct Tracing of photons in Cloudy atmospheres (MYSTIC), part of the libRadtran software package (Mayer & Kylling, 2005b; Emde et al., 2016), to simulate the Earth as an exoplanet. MYSTIC incorporates 3D Earth-like atmospheres, full Stokes vectors to account for polarization, and 2D inhomogeneous surface models. We further improved the surface modeling setup by adding 2D inhomogeneous planetary surfaces, which can now couple the surface reflectance matrix for the ocean with Lambertian albedo maps for land surfaces, and inhomogeneous surface wind maps over the ocean, which improve the accuracy of the simulation of the ocean glint feature. Additionally, we developed a new 3D Cloud Generator algorithm to take into account subpixel cloud inhomogeneities with variable water content, using data from ERA5, the European Centre for Medium-Range Weather Forecasts (ECMWF) ReAnalysis fifth-generation product, and satellite observations.
Finally, we conducted sensitivity studies to assess how these improvements impact the planet's computed spectra and phase curves, highlighting the pronounced differences between true fine-scale surface and cloud structures versus simplified, coarse, and smeared-out models in observed intensity and polarization spectra. In the second paper in this series, we will apply our novel methodology to Earth-like exoplanets and explore its implications for a putative Earth 2.0 observed in reflected and polarized light. The third and final paper will compare our updated model with our entire catalog of Earthshine observations, validating our approach and establishing a baseline for using our models as ground-truth prescriptions in future studies on rocky exoplanet characterization and habitability assessment.

4.2 Theoretical background

Observing an exoplanet in reflected light, the contrast between the planet and the star can be expressed as

$$\frac{F_p}{F_\star} = \left(\frac{R_p}{a}\right)^2 A_g \cdot g(\alpha), \tag{4.1}$$

where F_p and $F_\star$ are the fluxes of the planet and the star, respectively, R_p is the radius of the planet, a is the semimajor axis of the star-planet system, A_g is the geometric albedo of the planet and $g(\alpha)$ is the phase function, and α the phase angle (e.g., the angle between the star, the planet, and the observer). A reflected light spectrum of an exoplanet appears like the stellar spectrum with additional absorption and Rayleigh scattering features.
The geometric albedo is a wavelength-dependent quantity, while the phase function depends on both the wavelength and the phase angle. Both quantities are independent of the stellar spectrum.
By fixing the radius of the planet and the semimajor axis, we can express the contrast in fluxes only as a function of A_g and $g(\alpha)$. This way, we can study the properties of different

surfaces and clouds in the reflected light spectrum of an Earth-like planet. We define this quantity as the reflectance, which is the product of the geometric albedo and the phase function. Thus the reflectance $R = A_g \cdot g(\alpha)$ is also independent of the stellar spectrum.
The incident starlight to the planet is expected to be almost unpolarized. The disk-integrated sunlight is polarized at the level of 10^{-6} (Kemp et al., 1987). For active FGK-stars, the degree of linear polarization was calculated to be on the order of 23.0 ± 2.2 ppm, while for inactive stars the polarization signal is expected to be about 2.9 ± 1.9 ppm (Cotton et al., 2017). Also, stellar flares and spots should contribute with small degrees of linear polarization on the order of 10^{-6} (Berdyugina et al., 2011).
By contrast, stellar light reflected by the surface of the planet or scattered by processes happening in the exoplanet atmosphere can be linearly polarized at the level of several tens of percent. Rayleigh scattering produced by molecules in the atmosphere polarizes light, although multiple scattering processes involving cloud and aerosol particles can strongly depolarize the radiation. Similarly, certain surface features, like the ocean glint, produce strong linear polarization signatures, while scattering by other surface types can depolarize light previously polarized by Rayleigh scattering. Thus, observations of polarized light enhance the contrast between the planet and stellar fluxes.
We can describe the total (polarized and unpolarized) flux of the disk-integrated planetary signal with a Stokes vector (Chandrasekhar, 1950)

$$F = [I, Q, U, V], \tag{4.2}$$

where I is the intensity, Q and U are the linearly polarized fluxes and V the circularly polarized flux. Q and U are described with respect to a reference frame. In our simulations, the reference plane corresponds to the planetary scattering plane, which is the plane through the centers of the planet, the host star and the observer.
We define the degree of polarization

$$P = \frac{\sqrt{Q^2 + U^2 + V^2}}{I}, \tag{4.3}$$

which describes the fraction of photons which get polarized over the total flux coming from the planet, and it is independent on the reference plane. For an Earth-like atmosphere, V, the circular polarization component, is very small compared to the linear polarization terms, and thus we can express the degree of polarization,

$$P = \frac{\sqrt{Q^2 + U^2}}{I}, \tag{4.4}$$

only as a function of the linearly polarized components, thus becoming the degree of linear polarization.
While the total flux intensity spectrum of an exoplanet is an absolute measurement, the degree of linear polarization is a relative measurement and does not need to be calibrated with the distance or type of the star. Additionally, only the first few scattering orders contribute to the polarization signal. Multiple scattering depolarizes light because higher-order scattering events disrupt the predominant direction of radiation, reducing their contribution

to the Stokes parameters Q and U. In contrast, multiple scattering primarily contributes to I, thereby decreasing the degree of polarization P. Thus, the features in Q and U are better constrained compared to unpolarized light, because they are less smeared out by multiple scattering. For example, features like the cloudbow are due to single-scattering.

4.3 3D Radiative transfer simulations

We perform our simulations with MYSTIC (Mayer, 2009), a versatile radiative transfer model for Earth's and planetary atmospheres in the libRadtran software package[1] (Mayer & Kylling, 2005b; Emde et al., 2016). The code is used here to calculate reflected and polarized light radiances of the Earth with realistic 3D atmospheres and 2D surface reflectance properties maps. The implementation of polarization in MYSTIC is described in Emde et al. (2010). Accurate and efficient cloud scattering simulations require the sophisticated variance reduction methods by Buras & Mayer (2011a). The absorption lines importance sampling method (Emde et al., 2011) enables high spectral resolution simulations. In order to calculate the radiance reflected by the whole planet, a 3D spherical model setup is required (Emde et al., 2017). The polarization results of MYSTIC show good agreement compared with other codes (Emde et al., 2015; Emde et al., 2018; Korkin et al., 2022).
Here we summarize the major initial setup for generating spatially unresolved spectra of an Earth-like exoplanet:

- The Sun-Earth-Moon geometry (e.g., phase angle) is simulated by selecting the Sun's and Moon's latitudes and longitudes relative to the Earth, along with the Earth-Moon distance. These values can be obtained, for example, from the Earth and Moon Viewer.[2]

- A sensor is placed at a distance $d = 384\,400$ km, the typical Earth-Moon distance, with an aperture $\theta = 1.25°$. As a result, the scene consists of the Earth at the center of the field of view, surrounded by empty space. The reflectance values produced by MYSTIC are artificially reduced due to photons traveling into empty space without being reflected back. To correct for this effect, all reflectance values are divided by a geometrical factor

$$f = \frac{(2d \tan\theta)^2}{\pi R_\oplus^2}, \tag{4.5}$$

  where $R_\oplus$ is the Earth radius.

- We run 10^7 photons to generate each spectrum, resulting in a standard deviation below 0.1% (Emde et al., 2017), which is significantly smaller than the expected

[1] http://www.libradtran.org/doku.php
[2] https://www.fourmilab.ch/earthview/

observational errors. For the single-wavelength simulations used in phase curve calculations, we run 10^6 photons, reaching a relative error of roughly 0.3%. To generate the images, we divide each image into a 1000 × 1000 pixel grid and run 1000 photons per pixel, resulting in a total of 10^9 photons.

- All spectra are obtained with a spectral resolution of 1 nm over the 400–1000 nm wavelength range. The phase curves are computed with an angular resolution of 2°. While the spectra are calculated in the optical wavelength regime, they can also be computed in the ultraviolet (UV), near-infrared (NIR), and mid-infrared (MIR) regimes. Additionally, the spectral resolution can be adjusted to achieve high spectral resolutions of up to $R = 100000$.

- An atmosphere is specified by a vertical pressure and temperature profile, as well as the vertical mixing ratios of the most common gas species. We use the US standard amtosphere properties (Anderson et al., 1986).

- 3D ice and liquid water clouds are included from a cloud file which specifies the 3D spatial position, liquid water content, ice water content, and effective radius of cloud droplets and ice crystals. The optical properties of liquid water clouds are computed using the Mie scattering tool of the libRadtran package (Emde et al., 2016; Wiscombe, 1980). The ice crystals are composed of smooth randomly oriented crystals treated as a mixture of six habits, and their optical properties are parameterized following the HEY (Hong, Emde, Yang) parameterization, which includes the full phase matrices for the 0.2 to 5 μm wavelength range (Emde et al., 2016, Appendix A).

- We generate realistic cloud distributions from the ECMWF ERA5 data for a particular date and time, and in this paper we introduce a new 3D Cloud Generator approach (Sect. 4.5.1) to account for cloud inhomogeneities and subgrid variability.

- Land surfaces are treated as Lambertian surfaces with different albedos, and in this paper we introduce new wavelength-dependent surface albedo maps (Roccetti et al., 2024) in 3D radiative transfer simulations (Sec. 4.4.1) to treat spectral features of different land components.

- The ocean surface is simulated using the bidirectional surface reflection functions (BPDFs) coupled with a surface wind speed maps acquired from ERA5 data and accounts for the influence of waves, including shadowing effects (Mishchenko & Travis, 1997).

Emde et al. (2017) used MYSTIC to simulate the Earth as an exoplanet and compare the results with Earthshine observations. We build upon the approach of Emde et al. (2017) by greatly enhancing the representation of surface properties. While Emde et al. (2017) could only simulate either an ocean surface with its BPDF or a purely Lambertian surface, our novel method allows for a combination of both. It is now possible to represent inhomogeneous planetary surfaces coupling an ocean surface with a Lambertian representation

of land, which greatly improves the realism of surface modeling. Additionally, we now include inhomogeneous surface wind maps provided by the ERA5 reanalysis products for the treatment of surface wind speed, expanding from the homogeneous wind maps available in Emde et al. (2017).
A second, more important, improvement is the refinement of the 3D cloud profile implementation. We perform sensitivity studies to address the need of introducing cloud inhomogeneities and subgrid variability, which reduces the bias from the former cloud representation (Emde et al. (2017), see Sec. 4.5.1 for more details). Lastly, we introduce variable effective cloud droplet radii based on realistic parameterizations from ECMWF (ECMWF, 2024).
To generate true color images of the planet, we first perform MYSTIC simulations at three wavelengths: 469 nm, 555 nm and 645 nm. From these three wavelengths, a simplified spectrum is constructed as a step function in the visible range, where intensity values at all wavelenghts in the continuum are associated with the output of the closest simulated wavelength. The simplified spectrum is then convoluted with the color matching functions from the International Commission on Illumination (CIE) to obtain colors in the CIE color space. CIE colors are then converted to RGB colors using the transformation of the RGB standard. The resulting colors have a linear brightness scale and need to be transformed into a power-law brightness scale by applying a gamma transfer function, as specified by the RGB standard.

4.4 Surface modeling

Ocean and land surfaces exhibit distinct albedo characteristics due to their differing properties. Oceans have low albedo because water absorbs most visible and near-infrared sunlight. In contrast, land surfaces vary in reflectance based on composition: snow-covered regions are highly reflective, while forests and deserts show lower albedo depending on their vegetation and soil type. Surface roughness further influences reflectance. Smooth surfaces, like calm oceans or bare rock, reflect more light than uneven surfaces, such as forests and grasslands. Additionally, the angle of incoming sunlight affects reflectance. Sunlight striking the ocean surface at a steep angle tends to penetrate the water, while shallow-angle sunlight is more likely to be reflected.
In Emde et al. (2017), simulating both ocean and Lambertian land surfaces simultaneously was not possible in polarization mode. In our updated approach, we now implement a Lambertian surface for land pixels, specifying albedo values, and a BPDF for ocean pixels. This is the only model available in the literature that can effectively handle a mixture of BPDF and Lambertian surfaces, compared to previous work by Emde et al. (2017); Trees & Stam (2019, 2022); Vaughan et al. (2023). This enables realistic simulations of inhomogeneous planetary surfaces, combining ocean and land, and improving the treatment of varying albedo effects for Earth and exoplanets.
All land surface types, apart from oceans, are treated as pure Lambertian surfaces in our model. Although materials like forest leaves and sand can polarize light via surface reflec-

tion, land BPDFs are unavailable for our model. However, the largest polarized reflectances observed by the PARASOL instrument over land are of the order of 0.02 and 0.04 (Maignan et al., 2009), and their contribution to Earth's disk integrated polarized radiance is expected to be minor, as shown in Groot et al. (2020).
In the case of water reflections, surface roughness significantly expands the area where sunlight is directly reflected, extending beyond the solar disk's size on Earth. This phenomenon, known as ocean glint, becomes more pronounced with increasing wind speed over the water surface. For our simulations, the ocean is modeled using the realistic BPDF from Mishchenko & Travis (1997). This model also incorporates the shadowing effects of ocean waves, as described by Tsang & Li (1999).

4.4.1 Hyperspectral albedo maps

Albedo varies with wavelength, and accurately representing this spectral variability is crucial for correct energy balance calculations in radiative transfer simulations. Proper treatment of the spectral variability of surface types is essential for capturing the continuum in simulated spectra and identifying features like the VRE around 780 nm. However, no global hyperspectral albedo maps are provided by current satellite or reanalysis products. Gordon et al. (2023) addressed this issue by classifying surface pixels into five categories (ocean, forest, grass, sand, and snow/ice) using the Level-3 MODIS Yearly Global Land Cover Types (YGLCT) product. They coupled these categories with the ECOSTRESS spectral library (Baldridge et al., 2009; Meerdink et al., 2019) to account for spectral variability. A similar approach was used by Kofman et al. (2024), who applied linear mixing of land surface spectra to represent mixed surface types.
Roccetti et al. (2024) developed a hyperspectral albedo map dataset, HAMSTER, which captures the spatial, temporal, and spectral variability of Earth's surface albedo, based on MODIS surface albedo satellite measurements (Schaaf et al., 2002). This dataset significantly improves land surface representation by treating them as a mixture of soils and vegetation. In terms of seasonal variability, HAMSTER shows that rainforests exhibit almost no seasonal changes, whereas boreal forests experience variations due to snow, with their summer profile closely resembling that of a rainforest. Similarly, for deserts, HAMSTER reveals that the Sahara and Australian deserts show little to no seasonal variation, while high-altitude deserts are affected by seasonal snow cover. In contrast, the typical profile of a savanna is strongly season-dependent, resembling a desert during the dry season and a forest during the wet season (Roccetti et al., 2024).
In Fig. 4.1, we compare the typical reflectance spectra of different soils and vegetation components from the ECOSTRESS library with the yearly average, spatially integrated spectra of a forest and a desert from HAMSTER (Roccetti et al., 2024). Specifically, we compare the Sahara and Australian deserts in ECOSTRESS with dry soil and sandstone materials. Similarly, we compare the Amazon rainforest and the Siberian boreal forest with the grass and oak leaf spectra from ECOSTRESS.
We find that without such detailed treatment, land reflectance can be over- or underestimated. For instance, the VRE peak at 780 nm reaches around 0.3 in Roccetti et al. (2024),

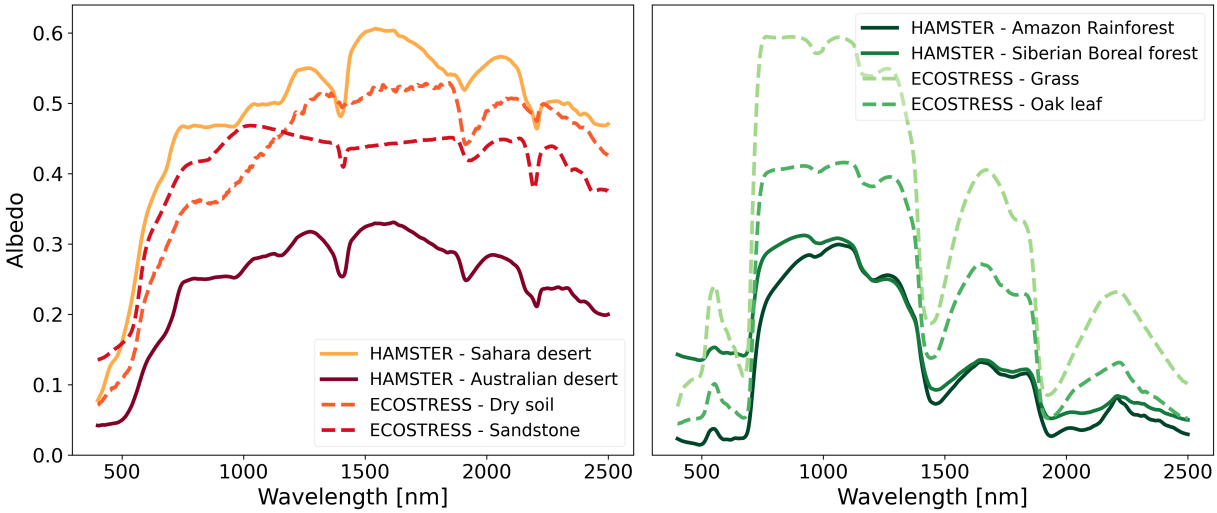

Figure 4.1: Comparison of desert and forest spectra from HAMSTER (solid lines) with typical soil and leaf spectra from the ECOSTRESS library (dashed lines).

whereas ECOSTRESS data for a broadleaf tree shows an albedo of approximately 0.6, underscoring the importance of combining soil and vegetation properties in land surface simulations. A similar trend is observed for the green bump around 500-600 nm, which is also overestimated when the combination of various surface types is not considered.
We use HAMSTER to represent surface reflectance in our model and explore the sensitivity of surface albedo to seasonal variability in Sec. 4.6.3. HAMSTER provides a spatial resolution of 0.05° in latitude and longitude, a temporal resolution of one day, and a spectral resolution of 10 nm, allowing it to capture key spectral features such as chlorophyll absorption and other soil properties.
To evaluate the impact of HAMSTER, we replicated the simplified hyperspectral albedo maps described in Kofman et al. (2024). This was achieved by generating a linear combination of spectra from the ECOSTRESS spectral library, guided by land cover type information from the MODIS MCD12C1 product. The 17 land cover types were grouped in five categories (grass, forest, soil, snow and water bodies) as in Gordon et al. (2023) and Kofman et al. (2024). The resulting spectra and phase curves were then compared to assess their differences.

4.4.2 Inhomogeneous surface wind maps

The reflective properties of the ocean glint depend on the water surface structure, which is influenced by wind speed. In our model, we use horizontal surface wind data from meteorological sources as input to the BPDF function for water surfaces (Tsang & Li, 1999; Mishchenko & Travis, 1997). For each surface grid cell, the wind speed is calculated from the northward and eastward wind components provided by the "ERA5 hourly data on single levels from 1940 to present" (Hersbach et al., 2020). This approach generates

inhomogeneous surface wind maps that affect the shape and size of the glint, although the wind direction is not considered. This is the first time that inhomogeneous surface wind speed maps are introduced, while previous approaches used a constant wind speed of $10\,\mathrm{m\,s^{-1}}$ (Emde et al., 2017), and between 1 to $13\,\mathrm{m\,s^{-1}}$ (Trees & Stam, 2022). This setup provides a realistic representation of the glint, which, together with cloud cover, impacts the spectra and phase curves of the planet. The relationship between ocean glint and wind speed is explored in Appendix 4.11.

4.5 Cloud modeling

We introduce a novel approach to modeling clouds in our 3D simulations to achieve a highly realistic representation of global cloud systems on Earth. As the detailed combination of clouds and surfaces determines the geometrical albedo, accurate prescriptions are essential to model reflectance and polarization correctly (Eq. 4.1). In our model, we represent clouds using 3D maps of liquid water content (LWC) and ice water content (IWC) from the ECMWF's ERA5 reanalysis product (Hersbach et al., 2020). Reanalysis products combine past observations with advanced weather forecast models to generate a consistent and complete picture of past atmospheric conditions. This involves the use of data assimilation techniques to integrate observations from various sources (such as satellites, weather stations, and buoys) into a weather model. The ERA5 reanalysis product comes with a high horizontal spatial resolution of approximately 28 km on a global grid (or 0.25°) and 37 vertical levels from the surface up to 1 hPa (about 48 km altitude), providing detailed information on the state of the atmosphere. The LWC and IWC are the starting point to calculate the optical thickness of clouds. In the approximation of geometrical optics, which is accurate in the visible, the optical thickness is given by

$$\tau = \frac{3}{2}\frac{\Delta H \cdot LWC}{\rho_{\mathrm{w}} \cdot r_{\mathrm{eff}}}, \tag{4.6}$$

where ΔH is the height of the cloud, ρ_{w} is the density of liquid water and r_{eff} is the cloud droplet effective radius. For an ice water cloud, τ is calculated as in Eq. 4.6 by substituting LWC with IWC. The ERA5 data comes with mass mixing ratios which are converted to LWC/IWC by computing the local air density using the ideal gas law.
ERA5 provides hourly data, allowing for detailed temporal analysis of weather and climate patterns. This high temporal resolution is valuable for studying diurnal cycles, extreme weather events, and other time-sensitive phenomena. The consistency of the ERA5 reanalysis product is crucial for long-term climate studies, trend analysis, and the validation of climate models.
To model a representative planet, we run all our cloudy spectra and phase curves with 12 different cloud fields selecting one random day from each month during 2023. This way, we can represent the variability of the planet, like its seasonal and internal variability. We select different random days for the two different geometries we are representing:

- for an ocean planet, defined as a scenery over the Pacific Ocean, we simulate cloudy planets of the days reported in Table 4.1, at UTC 22:00 to catch the cloud properties as they are over the Pacific ocean, better representing an ocean planet configuration;

- for an Earth-like planet, we select a scenery over the Indian ocean, with Asia, Europe and Africa visible in the scene. The cloud fields are randomly selected by day, but are all selected for UTC 06:00, to better represent cloud properties which are a mixture of land and ocean components. This prevents introducing a bias associated with cloud properties over different surfaces. The cloud properties for the Earth-like planet are displayed in Table 4.2.

When comparing cloud properties over the ocean and the Earth-like planet, we observe small differences in cloud cover, optical thickness, and the effective radii of water and ice cloud droplets. Throughout the study, we represent the variability due to cloud properties in all spectra and phase curves by averaging the final spectra across 12 independent simulations, each using different cloud fields, and indicating the 1σ spread resulting from cloud variability.
We also find that the cloud cover value we find from the ERA5 reanalysis cloud product is rather large. A possible explanation is the "resolution effect" problem. Dutta et al. (2020) found the total cloud cover measured by finite resolution satellites to be overestimated. This bias can be overcome with finer angular resolution satellite instruments.
Emde et al. (2017) used the predecessor of ERA5, ERA Interim, to represent cloud properties within MYSTIC. ERA Interim was provided on a coarser grid than the ERA5 product. Using hourly data such as the ones provided by ERA5 is useful to compare with Earthshine observations, as it provides the opportunity to represent the cloud properties at the exact date and time of the observations. However, Emde et al. (2017) assumed that the LWC and IWC provided by ERA Interim were the in-cloud values, thus they mutiplied them by the cloud fraction of each gridbox to obtain the gridbox average LWC and IWC, which are the quantities needed to estimate the cloud optical thickness in MYSTIC. However, as in ERA5, also ERA Interim was providing already the gridbox averages LWC and IWC, thus the multiplication for the cloud fraction substantialy underestimated the cloud optical thickess and impacted the representation of the radiative and microphysical properties of clouds. This effect has significant impact and is the major reason why the Earthshine polarization spectra modeled in Emde et al. (2017) did not match well observations.
While ERA5 presents a rather fine spatial resolution for a global cloud model, the grid size of each pixel (around 31 km) is still rather large and fails to represent the more realistic, patchy nature of clouds. In fact, smoothing microphysical cloud properties over large grid scales results in an average state of clouds and spreads the LWC and IWC information on the entire grid cell. However, in nature, clouds appear to be patchy and a more correct representation is required to account for horizontal inhomogeneities among clouds and the presence of clear-sky and cloudy subpixels inside the same grid cell. This effect of cloud representation is very relevant in 3D radiative transfer models, and in particular for polarized spectra and phase curves, which are more sensitive on the effect of clouds and

their microphysical properties. Thus we developed a new approach to treat 3D cloud subpixel variability and inhomogeneities, called the 3D Cloud Generator approach, in order to calculate reference (ground-truth) spectra and phase curves of Earth as an exoplanet in reflected and polarized light.

4.5.1 3D Cloud Generator

The 3D Cloud Generator (3D CG) is based on the Hogan & Bozzo (2018) one-dimensional cloud generator, but adapted for a 3D radiation scheme. This is crucial to generate realistic spectra and phase curves of Earth as an exoplanet, due to the horizontal and vertical distribution of clouds, and in particular their overlap over the ocean glint area. Our 3D CG, being based on the one used from the 1D radiation scheme ecRAD, does not include any correlation between columns, which is left for a future implementation.
The first step in the 3D CG is to compute the cumulative cloud cover profile, $c_{i+1/2}$, from the top of the atmosphere (TOA) to the i-th layer, using ERA5 cloud cover data (a_i) for individual layers. Additionally, the pairwise cloud cover, $p_{i+1/2}$, between adjacent layers i and $i+1$ is calculated. However, without subgrid information on the horizontal cloud distribution, determining $p_{i+1/2}$ from a_i and a_{i+1} is not straightforward. Clouds can be vertically overlapping, randomly arranged or a mixture of both. To address this ambiguity, various cloud overlap assumptions have been developed and validated against observations (Hogan & Illingworth, 2000). In Fig. 4.2 we show a schematic illustration of four cloud overlap assumptions.
The two most simple cloud overlap assumptions are the maximum and the random overlaps. The maximum overlap assumes clouds are perfectly vertically aligned, while the random overlap assumes a completely stochastic distribution between layers. These two assumptions represent opposite extremes, while the maximum-random (MAX-RAN) overlap (Morcrette & Jakob, 2000) offers a more balanced and realistic approach. In MAX-RAN overlap, clouds in vertically contiguous layers are maximally overlapped, while those separated by cloud-free layers are randomly overlapped.
Assuming MAX-RAN overlap, the pairwise cloud cover of two adjacent layers is

$$p_{i-1/2} = \max(a_{i-1}, a_i). \tag{4.7}$$

An alternative approach is the exponential-random (EXP-RAN) overlap (Hogan & Illingworth, 2000), where an "overlap parameter" α is used to interpolate between the maximum and the random overlap assumptions for adjacent cloudy layers. The α parameter decays as the distance between layers increases:

$$\alpha_i = \exp\left(-\frac{\Delta z_i}{z_0}\right). \tag{4.8}$$

Here Δz_i is the thickness of the i-th layer and z_0 is the cloud cover decorrelation length. The ECMWF Integrated Forecast System (IFS) documentation (ECMWF, 2024) presents

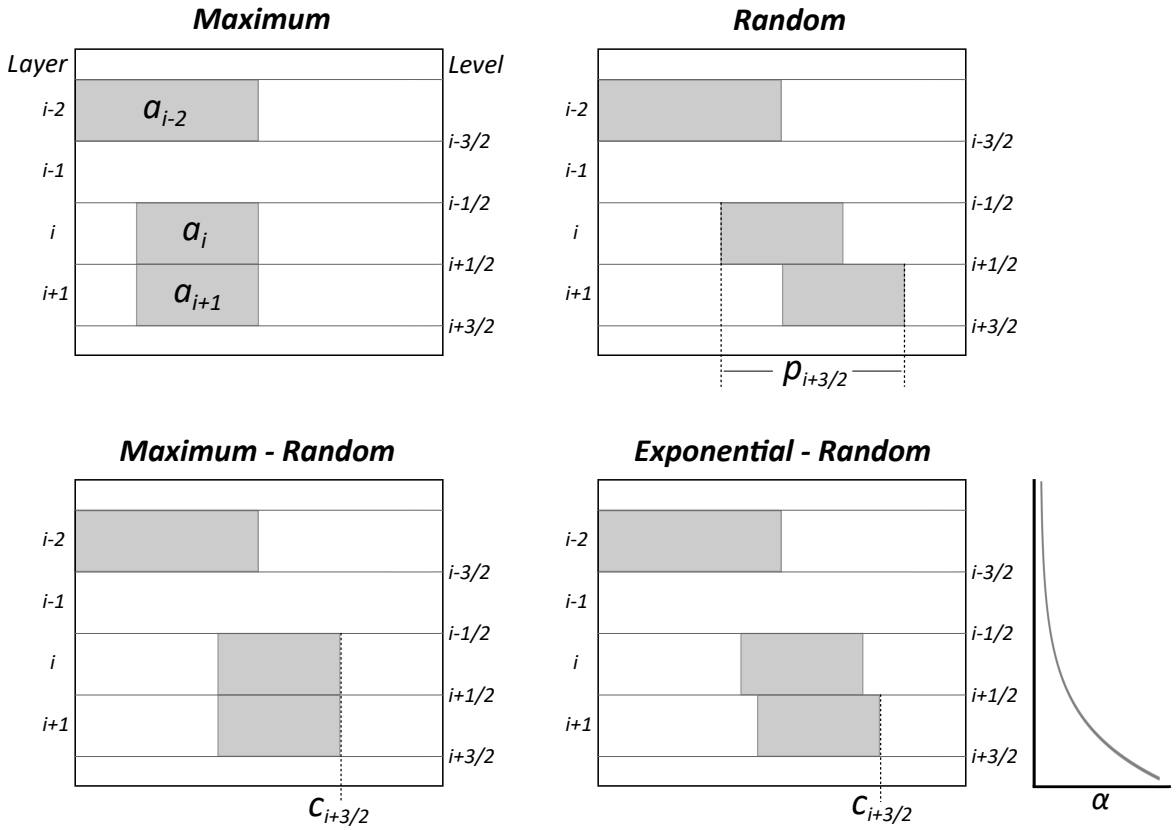

Figure 4.2: Schematic illustration of four cloud overlap assumptions: maximum, random, maximum-random (MAX-RAN), and exponential-random (EXP-RAN) overlap. The figure also shows the meaning of three important quantities: the cloud cover of a given layer, a_i; the pairwise cloud cover $p_{i+1/2}$; and the cumulative cloud cover $c_{i+1/2}$. For the EXP-RAN overlap, a schematic illustration of the exponentially decaying α parameter is also included, showing how it decreases with altitude as the separation between layers increases.

a parameterization of z_0 based on latitude, following the ideas of Shonk et al. (2010):

$$z_0[\text{km}] = 0.75 + 2.149 \cos^2 \phi. \tag{4.9}$$

The thickness of the layers, Δz_i, increases with altitude for ERA5 reanalysis data, hence the α parameter decreases exponentially with altitude.
The pairwise cloud cover computed assuming EXP-RAN overlap is

$$p_{i-1/2} = \alpha_{i-1/2} \max(a_{i-1}, a_i) + (1 - \alpha_{i-1/2})(a_{i-1} + a_i - a_{i-1}a_i), \tag{4.10}$$

where the α parameter weights more the maximum overlap for close layers and the random overlap for distant ones.
For both assumptions, we compute the cumulative cloud cover iteratively as

$$c_{i+1/2} = 1 - (1 - c_{i-1/2}) \frac{1 - p_{i-1/2}}{1 - a_{i-1}}. \tag{4.11}$$

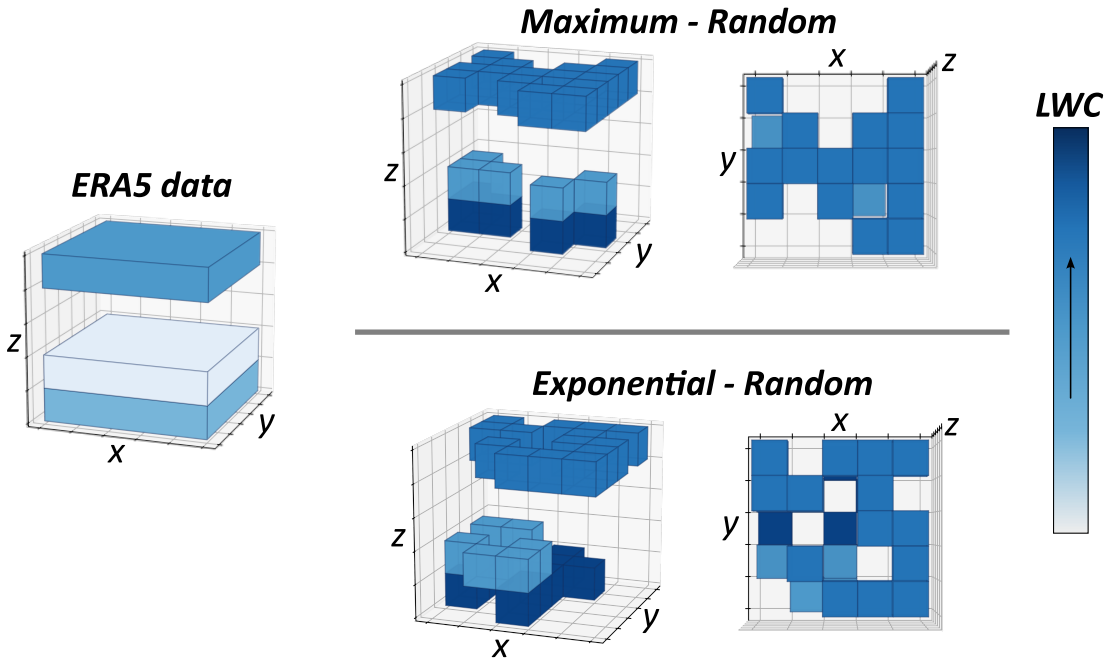

Figure 4.3: 3D schematic illustration depicting the input and output of the 3D CG for liquid water clouds, without including horizontal inhomogeneity. The original ERA5 pixels are subdivided into smaller columns, with clouds assigned based on the procedure outlined in the main text. The color of the boxes represents the associated LWC, which is adjusted to conserve the ERA5 LWC layer by layer.

This first step is completely deterministic, and only depends on the cloud overlap assumption employed.
The next step of the 3D CG is to divide the original ERA5 column in $N \times N$ subcolumns and assign, along each subcolumn (independently) cloudy and non-cloudy subpixels. This procedure is stochastic and is again based on Hogan & Bozzo (2018). Initially, we determine the highest cloudy layer by generating a first random number R_0 from a uniform distribution between 0 and 1. The i-th layer is chosen as the highest cloudy one if $c_{i-1/2}/C < R_0 \leq c_{i+1/2}/C$, where $C = c_{n+1/2}$ is the total cloud cover. Next we proceed further down to the layer $i+1$ and determine if that layer is also cloudy by generating a further random number R_i. If the present layer i is cloudy, the next one is cloudy too if

$$R_i < \frac{a_i + a_{i+1} - p_{i+1/2}}{a_i}. \tag{4.12}$$

On the other hand, if the current layer i is not cloudy, the next one is set to be cloudy if

$$R_i < \frac{p_{i+1/2} - a_i - c_{i+3/2} + c_{i+1/2}}{c_{i+1/2} - a_i}. \tag{4.13}$$

The right-hand side of Eq. 4.12 (and Eq. 4.13) represents the conditional probability of finding a cloudy pixel in layer $i+1$ given that the previous layer i was cloudy (or not). For a more thorough discussion on how this probability is derived, see Fig. 3 in Hogan & Bozzo (2018) and the accompanying explanation.
By the end of this procedure, we obtain a binary matrix $\mathcal{C}$ with dimensions (N, N, N_z), with N_z the number of vertical layers, recording which pixels are populated by clouds and which are non-cloudy.
The last step of the 3D CG consists of assigning to all cloudy pixels a value for LWC and IWC. Contrary to Hogan & Bozzo (2018), we start directly from the ERA5 gridbox averages $\overline{LWC}_i$ and $\overline{IWC}_i$ instead of scaling the optical depth.
First we convert the gridbox average $\overline{LWC}_i$ to the in-cloud LWC_i^{ic} of layer i by dividing by the cloud cover a_i:

$$LWC_i^{ic} = \frac{\overline{LWC}_i}{a_i}. \tag{4.14}$$

The same holds for the in-cloud IWC_i^{ic}. In principle we could set all cloudy pixels in a given layer i of the matrix $\mathcal{C}$ to this in-cloud LWC_i^{ic} value. In practice, we follow the algorithm of Räisänen et al. (2004) to generate a distribution of LWC that resembles more closely the cloud cover vertical distribution and to introduce some horizontal inhomogeneity. The uppermost cloudy layer LWC_i is determined by scaling the LWC_i^{ic} by a random value γ extracted from a gamma distribution of mean value $\mu = 1$ and fractional standard deviation $\sigma = 0.75$. If the next layer $i+1$ is cloudy, we extract a random number R_{i+1} and compare with the cloud condensate cumulative frequency α_{i+1}^{lwc}. If $R_{i+1} < \alpha_{i+1}^{lwc}$, the next layer is filled with the same LWC as the previous layer; if the opposite is true, a new random value from the gamma distribution is extracted. In summary:

$$LWC_{i+1} = \begin{cases} LWC_i & \text{if } R_{i+1} < \alpha_{i+1}^{lwc} \text{ and } \mathcal{C}_i = 1 \\ \gamma \cdot LWC_{i+1}^{ic} & \text{otherwise} \end{cases}. \tag{4.15}$$

The cloud condensate cumulative frequency α^{lwc} is computed as the exponential overlap parameter α (Eq. 4.8), the only difference being that the decorrelation length z_0 of the cloud parameters is half the one for the cloud cover (ECMWF, 2024).
By the end of this procedure, the randomness intrinsic to the attribution of LWC values may have changed the total amount of LWC compared to the initial gridbox average data from ERA5. Therefore, we add an additional step compared to the original procedure by Räisänen et al. (2004) and we correct for this randomness by rescaling, layer by layer, each value of LWC_i by

$$LWC_i^r = LWC_i \cdot \frac{LWC_i^{ic}}{< LWC_i >}, \tag{4.16}$$

where the mean $< LWC_i >$ is performed over all subcolumns and LWC_i^r is the rescaled LWC of the layer i. The same procedure is performed also to obtain the values for the IWC.
The 3D CG input and output are shown in Fig. 4.3. The original ERA5 pixel is divided into subcolumns, which are populated by cloudy and non-cloudy pixels according to the procedure described above. Additionally, LWC and IWC values for all pixels are obtained using Eq. 4.15 and Eq. 4.16. As shown in the figure, the EXP-RAN overlap scheme generates slightly more cloudy columns, as it introduces randomness even in contiguous cloud layers, unlike the MAX-RAN overlap.

4.5.2 Variable cloud effective radius

The optical thickness depends also on the effective radius of the cloud droplets as in Eq. 4.6. r_{eff} is calculated following the ECMWF parameterizations (ECMWF, 2024). The liquid water effective radius is

$$r_{\text{eff}}^{\text{liquid}} = \left[\frac{3E_d(LWC + RWC)}{4\pi\rho_{\text{w}}kN_d}\right]^{1/3}, \tag{4.17}$$

where RWC is the rain water content, E_d is an enhancement factor accounting for drizzle dispersion introduced in Wood (2000), k is a shape-dependent factor and N_d is the number concentration of cloud droplets, parameterized differently between pixels above sea and pixels above land following Martin et al. (1994) and computed using the wind speed as an input.
The ice effective radius is parameterized following Sun & Rikus (1999) and Sun (2001),

$$r_{\text{eff}}^{\text{ice}} = \frac{3\sqrt{3}}{8} D_{\text{eff}}^{\text{ice}}, \tag{4.18}$$

where $D_{\text{eff}}^{\text{ice}}$ is the ice particle effective diameter. For all the details regarding these parameterizations, we refer to ECMWF (2024).
We also investigate the effect of using a constant effective radius, instead of a variable effective radius calculated for each gridbox from the ECMWF parameterization, while keeping

the same optical depth. This requires us to rescale the LWC of the cell accordingly, given the equation for the optical depth Eq. 4.6:

$$LWC' = LWC_0 \cdot \left(\frac{r'_{\text{eff}}}{r_{\text{eff},0}} \right). \tag{4.19}$$

Here LWC_0 and $r_{\text{eff},0}$ refer to the standard quantities, using the parameterized effective radius, and LWC' and r'_{eff} represent the variables in the case of constant effective radius.

4.5.3 Cloud zoom-out algorithm

To further investigate the effect of the horizontal grid resolution in simulating spectra and phase curves of spatially unresolved exoplanets, we now move to coarser grid scales. We call this procedure cloud zoom-out, as we average out the cloud properties from the fine grid scales of the 3D CG and the ERA5 product to coarser resolutions. To generate 3D cloud maps at coarser resolutions, we average out the ERA5 data across $N \times N$ horizontal grid-cells, while keeping the vertical direction intact and the optical depth constant. In order to do so, we first compute the average ratio between LWC and r_{eff} and then we multiply it by the average r_{eff}. In this way, we keep the optical depth of the new, merged, column, equal to the mean of the original subcolumns on which we performed the averaging.

$$\overline{r_{\text{eff}}} = \langle r_{\text{eff}} \rangle \tag{4.20}$$

$$\overline{LWC} = \left\langle \frac{LWC}{r_{\text{eff}}} \right\rangle \times \langle r_{\text{eff}} \rangle, \tag{4.21}$$

where the brakets indicate the average over the $N \times N$ horizontal window. $\overline{r_{\text{eff}}}$ and $\overline{LWC}$ are the values assigned to the averaged column.

4.6 Results

Using MYSTIC, we generate true color images of an ocean planet, which corresponds to a geometry over the Pacific ocean, where we removed all continents, and of an Earth-like scenario, showing a configuration with Asia, Africa, Europe, and the Indian Ocean in the scenery. In Figs. 4.4 and 4.5 we show how the ocean and Earth-like planets look at different phase angles (α = 0, 30, 60, 90 and 120°). These two configurations are the starting point to generate spatially unresolved spectra and phase curves of the ocean and Earth-like configurations, averaging over the full disk of the simulations. We selected the Earth-like configuration to maximize the land surface component, and to let it cover almost completely the ocean glint feature at high phase angles ($\alpha > 90°$), where the ocean glint presents a major effect.

In Figs. 4.4 and 4.5 we also show the same configurations with realistic clouds simulated through the 3D CG approach. When showing spectra and phase curves for a cloudy planet, we always run the same configurations with 12 different cloud fields, one for each month

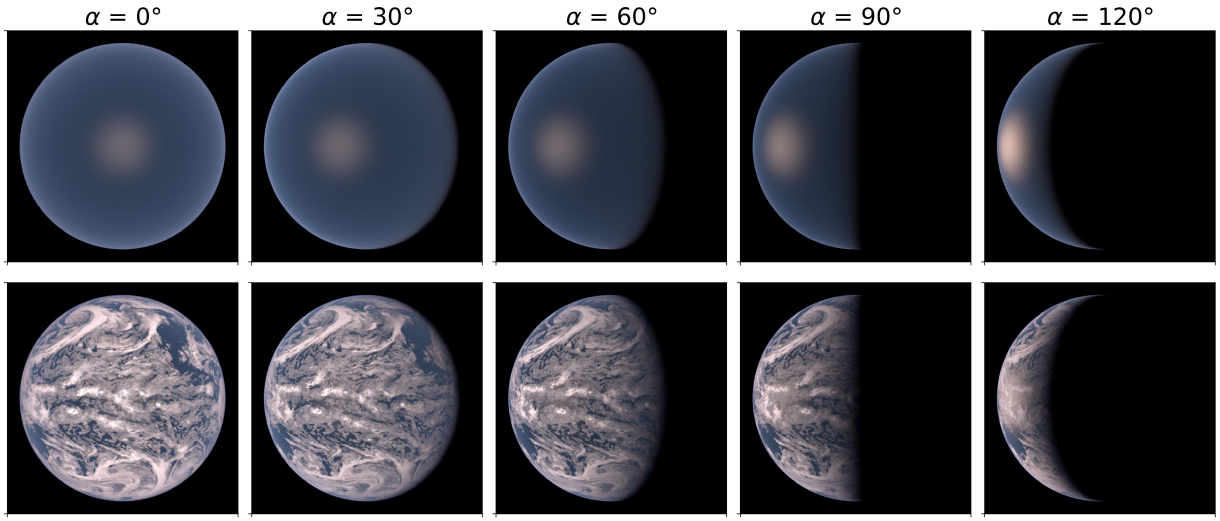

Figure 4.4: True color simulations of the ocean planet configuration with an Earth-like atmosphere for different phase angles (different columns). The same geometry is simulated without clouds (first row) and with clouds (second row) using the ERA5 reanalysis dataset from 2023-09-18 UT22:00 for the cloud setup. The glint feature becomes covered by inhomogenous realistic clouds in the second row.

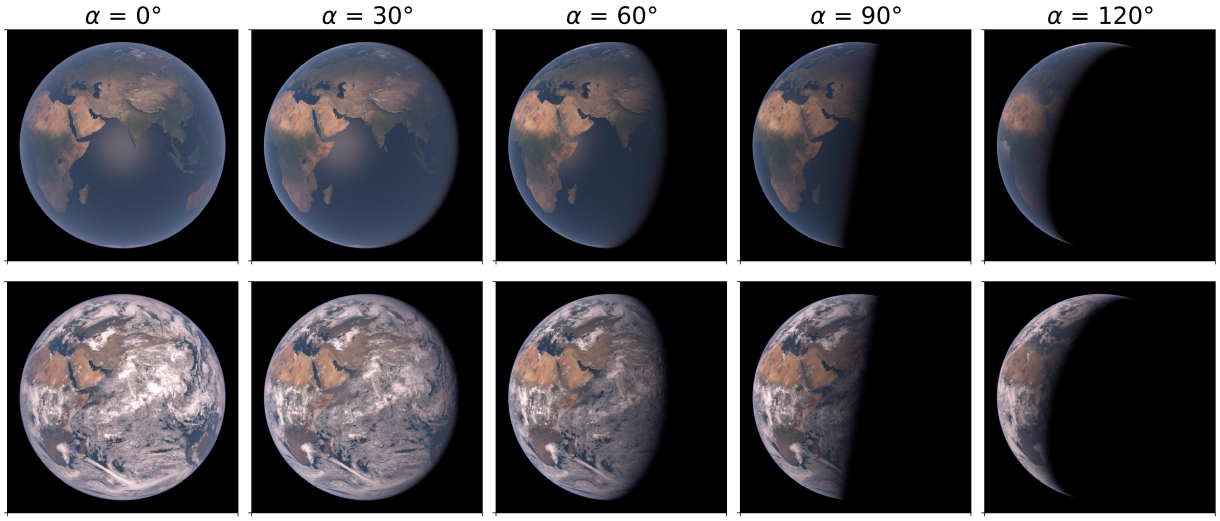

Figure 4.5: True color simulations of the Atlantic configuration of an Earth-like exoplanet for different phase angles (different columns). The same geometry is simulated without clouds (first row) and with clouds (second row) using the ERA5 reanalysis dataset from 2023-09-18 UT06:00 for the cloud setup. The glint feature becomes partially hidden by continents in the first row, and covered by inhomogenous realistic clouds in the second row.

of the year, randomly selecting the date. This will allow us to show the 1σ range in the spectra and phase curves that represent the seasonal variability of the clouds.

In Tables 4.1 and 4.2 we report the selected dates for the ocean and Earth-like configurations, respectively. To better represent typical cloud properties over an ocean or land surfaces, we selected the cloud fields from the "ERA5 hourly product on pressure levels from 1940 to present" to be at UT 22:00 for the ocean configuration, where the illuminated side of the planet maximized the Pacific ocean, and at UT 06:00, to have the illuminated side representing the Earth-like configurations described above. In Tables 4.1 and 4.2 we report the calculated cloud properties of the different cloud configurations for $\alpha = 90°$, in particular their cloud cover, optical thickness, altitude, and effective radius for liquid and ice water clouds. We also present the cumulative cloud cover for both liquid and ice water clouds as it depends non-trivially on their vertical overlap, while the cumulative optical thickness can be obtained as the sum of the individual ice and liquid water clouds optical thicknesses. We calculate the cloud properties only for the visible scene. The cloud cover is estimated using recursively Eq. 4.11 to compute $c_{n+1/2}$ for each column and averaging over the visible scene. To estimate cloud altitudes more accurately in Tables 4.1 and 4.2, we use the procedure described in Appendix 5.8, while MYSTIC simulations assume constant height levels over the full globe.
Tables 4.1 and 4.2 show seasonal variability across different dates, particularly in cloud cover and optical thickness. They also reveal statistical differences in the average cloud properties between the ocean and Earth-like configurations. Specifically, we find that cloud cover over the ocean (cloud fields with UT 22:00) is about 5% higher than over the Earth-like configuration. This is expected due to the presence of dry regions, such as the Sahara Desert, in the selected geometry. Additionally, the Earth-like configurations exhibit lower τ due to the lower cloud cover. We also observe that clouds tend to form at higher average altitudes over ocean surfaces and exhibit larger effective radii for both liquid and ice water clouds. These differences are in agreement with cloud patterns found in satellite observations and reanalysis products and allow us to represent in our spectra and phase curves of the Earth as an exoplanet the variability due to seasonal changes in cloud properties and their differences as a function of ocean versus land coverage.

4.6.1 Impact of the 3D Cloud Generator

To investigate the impact of cloud representation, particularly the cloud radiative response in the 3D radiative transfer simulations, we selected an ocean surface with constant wind speed of $10\,\mathrm{m\,s^{-1}}$ as our configuration (Fig. 4.4). Starting from cloud properties from the ERA5 reanalysis product, we introduce subgrid cloud inhomogeneities using the 3D CG approach as described in Sec. 4.5.1.
In Appendix 4.9 we analyze the impact of the zoom-in factor on the radiative transfer effects of clouds and find that it quickly converges to a stationary value, even at a zoom factor of 3. In Fig. 4.6, we show the reflectance and polarization spectra of an ocean planet with different cloud models for three different phase angles: 60, 90, and 120°. We can clearly see that the reflectance of the ERA5 cloud configurations is greatly overestimated when not accounting for the subgrid variability of the clouds. This strongly influences the albedo of the planet, in particular at high phase angles. For the polarization spectra, we find

date	All clouds cc [%]	Liquid water clouds cc [%]	H [km]	r_{eff} [μm]	τ	Ice water clouds cc [%]	H [km]	r_{eff} [μm]	τ
2023.01.15 UT22:00	58.1	47.3	1.83	9.3	7.14	51.1	4.51	50.7	0.54
2023.02.16 UT22:00	59.6	48.5	1.79	9.5	7.22	53.8	4.97	50.9	0.66
2023.03.29 UT22:00	64.6	54.2	1.56	9.2	7.00	59.9	4.36	48.1	0.66
2023.04.10 UT22:00	57.7	49.5	1.67	9.4	6.62	52.2	5.43	50.1	0.61
2023.05.17 UT22:00	63.1	56.6	1.67	9.4	6.88	59.5	4.45	51.0	0.69
2023.06.21 UT22:00	64.7	57.7	1.54	9.4	9.46	59.5	5.14	49.2	0.62
2023.07.14 UT22:00	66.6	59.0	1.56	9.8	9.55	57.0	6.18	48.8	0.69
2023.08.06 UT22:00	62.6	55.4	1.59	9.7	9.92	57.5	4.66	48.5	0.64
2023.09.12 UT22:00	61.7	53.6	1.71	9.7	7.86	57.8	4.96	49.4	0.69
2023.10.07 UT22:00	61.2	54.1	1.53	9.3	7.45	55.4	4.28	48.7	0.61
2023.11.27 UT22:00	63.7	51.7	1.64	9.0	5.61	59.5	4.23	50.7	0.65
2023.12.30 UT22:00	61.9	49.0	1.61	9.0	6.30	54.7	4.43	50.0	0.68
average	62.1	53.1	1.64	9.4	7.58	56.5	4.80	49.7	0.64

Table 4.1: Cloud properties for the 12 different cloud fields and their average used for the ocean planet scenario at $\alpha = 90°$.

date	All clouds cc [%]	Liquid water clouds cc [%]	H [km]	r_{eff} [μm]	τ	Ice water clouds cc [%]	H [km]	r_{eff} [μm]	τ
2023.01.22 UT06:00	50.5	38.1	1.58	8.7	5.11	45.5	4.95	47.5	0.45
2023.02.08 UT06:00	57.1	41.5	1.46	8.5	5.81	52.5	3.91	46.5	0.55
2023.03.02 UT06:00	53.2	38.3	1.49	8.6	5.23	47.7	3.44	45.6	0.53
2023.04.09 UT06:00	50.1	35.0	1.48	8.8	4.51	44.2	3.77	46.1	0.45
2023.05.14 UT06:00	61.5	36.5	1.52	8.7	5.62	57.2	3.89	42.0	0.68
2023.06.05 UT06:00	63.0	37.1	1.64	8.3	5.56	57.5	3.69	42.7	1.10
2023.07.26 UT06:00	61.4	36.2	1.79	8.6	5.19	54.7	3.59	42.1	0.70
2023.08.29 UT06:00	55.9	35.9	1.54	8.7	5.61	48.3	4.19	42.6	0.56
2023.09.18 UT06:00	60.2	40.0	1.51	8.5	5.36	54.4	3.85	42.2	0.64
2023.10.05 UT06:00	57.5	35.0	1.53	8.5	5.42	51.8	3.24	42.0	0.58
2023.11.12 UT06:00	60.7	41.5	1.50	8.7	6.29	56.3	3.71	45.1	0.70
2023.12.24 UT06:00	52.9	41.5	1.51	8.5	5.53	48.4	4.35	47.4	0.50
average	57.0	38.0	1.55	8.6	5.44	51.5	3.88	44.3	0.62

Table 4.2: Cloud properties for the 12 different cloud fields and their average used for the Earth-like planet scenario at $\alpha = 90°$.

that the 3D CG representation has an impact on the slope of the spectra at small phase angles ($\alpha = 60°$), it shows an important difference in the polarization at $\alpha = 90°$, while the effect becomes substantial at high phase angles ($\alpha = 120°$). In particular, this large discrepancy at high phase angle can be explained by the effect of the ocean glint. Making the clouds more "patchy" and increasing their horizontal inhomogeneities allows for the glint to be less masked by the clouds and to greatly increase the polarization compared to the ERA5 clouds. Additionally, the 1σ spread due to cloud variability increases at larger

phase angles. This is because the ocean glint feature has its strongest impact on polarization spectra and phase curves at these angles. Running simulations at large phase angles with different cloud fields, each containing a different spatial cloud distribution, results in varying degrees of cloud coverage over the ocean glint region. As a result, some cases exhibit a more pronounced glint effect, while others are more obscured by clouds, leading to an increased spread in the simulations.
In polarization, we also observe a change in the behavior of atmospheric absorption lines. We define an absorption feature as a case where the absorption line in polarization falls below the continuum, whereas we refer to it as emission when the line appears above the continuum. In particular, the O_2-A line around 770 nm is shown in emission for most of the polarized spectra, while it changes behavior between the 3D CG simulations (absorption) and the ERA5 clouds (emission) at $\alpha = 120°$. This change in behavior is due again to the different cloud properties, in particular cloud optical depth and cloud height, and how they are represented in the radiative transfer simulations. A different behavior is also observed for the water band around 950 nm, where the feature appears in absorption only when including subgrid cloud variability, while otherwise shown with weak emission features. These last finding is in agreement with Trees & Stam (2022), where they describe how sensitive polarization is, contrary to intensity spectra, to the ocean glint feature. In their simulations, water bands appear in absorption in polarization when there is an ocean glint feature not fully covered by clouds, while they appear in emissions in the case of full cloud cover over the ocean glint or for a dry surface. With our simulations we show that, even when applying realistic cloud cover and horizontal cloud patterns and taking into account the subgrid variability, the ocean glint feature still retains its typical effect of changing from emission to absorption depending on the surface type of the planet. This difference will become even more significant later for the comparison with the Earth-like scenario, where the ocean glint will be hidden by the African continent for $\alpha > 90°$.
In Fig. 4.6 we not only highlight the impact of the 3D CG, but we also study the effect of assuming different schemes for the vertical overlap of clouds, nominally the MAX-RAN and EXP-RAN overlaps. As described in Sec. 4.5.1, the EXP-RAN overlap generally increases the total cloud cover of a single cloudy pixel at the TOA, making the clouds more reflective but also more realistic by introducing some random overlap even for continuous cloudy layers. This is also the case for the disk-integrated simulations, where the simulations with EXP-RAN overlap have a slightly increased reflectance compared to the same MAX-RAN simulations with the 3D CG. Polarization exhibits the opposite behavior. The EXP-RAN overlap scheme leads to more cloud cover, blocking a larger part of the ocean, where glint reflection produces polarization. It also obscures more of the lower atmosphere, which contributes to polarization through Rayleigh scattering. As a result, the overall polarization in the spectra is lower than in the MAX-RAN overlap simulations.
We also explore the effect of different zoom-in factors for each ERA5 pixel in the 3D CG. Comparing between a zoom-in factor of x3 and x5 per size (meaning that we are creating 9 and 25 subpixels, respectively), we study the impact of the increase in horizontal resolution on the reflectance and polarized spectra of spatially unresolved planets. Intuitively, the more pixels we have in a simulation, the better we can resolve the 3D cloud structure and

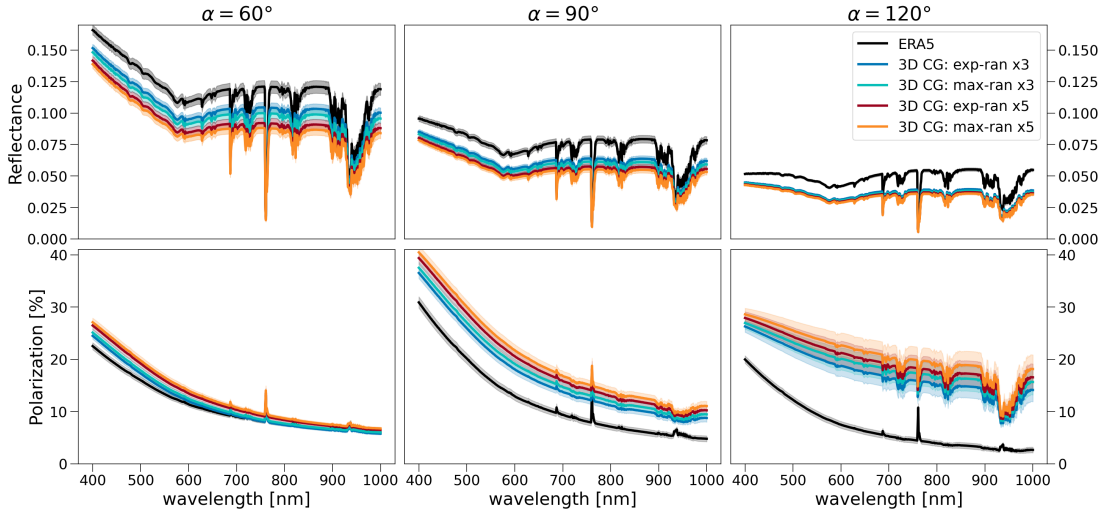

Figure 4.6: Reflected light (first row) and polarized light (second row) spectra showing the influence of the 3D CG approach applied to the ERA5 reanalysis data for the clouds compared to the ERA5 data themselves (black line). The 3D CG was run assuming different vertical overlap schemes: EXP-RAN and MAX-RAN and different zoom-in factors (x3 and x5). The different columns refer to spectra at different phase angles α: 60, 90, 120°.

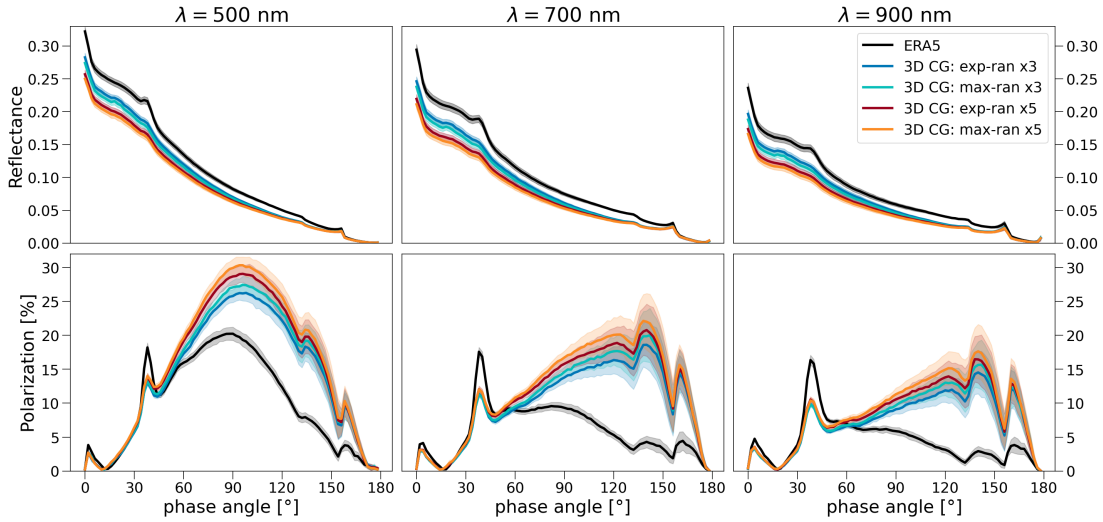

Figure 4.7: Reflected light (first row) and polarized light (second row) phase curves showing the influence of the 3D CG approach applied to the ERA5 reanalysis data for the clouds compared to the ERA5 data themselves (black line). The 3D CG was run assuming different vertical overlap schemes: EXP-RAN and MAX-RAN and different zoom-in factors (x3 and x5). The different columns refer to different wavelengths (λ): 500, 700, 900 nm.

the closer to reality it should look like. However, running global simulations with pixels size that can reach up to the fractal dimension of clouds, where cloud structures can be

resolved, is unfeasible. Starting from the ERA5 reanalysis product, which has a pixel size of around 31 km, with a x3 and x5 zoom-in we obtain pixel sizes of approximately 9 and 6 km, respectively (or 0.08° and 0.05°), still far from the fractal dimension of clouds, yet reaching a great level of details and accuracy. Comparing the x3 and x5 spectra with the same vertical overlap scheme (MAX-RAN or EXP-RAN), we see that by increasing the zoom-in factor we also slightly decrease the reflectance of the planet and slightly increase its polarization, as already expected by our convergence study in Fig. 4.15. However, a zoom-in factor of 5 is significantly more computationally expensive than a zoom-in factor of 3, while not substantially affecting the results. Additionally, we clearly see that the impact of the 3D CG applied to the ERA5 clouds is much more significant than the differences among different zoom-in factors and vertical overlap schemes. Thus, from now on we use the 3D CG with EXP-RAN overlap and x3 zoom-in factor as the ground-truth model to treat clouds in our simulations.

For the reflected light spectra, we find that reflectance decreases with increasing phase angles, as expected due to the progressively smaller illuminated portion of the planet. For the polarized spectra, we show that the largest polarization fraction can be found around $\alpha = 90°$, where there is a peak in the polarization due to Rayleigh scattering. Also the slope of the polarized spectra is affected by both Rayleigh scattering and the ocean surface. The slope is particularly affected at $\alpha = 120°$ due to the ocean glint polarization, which is spectrally independent and dominates over Rayleigh scattering at large phase angles, especially when there are more gaps in the clouds introduced by the 3D CG.

After assessing the influence of the 3D CG on the reflectance and polarized spectra, in Fig. 4.7 we also assess its impact on the phase curves, again for the ocean planet configuration. As discussed for the reflectance spectra, the 3D CG has an impact on the reflectance of the planet, lowering it at all wavelengths ($\lambda = 500$, 700 and 900 nm.) But the impact is even larger when comparing the ERA5 clouds with the 3D CG approach for the phase curves in polarization, where it significantly increases the amount of linear polarization expected for a disk-integrated observation of the planet. This is a consequence of introducing subgrid cloud variability, thus allowing radiation to travel into the 3D cloud inhomogeneous structure, instead of photons being reflected by smeared homogeneous clouds as represented in ERA5. The effect of the different vertical overlap schemes (MAX-RAN and EXP-RAN) and of the zoom-in parameter is the same as described for the spectra, and it is still less significant than the difference between including or not subgrid variability and inhomogeneities through the 3D CG.

As expected, for $\lambda = 500$ nm we find the largest reflectance and polarization due to Rayleigh scattering, while it decreases moving towards 700 nm and 900 nm. However, the impact of the 3D CG appears increasingly relevant after $\alpha > 60°$, where the impact of the ocean glint feature becomes larger and the subgrid cloud inhomogeneity impacts the radiative transfer. This happens at all wavelengths, confirming the weak chromatic effect of the ocean glint feature. At small phase angles ($\alpha \sim 5°$), we find the glory feature, which is linked to the optical properties of the cloud droplets. This feature does not seem to be affected by the 3D CG approach. Around $\alpha = 40°$, we find the cloudbow feature, which is a consequence of the first internal reflection of the liquid water droplets. Its location and height is strongly

linked with the microphysical properties of clouds, in particular their optical thickness, effective radius and particle composition. As shown, the cloudbow feature appears more pronounced in the polarization spectra, allowing to break down possible retrieval degeneracies about cloud properties as discussed in Sterzik et al. (2020). We observe that the cloudbow feature is significantly influenced by the 3D CG in both reflected light and polarized phase curves. This effect can be attributed to the higher in-cloud LWC in the 3D CG configurations compared to ERA5, which leads to a smaller peak in polarization. In the phase curves, we observe that, for $\lambda = 500\ nm$, the polarization peak caused by Raileigh scattering occurs at approximately $\alpha = 90°$ for the ERA5 clouds, whereas it shifts to larger phase angles when using the 3D CG. For larger wavelenght, Raileigh scattering weakens. Additional features found at $\alpha = 138°$ and $158°$ arise from the scattering properties of ice clouds and depend on their optical characteristics (Emde et al., 2017).

4.6.2 Clouds zoom-out

After assessing the impact of the 3D CG, we want to study the effect of averaging out cloud properties on larger and larger grid scales in order to mimic exoplanet atmosphere simulations. Using different zoom-out factors, from x3 ($\sim$ 84 km, 0.75°), x10 ($\sim$ 278 km, 2.5°), x100 ($\sim$ 2670 km, 24°) and a single pixel simulation, we average out layer by layer the cloud properties, conserving the optical thickness as described in Sec. 4.5.3. In Fig. 4.8, we show the ocean planet images for the different cloud models, from the 3D CG (EXP-RAN overlap, zoom-in x3) to the ERA5 image and the different zoom-out cases for $\alpha = 0°$. Reducing the amount of pixels, we observe an increase in reflectance of the planet, as the LWC and IWC present in the subgrid need to be smeared out in larger pixels. This effect is already present in the comparison between the 3D CG and the ERA5 images, as discussed above.

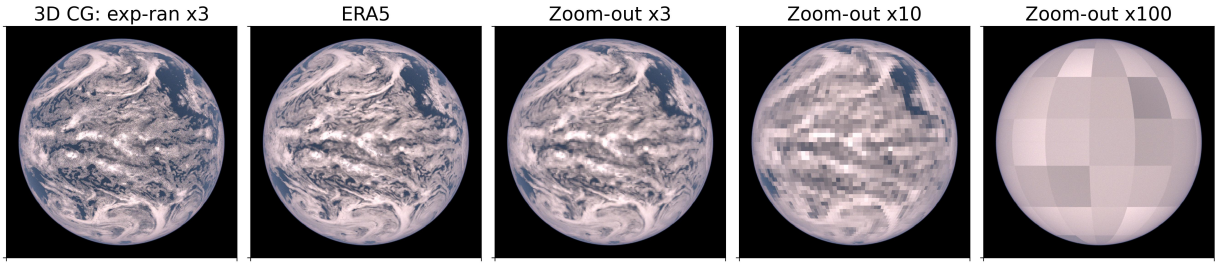

Figure 4.8: True color images of the ocean planet scenario showing the impact of different grid resolutions in representing the clouds. We show the 3D CG image with a zoom-in x3 factor compared to the ERA5 image, and zoomed-out images with factors x3, x10, and x100. Reducing the grid size we note an increase in the total reflectance of the planet.

In Fig. 4.9, we show the impact on the reflected and polarized light spectra of running simulations with coarser grids. As a reference, we have the 3D CG and the ERA5 cloud models from the previous plot, and new spectra with zoom-out factors of x3, x10, x100,

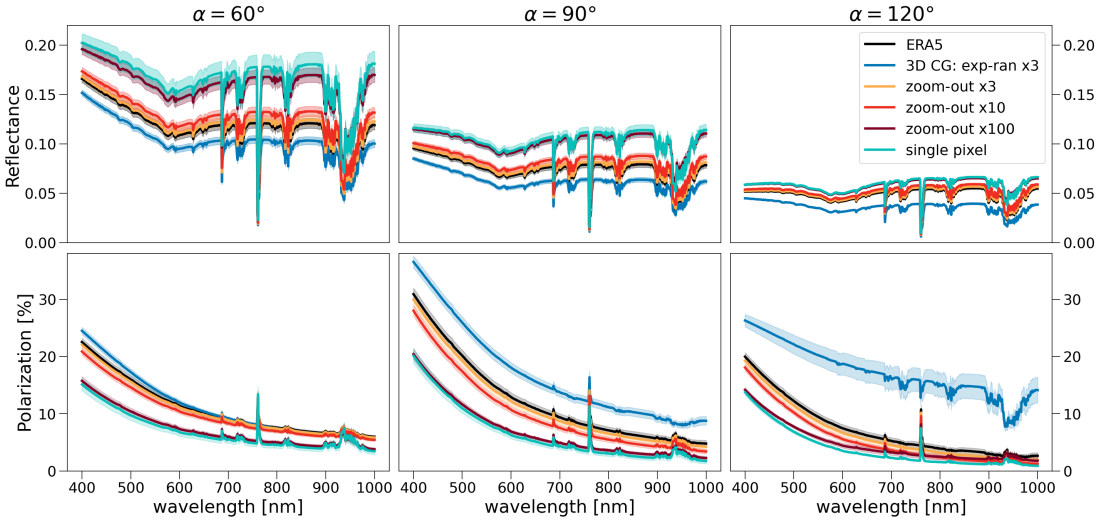

Figure 4.9: Reflected light (first row) and polarized light (second row) spectra showing the influence of the number of pixels in the simulations. From the 3D CG EXP-RAN zoom-in x3 and ERA5 simulations, we apply the cloud zoom-out algorithm, with zoom-out factors x3, x10, x100, until a single-pixel simulation. With the zoom-out, the reflectance of the planet is substantially overestimated, while the polarization is influenced both in the spectral slope and molecular lines. The different columns refer to spectra at different phase angles (α): 60, 90, 120°.

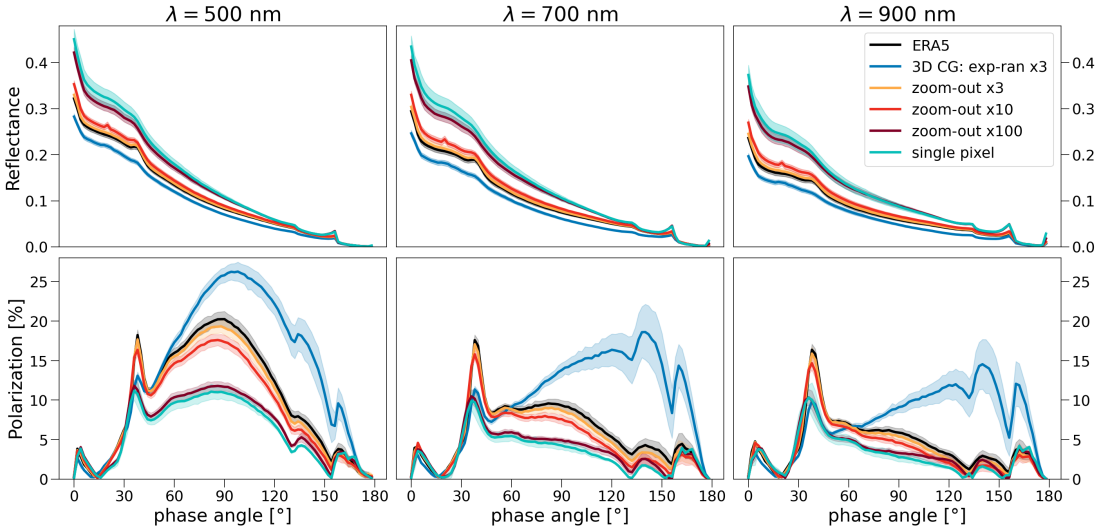

Figure 4.10: Reflected light (first row) and polarized light (second row) phase curves showing the influence of the cloud zoom-out algorithm. The different columns refer to different wavelengths (λ): 500, 700, 900 nm.

until arriving to a single pixel simulation. As expected, the general trend we observe is an increase of the reflectance of the planet at all phase angles, without any large impact on the

spectral slope. While the zoom-out ×3 and zoom-out ×10 simulations remain comparable with ERA5, the zoom-out ×100 and single-pixel simulations show a significant increase in reflectance. This occurs because they can no longer accurately represent the 3D cloud structure of the planet, instead displaying nearly homogeneous cloud properties across the entire disk. For the polarization, we observe again a large jump between the zoom-out x10 and zoom-out x100 simulations, also with a substantial impact on the slope of the polarized spectra. Again, also the O_2A band and water bands are affected by the coarser cloud grid.
Studying the effect of the zoom-out on the phase curves (Fig. 4.10), we observe a large impact from the zoom-out x10 to the zoom-out x100 case, as the planet becomes almost homogeneous. The impact is still affecting both the reflected and polarized light spectra, with a larger effect in polarization for $\alpha > 90°$. In addition, the cloudbow feature ($\alpha \sim 40°$) is impacted by the zoom-out factor in polarization, with the zoom-out x100 being almost identical to the single pixel simulations.
Comparing the zoom-in and zoom-out studies, we can clearly see that the zoom-in process, even with just a factor of x3, has a much more important effect on both spectra and phase curves if compared with a zoom-out of x3. This suggests the importance of treating the subgrid cloud variability and finding better solutions on how to parameterize clouds in exoplanet atmosphere simulations, where such high resolution will not be possible. However, it remains fundamental to treat clouds in a more realistic way, as their radiative effect has a strong influence on both spectra and phase curves, in particular for polarization studies. This suggests how polarization spectra contain more information about cloud properties and might be used to improve degeneracies among different models and interpretations for exoplanet studies.
Additionally, in Appendix 4.10 we conduct sensitivity studies on the impact of the cloud droplet effective radius and find no significant differences when the optical thickness of the clouds is conserved.

4.6.3 Hyperspectral albedo maps

To study the sensitivity of surface properties, we first investigate the role of homogeneous and inhomogeneous surface wind speed maps on the ocean glint feature in Appendix 4.11 and find no significant differences within the 1σ cloud variability spread.
To simulate the Earth-like planet scenario (Fig. 4.5), we incorporate the modeling of land surfaces. Using the hyperspectral albedo maps dataset HAMSTER (Roccetti et al., 2024), we include a wavelength-dependent treatment of surface reflectance for land surfaces. This is crucial for accurately representing the planet's albedo and capturing spectral features resulting from surface reflection. We also note that previous works (Gordon et al., 2023; Kofman et al., 2024) that included wavelength-dependent surface albedo treatments typically coupled spectral libraries with land surface types from satellite observations to define the albedo in each simulation pixel. This approach may lead to highly biased surface reflectance spectra, as spectral libraries do not account for the fact that forests consist of a combination of components, such as leaves and soils, not just the spectrum of a single leaf.

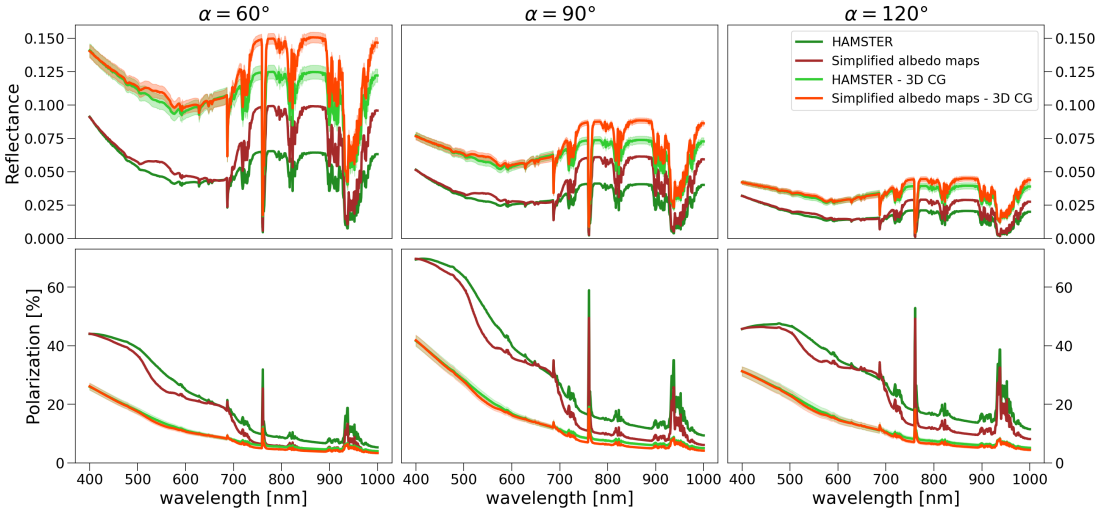

Figure 4.11: Reflected light (first row) and polarized light (second row) spectra comparing HAMSTER with simplified hyperspectral albedo maps, generated using a linear combination of five ECOSTRESS spectra. The different columns refer to spectra at different phase angles (α): 60, 90, 120°.

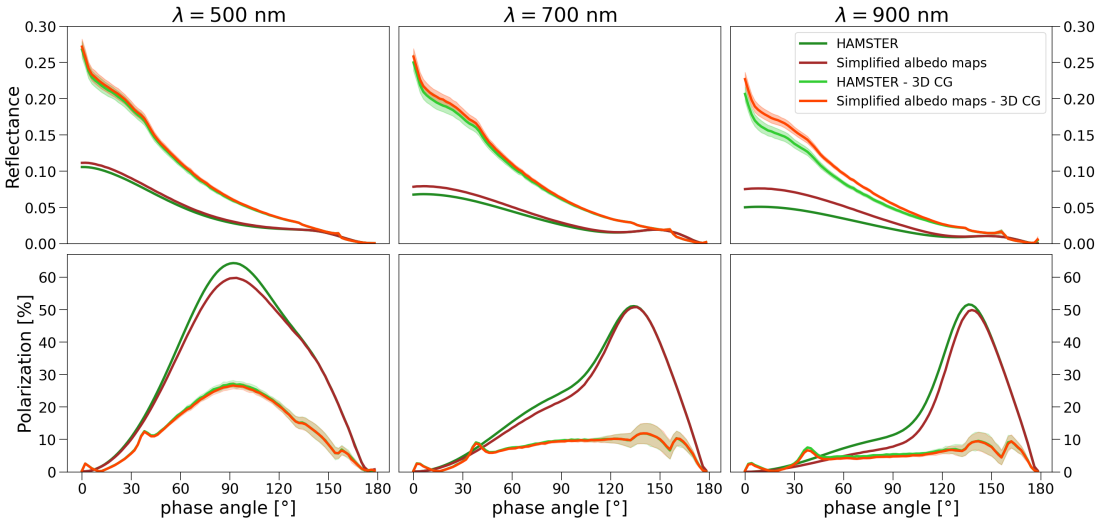

Figure 4.12: Reflected light (first row) and polarized light (second row) phase curves comparing HAMSTER with simplified hyperspectral albedo maps, generated using a linear combination of five ECOSTRESS spectra. The different columns refer to different wavelengths (λ): 500, 700, 900 nm.

By using HAMSTER, we are able to incorporate the first remote sensing-calibrated dataset of wavelength-dependent surface albedo maps, enhancing our representation of land surfaces. In particular, we find a substantially reduced VRE feature (see Fig. 6.5), which has been highly overestimated in previous Earth-like simulations.
In Fig. 4.11, we show the difference between HAMSTER and the simplified hyperspectral albedo maps. The VRE feature and the green bump (around 550 nm) are clearly visible in the reflectance spectra. However, when using a linear combination of ECOSTRESS spectra from MODIS land surface type maps, these features are significantly overestimated in reflected light spectra. This overestimation is particularly pronounced at small phase angles, nearly doubling the expected continuum beyond the VRE feature (750 nm) for a cloudless planet. In cloudy scenarios, where we apply the 3D CG treatment, the effect remains substantial, highlighting the impact of HAMSTER's improved surface albedo model. In particular, with HAMSTER, the green bump is completely washed out in the disk-integrated spectra, even in a clear atmosphere.
In polarized spectra, we observe the opposite trend. Since all land surfaces are treated as Lambertian, they do not polarize radiation and instead scale inversely with intensity. As a result, the VRE and green bump features are underestimated in polarized spectra for a cloudless planet. The difference is most pronounced at $\alpha = 90°$ in cloudless simulations, reaching approximately a 25% difference in polarization, but is less significant for cloudy planets, where the difference falls within the 1σ cloud variability spread.
In Fig. 4.12, we also examine the effect on phase curves. At $\lambda = 500$ and 700 nm, we find no significant differences between HAMSTER and the simplified hyperspectral albedo maps. However, at $\lambda = 900$ nm, within the VRE peak, the simplified albedo maps produce an unphysical increase in reflectance. This effect is particularly noticeable in cloudless simulations, where the reflectance is increased by 50% when using the simplified albedo maps, and remains significant even for a cloudy planet, showing an increase of approximately 20% at small phase angles. In polarization, the impact on phase curves is only relevant for the cloudless scenario at wavelengths beyond the VRE. We also see a difference in the phase curve shape for polarized light if compared to the ocean planet scenario (Fig. 4.20). Introducing different albedo surfaces, we see not only the peak of polarization around $\alpha = 90°$ due to Rayleigh scattering, but also another jump, becoming evident for $\lambda = 700$ and 900 nm. This additional jump is due to the reflectance of different albedo components compared to the ocean surface, such as vegetation or deserts, and they show their typical signatures at longer wavelengths. This shows that polarization is a more powerful diagnostic tool for surface features than intensity alone when looking at disk-integrated spectra and phase curves.
Additionally, we also address the impact of the albedo seasonal variability in HAMSTER in the spectra and phase curves. The results are shown in Appendix 4.12.

4.6.4 Comparing the ocean and Earth-like planets

After introducing various surface and cloud modeling improvements, we now want to compare between the ground truth ocean and Earth-like planet scenarios. We are comparing

the following cases:

- Ocean surface (including BPDF) with the 3D CG clouds and their 1σ spread;
- Earth-like scenario including ocean surface treated with the BPDF (but ocean glint almost always covered by land) and hyperspectral albedo maps with the 3D CG clouds and their 1σ spread.

In Fig. 5.5 we show the reflected and polarized light differences in the spectra due to the different models. We find a significant spread between the ocean and Earth-like scenario, way beyond the cloud variability in the models found in the 1σ spread (shaded areas). This is particularly evident for $\alpha = 60°$ in intensity, while the difference gets larger for $\alpha = 120°$ in polarization, where we observe a different behavior both in the spectral sloples of the models, their continuum in the near-infrared (NIR) and in the spectral lines behavior. Due to the presence (ocean scenario) and absence (Earth-like scenario) of the ocean glint feature, we see a different behavior of the water bands around 950 nm, as they are shown in absorption for the ocean planet and in emission for the Earth-like case. This effect is already present in the $\alpha = 90°$ case, but gets enhanced at larger phase angles. Additionally, at large phase angles, cloud variability is significantly larger for the ocean planet than for the Earth-like scenario. This effect is most pronounced at larger phase angles, where the spread is dominated by ocean glint.
In Fig. 5.6, we study the same differences in reflected and polarized light over the phase curves again at three different wavelengths: $\lambda = 500$, 700 and 900 nm. Among the ocean and Earth-like scenario, large differences are found only in the polarization case, in particular for $\lambda = 700$ and 900 nm. We note an increase in polarization due to the ocean glint which goes beyond the cloud variability spread we introduce in the models. To distinguish among any possible features in reflected light is more challenging than in polarization. For comparison, we also include the phase curve of a purely Lambertian sphere, modeled using the Lambertian phase function

$$g(\alpha)_L = \frac{\sin(\alpha) + (\pi - \alpha)\cos(\alpha)}{\pi}. \tag{4.22}$$

The Lambertian phase function is scaled by the geometric albedo of the ocean planet case at each wavelength.
In Appendix 4.13 we also present the same spectral comparison for the ocean and Earth-like planet scenarios, but in terms of albedo instead of reflectance (Fig. 4.23).

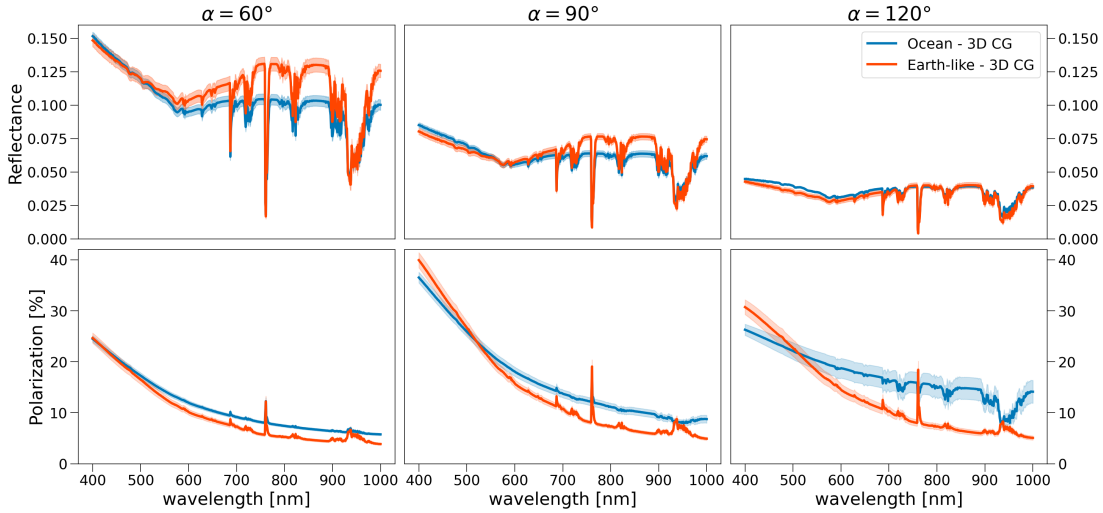

Figure 4.13: Comparison among spectra in reflected (first row) and polarized light (second row) of the ocean and Earth-like planet scenarios. The different columns refer to different phase angles (α): 60, 90, 120°.

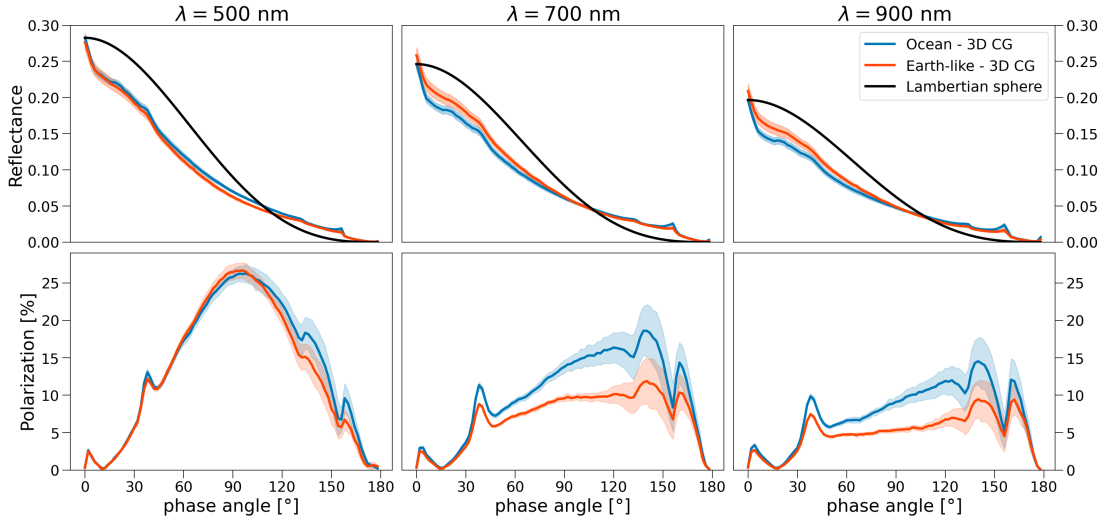

Figure 4.14: Reflected light (first row) and polarized light (second row) phase curves comparing the ocean and Earth-like planet scenarios. The different columns refer to different wavelengths (λ): 500, 700, 900 nm.

4.7 Discussion and conclusions

In this paper, we assessed the importance of incorporating inhomogeneous surfaces and atmospheres into 3D radiative transfer models of Earth-like exoplanets. Specifically, we studied the effect of implementing, for the first time, wavelength-dependent surface albedo maps derived from Earth remote sensing observations. In parallel, we addressed the im-

portance of integrating inhomogeneous 3D cloud maps into our models, with a focus on subgrid cloud variability and cloud inhomogeneities. While exoplanet forward models must be computationally efficient to explore key parameters and perform spectral retrievals for interpreting observations, this study focused on assessing the impact of different model complexities on the resulting spectra and phase curves of an Earth-like exoplanet observed in reflected and polarized light. Future studies should further assess the importance of fine details in modeling observations for the next generation of telescopes, particularly in relation to the typical integration times required to achieve a sufficient signal-to-noise ratio.
By studying the effects of the 3D CG and the cloud zoom-out process, we conclude that the cloud grid size in simulations plays a critical role in the reflectance and polarized spectra and phase curves. Specifically, without accounting for subgrid cloud variability and cloud inhomogeneities introduced by the 3D CG, the planet's reflectance is significantly overestimated. Additionally, clouds become too widespread within grid cells, which lowers the planet's linear polarization. The effect of insufficient spatial resolution implies that models that are too simple may lead to expectations of a reflectance that is too high and a polarization that is too low. This is particularly relevant in exoplanet models, where homogeneous cloud properties are often assumed, potentially leading to biases in data interpretation. Although obtaining such fine-scale details for exoplanets is impossible, and developing models that resolve cloud properties at these detailed spatial and vertical scales remains infeasible, improved parameterization schemes must be developed to preserve the radiative effects of clouds in coarser-resolution models. Our results should inform the appropriate resolution at which radiative transfer codes, coupled with general circulation models (GCMs), should be run to avoid biasing the interpretation of observed spectra and phase curves. Furthermore, in our sensitivity analysis regarding the effective radius of cloud particles, we find that its impact is minimal when the optical thickness of grid cells is conserved. This highlights the need to appropriately scale cloud optical thickness during the zoom-out process for coarser models.
All spectra and phase curves generated for cloudy planets are accompanied by a 1σ cloud variability spread, which helps in building ground-truth models of Earth as an exoplanet. This spread also aids in determining whether potential diagnostic features used to distinguish exoplanet properties might be obscured by cloud variability.
We introduced the use of a new dataset to account for the pixel-by-pixel spectral variation of surface albedo, as well as its seasonal variability. Using HAMSTER (Roccetti et al., 2024), we demonstrated that previous attempts to incorporate wavelength-dependent surface reflectance for different surface types, such as forests and deserts, greatly overestimated reflectance. For instance, the VRE is often overestimated by nearly 100% due to the assumption that forested areas could be represented by laboratory spectra of individual leaves. This study underscores the necessity of incorporating realistic spectral albedo maps to accurately capture spectral features in the reflectance and polarized spectra of spatially unresolved exoplanets. As shown by Gomez Barrientos et al. (2023), a wavelength-dependent surface albedo model more accurately retrieves reflected light spectra than a uniform albedo model, even in the presence of clouds. In this paper we demonstrated that constructing such albedo maps requires careful consideration. Relying solely on laboratory-

based wavelength-dependent measurements can lead to a substantial overestimation of the VRE feature in reflected light spectra, even with realistic cloud coverage. However, detecting seasonal variability, such as snow cover changes, remains extremely challenging as these effects are masked by the planet's cloud abundance and variability. Additionally, we investigated the role of surface wind speed in shaping ocean glint features but find no significant impact on the spectra or phase curves.

After constructing these advanced models, we compared their effects on reflected and polarized light spectra and phase curves. These results indicate that polarization is far more sensitive to surface features, as evidenced by differences between ocean and Earth-like planet scenarios in reflected and polarized light. In polarization, spectral slopes and absorption lines differ more prominently than in intensity, particularly at large phase angles. Despite the improved cloud modeling, we still observe unique water line features in polarization, as reported by Trees & Stam (2022) for homogeneous planets. Specifically, water lines appear in absorption when ocean glint is present but in emission for dry planets. These findings suggest that combining polarization with intensity-only spectroscopy can greatly enhance the characterization of rocky exoplanets and provide greater diagnostic power to differentiate surface and atmospheric properties, reducing retrieval degeneracies. Future studies should explore the feasibility of conducting polarized light observations with upcoming telescopes and missions, assessing whether sufficient contrast can be achieved for further exoplanet characterization. Polarization is particularly advantageous because stellar contamination can be significantly reduced as most FGK-type stars are nearly unpolarized. Contrast estimates for observing rocky exoplanets in reflected and polarized light will be presented in the second paper in this series, using the fully improved modeling setup described in this work.

The improved modeling approaches presented here will be validated against a large catalog of Earthshine observations obtained in polarized light to assess the model's ability to reproduce observed spectral features. This validation will be addressed in the third paper in this series.

In conclusion, the ground-truth spectra and phase curves simulated for Earth-like and ocean planet scenarios will be made available to the exoplanet community. These datasets can improve predictions for next-generation telescopes and instruments, validate other exoplanet models, and facilitate studies of Earth as an exoplanet.

Data availability

All spectra and phase curve data are openly accessible via a Jupyter notebook on the GitHub repository.[3] Additionally, we also provide public access to the 3D Cloud Generator.[4]

[3] https://github.com/giulia-roccetti/Earth_as_an_exoplanet_Part_I

[4] https://github.com/giulia-roccetti/3D_Cloud_Generator

Acknowledgements

We thank the anonymous referee for the useful and constructive comments, which greatly helped improving this paper. GR and JVS were supported by the Munich Institute for Astro-, Particle and BioPhysics (MIAPbP) which is funded by the Deutsche Forschungsgemeinschaft (DFG, German Research Foundation) under Germany´s Excellence Strategy – EXC-2094 – 390783311.

4.8 Appendix A: ERA5 inhomogeneous pressure level heights

To compute the heights of the ERA5 pressure levels, we start from assuming hydrostatic equilibrium and an ideal gas law for dry air:

$$\frac{dP(z)}{dz} = -\rho(z)g = -\frac{P(z)g}{R_L T(z)}. \tag{4.23}$$

Here $P(z)$ is the pressure as a function of height, $R_L \simeq 287.05\,\mathrm{J\,kg^{-1}\,K^{-1}}$ is the specific gas constant for dry air and $g \simeq 9.807\,\mathrm{m\,s^{-2}}$ is Earth's gravitational acceleration. We also assume temperature to be linearly dependent on height, within every layer:

$$T(z) = T_i + (z - z_i)\frac{T_{i+1} - T_i}{z_{i+1} - z_i}. \tag{4.24}$$

Integrating Eq. 4.23 between level i and $i+1$ we obtain the following equation for the thickness of the layer:

$$\Delta z_i = \ln\left(\frac{P_i}{P_{i+1}}\right) \cdot \frac{R_L(T_{i+1} - T_i)}{g \ln\left(\frac{T_{i+1}}{T_i}\right)}. \tag{4.25}$$

The height of a given layer i is then computed by summing all the layers below:

$$z_i = \sum_{k=0}^{i} \Delta z_k. \tag{4.26}$$

4.9 Appendix B: Convergence of the 3D Cloud Generator

The 3D CG described in Sec. 4.5.1 can generate finer cloud distributions starting from ERA5 realanysis data for an arbitrary zoom-in factor. In this appendix we analyze the impact of the zoom-in factor on the radiative transfer effects of clouds. Specifically, we generate cloud fields with zoom-in factors ranging from 2 to 16 of a region spanning 10° in both latitude and longitude, using a constant surface albedo of 0.3. This is done because running a global simulation with such a fine cloud grid up to a zoom factor of 16 is too computationally expensive. A sensor is placed at the center of this patch, at an altitude of 1000 km, with a 30° aperture, ensuring that the entire patch remains within its field of view. The results are shown in Fig. 4.15 for both the MAX-RAN and EXP-RAN overlap schemes and for the 500, 700 and 900 nm wavelengths. As shown in the figure, introducing a finer grid of clouds greatly impacts the normalized reflectance in radiative transfer calculations, leading to a decrease of approximately 40%, depending on the wavelength. Additionally, the radiative response to the 3D CG quickly converges to a stationary value already for a zoom factor of 3 for all wavelengths and for both methods. Since this provides the best balance between convergence and computational cost, we adopt a zoom-in factor of 3 for most of the results presented in this paper.

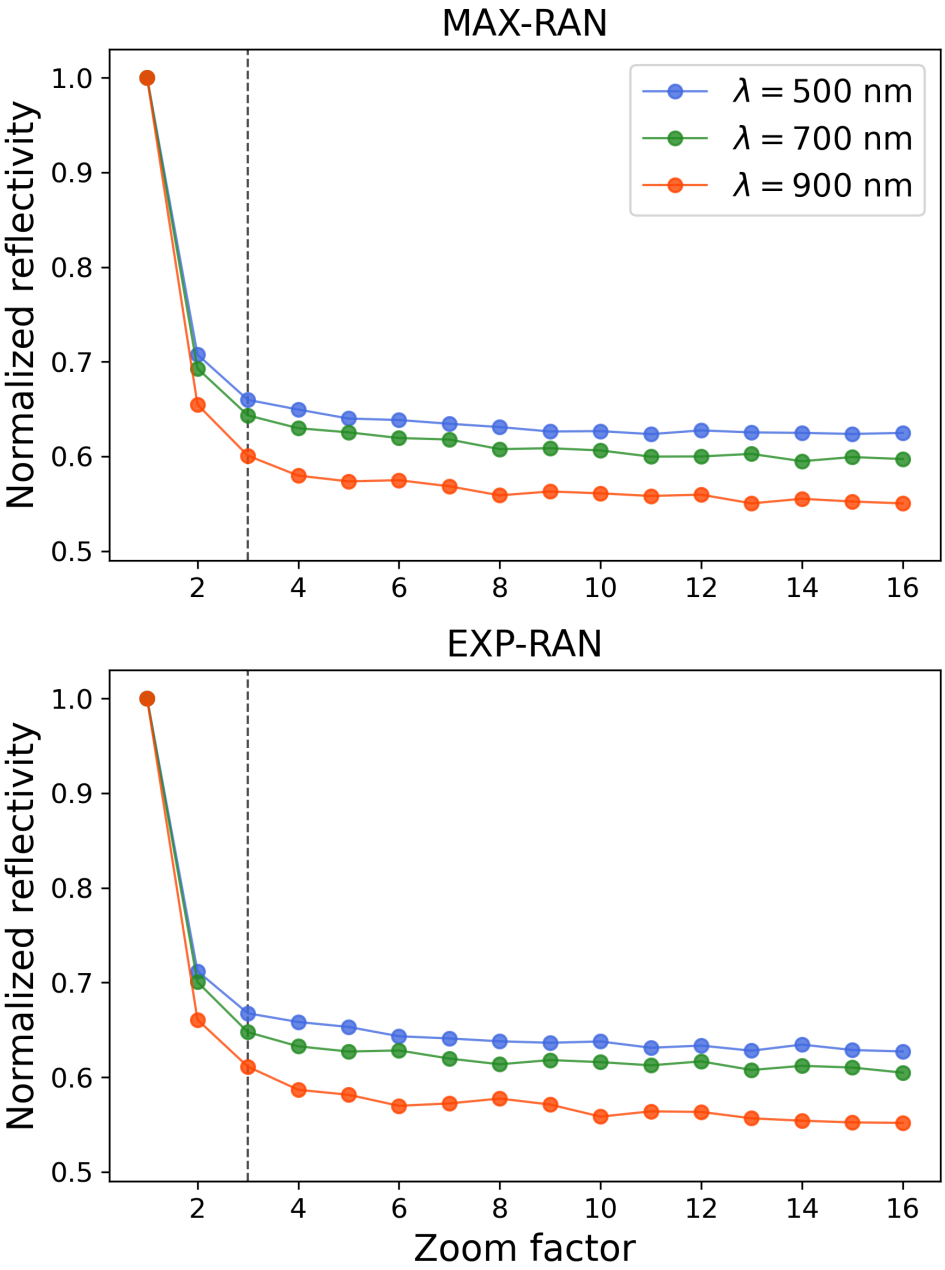

Figure 4.15: Convergence study on the impact of the zoom-in factor on the radiative response of clouds in a region spanning 10° in latitude and in longitude. The MAX-RAN and the EXP-RAN overlap methods are both shown for three wavelengths in the visible and NIR range. The reflectance is normalized to its value without zoom-in. The vertical dashed line represents a zoom-in factor of 3, which will be used for most of the results below as it provides the optimal balance between convergence and computational cost.

4.10 Appendix C: Impact of the cloud droplet effective radius

As an additional parameter, we test the role of the effective radius of liquid and ice water droplets on the spectra and phase curves over an ocean planet. Starting from the 3D CG, we conserve the optical thickness of clouds scaling the LWC and IWC while changing the effective radius to constant values of 5, 10 and 15 μm. We then compare it with the variable effective radius distribution obtained with the ERA5 parameterization. When conserving the optical thickness, we did not find any significant variations for all spectra in both reflected and polarized light (Fig. 4.16). This suggests that only introducing variations in the optical thickness of clouds has a direct impact on the spectra, and since the effective radius enters in the calculation of τ, it plays a role only when the LWC and IWC are not adjusted accordingly to conserve τ. However, in the phase curves (Fig. 4.17) we observe the impact of the effective radius on the cloudbow feature ($\alpha \sim 40°$), in both reflectance and polarization, greatly enhanced in the polarized phase curves. In polarization, we observe both a shift towards larger phase angles and an increase in the cloudbow feature for larger effective radii, showing again the sensitivity of linear polarization in assessing cloud particle size through the cloudbow feature. This effect gets enhanced at longer wavelengths ($\lambda =$ 900 nm). All the other differences are within the 1σ cloud variability and cannot be clearly distinguished.

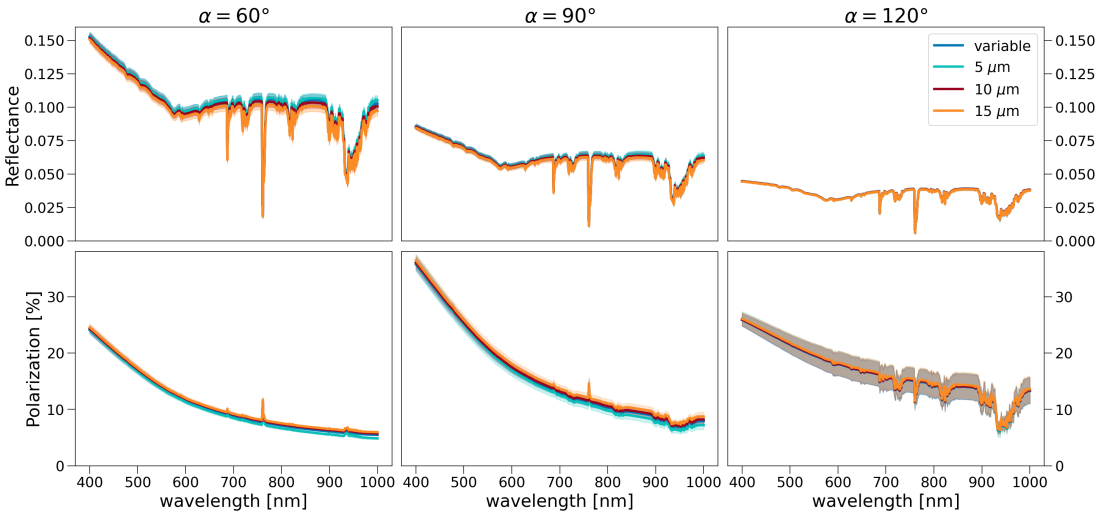

Figure 4.16: Reflected light (first row) and polarized light (second row) spectra showing the influence of the effective radius of cloud particles. Here, we compare a variable effective radius from the ECMWF parameterization to constant effective radius values, but always conserving the optical thickness of each gridbox. The different columns refer to spectra at different phase angles (α): 60, 90, 120°.

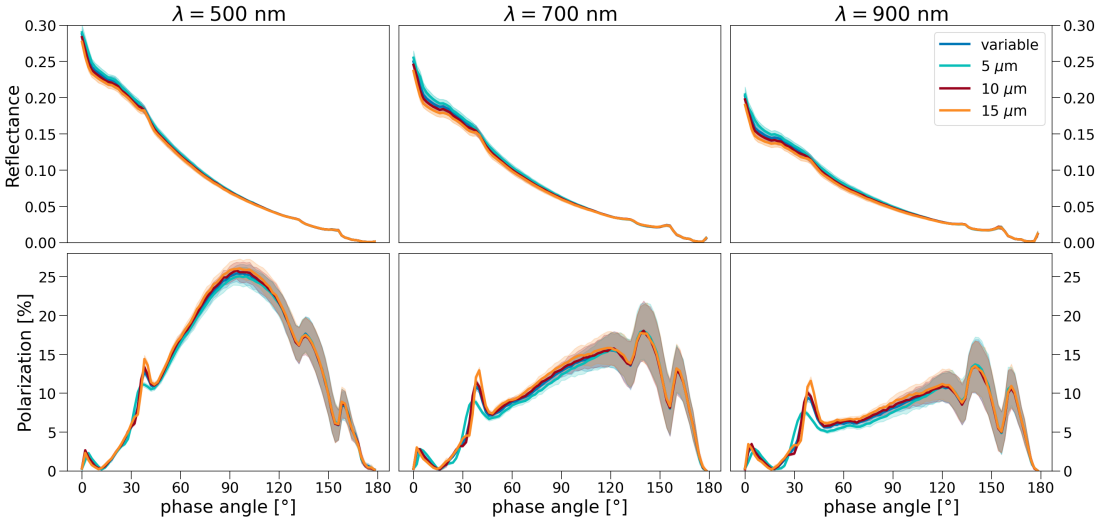

Figure 4.17: Reflected light (first row) and polarized light (second row) phase curves showing the influence of a constant effective radius, while conserving the optical thickess of the gridbox. The different columns refer to different wavelengths (λ): 500, 700, 900 nm.

4.11 Appendix D: Impact of the wind speed

We also discuss the impact of changing the wind speed over the surface for the ocean planet configuration. Fig. 4.18 shows the effect of changing the surface wind speed on the ocean glint feature. While the integrated brightness of the ocean glint remains the same, it gets distributed over a larger area when the surface of the ocean gets rougher due to increased wind speed. In the second row of Fig. 4.18 we show how the ocean glint appears with surface wind speed maps data from the ERA5 reanalysis product. Including realistic wind speed maps, the ocean glint feature does not appear to be symmetric anymore, and shows different features due to weather patterns over the ocean. Although different wind speeds do not have any impact on the total reflectance of the planet, this might change when simulating cloudy exoplanets, as different spatial distributions of clouds can obscure the ocean glint. In Fig. 4.19 we show the impact of homogeneous and inhomogeneous (from the ERA5 renalysis product) wind speed maps over the reflected and polarized spectra. As expected, for simulations without clouds we did not find any difference among homogeneous and inhomogeneous surface winds, and we find also no significant differences among the 1σ cloud spread. A similar behavior is also observed in the reflected and polarized phase curves (Fig. 4.20), where we find no significant impact due to homogeneous or inhomogeneous wind speed maps.

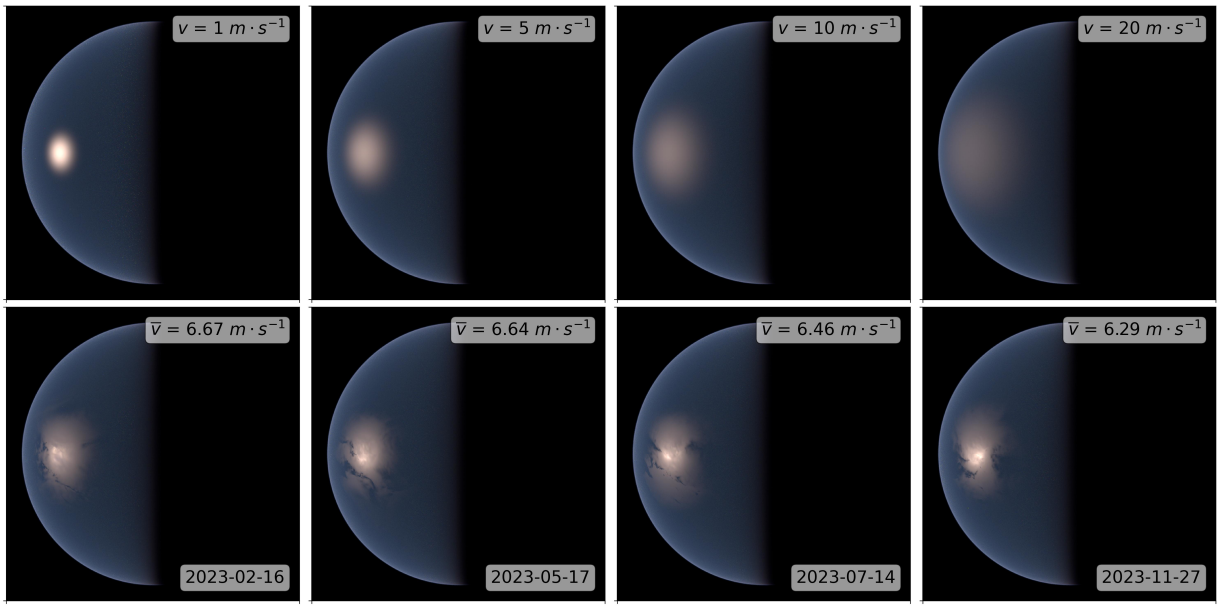

Figure 4.18: True color image of a cloud-free ocean planet at $\alpha = 90°$ with different surface wind speed maps. In the first row, we use a constant wind speed and observe the impact on the brightness and size of the ocean glint. In the second row, we use realistic wind speed maps from ERA5, and we note the inhomogeneous shape of the ocean glint. We report the average wind speed from the various ERA5 fields in the subfigures.

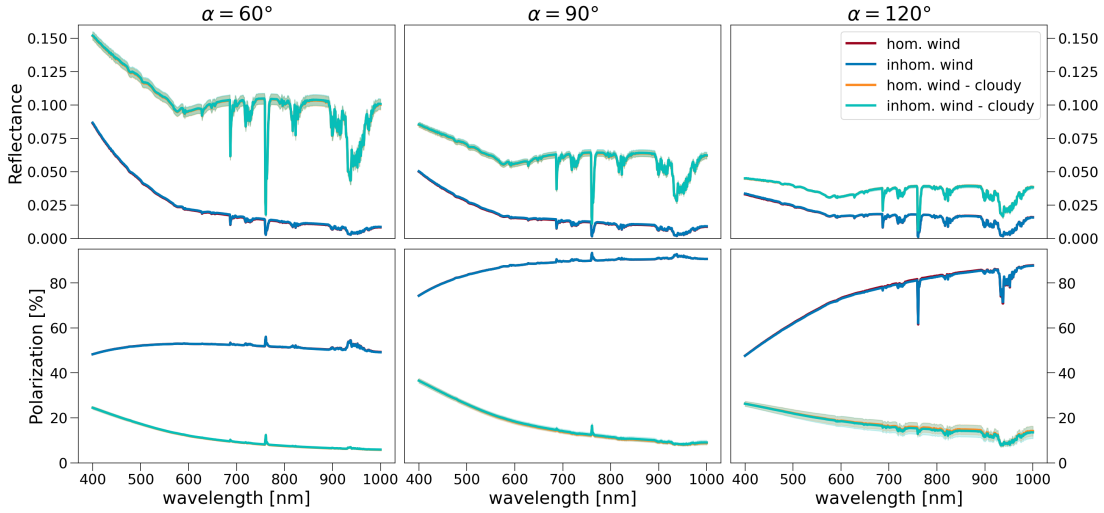

Figure 4.19: Reflected light (first row) and polarized light (second row) spectra showing the influence of homogeneous and inhomogeneous wind speed maps. The different columns refer to spectra at different phase angles (α): 60, 90, 120°.

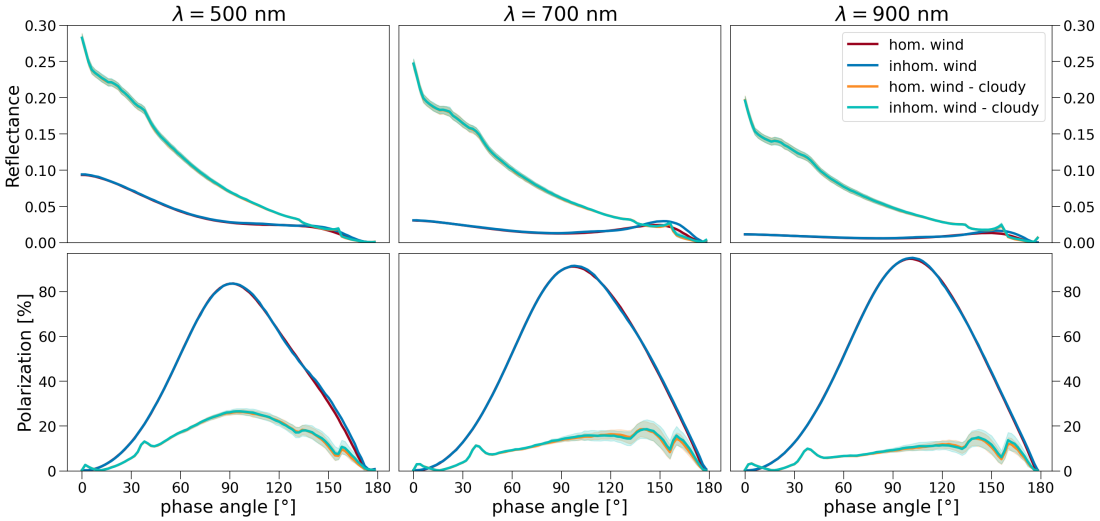

Figure 4.20: Reflected light (first row) and polarized light (second row) phase curves showing the influence of homogeneous and inhomogeneous wind speed maps. The different columns refer to different wavelengths (λ): 500, 700, 900 nm.

4.12 Appendix E: Impact of albedo seasonal variability

Using hyperspectral albedo maps from the HAMSTER dataset (Roccetti et al., 2024) for different days of the year (DOYs), we examine the impact of seasonal variability on the planet's surface albedo. We compare between the DOY 080 (spring equinox) and DOY 266 (autumn equinox). As shown in Roccetti et al. (2024), there is an increase in the overall planet reflectance in the spring due to the fact that the Northern Hemisphere, which hosts almost 80% of land surface of the planet, exhibits a more significant snow coverage compared to DOY 266, which increases the reflectance of the planet in the visible wavelength range. This is what we also find in Fig. 4.21 for the reflected light spectra, where in the cloudless scenario we find a larger reflectance for the spring albedo case. The largest spread is found for the $\alpha = 60°$, which also presents the largest illuminated fraction of the planet, thus the largest differences between snow coverage among spring and autumn. When introducing clouds with the 3D CG treatment, we find that the seasonal variability patterns due to surface albedo cannot be distinguished anymore, since they are inside the 1σ cloud variability spread for both reflected and polarized light spectra.
In the phase curve comparison (Fig. 4.22) we find a similar trend than in the reflectance spectra, showing the seasonal variability spread of land surface albedo only in the cloudless simulations. A larger spread is shown at smaller wavelengths, as expected by the typical spectral shape of snow and ice surfaces. In polarization, the spring scenario shows less polarized signal than the autumn case, since polarization behaves as the inverse of the reflectance. In addition, for the cloudless scenario, we also observe a shift in the Rayleigh

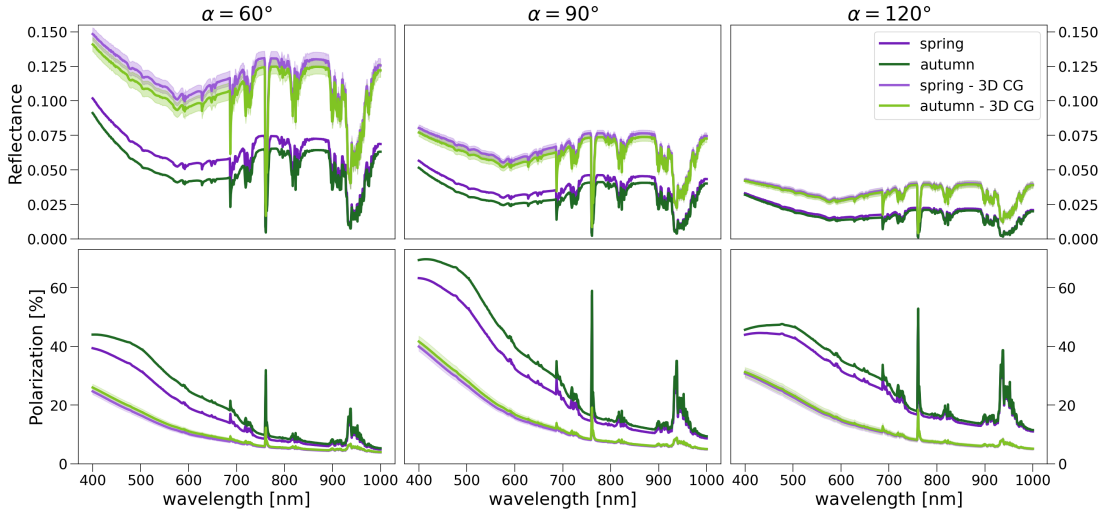

Figure 4.21: Reflected light (first row) and polarized light (second row) spectra showing the influence of surface albedo seasonal variability. The different columns refer to spectra at different phase angles (α): 60, 90, 120°.

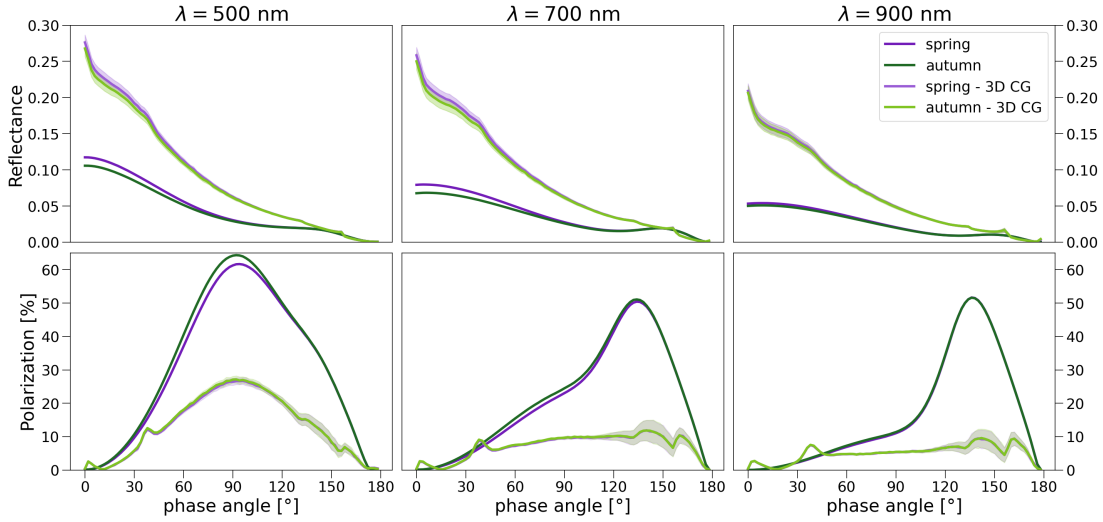

Figure 4.22: Reflected light (first row) and polarized light (second row) phase curves showing the influence of surface albedo seasonal variability. The different columns refer to different wavelengths (λ): 500, 700, 900 nm.

scattering peak between the spring and autumn cases. However, as for the spectra, all these differences cannot be distinguished anymore adding clouds in the simulations.

4.13 Appendix F: Spectral albedo of the ocean and Earth-like planet scenarios

In Fig. 4.23 we show the same spectra as in Fig. 5.5, but now as an albedo rather then a reflectance, by simply dividing the reflectance by a Lambertian phase function (Eq. 4.22).

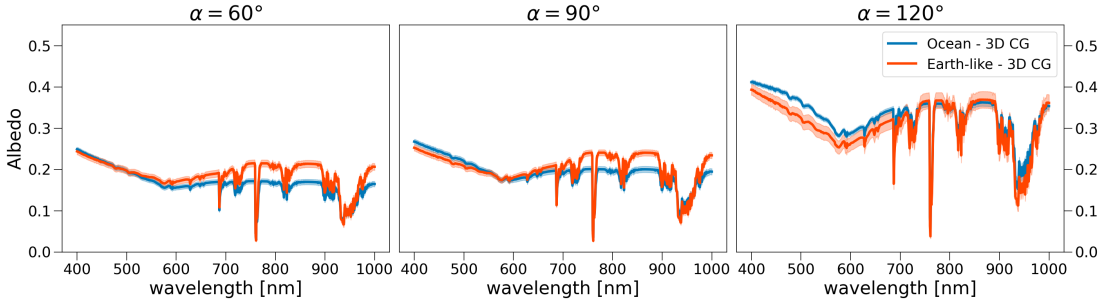

Figure 4.23: Comparison among the spectral albedo of the ocean and Earth-like planet scenarios. The different columns refer to different phase angles (α): 60, 90, 120°. The albedo was obtained from the reflectance by dividing by a Lambertian phase function (Eq. 4.22).

5

Planet Earth in reflected and polarized light. II. Refining contrast estimates for rocky exoplanets with ELT and HWO

Published as
Roccetti et al., 2025b, Astronomy & Astrophysics, Volume 700, A62

Full authors list:
Giulia Roccetti; Michael Sterzik; Julia V. Seidel; Claudia Emde; Mihail Manev and Stefano Bagnulo.

The characterization of nearby rocky exoplanets will become feasible with the next generation of telescopes, such as the Extremely Large Telescope (ELT) and the mission concept Habitable Worlds Observatory (HWO). Using an improved model setup, we aim to refine the estimates of reflected and polarized light contrast for a selected sample of rocky exoplanets in the habitable zones of nearby stars. We perform advanced 3D radiative transfer simulations for Earth-like planets orbiting G-type and M-type stars. Our simulations incorporate realistic, wavelength-dependent surface albedo maps and a detailed cloud treatment, including 3D cloud structures and inhomogeneities, to better capture their radiative response. These improvements are based on Earth observations. We present models of increasing complexity, ranging from simple homogeneous representations to a detailed Earth-as-an-exoplanet model. Our results show that averaging homogeneous models fails to capture Earth's full complexity, especially in polarization. Moreover, simplistic cloud models distort the representation of absorption lines at high spectral resolutions, particularly in water bands, potentially biasing atmospheric chemical abundance estimates. Additionally, we provide updated contrast estimates for observing rocky exoplanets around nearby stars with upcoming instruments such as ANDES and PCS at the ELT. Compared to previous studies, our results indicate that reflected light contrast estimates are overestimated by a factor of two when simplified cloud and surface models are used. Instead, measuring the fractional polarization in the continuum and in high-contrast, high-resolution spectra may be more effective for characterizing nearby Earth-like exoplanets. These refined estimates are essential for guiding the design of future ELT instruments and the HWO mission concept.

5.1 Introduction

The search for Earth-like exoplanets and the quest to characterize their atmospheres remain among the most compelling goals of modern astrophysics. However, a major challenge in directly imaging and characterizing rocky exoplanets is the extreme contrast between the planet and its much brighter host star. Overcoming this challenge requires innovative observational techniques and a deeper understanding of planetary light scattering.
Currently, most mature exoplanet atmosphere characterization relies on transmission spectroscopy, which is limited to transiting planets. Although highly successful for studying the atmospheric dynamics of hot Jupiters during transit (e.g., Nortmann et al. 2025; Seidel et al. 2025) and secondary eclipse (e.g., Pino et al. 2020; Costa Silva et al. 2024) and their atmospheric chemical composition (e.g., Snellen et al. 2008; Prinoth et al. 2024b), this method faces significant challenges when applied to rocky exoplanets. Temperate rocky exoplanets are less likely to transit due to their typically longer orbital periods, making transmission spectroscopy impractical for a broad population of potentially habitable worlds. Furthermore, their atmospheres are generally thinner than those of Jupiter-like planets, making atmospheric characterization even more challenging. In addition, in-transit radial velocity changes for longer period planets (like warm Jupiters) are too small to directly separate the planetary signal's wavelength shift from stellar and telluric lines, further complicating the detection of atmospheric absorption lines (Borsa et al., 2019; Seidel et al., 2020b,c; Prinoth et al., 2024a). Moreover, transmission spectroscopy primarily probes the upper atmospheric layers, providing limited information about surface conditions and lower atmospheric composition, both crucial for assessing habitability. Importantly, in this context, habitability refers specifically to the potential for surface liquid water, not necessarily to conditions sufficient for supporting life.
Reflected light observations offer a promising alternative, enabling the study of both transiting and non-transiting exoplanets. By analyzing the light scattered by the atmosphere and reflected off the planet's surface, it is possible to retrieve key properties such as albedo across different wavelengths and phase angles (Roccetti et al., 2025a), which can reveal the presence of clouds, oceans, and ice (Turbet et al., 2016). Additionally, spectral features in reflected light provide direct constraints on atmospheric composition, allowing for the detection of key molecules such as O_2, H_2O, CH_4, CO_2, and potentially CO. These observations can offer a more comprehensive view of an exoplanet's climate, surface conditions, and habitability.
The upcoming RISTRETTO (Lovis et al., 2022) spectrograph at the Very Large Telescope (VLT) is designed for detecting and analyzing exoplanetary atmospheres in reflected light, with a primary focus on the temperate rocky planet Proxima b (Bugatti et al., 2024). This scientific mission leverages the synergy between a high-contrast adaptive optics (AO) system and high-resolution spectroscopy and will serve as a precursor to the Extremely Large Telescope (ELT). The ELT, with its unprecedented light-collecting capacity and angular resolution, will pioneer the detection of reflected light from rocky exoplanets. Although current attempts have mostly yielded upper limits (Charbonneau et al., 1999;

Collier Cameron et al., 1999, 2002; Rodler et al., 2013; Martins et al., 2015; Hoeijmakers et al., 2018; Scandariato et al., 2021; Spring et al., 2022), high-contrast, high-resolution (HCHR) observations with the ELT's ANDES instrument are expected to achieve contrasts on the order of 10^{-7} within a few tens of nights (Pallé et al., 2025). A promising golden sample for future observations includes Proxima b, GJ 682 b, Wolf 1061 c, GJ 273 b, and Ross 128 b, all orbiting M dwarfs. Observationally, M dwarfs are favorable targets because their close-in habitable zones (Kasting et al., 1993; Selsis et al., 2007; Kopparapu et al., 2013) enable the detection and characterization of more transiting planets on shorter orbits. Additionally, other ELT instruments like HARMONI may also allow for the characterization of the atmosphere of Proxima b (Vaughan et al., 2024), while the proposed PCS instrument (Kasper et al., 2021) will leverage its extreme AO system and spectrograph for imaging rocky exoplanets.

Rocky planets orbiting M dwarfs may face significant challenges in retaining substantial atmospheres due to intense stellar activity and irradiation (Luger & Barnes, 2015; Dong et al., 2018). Recent JWST results offer mixed findings: 55 Cancri e is proposed to have an atmosphere (Hu et al., 2024), while TRAPPIST-1 b and c showed upper limits on the absence of thick atmospheres (Greene et al., 2023; Zieba et al., 2023). Detecting atmospheres around habitable zone planets remains difficult due to stellar contamination, as shown in the case of LHS 1140 b (Cadieux et al., 2024).

G-type stars, with their relatively stable stellar activity, are more promising targets for finding true Earth analogs. Ongoing efforts like the Terra Hunting Experiment (THE, Hall et al. 2018) are focused on detecting Earth-mass planets around G-type stars through precise radial velocity measurements. Moreover, the PLATO mission (Rauer et al., 2025) will play a key role in detecting and characterizing Earth-sized planets around Sun-like stars by leveraging high-precision photometry to measure their transits and constrain their bulk properties. Additionally, the ARIEL space mission (Tinetti et al., 2018) will begin characterizing a subset of temperate sub-Neptunes and super-Earths (Edwards & Tinetti, 2022), providing valuable input for the target selection of upcoming space missions like the mission concepts Habitable World Observatory (HWO, National Academies of Sciences & Medicine 2021) and Large Interferometer For Exoplanets (LIFE, Quanz et al. 2022), which aim to search for and characterize rocky exoplanets. HWO, for instance, will aim to image and study the reflected light of exoplanets, while LIFE will focus on thermal emission to provide insights into atmospheric pressure-temperature profiles and molecular signatures (Alei et al., 2024).

A complementary approach to characterize distant worlds through spectroscopy and direct imaging is by measuring their degree of polarization in reflected light. The light reflected by an exoplanet becomes partially linearly polarized due to atmospheric scattering and surface reflection (Stam, 2008). Previous modeling efforts by Stam (2008); Karalidi & Stam (2012); García Muñoz (2015); Emde et al. (2017); Trees & Stam (2019, 2022); Gordon et al. (2023); Vaughan et al. (2023) have demonstrated how polarization can aid in characterizing Earth-like exoplanets and distinguishing between different atmospheric and surface properties, which intensity-only simulations cannot achieve. Roccetti et al. (2025a) performed detailed simulations of reflectance and polarized spectra and phase curves for

an ocean and an Earth-like planetary scenarios. Their results suggest that the polarization fraction for an Earth-like planet ranges between 10% and 30%, depending on the wavelength and phase angle. Studying polarized light offers a valuable way to enhance the contrast between the planet and its host star, as most F-, G-, and K-type stars emit nearly unpolarized light (Cotton et al., 2017). However, this method comes with the trade-off of reduced sensitivity. Furthermore, polarization measurements help break degeneracies in atmospheric retrievals by distinguishing between clouds and surface features across different models (Karalidi & Stam, 2012). Unlike intensity-based observations, polarized light is not affected by transmission through Earth's atmosphere, as polarization arises from scattering processes with molecules or surface reflections, eliminating the need for telluric correction.

Roccetti et al. (2025a) introduced an improved cloud and surface modeling framework for simulating the reflected and polarized light of rocky exoplanets, highlighting the impact of realistic cloud and surface modeling. Their study demonstrated that neglecting sub-grid cloud variability leads to a significant overestimation of the planet's overall reflectance. Additionally, the vegetation red edge (VRE) feature is largely overestimated if surface albedo maps do not account for wavelength-dependent variations of complex mixture of different surface materials.

Building on this refined modeling approach, this second paper in the series extends contrast estimations for the reflected and polarized light of future rocky exoplanet observations. Specifically, we construct homogeneous planetary models and evaluate how their spectral and phase curve features compare to the more detailed, realistic models presented in Roccetti et al. (2025a). Using the defined golden sample of rocky exoplanets expected to be observed in reflected light by ANDES (Pallé et al., 2025), we provide improved contrast estimates and compare them with values reported in the literature. This analysis assesses the impact of detailed cloud and surface modeling in 3D radiative transfer simulations. Additionally, we explore contrast predictions for polarized observations and evaluate their feasibility with the upcoming ELT and HWO. These results are crucial for guiding the design of future instruments dedicated to the characterization of rocky exoplanets.

5.2 Reflected and polarized light contrasts

Pallé et al. (2025) identified a golden sample of non-transiting rocky exoplanets orbiting nearby M-type stars, for which ANDES is expected to detect reflected light within a few tens of nights. This sample consists of the five most promising targets in terms of reflected light signal-to-noise ratio (SNR): Proxima b, GJ 273 b, Wolf 1061 c, GJ 682 b, and Ross 128 b. With the planned launch of PLATO in 2026, serving as a key pathfinder survey, the target list is expected to expand in the coming years. Building on the golden sample, we include the recently discovered Barnard b (González Hernández et al., 2024), a sub-Earth-mass exoplanet orbiting the closest single star to the Sun. Since all six of these rocky exoplanets orbit M-dwarfs, we extend our study to include a comparison with a G-type star by estimating the contrast of potential Earth-like exoplanet in the habitable zone of Alpha

Cen A. Notably, Wagner et al. (2021) reported the detection of a point-like source in this system, which could be attributed to an exoplanet, exozodiacal dust, or an instrumental artifact, pushing the current exoplanet imaging mass detection limits.
Our goal is to provide refined flux contrast estimates for these nearby planetary systems by improving the modeling of clouds and surface albedo in reflected light calculations. In general, the contrast between an exoplanet and its host star in reflected light is

$$C_{\text{flux}} = \frac{F_{\text{p}}}{F_{\star}} = \left(\frac{R_{\text{p}}}{d \sin \theta_{\text{sep}}}\right)^2 A_{\text{g}} \cdot g(\alpha), \tag{5.1}$$

where F_{p} and $F_{\star}$ are the fluxes of the planet and the star, respectively, R_{p} is the radius of the planet, d is the distance from the Earth, A_{g} is the geometric albedo of the planet, $g(\alpha)$ is the phase function and α the phase angle (e.g., the angle between the direction to the star and the direction to the observer as seen from the planet). The angular separation θ_{sep} of the star-planet system is dependent on the phase angle, and we report values for $\alpha = 90°$, corresponding to the maximum elongation of the planet, to allow for a direct comparison with the contrast estimates presented in Pallé et al. (2025). However, ANDES can operate at smaller inner working angles and observe planets at phase angles below 90°, which are more favorable for detecting reflected light, thereby enhancing contrast (Pallé et al., 2025).
In Roccetti et al. (2025a), we present extensive sensitivity studies on estimating planetary reflectance, defined as the product of the geometric albedo and the phase function: $R = A_{\text{g}} \cdot g(\alpha)$. Since reflectance is independent of the stellar spectrum, the flux contrast can be determined using the planetary radius and angular separation for different planetary systems. In Table 5.1, we provide typical values of the scale factor (s), defined as

$$s = \left(\frac{R_{\text{p}}}{d \sin \theta_{\text{sep}}}\right)^2. \tag{5.2}$$

In addition to the reflected light contrast, we also introduce the contrast in polarization. The incident starlight reaching the planet is expected to be nearly unpolarized, with the disk-integrated sunlight exhibiting a polarization level of approximately 10^{-6} (Kemp et al., 1987). Conversely, light reflected from a planet's surface or scattered within its atmosphere can be polarized at levels of several tens of percent. Rayleigh scattering by atmospheric molecules polarizes light, though multiple scattering with clouds and aerosols can depolarize previously polarized photons. Similarly, the ocean glint produces strong linear polarization, while other surface types may depolarize light. Polarized light observations enhance the contrast between the planet and its host star and offer advantages over total flux measurements. Unlike absolute intensity, polarization is a relative measurement, independent of the star's type or distance. In polarization, the reflected light contrast can be expressed as

$$C_{\text{pol}} = C_{\text{flux}} \cdot P, \tag{5.3}$$

where P is the degree of linear polarization normalized between 0 and 1. The polarization contrast is function of α (Buenzli & Schmid, 2009).

Name	SpecType (T_{eff})	d [pc]	θ_{sep}[mas]	V [mag]	$R_p[R_\oplus]$	s
Proxima Cen b	M (2900 K)	1.30	37.3	11.01	1.07	$8.85 \cdot 10^{-7}$
Ross 128 b	M (3163 K)	3.37	14.7	11.12	1.15	$9.79 \cdot 10^{-7}$
GJ 273 b	M (3382 K)	3.80	24.0	9.84	1.64	$5.88 \cdot 10^{-7}$
Wolf 1061 c	M (3309 K)	4.31	20.7	10.10	1.81	$7.48 \cdot 10^{-7}$
GJ 682 c	M (3237 K)	5.01	16.0	10.94	2.11	$1.26 \cdot 10^{-6}$
Barnard b	M (3195 K)	1.83	12.9	9.51	0.76	$1.88 \cdot 10^{-6}$
Alpha Cen A	G (5804 K)	1.34	747	0.01	1.0	$1.82 \cdot 10^{-9}$

Table 5.1: Scale factor for exoplanets orbiting nearby M-type stars and a potential Earth-like planet around Alpha Cen A.

While it is true that the polarized contrast is lower than the contrast in intensity alone, polarimetric differential imaging (DPI) can greatly push the sensitivity down to a few orders of magnitude due to fast modulation. The Zurich IMaging POLarimeter (ZIMPOL), the visible focal plane instrument of SPHERE can, in principle, reduce the achievable contrast from 10^{-4} (with Adaptive Optics alone) to 10^{-8} in polarization (Hunziker et al., 2020). This advantage is particularly significant for planets with smaller angular separations from their host star, as polarimetric observations can reduce, or, in principle, cancel, speckle noise around the coronagraph. Beuzit et al. (2019) conducted polarimetric observations of a sample of targets and demonstrated that ZIMPOL achieves polarization contrast detection limits much deeper than those of intensity-based observations. For Alpha Cen A, polarization lowered the achievable contrast from 10^{-5} to 10^{-7} close to the star, at an angular separation of 0.35 arcsec, and from 10^{-7} to 10^{-8} at the wider separation angle of 1.5 arcsec.

5.3 3D radiative transfer simulations

We perform 3D radiative transfer simulations using MYSTIC (Mayer, 2009), the Monte Carlo code for the phYsically correct Tracing of photons in Cloudy atmospheres, which is part of the libRadtran library (Mayer & Kylling, 2005b; Emde et al., 2016). MYSTIC incorporates the Absorption Lines Importance Sampling (ALIS) method (Emde et al., 2011), enabling fast calculations of high-resolution spectra by tracing photons at a single wavelength. Moreover, the variance reduction method VROOM (Buras & Mayer, 2011b) is used to correctly simulate clouds. Emde et al. (2017) adapted MYSTIC to simulate disk-integrated properties of the Earth as an exoplanet in polarization, accounting for surface reflection, multiple scattering by molecules, aerosol particles, cloud droplets, and ice crystals.
Building on this foundation, Roccetti et al. (2025a) further advanced the modeling framework by introducing the capability to simulate fully inhomogeneous and realistic planets. This includes a new treatment of cloud sub-grid variability and inhomogeneities through the 3D Cloud Generator (3D CG) algorithm[1]. The 3D CG employs 3D cloud fields from

[1] https://github.com/giulia-roccetti/3D_Cloud_Generator

the ERA5 reanalysis dataset (Hersbach et al., 2020), the European Centre for Medium-Range Weather Forecasts (ECMWF) ReAnalysis fifth-generation product. It provides atmospheric data on a global grid of 1440 × 721 horizontal pixels and 37 vertical levels. For each grid cell, ERA5 provides liquid water content, ice water content, and cloud cover. Although the ERA5's spatial resolution (∼31 km or 0.25°) is more than adequate for exoplanet modeling, Roccetti et al. (2025a) demonstrated that introducing sub-pixel cloud variability significantly affects disk-integrated reflectance and polarization spectra and phase curves. To address this, the 3D CG redistributes the liquid water and ice water content within each ERA5 grid cell into sub-grid structures, generating patchier cloud distributions. This allows more photons to reach the surface and mitigates the over-smoothing of cloud effects at coarse spatial resolution. The algorithm conserves both the in-cloud optical thickness and total planetary cloud cover. A specified vertical overlap scheme is applied to distribute sub-grid clouds vertically. Roccetti et al. (2025a) found that the algorithm converges when each ERA5 grid cell is divided into nine sub-pixels (a zoom-in factor of 3), with no significant differences observed between maximum-random and exponential-random vertical overlap schemes. Therefore, all 3D CG simulations in this work are performed using a x3 zoom-in factor with exponential-random overlap.
The improved modeling framework presented in Roccetti et al. (2025a) also includes the implementation of wavelength-dependent surface albedo maps using HAMSTER (Roccetti et al., 2024). Additionally, the framework incorporates more sophisticated surface treatments, allowing Lambertian surfaces with spectral albedo variations and oceans modeled with bidirectional reflectance distribution functions (BRDFs) or bidirectional polarization distribution functions (BPDFs), enabling the ocean glint to be treated correctly.
The results and sensitivity studies presented in Roccetti et al. (2025a) serve as a starting point for this work. Here, we assess whether a linear combination of homogeneous planet models can accurately reproduce the ground-truth ocean and Earth-like planet scenarios explored in Roccetti et al. (2025a). Furthermore, we investigate the impact of advanced 3D inhomogeneous radiative transfer simulations on estimating the contrast in reflected and polarized light for the golden sample of rocky exoplanets orbiting nearby stars (Pallé et al., 2025).

5.3.1 Homogeneous planets model setup

We construct homogeneous, cloud-free planetary models by incorporating wavelength-dependent surface albedo properties characteristic of four distinct surface types: desert, forest, polar ice cap, and ocean, all beneath an Earth-like atmosphere with US standard atmospheric properties (Anderson et al., 1986). The wavelength-dependent surface albedo properties are extracted from HAMSTER (Roccetti et al., 2024). Specifically, we use the typical reflectance spectrum of the Amazon rainforest region in HAMSTER for the forest planet. For the desert planet, we adopt the wavelength-dependent surface albedo from the Australian desert dataset. For the polar region, we use the boreal summer Antarctica spectrum as a benchmark.
For the ocean surface, while it lacks strong wavelength-dependent features, we account

for ocean glint reflection by implementing the BRDF in reflected light and the BPDF in polarized light, assuming a constant surface wind speed of $10\,\mathrm{m\,s^{-1}}$. To approximate an Earth-like planet scenario, we construct a linear combination of these homogeneous planets, assuming the Earth's surface composition consists of 70% ocean, 10% forest, 10% desert, and 10% polar regions.
To simulate homogeneous cloudy planets, we retain the same wavelength-dependent surface properties while introducing an idealized homogeneous cloud field based on the properties detailed in Roccetti et al. (2025a) (Tables 1 and 2). Specifically, we assume a 46% cloud cover, with a liquid water (LW) cloud optical depth of 6.51 at a bottom altitude of 1.59 km. To ensure consistency across different horizontal resolutions, we first generate a cloud field matching the 3D CG resolution with a zoom-in factor of ×3 (Roccetti et al., 2025a), resulting in a grid box size of approximately 9 km. The cloud layer is set to a 1 km vertical extent, and we calculate the in-cloud liquid water content to maintain the prescribed LW cloud optical depth. The cloud effective droplet radius is also fixed at 8.99 μm, from the averaged properties of the ERA5 reanalysis product found in Roccetti et al. (2025a). In these homogeneous planet models, 60% of the sub-grid cells are randomly assigned to be cloudy, resulting in horizontally patchy cloud structures. Also for the Earth-like cloudy scenario, we build it as a linear combination of the cloudy homogeneous simulations, maintaining the assumed surface composition of 70% ocean, 10% forest, 10% desert, and 10% polar regions.

5.3.2 Setups for models of increasing complexity

By building models of increasing complexities, we assess the impact of the improved cloud and surface modeling approaches presented in Roccetti et al. (2025a) on the simulated spectra and phase curves compared to homogeneous planet simulations. To perform this comparison, we use the same 3D radiative transfer code MYSTIC and the same grid size. We simulate models of different complexities, from uniform surface and clouds to more complex and inhomogeneous cases. The increasing complexity scales as follows:

- uniform surface, with a constant surface albedo of 0.2 (Kopparapu et al., 2013), not wavelength-dependent, and uniform LW clouds (fully cloudy layer with $\tau = 6.51$, $r_{\mathrm{eff}} = 8.99$ μm and altitude thickness 1 km from 1.59 to 2.59 km);

- uniform surface (as above) and a homogeneous LW cloud layer with 46% patchy cloud cover (making the previous cloud layer patchy and redistributing the liquid water content among only cloudy pixels);

- linear combination of surfaces, taking a representative spectra of a forest, a desert, a polar region and the ocean (including BRDF and BPDF), and averaging them as 70% ocean, 10% forests, 10% deserts and 10% polar to reproduce the Earth, and patchy LW clouds with 46% cloud cover (as above);

- linear combination of surfaces (as above) with two cloud layers, the patchy LW clouds

and the patchy ice water (IW) clouds. For the IW clouds we use 54% of cloud cover, $\tau = 0.63$, altitude range from 4.34 to 5.34 km and $r_{\text{eff}} = 46.9$ μm taken from Roccetti et al. (2025a) (Tables 1 and 2);

- ocean surface (with BRDF and BPDF) with the 3D CG clouds, including their LW and IW clouds and their 1σ spread, this scenario obviously includes the effects of an ocean glint;
- Earth-like scenario including ocean surface treated with the BRDF and BPDF (but ocean glint almost always hidden by land) and hyperspectral albedo maps with the 3D CG clouds including their LW and IW clouds and their 1σ spread.

5.3.3 Setup for high spectral resolution simulations

With the same model setup as in Roccetti et al. (2025a), we run high-spectral-resolution simulations at ANDES resolution R = 100 000 to study the effect of different surface and cloud properties not only on the continuum, but also on the absorption lines. Upcoming instruments at the ELT, such as ANDES, will allow us to image the closer rocky exoplanets orbiting M dwarfs using HCHR observations. We study in detail the O_2-A band around 780 nm and the H_2O absorption lines in the Y band, between 920 and 950 nm. To perform high-spectral-resolution simulations, we couple the Atmospheric Radiative Transfer Simulator (ARTS version 2.2; Buehler et al. 2005, Eriksson et al. 2011) with MYSTIC. ARTS provides accurate line-by-line absorption calculations for molecular species, ensuring precise spectral resolution across a wide wavelength range. The computed absorption coefficients are then used as input for MYSTIC, which simulates the 3D radiative transfer.

5.3.4 M-dwarf simulations model setup

We extend the comparison between the ocean and Earth-like planet scenarios from Roccetti et al. (2025a) to an exoplanet orbiting an M dwarf star. Using the same models, we simulate reflected and polarized light spectra across a wavelength range of 400–2500 nm at a spectral resolution of 1 nm using the REPTRAN absorption parametrization (Gasteiger et al., 2014). While the stellar spectrum is updated as an input, the resulting spectra are only affected by the planet's surface, atmosphere, and cloud properties, and not by the stellar spectrum. As expected, the reflected light contrast decreases toward the near-infrared (NIR), but this analysis provides valuable predictions for upcoming NIR observations. Moreover, the NIR contains a higher density of absorption features compared to the visible range, enabling the detection of key atmospheric species such as H_2O, CO_2, CH_4, and O_2, which are crucial for exoplanet characterization.

5.4 From homogeneous to realistic Earth-like planets

5.4.1 Homogeneous planets spectra and phase curves

We perform simulations for homogeneous planets using wavelength-dependent albedo properties from HAMSTER (Roccetti et al., 2024). As demonstrated in Roccetti et al. (2025a), accurately modeling surface reflectance, whether for forests, deserts, or other surface types, significantly impacts the planet's total reflectance, particularly in the VRE region. Roccetti et al. (2025a) showed that previous models substantially overestimated the VRE because they represented vegetated surfaces using the laboratory-measured reflectance of a single leaf. However, a forest is a far more complex environment, with its spectral signature arising from a combination of leaves, soil, and other materials. By incorporating HAMSTER into our radiative transfer simulations, (Roccetti et al., 2025a) demonstrates that the increase in reflectance around 750 nm due to the VRE is notably smaller than previously estimated. This finding helps explain why the observed intensity of the VRE in Earth as an exoplanet intensity observations is weaker than previously expected, as seen in Earthshine studies (Montañés-Rodríguez et al., 2006).
Here, we present reference spectra and phase curves for homogeneous, cloud-free planets with different surface types in both reflected and polarized light. The ocean planet includes BRDF and BPDF treatments, while other land surface types are derived from the HAMSTER hyperspectral albedo maps dataset (Roccetti et al., 2024) and treated as Lambertian surfaces. The Earth-like case, shown in orange, is modeled as a linear combination of ocean, desert, forest, and polar surface types.
In the absence of clouds, distinct surface-dependent features emerge both in the spectra (Fig. 5.1) and phase curves (Fig. 5.2). The polar ice cap planet (cyan model) exhibits high reflectance across all wavelengths, while the forest model (green) shows a pronounced VRE feature, which is clearly visible in the spectral reflectance of a purely forested planet. Polarization spectra, however, show the opposite trend. The ocean planet (dark blue) exhibits strong polarization due to the ocean glint effect, while the VRE feature manifests as a steep decline in polarization between 700 and 800 nm. Additionally, phase curves in polarization reveal a shift in the peak of the polarization curve depending on surface properties. For an ocean planet, the polarization peak occurs at almost 90° only at 500 nm, but at higher phase angles at 700 and 900 nm. The polarization peak for an ocean surface without atmosphere would be at 106° (double the Brewster angle for water). For the ocean planet with a Rayleigh atmosphere, it is a mixture of effects: at shorter wavelengths, Rayleigh scattering dominates and the peak is at 90°, at longer wavelengths, surface interactions are decisive and the peak gets closer to 106°. For a forest planet, the peak shifts to larger phase angles compared to an ocean planet, with a wavelength-dependent trend. At $\lambda = 500$ nm, where forests are darker and Rayleigh scattering dominates, the polarization peak remains close to $\alpha = 90°$. However, at longer wavelengths ($\lambda = 700$ and 900 nm), the increased reflectance of forests after the VRE causes the polarization peak to shift to approximately $\alpha = 110$ and 130°, respectively.

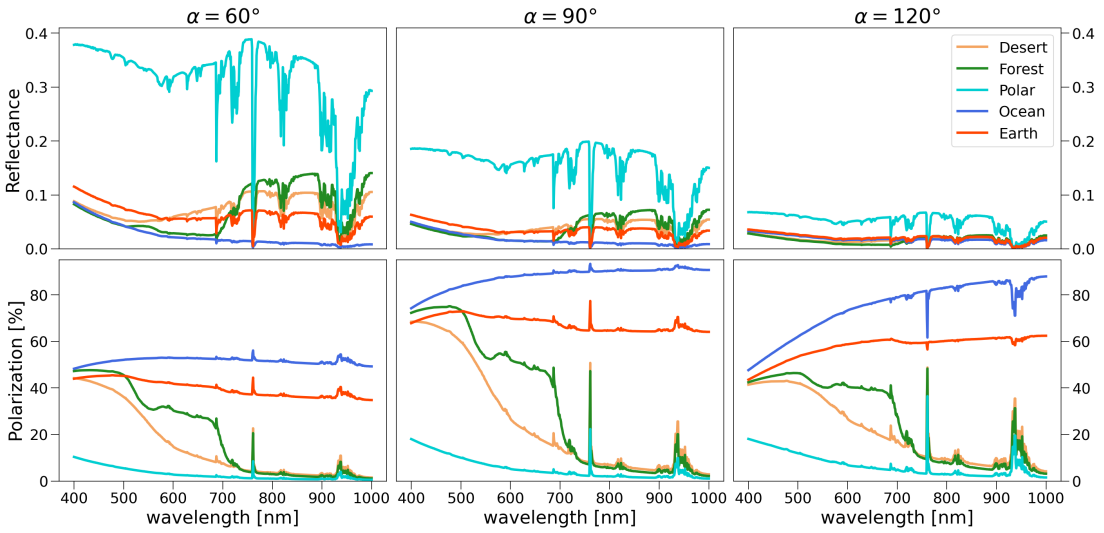

Figure 5.1: Reflected light (top row) and polarized light (bottom row) spectra for various homogeneous, cloud-free planets with different surface types. The wavelength-dependent spectral features of desert, forest, and polar surfaces are taken from HAMSTER (Roccetti et al., 2024) and modeled as Lambertian reflectors, while the ocean surface incorporates BRDF and BPDF treatments. Each column corresponds to spectra at different phase angles α: 60, 90, 120°.

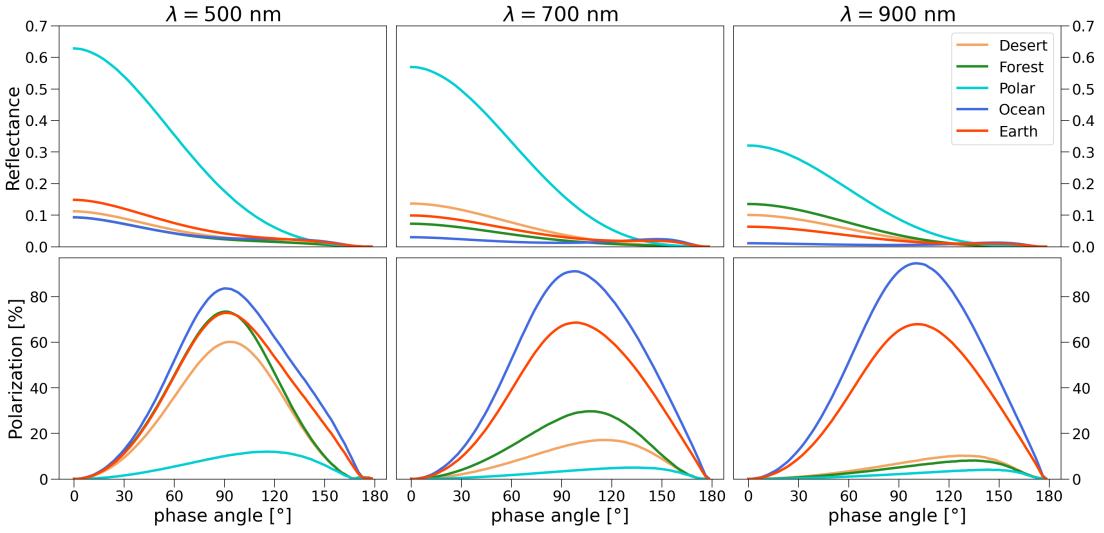

Figure 5.2: Reflected light (top row) and polarized light (bottom row) phase curves showing homogeneous cloud-free planets. The wavelength-dependent spectral features of desert, forest, and polar surfaces are taken from HAMSTER (Roccetti et al., 2024) and modeled as Lambertian reflectors, while the ocean surface incorporates BRDF and BPDF treatments. Different columns refer to different wavelengths (λ): 500, 700, 900 nm.

5.4.2 Patchy clouds over homogeneous surfaces

For the same homogeneous planets, we simulate spectra and phase curves assuming a homogeneous cloud cover of 46% (see Sec. 5.3.1). Fig. 5.3 presents the reflected (first row) and polarized (second row) light spectra for these cloudy planets. In reflected light, we observe a general increase in brightness compared to the cloud-free simulations (Sec. 5.4.1), with the effect being particularly pronounced for the ocean planet (dark blue). The polar planet (cyan), which already exhibits a very high surface albedo, is less affected by the presence of clouds. The addition of clouds also impacts the forest planet (green), where the VRE feature becomes less prominent in reflectance due to an increase in the continuum level before 750 nm. However, the effect is significantly stronger in polarization. With a cloudy atmosphere, the overall degree of polarization decreases substantially. For instance, in the ocean planet case, polarization at $\alpha = 90°$ drops from more than 80% in the cloud-free scenario to between 5% and 40% in the cloudy case. The presence of clouds, due to multiple scattering, steepens the slope of the polarized spectra for the forest and desert planets while inverting the slopes for the ocean and Earth-like planet configurations. This highlights the superior diagnostic power of polarization compared to reflectance alone, as it becomes easier to distinguish between cloud-free and cloudy spectra. Moreover, the VRE feature is affected in polarization, as the characteristic drop in polarization between 700 and 800 nm is reduced.

A similar trend is observed in the phase curves for both reflected and polarized light (Fig. 5.4). In reflected light, the overall brightness increases slightly, particularly for the ocean planet, and additional features appear around $\alpha = 40°$, corresponding to the cloudbow feature. In polarization, we again observe a significant reduction in the degree of linear polarization, yet new cloud-related features emerge compared to the cloud-free case (Fig. 5.2). The cloudbow is especially prominent in polarization and carries valuable information about cloud droplet microphysical properties, including size, composition, and shape (Emde et al., 2017; Sterzik et al., 2020). Additional polarization features also appear at large phase angles ($\alpha = 120°$ and $160°$ for $\lambda = 900$ nm), which are associated with the change of the polarization direction.

5.4.3 Models of increasing complexity

Building on our simulations of homogeneous planets, we now investigate the impact of introducing inhomogeneities and increasing model complexity on reflectance and polarization. Karalidi & Stam (2012) demonstrated that models with horizontal inhomogeneities leave distinct traces in the polarization phase function and affect both the absolute values of reflectance and polarization in Earth-like exoplanet simulations. In this sensitivity study, we transition from homogeneous surface and cloud models to fully realistic Earth-like and ocean planet simulations.

In Fig. 5.5 we show the reflected and polarized light differences in the spectra due to the models of varying complexity. First, we notice the significant spread between the ocean and Earth-like scenario already shown in Roccetti et al. (2025a), way beyond the 1σ cloud

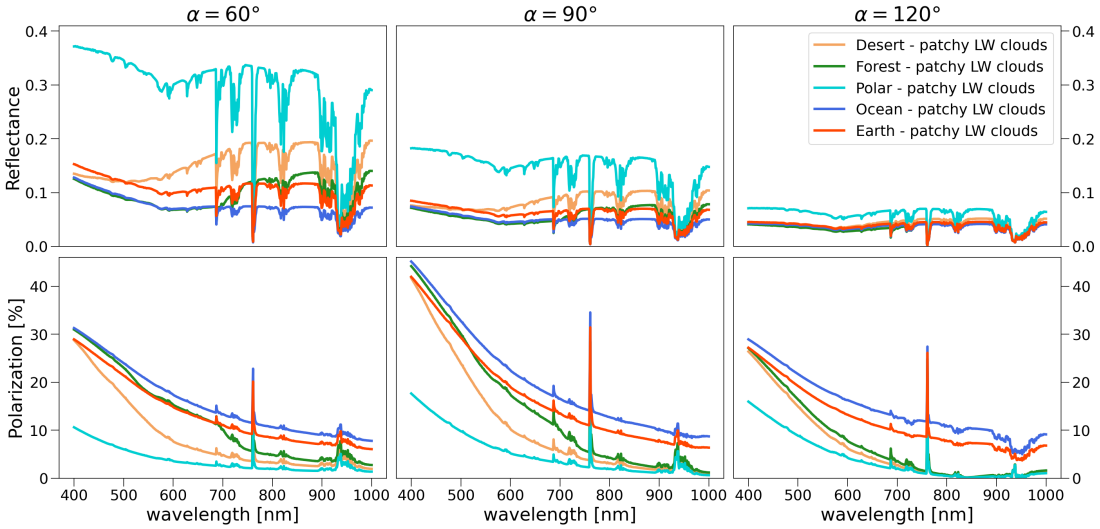

Figure 5.3: Reflected light (top row) and polarized light (bottom row) spectra for various homogeneous planets with different surface types and homogeneous clouds. The wavelength-dependent spectral features of desert, forest, and polar surfaces are taken from HAMSTER (Roccetti et al., 2024) and modeled as Lambertian reflectors, while the ocean surface incorporates BRDF and BPDF treatments. Each column corresponds to spectra at different phase angles α: 60, 90, 120°.

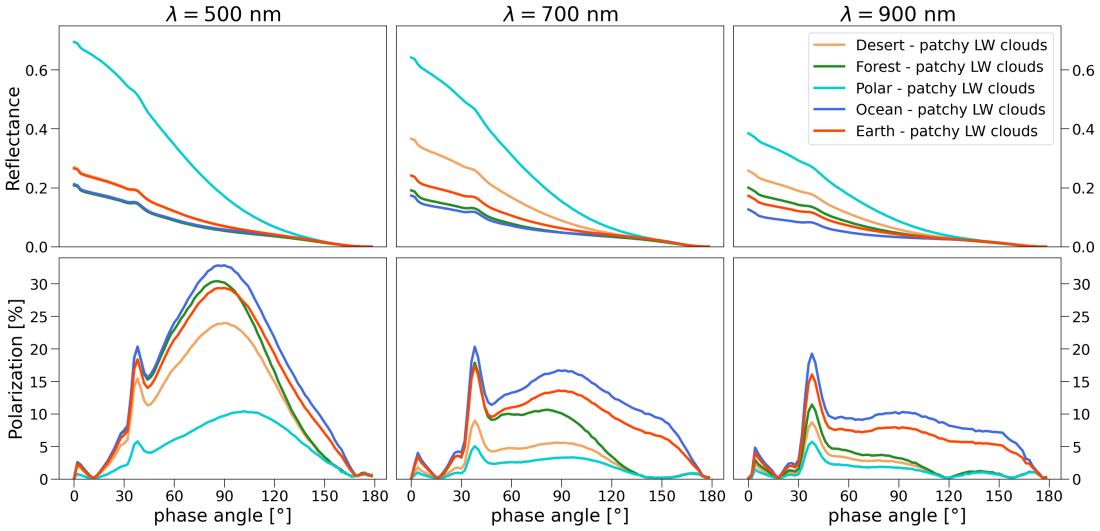

Figure 5.4: Reflected light (top row) and polarized light (bottom row) phase curves showing planets with homogeneous clouds and surfaces. The wavelength-dependent spectral features of desert, forest, and polar surfaces are taken from HAMSTER (Roccetti et al., 2024) and modeled as Lambertian reflectors, while the ocean surface incorporates BRDF and BPDF treatments. Different columns refer to different wavelengths (λ): 500, 700, 900 nm.

variability spread in the models (shaded areas) computed using various cloud fields from the ERA5 reanalysis product. This is particularly evident for $\alpha = 60°$ in reflectance, while the difference gets larger for $\alpha = 120°$ in polarization, where we observe a different behavior both in the spectral slopes of the models, their continuum in the near-infrared (NIR), and in the behavior of the spectral lines. Due to the presence (ocean scenario) and absence (Earth-like scenario) of the ocean glint feature, we see a different behavior of the water bands around 950 nm, as they are shown in absorption (spectral lines below the continuum) for the ocean planet and in emission (spectral lines above the continuum) for the Earth-like case. This effect is already present in the $\alpha = 90°$ case, but gets enhanced at larger phase angles. For the uniform clouds and surface model (black line), we find it to substantially overestimate the reflectance of the planet and underestimate its polarization at $\alpha = 120°$, as expected by a uniform cloud layer, where photons are reflected above the cloud deck. Making the LW clouds more patchy (uniform surface - patchy LW clouds, dark gray line) shows improvement in the comparison with the more complex and realistic simulations in reflected light and at large phase angles.
We now change the uniform surface with a linear combination of surfaces with patchy LW clouds (light gray line). Only for $\alpha = 90$ and $120°$, we find a much better correspondance with the Earth-like scenario in reflected light, where the Rayleigh scattering spectral slope more closely matches the realistic Earth-like case. This improvement is due to the wavelength-dependent linear combination of surface types, which provides a more accurate representation of surface albedo. As a last improvement, we add IW clouds on top of the patchy LW clouds over the linear combination of surfaces (silver line). In reflected light, we notice a slight increase in the reflectance for small phase angles.
However, in polarization, we observe a notable difference between the simpler and more complex models, particularly at $\alpha = 90$ and $120°$. At $\alpha = 90°$, uniform surfaces reduce the level of polarization compared to the linear combination of surfaces. This effect becomes even more pronounced at $\alpha = 120°$, where polarization drops to zero just before 700 nm due to changes in the direction of the Stokes vectors when using a uniform surface. Additionally, the degree of linear polarization is significantly lower than in the Earth-like and ocean planet scenarios, and the spectral slope is steeper than in the more realistic models. When introducing a linear combination of wavelength-dependent surfaces, the level of polarization becomes more comparable to the Earth-like scenario. This finding suggests that polarization is more sensitive to planetary surface features than reflectance alone, particularly at large phase angles. Accurately modeling wavelength-dependent surfaces is essential for properly interpreting disk-integrated spectra of exoplanets. However, while this approach improves polarization estimates, the slope in the Rayleigh scattering region and the direction of the water absorption bands still do not fully match the realistic model. This indicates that horizontally patchy clouds alone are insufficient to accurately model polarization, especially at high phase angles. These results suggest that capturing inhomogeneities in both cloud and surface modeling will be crucial for interpreting observations from the next generation of telescopes. Moreover, polarization provides stronger diagnostic capabilities for distinguishing different planetary scenarios and resolving potential retrieval degeneracies.

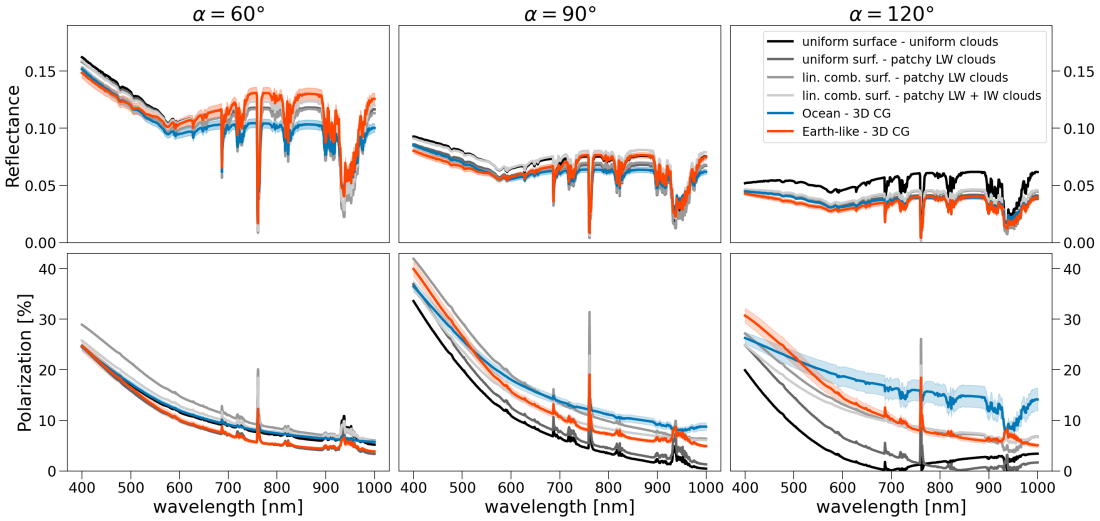

Figure 5.5: Comparison among spectra in reflected (first row) and polarized light (second row) of models of different complexity, from fully homogenous to complex Earth as an exoplanet simulations. Different columns refer to different phase angles (α): 60, 90, 120°.

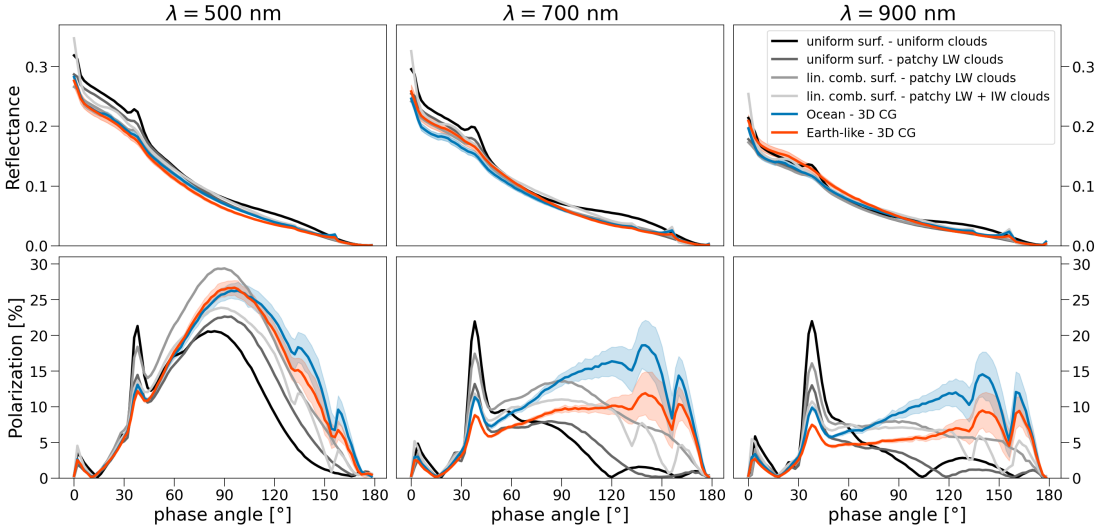

Figure 5.6: Reflected light (first row) and polarized light (second row) phase curves showing the influence of models of different complexities, from fully homogeneous to more complex Earth as an exoplanet simulations. Different columns refer to different wavelengths (λ): 500, 700, 900 nm.

In Fig. 5.6, we analyze the impact of increasing model complexity on reflected and polarized phase curves at three different wavelengths: λ = 500, 700, and 900 nm. Significant differences between the ocean and Earth-like scenarios emerge primarily in polarization, particularly at 700 and 900 nm. We observe an increase in polarization due to ocean glint, which exceeds the variability introduced by cloud properties in our models, as discussed

in Roccetti et al. (2025a). In reflected light, uniform surface simulations slightly overestimate planetary reflectance, especially at shorter wavelengths. This discrepancy is more pronounced in polarization, affecting the polarization peak associated with Rayleigh scattering (around $\alpha = 90°$) at 700 and 900 nm. Moving from uniform clouds to horizontally patchy LW clouds on a uniform surface alters both the phase angle at which maximum polarization occurs and the prominence of the cloudbow feature. When introducing a linear combination of surfaces, we find improved agreement mostly in polarized light phase curves. However, the cloudbow feature remains substantially overestimated compared to the realistic 3D CG model without IW clouds. Additionally, including IW clouds generates polarization features at large phase angles ($\alpha = 138$ and $158°$), which result from ice crystal scattering properties, as explained in Emde et al. (2017). Overall, for $\lambda = 700$ and 900 nm, simplified polarized phase curves fail to reproduce the benchmark Earth-like and ocean models. These findings underscore the importance of accurately modeling 3D cloud inhomogeneities and subgrid variability when interpreting exoplanet phase curves, particularly in polarization. Our results suggest that distinguishing surface and atmospheric features using reflected light alone is more challenging than with polarization. However, in polarization, a homogeneous treatment of clouds and surface properties has a stronger impact on observational interpretation. This further emphasizes that polarization provides deeper insights into cloud properties than reflected light alone.

Since the next generation of telescopes and instruments, such as ANDES, will require long integration times to characterize rocky exoplanets, we examine in Appendix 5.8 the effect of time-averaging evolving cloud patterns over a typical 8-hour night of observation. In Figs. 5.11 and 5.12, we present the resulting impact on the spectra and phase curves for an ocean planet under different cloud scenarios: a uniform LW cloud layer (with cloud properties as in Sec. 5.3.2), the 3D CG model with a 1σ spread over 12 months, and an averaged model based on eight consecutive simulations, each using a distinct ERA5 cloud field as input to the 3D CG algorithm over an 8-hour period. This latter setup is designed to mimic the observation of an exoplanet over a single night, accounting for evolving weather patterns and changing scenery due to planet rotation. Our results show that even when cloud patterns are averaged over long integration times, the model predictions differ significantly from those based on a uniform cloud layer and closely resemble the results from the 3D CG 1σ spread model. This is because, even over extended integration periods, the instantaneous cloud distribution imprints its patchy structure on the reflected light. As a result, the ocean glint remains visible through cloud gaps at all times, and each timestep contributes to enhanced reflectance at small phase angles and increased polarization at large phase angles. Therefore, the resulting spectra and phase curves are not equivalent to those produced by a homogeneous, thinner cloud model.

5.4.4 Absorption lines in high spectral resolution

We extensively discussed the influence of cloud and surface modeling approaches on the continuum levels of reflected and polarized light spectra. Now, we investigate the impact of models of varying complexity, ranging from uniform to patchy cloud modeling and different

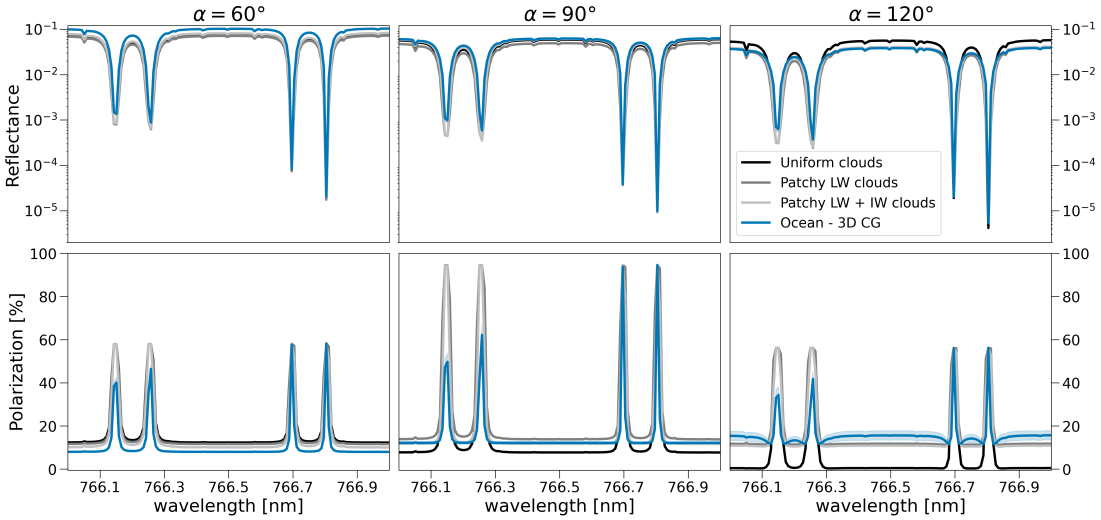

Figure 5.7: O_2-A band in reflected (top row) and polarized light (bottom row) at a spectral resolution of R = 100 000. The absorption lines are modeled for an ocean planet with three cloud treatments: uniform, homogeneous, and 3D CG clouds. Different columns refer to different phase angles (α): 60, 90, 120°.

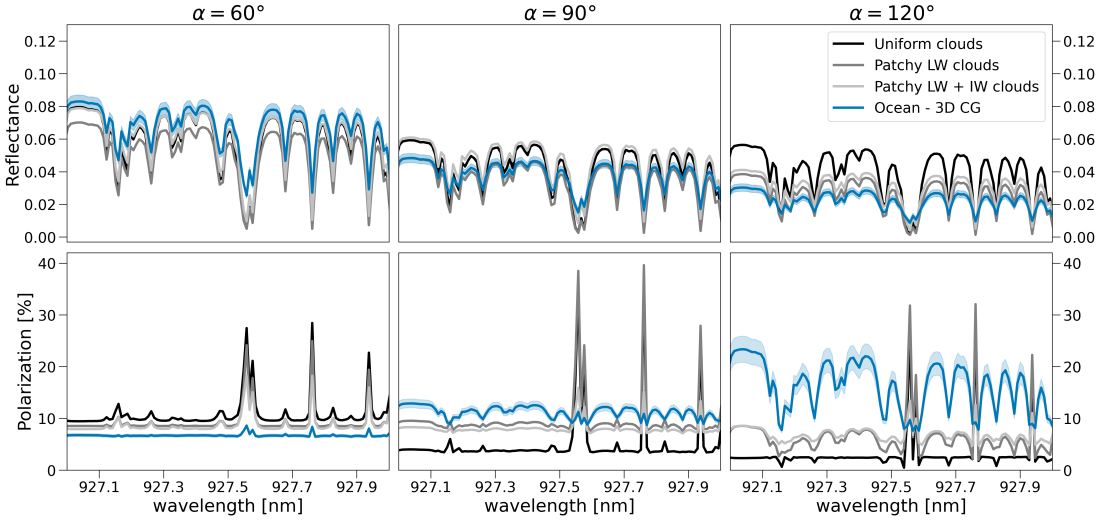

Figure 5.8: H_2O absorption lines in the Y band in reflected (top row) and polarized light (bottom row) at a spectral resolution of R = 100 000. The absorption lines are modeled for an ocean planet with three cloud treatments: uniform, homogeneous, and 3D CG clouds. Different columns refer to different phase angles (α): 60, 90, 120°.

surface types, on absorption lines. Specifically, we focus on two molecular species: the O_2-A band around 780 nm and the H_2O lines in the Y band (920–950 nm). We perform high-resolution simulations with a spectral resolution of 100 000, matching the expected capabilities of upcoming instruments on the ELT, such as ANDES.

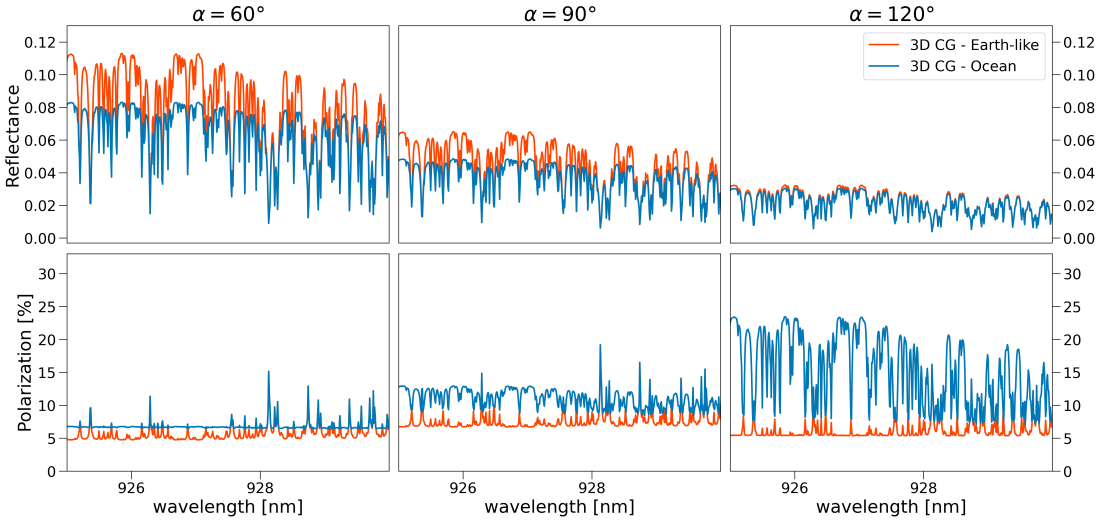

Figure 5.9: H_2O absorption lines in the Y band in reflected (top row) and polarized light (bottom row) at a spectral resolution of R = 100 000. The absorption lines are modeled for an ocean and an Earth-like planet scenario with 3D CG clouds. Different columns refer to different phase angles (α): 60, 90, 120°.

Fig. 5.7 illustrates the effect of different cloud models (uniform, patchy LW clouds, patchy LW and IW clouds, and 3D CG simulations) over an ocean surface. In reflected light (please note the log scale), while the continuum is influenced by cloud modeling, the depth of the O_2-A line forest remains unaffected. In polarization, however, we observe changes not only in the continuum, particularly at $\alpha = 120°$, but also in the depth of the absorption lines, which appear in emission. Notably, within the O_2-A band, the more saturated lines in reflectance remain unaffected by the choice of cloud model, while a more realistic treatment of clouds with the 3D CG lowers the polarization level of the emission lines, which are less saturated. This suggests that the conventional approach of retrieving cloud deck height using O_2-A line depth (Stam, 2008) is influenced by the presence of patchy clouds on a global scale.
We conduct the same comparison between uniform, patchy LW clouds, patchy LW and IW clouds, and 3D CG models for the H_2O lines in the Y band, as shown in Fig. 5.8. Here, we observe that uniform and patchy clouds affect the continuum, increasing the continuum level in reflected light and lowering it in polarization compared to the 3D CG ground truth models at $\alpha = 90$ and 120°. Additionally, we identify an interesting behavior in the spectral lines. In reflected light, discrepancies appear in the line depths, while in polarization, the water lines are seen in absorption relative to the continuum in the 3D CG model, while they appear in emission for the simplistic uniform and patchy cloud approaches. The addition of the IW clouds does not have a large impact on the absorption lines.
In Fig. 5.9, we assess the impact of different surface types on water lines. The 3D CG ocean and Earth-like models correspond to the spectra in Fig. 5.5, but here we use a spectral resolution of 100 000, focusing on the water band region. We observe that while

the continuum is influenced by surface type, the water bands are shown in absorption for an ocean surface, while they appear in emission for a dry surface. This occurs because, in the Earth-like scenario, ocean glint is obscured by continents at large phase angles (see Roccetti et al. 2025a). This effect becomes more pronounced at larger phase angles, with the line depth remaining nearly consistent across all molecular lines both in absorption and emission.
This behavior was previously discussed by Trees & Stam (2022) for low spectral resolution simulations and homogeneous models. Here, we confirm that it persists even in more sophisticated simulations that incorporate sub-grid cloud inhomogeneities within the 3D CG framework. Furthermore, we demonstrate that the choice of cloud simulation approach also influences this line behavior in polarization. Therefore, accurately modeling clouds and their complex 3D structure is crucial for potential observations and for reliably extracting surface information from water lines.

5.5 Contrast estimates for the ANDES golden sample

In Fig. 5.10, we extend the ground-truth models for the ocean and Earth-like planet scenarios from Roccetti et al. (2025a) into the NIR, up to 2500 nm. The figure illustrates that in reflected light, these two scenarios can be distinguished at small phase angles, where the Earth-like planet appears more reflective due to the high albedo of deserts, which is particularly significant in the NIR. In polarization, the distinction between the two scenarios becomes apparent at $\alpha = 90°$, where water lines appear in absorption or emission depending on the underlying surface. This effect becomes even more pronounced at larger phase angles, further enhancing the diagnostic potential of polarized light.
With the enhanced cloud and surface modeling techniques presented in this work, we also provide updated flux contrast estimates for both intensity and polarization to support the preparation of future ground-based instruments, such as ANDES and PCS on the ELT, and space-based mission concepts like HWO. Using the scale factors for nearby exoplanets provided in Table 5.1, we refine the contrast estimates from previous studies (e.g., Pallé et al. 2025). It is important to note that rocky exoplanets orbiting M dwarfs are almost always tidally locked. Previous studies (e.g., Way et al. 2017; Kopparapu et al. 2017) have shown that tidal locking can result in atmospheric circulation and cloud patterns that differ significantly from those of Earth. In contrast, rocky exoplanets orbiting G-type stars, such as those targeted by HWO, are not expected to be tidally locked, and thus may exhibit more Earth-like cloud cover and distribution.
Pallé et al. (2025) presented a golden sample of rocky exoplanets around nearby M dwarfs to be characterized within a few observing nights with ANDES at the ELT. The reflected light contrast between the planet and the star is calculated using the maximum projected planet-star distance (i.e., when the planet is at $\alpha = 90°$) and assuming an Earth-like albedo of 0.3. We now have the capabilities to provide improved reflected light contrast for this golden sample of exoplanets, assuming both an Earth-like and an ocean planet scenario. In Table 5.2 we provide our estimate of the contrast for the ANDES golden sample, with

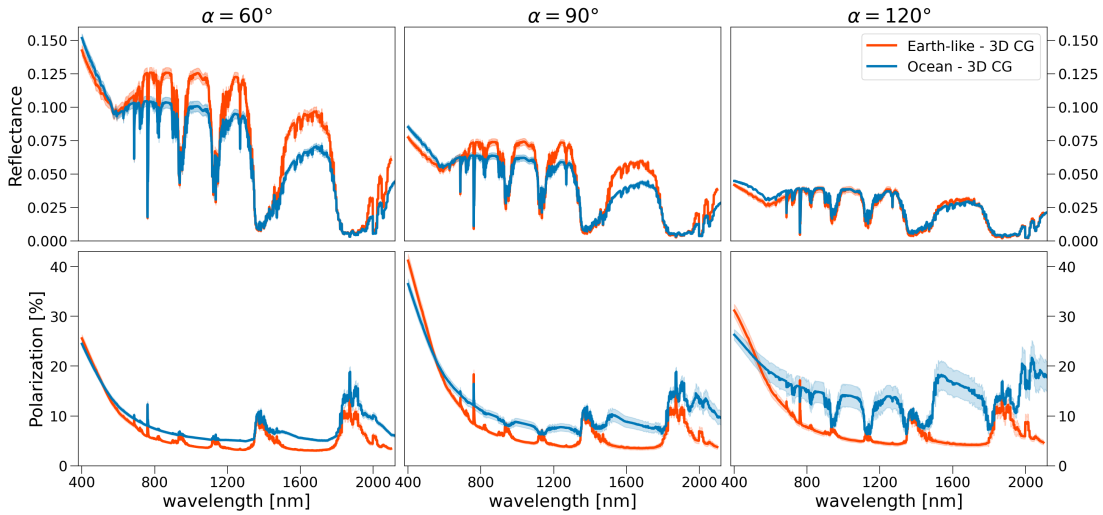

Figure 5.10: Comparison among spectra in reflected (first row) and polarized light (second row) of the ocean and Earth-like planet scenarios for a M-dwarf star, for a wavelength range from 400 to 2500 nm. Different columns refer to different phase angles (α): 60, 90, 120°.

the addition of the newly discovered Barnard b exoplanet and a potential planet located at 1 AU orbiting Alpha Cen A.

We find that our contrasts are lower than the ones obtained by Pallé et al. (2025) by a factor of two, and that the flux and polarization contrasts between Earth-like and ocean planet scenarios are remarkably similar. For example, for Proxima b with a phase angle of 90°, Pallé et al. (2025) estimated a contrast of 11.2 $\cdot 10^{-8}$, while our calculated value is 5.8 $\cdot 10^{-8}$ for an Earth-like planet. This discrepancy arises from differences in reflectance estimation. Pallé et al. (2025) used planetary albedo estimates from Turbet et al. (2016), who simulated various possible climates and atmospheric states for Proxima b using a general circulation model (GCM). However, GCMs operate at relatively coarse grid resolutions, and when coupled with a 3D radiation scheme, they simulate planets with a lower spatial resolution than our approach.

The impact of spatial resolution on radiative transfer calculations has been previously highlighted by Robinson et al. (2011), who demonstrated that a minimum resolution of 100 pixels was necessary to achieve acceptable fits to EPOXI spacecraft data of Earth as an exoplanet. In Roccetti et al. (2025a), we further explore how planetary reflectance varies with horizontal resolution. Specifically, when comparing our results to those of Turbet et al. (2016), who employed a 64 × 48 grid (closer to our zoom-out x100 case), we find that our reflected light contrasts closely match theirs. Moreover, when applying the same zoom-out x100 resolution to cloud modeling, our contrast estimates align closely with those from Pallé et al. (2025). This underscores the crucial role of horizontal resolution in obtaining accurate contrast predictions and reconciling model outputs with observations. Additionally, we find that Barnard b exhibits a higher contrast compared to the original

!

Name	C_{flux}[3D CG] ocean	C_{flux}[3D CG] Earth-like	C_{flux}[zoom-out] ocean	C_{flux}[Pallé et al. (2025)]	C_{pol}[3D CG] ocean	C_{pol}[3D CG] Earth-like
Proxima Cen b	$5.69 \cdot 10^{-8}$	$5.83 \cdot 10^{-8}$	$9.01 \cdot 10^{-8}$	$11.2 \cdot 10^{-8}$	$1.15 \cdot 10^{-8}$	$1.11 \cdot 10^{-8}$
Ross 128 b	$6.23 \cdot 10^{-8}$	$6.45 \cdot 10^{-8}$	$9.97 \cdot 10^{-8}$	$12.5 \cdot 10^{-8}$	$1.28 \cdot 10^{-8}$	$1.23 \cdot 10^{-8}$
GJ 273 b	$3.78 \cdot 10^{-8}$	$3.87 \cdot 10^{-8}$	$5.98 \cdot 10^{-8}$	$7.52 \cdot 10^{-8}$	$0.77 \cdot 10^{-8}$	$0.74 \cdot 10^{-8}$
Wolf 1061 c	$4.81 \cdot 10^{-8}$	$4.93 \cdot 10^{-8}$	$7.62 \cdot 10^{-8}$	$9.57 \cdot 10^{-8}$	$0.97 \cdot 10^{-8}$	$0.94 \cdot 10^{-8}$
GJ 682 c	$8.09 \cdot 10^{-8}$	$8.29 \cdot 10^{-8}$	$12.8 \cdot 10^{-8}$	$16.0 \cdot 10^{-8}$	$1.64 \cdot 10^{-8}$	$1.58 \cdot 10^{-8}$
Barnard b	$12.1 \cdot 10^{-8}$	$12.4 \cdot 10^{-8}$	$19.1 \cdot 10^{-8}$		$2.44 \cdot 10^{-8}$	$2.35 \cdot 10^{-8}$
Alpha Cen A	$1.17 \cdot 10^{-10}$	$1.19 \cdot 10^{-10}$	$1.85 \cdot 10^{-10}$		$0.24 \cdot 10^{-10}$	$0.23 \cdot 10^{-10}$

Table 5.2: Refined contrast estimates for rocky exoplanets. We compare the ANDES golden sample with a potential Earth-like and ocean planet around Alpha Cen A. We compare the contrast estimates from Pallé et al. (2025) with our updated calculations using the 3D Cloud Generator (3D CG) in both reflected and polarized light. Additionally, we present contrast values obtained for an ocean planet with a coarser horizontal grid resolution (zoom-out x100) for comparison.

five exoplanets in the golden sample presented in Pallé et al. (2025), reaching $1.2 \cdot 10^{-7}$. We also provide contrast estimates in polarization, which are approximately one-fifth of the flux contrast obtained with the 3D CG. While the lower contrast significantly impacts the planet's detectability and characterization, polarization offers key advantages. It is largely unaffected by telluric contamination and enhances star-planet separation, as F-, G-, and K-type stars are expected to emit almost entirely unpolarized light. Moreover, when using a coronagraph, polarimetric techniques help suppress stellar speckles, as demonstrated with ZIMPOL (Hunziker et al., 2020), which is particularly beneficial at small angular separations (Beuzit et al., 2019).

5.6 Discussion and conclusions

In this work, we build upon the improved cloud and surface modeling presented in Roccetti et al. (2025a) to assess the importance of detailed cloud and surface properties in studying rocky exoplanets. Using the 3D radiative transfer model MYSTIC, with the same horizontal and vertical resolutions, we analyze how an improved treatment of clouds and surfaces affects reflected and polarized light spectra and phase curves. Additionally, our approach enables a comparison of the insights gained from combining spectroscopy and spectropolarimetry versus intensity-alone measurements for future observations of rocky exoplanets with ANDES and PCS at the ELT, as well as the mission concept HWO.
We compare the ground-truth models presented in Roccetti et al. (2025a) on reflected and polarized light spectra and phase curves to those of homogeneous planet models and models of increasing complexity. Our analysis leads to several key findings:

1. Polarization provides stronger diagnostic capabilities than intensity alone in distinguishing between cloud-free and cloudy exoplanets. The spectral slope and polarization fraction are highly sensitive to clouds, while the cloudbow feature offers valuable

insights into cloud microphysical properties. Reflectance loses diagnostic power as phase angles increase, while polarization shows the opposite trend.

2. A uniform surface fails to reproduce polarized spectra and phase curves, as well as reflected light spectra at large phase angles. Incorporating a linear combination of wavelength-dependent surface types significantly improves agreement with ground-truth spectra. Polarization spectra are particularly sensitive to surface properties, especially at large phase angles, both in the continuum and in water absorption lines.

3. Simplified cloud treatments, such as homogeneous cloud models and single-layer clouds with averaged properties, introduce significant inaccuracies, even when attempting to mimic the effects of long observational averaging. Polarization phase curves are more sensitive to cloud properties, particularly through the cloudbow and ice crystals features, making them a crucial tool for cloud characterization.

4. Water absorption lines in polarization appear in absorption when ocean glint is present and in emission for dry planets, as previously reported by Trees & Stam (2022) for homogeneous models. This behavior persists even at high spectral resolution (R = 100 000), confirming the potential of water lines as surface diagnostics. However, simplistic cloud models can alter the appearance of water lines, potentially affecting the interpretation of ocean detection on exoplanets.

5. Using our ground-truth reflected and polarized light models for an Earth-like scenario, we calculate contrast estimates for the ANDES golden sample (Pallé et al., 2025), including Barnard b and a hypothetical Earth-like planet at 1 AU from Alpha Cen A. Compared to previous studies (Turbet et al., 2016; Pallé et al., 2025), our results show that reflected light contrast estimates are overestimated by a factor of two when using coarse horizontal resolution and simplified cloud and surface models. Additionally, we provide contrast estimates in polarization, which are approximately one-fifth of the reflected light flux contrast.

These findings strongly suggest that retrieval frameworks for reflected-light observations of rocky exoplanets should account for wavelength-dependent surface albedo properties and patchy cloud models. As shown by Wang et al. (2022), neglecting wavelength-dependent variations in surface albedo in retrieval frameworks can lead to substantially biased estimates of atmospheric and cloud properties. Notably, we demonstrate that a linear combination of just four surface types (ocean, desert, forest, and polar regions) achieves good agreement with complex ground-truth models, highlighting a practical approach for future retrievals. Additionally, our results reinforce the potential impact of polarization in exoplanet characterization. By combining polarization with intensity-only spectroscopy, we can enhance diagnostic capabilities, reduce retrieval degeneracies, and improve the characterization of surface and atmospheric properties. Additionally, finer spatial grid resolutions for radiative transfer calculations should be considered to avoid biases when comparing models with observations.

Future studies should assess the feasibility of polarized-light observations with next-generation telescopes, determining whether sufficient contrast can be achieved for robust exoplanet characterization. More broadly, our results demonstrate that homogeneous models fail to accurately represent Earth as an exoplanet, emphasizing the need for more advanced modeling approaches in the exoplanet community. Clouds play a crucial role in shaping observables, making their accurate treatment essential for reliable simulations. Both simplistic cloud treatments and low horizontal resolution in radiative transfer models significantly impact the accuracy of simulations, reinforcing the need for high-resolution, state-of-the-art models for meaningful comparisons with observations.
Ultimately, we demonstrate that polarization is a powerful tool for characterizing rocky exoplanets, distinguishing between different planetary scenarios both in the visible and NIR, and providing deeper insights into their physical and chemical properties. As future telescopes and missions become operational, incorporating these advanced modeling techniques will be crucial for interpreting observations and understanding the diversity of rocky exoplanets. Furthermore, our refined contrast estimates play a key role in instrument design and in precisely determining integration times.

5.7 Data availability

The spectra and phase curve data from this study are publicly available via a Jupyter notebook[2].

Acknowledgements

We thank the anonymous referee for the constructive feedback, which helped improve our manuscript. GR and JVS were supported by the Munich Institute for Astro-, Particle and BioPhysics (MIAPbP) which is funded by the Deutsche Forschungsgemeinschaft (DFG, German Research Foundation) under Germany´s Excellence Strategy – EXC-2094 – 390783311.

[2] https://github.com/giulia-roccetti/Earth_as_an_exoplanet_Part_II

5.8 Appendix A: Cloud averaging over long integration times

To address the effect of time-averaging the planetary signal over long observational periods, we analyze how evolving cloud patterns influence the resulting spectra and phase curves. This consideration is particularly relevant for future instruments such as ANDES and PCS at the ELT, which will require extended integration times to characterize the golden sample exoplanets. Specifically, we selected one random date from the 12 ERA5 cloud fields used in Roccetti et al. (2025a) to construct the 3D CG 1σ cloud spread model. For that date (2023.10.07) we extracted cloud fields from ERA5 at hourly intervals between 16:00 and 23:00 UT, which corresponds to the highest temporal resolution available in ERA5. Using these eight consecutive hourly cloud fields as inputs to the 3D CG model, we ran eight independent simulations. We then computed the average and 1σ spread of the resulting outputs, referring to this configuration as the time-averaged signal case. This model is compared against the standard 3D CG 1σ spread over 12 months and a uniform cloud model, as described in Sec. 5.3.2, but for an ocean surface. The impacts on the reflected spectra and phase curves are shown in Figs. 5.11 and 5.12, respectively.

We find that the time-averaged signal model (purple curve) closely resembles the 3D CG model (blue curve) across all tested spectra and phase curves. Minor discrepancies with the 3D CG arise because the time-averaged signal model incorporates cloud fields not only over the ocean, but also over different geographic regions during the 8-hour window, starting with the American continent and later extending over the Pacific ocean. These regional differences explain the observed deviations. Nevertheless, the uniform cloud model (black curve) fails to reproduce the results of the time-averaged signal model, showing significant discrepancies, particularly at large phase angles in reflectance (Fig. 5.11, top-left panel), and in polarization, both in the spectral slope at $\alpha = 90°$ (bottom-center panel) and especially at large phase angles (bottom-right panel).

In the comparison of phase curves shown in Fig. 5.12, we again observe some small deviations between the time-averaged signal model and the 3D CG model, as well as with the uniform cloud model. In reflectance, these differences are not strongly pronounced; however, we note an overestimation of the cloudbow feature with uniform clouds and an underestimation of the continuum level. In polarization (second row), the differences become much more significant. The cloudbow feature is substantially overestimated in the uniform cloud model. At wavelengths of 700 and 900 nm, the uniform model fails to reproduce the polarization continuum at phase angles greater than 90°, due to its inability to capture the specular reflection from the ocean glint, an effect that strongly polarizes light. In contrast, the time-averaged signal model still exhibits the ocean glint signature in the polarization continuum. This is because the patchy nature of the evolving cloud fields allows photons to reach the surface at all times, even under changing weather conditions. Thus, even when averaging cloud coverage over long integration times, it is important to account for realistic cloud patchiness, as it has a significant impact on both reflected and polarized light signals, effects that cannot be replicated by homogeneous cloud models.

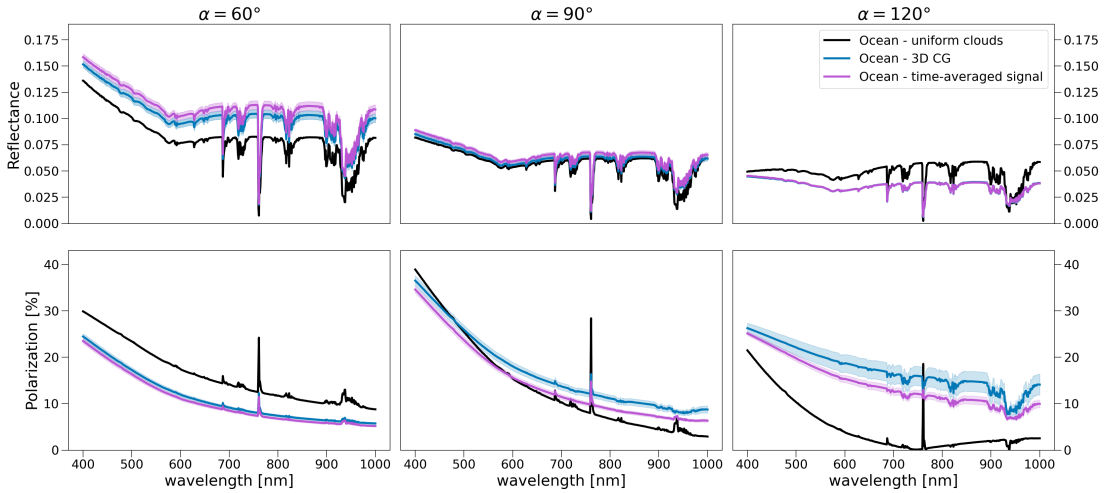

Figure 5.11: Comparison among spectra in reflected (first row) and polarized light (second row) for an ocean planet with a uniform cloud layer (black curve), the 3D CG model with 1σ variability over 12 months (blue curve), and the time-averaged signal model simulating 8 hours of integration time (purple curve). Different columns refer to different phase angles (α): 60, 90, 120°.

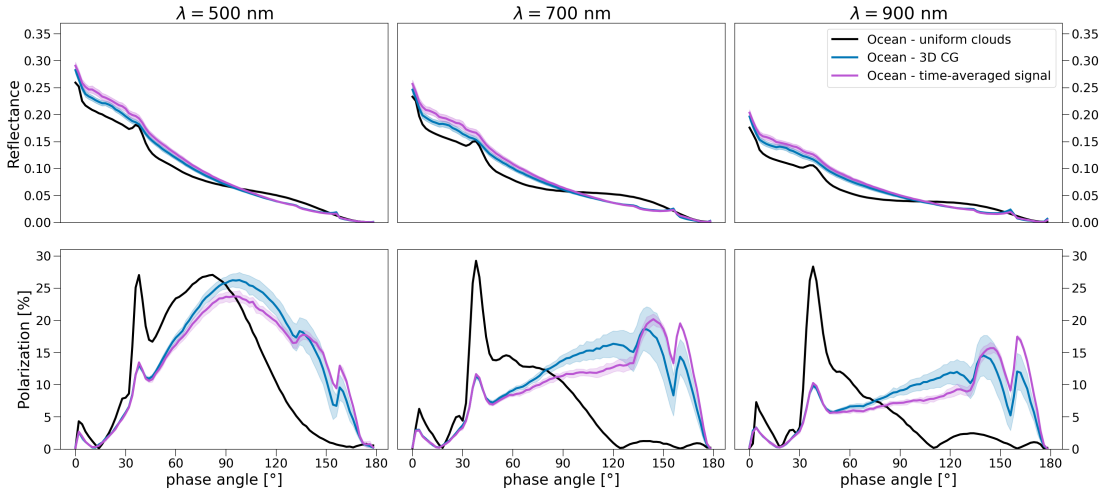

Figure 5.12: Reflected light (first row) and polarized light (second row) phase curves showing an ocean planet with a uniform cloud layer (black curve), the 3D CG model with 1σ variability over 12 months (blue curve), and the time-averaged signal model simulating 8 hours of integration time (purple curve). Different columns refer to different wavelengths (λ): 500, 700, 900 nm.

6

Planet Earth in reflected and polarized light. III. Modeling and analysis of a decade-long catalog of Earthshine observations

Published as
Roccetti et al., 2025c, Astronomy & Astrophysics, Volume 702, A262

Full authors list:
Giulia Roccetti; Michael Sterzik; Claudia Emde; Mihail Manev; Stefano Bagnulo and Julia V. Seidel.

Earthshine observations offer a unique opportunity to study Earth as an exoplanet seen from the Moon. As the Sun-Earth-Moon geometry changes, Earth can be observed as a spatially unresolved exoplanet at different phase angles, providing important context for future observations of Earth-like exoplanets. Here, we present a catalog of Earthshine polarization spectra obtained with FORS2 on the VLT, covering diverse scenes, surface conditions, cloud properties, and weather patterns for over a decade. For the first time, we model this extensive dataset in detail using a homogeneous modeling framework. Previous efforts to model some of these spectra struggled to reproduce the observed polarization continuum, even with advanced 3D radiative transfer models incorporating satellite-derived surface and atmospheric data. We improve upon this with a state-of-the-art 3D model that includes subgrid cloud variability, wavelength-dependent surface albedo maps, and an accurate treatment of ocean glint. Our simulations successfully reproduce most observed spectra to a much higher precision than previously possible. Additionally, our statistical analysis reveals that the spectral slope in the visible can distinguish between ocean and mixed surfaces in both reflected and polarized light, which is not possible using broadband filters alone. Polarized light at large phase angles, beyond the Rayleigh scattering regime, is particularly effective in differentiating oceans from land, unlike reflected light. While the vegetation red edge (VRE) is more pronounced in reflectance, it remains detectable in polarization. We also identify correlations between cloud optical thickness and the polarized spectral slope, and between cloud cover and broadband B–R differences in reflected light, demonstrating the diagnostic power of these observations. This catalog and its modeling highlight the potential of polarization for characterizing Earth-like exoplanets. From polarization alone, we can infer oceans, vegetation, and an active water cycle, key indicators of a habitable planet.

6.1 Introduction

The search for small, habitable exoplanets is a primary objective of upcoming observatories such as the Extremely Large Telescope (ELT) and the proposed mission concept Habitable Worlds Observatory (HWO). To fully interpret future data from these missions, we must significantly improve our ability to model observations. Earth remains the only known example of a habitable planet, and it provides a unique benchmark to address a fundamental question: how unique is our planet? While not all habitable exoplanets will closely resemble Earth, many are expected to share key features, such as oceans, clouds, and surface heterogeneities. Consequently, studying Earth as an exoplanet is vital for developing observational strategies and interpretative tools. A range of techniques have been used to examine Earth's disk-integrated properties, offering valuable insight for future photometric and spectroscopic observations of Earth-like exoplanets (Robinson & Reinhard, 2018).
The first effort to observe Earth as a planetary body using a space-based platform was carried out during the Galileo spacecraft's flybys of Earth (Johnson et al., 1992). Spatially resolved imagery and spectra revealed important atmospheric and surface characteristics. In particular, Sagan et al. (1993) identified specular reflection indicative of surface liquid water, high column densities of O_2 in disequilibrium with CH_4, and the vegetation red edge (VRE), a sharp increase in reflectivity beyond 700 nm associated with chlorophyll. These findings pointed to a biologically active planet with surface diversity and an atmosphere influenced by life.
When observing exoplanets, however, we cannot resolve them spatially. Instead, we receive light from the entire planet averaged into a single pixel. In such cases, the viewing geometry plays a critical role in shaping the reflected light signal. For instance, regions near the terminator contribute less to the disk-integrated signal, and features such as specular reflection depend on the directional reflectance of the surface. Properly accounting for geometry is essential to extracting accurate information from reflected light observations, a crucial aspect of the ELT.
Since the mid-20th century, Earth has been continuously monitored by a growing number of satellites. By stitching together high-resolution satellite imagery, it is possible to build datasets of disk-integrated Earth observations (Hearty et al., 2009), offering broad spectral, temporal, and spatial coverage. However, this approach does not replicate the conditions of typical exoplanet observations due to temporal gaps influenced by varying weather patterns and constraints in viewing geometry, especially for low Earth orbit satellites.
The ideal approach to mimic direct observations of the Earth as an exoplanet would be to acquire photometry and spectroscopic measurements for a truly distant Earth, from distances beyond low-Earth orbit or geostationary satellites. For example, the EPOXI mission captured disk-integrated Earth spectra, revealing key spectral features and enabling the mapping of unresolved planetary surfaces (Robinson et al., 2011). Observations from NASA's LCROSS mission helped quantify the effects of ocean glint and ozone absorption on Earth's disk-integrated reflectance spectra at various phase angles (i.e., the star-planet-observer angle) (Robinson et al., 2014). Additionally, NASA's DSCOVR mission, located

at the Earth-Sun L1 Lagrange point, provides continuous imaging of Earth's fully illuminated hemisphere that can be used to obtain disk-integrated reflected light spectra (Kofman et al., 2024). However, these measurements lack the phase angle diversity needed to replicate typical exoplanet observation conditions. Furthermore, most spacecraft datasets focus on photometry rather than spectroscopy, and disk-integrated observations beyond quadrature remain limited, with LCROSS being a rare exception (Robinson & Reinhard, 2018).

An alternative method to study Earth as an exoplanet is through Earthshine, which is sunlight scattered by Earth's dayside and reflected off the darker portion of the visible Moon. The Moon acts as a diffuse reflector, integrating light from the illuminated hemisphere of Earth. As early as the Renaissance, Leonardo Da Vinci noted that the faint glow of the darker portion of the visible Moon on clear nights was due to light reflected from Earth (Da Vinci, 1510), and named it Earthshine. Later, Galileo Galilei was the first to observe Earthshine with a telescope and to explain that different regions of Earth reflected light differently, emphasizing the role of planetary albedo (Galilei, 1632). The first quantitative measurements of Earthshine were carried out by Dubois (1947), who presented Earth's phase curve and demonstrated that broadband reflectivity varies significantly with phase angle due to cloud variability.

Modern Earthshine studies have progressed from photometry to spectroscopy, allowing for detailed characterization of Earth's disk-integrated spectrum (Goode et al., 2001). These studies have revealed daily to decadal variability in Earth's reflectivity (Pallé et al., 2003, 2009a, 2016), including changes in the VRE linked to cloud cover and surface vegetation (Arnold et al., 2002; Seager et al., 2005; Montañés-Rodríguez et al., 2006). Spectral features associated with habitability and life, such as H_2O, O_2, and CH_4, have been identified in Earthshine spectra spanning 0.7–2.4 μm (Turnbull et al., 2006).

Despite its advantages, Earthshine observations are not without challenges. The Moon is not a perfect Lambertian reflector, and the signal must pass through Earth's atmosphere twice, introducing telluric contamination. One way to mitigate this is through Earthshine observations using spectropolarimetry, thus obtaining the fractional polarization of Earthshine as a function of wavelength. Sterzik et al. (2012) obtained the first such observations that compare two different Earth's scenes: one with the illuminated side over the Pacific Ocean, and the other featuring a mixture of land and ocean surfaces. With these observations, changes in Earth's cloudiness, the presence of an ocean, and even the VRE, a biosignature caused by chlorophyll, were detected. Independent measurements of Earthshine obtained from different geographical regions of the world were conducted by Takahashi et al. (2013) and Bazzon et al. (2013), showing overall good agreement with the initial polarization spectra presented in Sterzik et al. (2012). Miles-Páez et al. (2014) further extended the wavelength coverage of Earthshine polarimetric measurements into the near-infrared (NIR), demonstrating sensitivity to molecular absorption lines. Sterzik et al. (2019) expanded the phase angle coverage of Earthshine observations, presenting 33 spectra obtained during an observational campaign and constructing polarized phase curves of Earth as an exoplanet in the visible (VIS) and NIR. For Earthshine, the phase angle changes with the relative positions of the Sun, Earth, and Moon. As a final ex-

tension to phase angle coverage, Sterzik et al. (2020) observed Earthshine at small phase angles (around 30°–40°) to probe the cloudbow feature, which depends on the properties of cloud droplets. This led to the first detection of cloudbow features in the disk-integrated Earth. Sterzik et al. (2020) used this feature to retrieve the refractive index and sizes of cloud droplets on Earth. This approach was proven highly successful on Venus, where disk-integrated observations at small phase angles revealed that the planet's thick clouds are composed of sulfuric acid with particle sizes of about 2 μm (Hansen & Travis, 1974). Moreover, Takahashi et al. (2021) have further extended the phase coverage of Earthshine observations.

In parallel with observational advances, modeling efforts have also progressed. Early models by Stam (2008) considered horizontally homogeneous planets in plane-parallel atmospheres. These were extended by Karalidi & Stam (2012) to include surface and cloud heterogeneities, with further work exploring the cloudbow as a diagnostic of liquid water in Earth-like atmospheres (Karalidi et al., 2012). Monte Carlo radiative transfer models capable of simulating both intensity and polarization were developed by García Muñoz (2015) and Emde et al. (2017), who demonstrated the sensitivity of polarization to clouds, aerosols, and surface properties. Additionally, Emde et al. (2017) demonstrated that light reflected by ocean surfaces in the sunglint region causes high degrees of polarization, consistent with the findings of Sterzik et al. (2012). Recent models by Trees & Stam (2022) predicted ocean glint signatures in polarization, including distinct absorption dips across the 950 nm water band. However, Gordon et al. (2023) found that matching observed polarization spectra from Miles-Páez et al. (2014) remains challenging, in part due to oversimplified surface models that neglect the ocean glint. Their follow-up work (Goodis Gordon et al., 2025) explored Earth's polarized appearance across geological epochs, showing that polarization offers greater discriminative power for cloud and haze properties than intensity-only observations.

In this paper, we present the first extensive modeling effort of a large catalog of Earthshine observations in polarization. This constitutes a critical step toward benchmarking model performance and understanding what Earth would look like as an unresolved exoplanet. Our modeling framework, based on Roccetti et al. (2025a), allowed us to simulate each Earthshine spectrum using cloud and surface data from the exact time of the observations. We also improve upon the data reduction and analysis techniques from Sterzik et al. (2019, 2020), creating a higher-quality, more uniform dataset. Our focus is on the spectral continuum and on features such as the ocean glint, the VRE, and cloud properties. Finally, we assessed the diagnostic potential of polarization relative to intensity-only observations and explored what could be learned about Earth when seen as a distant, spatially unresolved planet.

6.2 Earthshine observations

Our catalog of Earthshine polarization observations consists of 53 spectra covering phase angles from 37° to 136°, previously published in Sterzik et al. (2019) and Sterzik et al.

(2020). All observations were obtained using the FORS2 instrument (Appenzeller et al., 1998), a low-resolution spectrograph with polarimetric optics, mounted on the Antu telescope at the ESO Very Large Telescope (VLT) at Cerro Paranal, Chile. Table 6.9 reports the date, phase angle, and observational configurations of all Earthshine observations from Sterzik et al. (2012), Sterzik et al. (2019), and Sterzik et al. (2020).
FORS2 is equipped with Wollaston prisms and a rotating retarder waveplate, allowing the measurement of the wavelength-dependent reduced Stokes parameters $P_Q = Q/I$ and $P_U = U/I$, from which the total fractional linear polarization is calculated as:

$$P = \sqrt{P_Q^2 + P_U^2}. \tag{6.1}$$

The spectra were collected using two different grisms:

- The 300V grism was used for 45 spectra, covering the 420-920 nm range with a spectral resolution of ≈ 220 using a 2slit.
- The 600I grism was used for the remaining 8 spectra, covering 670-930 nm with a spectral resolution of 750.

Observations targeted the darker portion of the visible Moon, with the FORS2 detector oriented east-west along the lunar limb. The first detector chip contains five 22 long slitlets positioned across the lunar surface. A 4 gap separates it from the second chip, which contains four slitlets pointed at the empty sky for background subtraction. The lunar limb was consistently positioned in the gap between the two detector chips.
Polarimetric data were acquired using the beam-swapping technique (Bagnulo et al., 2009), which reduces instrumental systematics typical of dual-beam polarimetry. This was achieved by acquiring exposures at 16 retarder waveplate angles, from 0° to 337.5° in 22.5° increments.
Additionally, we applied a correction for lunar depolarization. The lunar depolarization factor $\epsilon(\lambda)$ is defined as:

$$\epsilon(\lambda) = \frac{P_{\text{out}}(\lambda)}{P_{\text{in}}(\lambda)}, \tag{6.2}$$

where $P_{\text{in}}(\lambda)$ is the fractional polarization of light incident on the Moon, and $P_{\text{out}}(\lambda)$ is the polarization of the reflected Earthshine.
Following Bazzon et al. (2013), we compute ϵ using the lunar albedo at the observation site, as a function of wavelength. The polarization efficiency $\log \epsilon$ depends on both the lunar albedo at 603 nm ($\log a_{603}$) and the wavelength ($\log \lambda$), and is given by:

$$\log \epsilon(\lambda, a_{603}) = -0.61 \log a_{603} - 0.291 \log \lambda\,[\mu\text{m}] - 0.955. \tag{6.3}$$

As in Sterzik et al. (2019) and Sterzik et al. (2020), we adopted this method and used their a_{603} values, extracted by comparison with the lunar albedo maps of Velikodsky et al. (2011).
For details on data acquisition and reduction, including preprocessing, flat-fielding, and

background subtraction, we refer to Sterzik et al. (2019). In particular, flat-fielding is essential for Earthshine spectropolarimetry since the sky background must be interpolated on chip 2 and linearly extrapolated to chip 1 to be subtracted from the Earthshine signal. This step relies on the assumption that Moonshine intensity decreases linearly with distance from the terminator. However, in practice, we observed an anti-correlation between intensity and fractional polarization along the slit. To address this, we developed a new procedure to average the five slitlets on chip 1 and improve the quality of the resulting polarization spectra. To do this, we searched for the best functional form to fit the spectra (and each slitlet), excluding the absorption lines. Looking at the spectra in $\log(P)$–$\log(\lambda)$ space, we determined that the spectra follow two power laws with a kink shifting its wavelength for each epoch. We then derived the following functional form:

$$P(\lambda) = P_1 \left(\frac{\lambda}{\lambda_1}\right)^{\gamma} \cdot (1 - s(\lambda)) + P_2 \left(\frac{\lambda}{\lambda_2}\right)^{\beta} \cdot s(\lambda), \tag{6.4}$$

where γ and β are the fitted slopes in the VIS and NIR, λ is the wavelength, $\lambda_1 = 600$ nm and $\lambda_2 = 800$ nm are fixed to facilitate the fit and P_1 and P_2 are left as free parameters. The $s(\lambda)$ function is a sigmoid defined as

$$s(\lambda) = \frac{1}{1 + e^{-k(\lambda - \lambda_0)}}, \tag{6.5}$$

with λ_0 representing the position of the kink and k representing the strength of the transition. Both λ_0 and k are also free parameters of the fit. These two power laws weighted by a sigmoid function ensure the fitting of all spectra, together with extracting their spectral slopes.
The improved slitlet-averaging procedure follows these steps:

1. We cut the spectra to the 450-900 nm range for the 300V grism and 680–920 nm for the 600I grism. Each slitlet is then corrected for lunar depolarization, as explained below.

2. Slitlets showing unphysical behavior, such as negative polarization values, extreme red-end increases, or spurious bumps, are removed. This is particularly necessary for the H and G epochs, which correspond to the smallest and largest phase angles, respectively (see Table 6.9), and are the most problematic.

3. We calculated the standard deviation across the remaining slitlets (typically five), averaged over all wavelengths. If the standard deviation was below 1%, the data are deemed high quality, and we computed the average over all slitlets. This is the case for most spectra at phase angles smaller than quadrature (e.g., epochs E, I, J, K).

4. For the remaining spectra, we selected the slitlet with the lowest noise, computed as the random mean squared error (RMSE) compared to the fit, as reference (best slitlet). We then averaged only those slitlets that lie within 1σ of the best slitlet

in VIS slope (γ), NIR slope (β), and average polarization distance. This excluded slitlets with inconsistent spectral shapes or anomalous polarization levels, which may indicate contamination. Typically, the last slitlet (closest to the limb) was found to be the least noisy and it was assumed as the best slitlet. At high phase angles (e.g., G epochs), this process often resulted in only the fifth slitlet being retained.

Earthshine observations become increasingly challenging with larger phase angles, particularly beyond quadrature, as the Moon's dayside terminator approaches the observational field, increasing Moonshine contamination. Observations above $\alpha \approx 130°$–$140°$ from the ground become nearly unfeasible. However, these geometries are crucial to studying the ocean glint feature. Our catalog includes three such epochs (G.7, G.8, and G.9, all with $\alpha > 135°$). Due to their particularly high noise and uncertainty, we treated them separately: for G.7, only slitlet 4 was used, while for G.8 and G.9, we averaged slitlets 3, 4, and 5.
A similar issue arises at very small phase angles ($\alpha < 40°$), when the thin crescent Moon is visible only briefly at twilight, resulting in short observing windows and high airmass. These conditions are also scientifically valuable, as they reveal the cloudbow feature, which provides key information on cloud microphysics. Epoch H.1, our lowest phase angle spectrum ($\alpha = 37°$), was carefully analyzed. We averaged slitlets 2 and 5 to obtain a consistent result from components with different spectral slopes.
In contrast, we excluded the J.1 and K.1 epochs from our updated catalog. These spectra, previously identified as uncertain in Sterzik et al. (2020), were acquired at very low phase angles (33° and 35°, respectively) during brief twilight windows, which prevented the completion of all 16 retarder positions. Only two positions were recorded, resulting in significant systematic errors that rendered our slitlet averaging procedure inapplicable.

6.3 3D radiative transfer simulations

For all observational epochs listed in Table 6.9, we performed 3D radiative transfer simulations using surface and atmospheric conditions corresponding precisely to the time of observation. To achieve this, we employed the Monte Carlo code MYSTIC (Monte Carlo code for the phYsically correct Tracing of photons in Cloudy atmospheres; (Mayer, 2009)), which is part of the libRadtran software package (Mayer & Kylling, 2005a; Emde et al., 2016). MYSTIC supports 3D Earth-like atmospheres, includes full Stokes vector calculations to account for polarization, and allows for 2D inhomogeneous surface representations. A modeling setup for using MYSTIC to simulate Earthshine observations was first introduced by Emde et al. (2017). However, it has been substantially improved in a previous paper of this series (Roccetti et al., 2025a), which presented a more sophisticated framework for simulating both cloud and surface properties. In particular, cloud modeling now incorporates a 3D Cloud Generator algorithm that captures sub-grid cloud variability and inhomogeneities, using input from the European Centre for Medium-Range Weather Forecasts (ECMWF) ReAnalysis fifth-generation product (ERA5) cloud data.

Regarding surface albedo treatment, oceans are modeled as specular reflectors using a BPDF approach for reflected light and polarized light. Land surfaces are treated as Lambertian reflectors with albedo values varying with wavelength, based on the hyperspectral albedo maps presented in Roccetti et al. (2024). These maps combine MODIS satellite data with a comprehensive set of in-situ and laboratory spectra of various soils and vegetation types, enabling wavelength-dependent albedo modeling, which is crucial for studying features such as the VRE.
In Roccetti et al. (2025a), we provide a detailed analysis of how the improved treatments of clouds and surface properties affect the spectra and phase curves of an ocean and an Earth-like exoplanet. In Roccetti et al. (2025b), we evaluate how these more realistic and detailed models compare to simulations that use spatially averaged homogeneous conditions and simplified representations of cloud and surface features.
For the simulations, the ERA5 cloud properties are rounded to the nearest full hour relative to the central time of each observation. The Sun and Moon coordinates used to replicate the viewing geometry are taken at the midpoint between the start and end times of each observational epoch listed in Sterzik et al. (2019) and Sterzik et al. (2020), based on data from the Earth-Moon viewer [1].

6.4 Comparison between observations and simulations

In Appendix 6.9, we present the comparison between the full catalog of Earthshine observations and their corresponding simulations. In addition to the spectra, we simulated an image of Earth for the same time and viewing geometry as the observation, using the actual cloud properties from ERA5 at the time of the observations, the Sun–Earth–Moon orientation, and wavelength-dependent albedo maps from HAMSTER on the specific observation date. The simulation of these images follows the method described in Roccetti et al. (2025a). In addition to the image, we present the simulated reflected light spectra in units of reflectance, defined as $A_g \cdot g(\alpha)$, as well as a comparison between the simulated and observed polarized spectra, expressed in percent polarization. All comparisons are displayed in Figs. 6.6 to 6.10. The simulations span the 400–1000 nm spectral range and are adjusted in resolution to match the specific setup used during each observation. The axes for reflectance and polarization are scaled to match the extrema of observations and simulations independently, in order to enhance the visual clarity of the comparisons.
Each observational spectrum is color-coded to indicate its viewing geometry. Spectra shown in turquoise correspond to what we define as the Pacific configuration, as described in Sterzik et al. (2019), which represents Earthshine observations taken at the beginning of the night from Paranal with the Pacific Ocean as the dominating scene and very little land visible, thus resembling the appearance of an ocean planet. Spectra shown in red correspond to the Atlantic configuration, which includes a mixture of land and ocean, with parts of the Atlantic Ocean, Africa, Europe, South America, or the Middle East in view.

[1] https://www.fourmilab.ch/earthview/

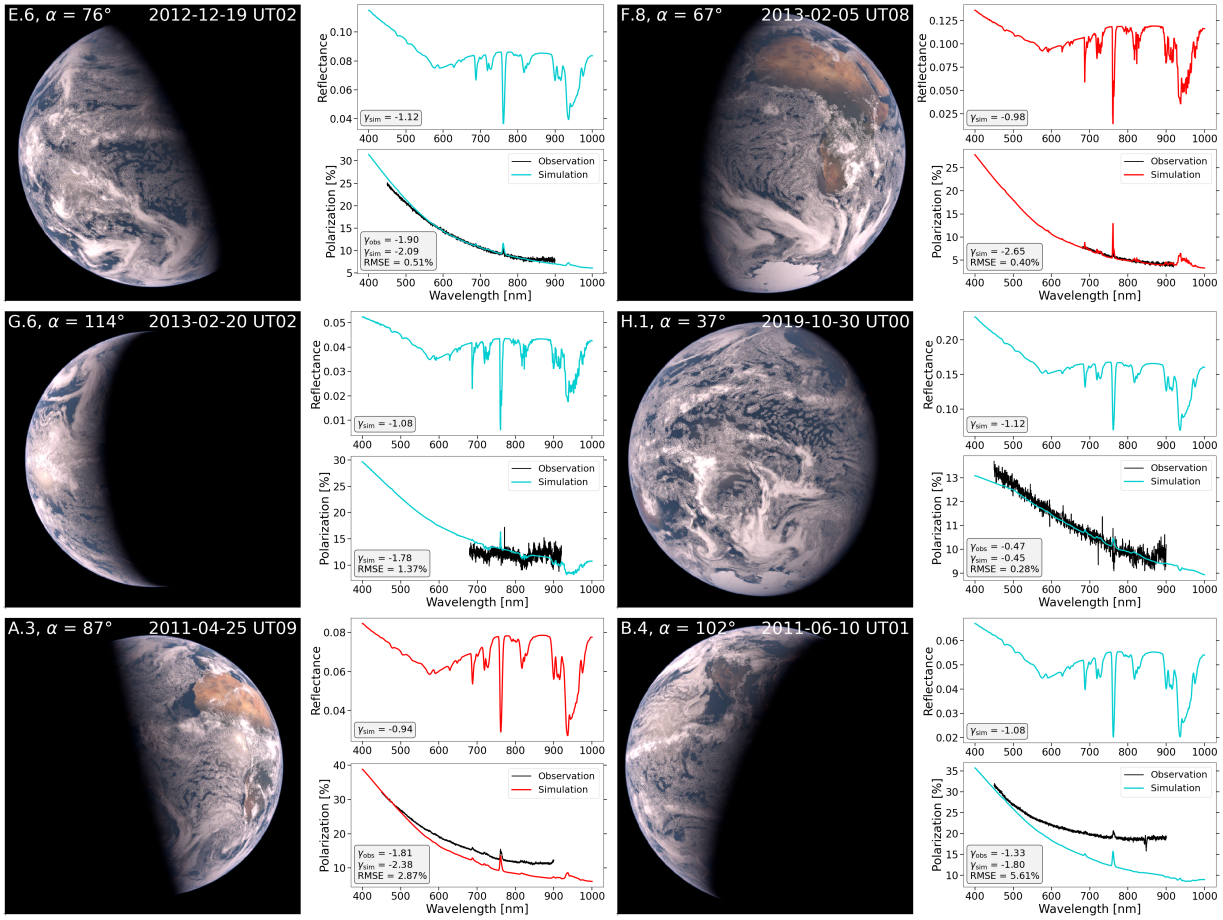

Figure 6.1: Selected examples of observed polarized Earthshine spectra, along with corresponding simulations of reflected and polarized light, as presented in Appendix 6.10. For each spectrum, we include a simulated observation image, fit the power-law slopes γ, and report the RMSE between simulations and observations.

For each epoch, we also fit a double power-law function as described in Section 6.2, reporting the power-law exponent in the visible range (400–700 nm) for both the simulated reflected and polarized light, and for the observed polarized spectra taken with the 300V grism, as the 600I grism covers only wavelengths longer than 680 nm. Additionally, we calculate the RMSE of each observed and simulated polarization spectrum within the spectral range where data is available to assess how well the simulations reproduce the observations. In Fig. 6.1, we present a representative selection of the catalog epochs to illustrate our sample. Throughout the paper, spectra shown in red correspond to an Atlantic scenario, while those in cyan correspond to a Pacific scenario. In the top left panel, we show epoch E.6, which is a Pacific scenario with nearly no land in view (only a small portion of Antarctica), observed at a phase angle $\alpha = 76°$ with grism 300V, covering the 450–900 nm range (note that the spectral edges are cut; see Section 6.2). This epoch shows very strong agreement with the simulation, as is typical for Pacific (ocean planet) configurations at phase angles

smaller than quadrature. In the top right panel, we show an Atlantic (mixed) scenario also at a phase angle smaller than quadrature, observed with grism 600I. The 600I grism does not include the shorter visible wavelengths, where Rayleigh scattering dominates, and has a higher spectral resolution than the 300V; thus, the simulation was adjusted in its spectral resolution. In the second row, we present two of the most challenging spectra to model: epoch G.6, with a very high phase angle, and epoch H.1, with the smallest phase angle in our sample. Both spectra are noisier than previous examples. This is due to increased contamination from Moonshine at phase angles beyond quadrature and to the challenging lunar position at small phase angles. Despite these challenges, both spectra show good agreement between observations and simulations in polarization, as confirmed by the RMSE and slope comparisons.

In the final row, we present epochs A.3 and B.4, which were previously discussed in Sterzik et al. (2012). These spectra, and all spectra from epochs A, B, and C, exhibit significantly flatter spectral slopes compared to observations obtained in later years. Even though we cannot reproduce the spectral slopes of A.1 to C.2, we achieve a clear improvement in matching the observations compared to earlier attempts using the models of Stam (2008) and Emde et al. (2017). This improvement arises from two key factors: the updated slitlet-averaging procedure, particularly important for phase angles beyond quadrature, and the improved modeling of cloud and surface properties as introduced in Roccetti et al. (2025a). Previous modeling efforts by Emde et al. (2017) and Gordon et al. (2023) attempted to simulate Earthshine polarization spectra. The former used MYSTIC as we do, while the latter used the VSTAR and DAP models. Both focused on a limited number of observations: Emde et al. (2017) examined epochs A.3 and B.4 from Sterzik et al. (2012), while Gordon et al. (2023) analyzed a single spectrum from Miles-Páez et al. (2014) extending into the NIR up to 2500 nm. In both cases, the models failed to match the observed slope in visible polarization. Moreover, Gordon et al. (2023) could not reproduce the polarization continuum, largely due to the treatment of the ocean as a dark Lambertian surface. However, the importance of the ocean glint effect had already been demonstrated by Emde et al. (2017), who showed its strong impact in disk-integrated Earthshine polarization observations at large phase angles. In contrast, our simulations achieve an excellent match for all spectra from epochs E.1 to K.3, something never accomplished before. High phase angle observations, previously considered particularly difficult due to the influence of ocean glint, now show strong agreement with simulations. This success is largely due to the implementation of the 3D Cloud Generator developed by Roccetti et al. (2025a), which captures cloud subgrid variability and heterogeneity beyond the already detailed ERA5 cloud data. For example, at a phase angle of $\alpha = 120°$, the inclusion of the 3D Cloud Generator significantly impacts the polarization spectral slope and enhances the continuum, which allows us to match the observed Earthshine spectra.

We are also now able to accurately simulate spectra from Atlantic (mixed) viewing geometries, which had not been successfully reproduced in the past. This is made possible by the combination of a BPDF for oceans and a Lambertian model for land surfaces, as well as by using wavelength-dependent albedo maps from HAMSTER (Roccetti et al., 2024). These maps account for realistic mixtures of soil and vegetation types and result in a significantly

lower modeled albedo for forested and desert regions compared to those used in Gordon et al. (2023) and Kofman et al. (2024). As shown in Roccetti et al. (2025a), this refinement is essential for matching the observed continuum.
Regarding the earlier observational epochs from A.1 to C.2, which we are unable to match, we explored several possible explanations. Notably, the B epochs, despite corresponding to Pacific (ocean) configurations, appear much flatter than later Pacific observations taken at similar phase angles (e.g., G.1 to G.4). A similar pattern is seen for the Atlantic (mixed) configurations in the A and C epochs, which differ significantly in both slope and polarization level from the F epochs at a similar phase angle. While these observations followed the same acquisition and reduction techniques, one notable difference is the use of screen flats for calibration instead of sky flats. However, Sterzik et al. (2019) found no significant difference when comparing screen and sky flat calibrations in the E epochs. Additionally, we are not aware of any major changes in the FORS2 instrument or its calibration procedures between 2011 and the following years. For an alternative explanation, we investigated whether any global atmospheric event could have affected the scattering properties of Earth's atmosphere during this period, but we found no evidence of major volcanic eruptions. We also checked whether this flattening of the spectra could depend on the sky condition over Paranal. A strong El Niño event occurred in 2011, which is known to influence observing conditions over Paranal, particularly in terms of turbulence, sunset temperature anomalies, and precipitable water vapor (Seidel et al., 2023). El Niño's effects can persist over time, potentially affecting observations up to epoch C.2 in October 2012. While 2019 was also an El Niño year, its impact was weaker, and all observations from that year were made at small to moderate phase angles. Within epochs A.1 to C.2, a trend toward flatter spectra with increasing phase angle is also evident. This is consistent with independent observations obtained in 2011 by Takahashi et al. (2013) and Bazzon et al. (2013), from Japan and Switzerland, respectively, who also reported a flattening of the spectra at large phase angles, as already discussed in Sterzik et al. (2019).
Because we have no definitive explanation for the behavior of these early spectra and find them problematic, we show them in the subsequent statistical analysis (Section 6.5) for completeness, but exclude them from the actual calculations. In the next plots, they are displayed with transparent colors to clearly distinguish them from the rest of the sample used to determine disk-integrated properties of Earth.

6.5 Population studies

Building on our extensive catalog of Earthshine observations and corresponding simulations in both reflectance and polarization, we now explore whether significant correlations can be identified between Earth's cloud and surface properties and the observed and simulated spectral features. To this end, we focus exclusively on the spectral continuum of the observations and test several diagnostic metrics: the spectral slope in the visible (VIS) range, a broadband color difference between the B and R filters (as defined by the typical Johnson filters), and the continuum value at a single reference wavelength. For the B filter

we use the spectral range from 435 to 455 nm, while for the R filter from 645 to 665 nm. Furthermore, to evaluate the detectability of the VRE, we compute two vegetation indices: the Normalized Difference Vegetation Index (NDVI) (Tinetti et al., 2006b) and the Polarized Difference Vegetation Index (PDVI) (Sterzik et al., 2019). In all subsequent plots, simulated data points are marked with stars, while observed polarization measurements are shown as dots. The different Earth viewing geometries are color-coded: Pacific (ocean-dominated) configurations in turquoise, and Atlantic (mixed land-ocean) configurations in red.

Error bars on the observational data are omitted from the figures, as they are smaller than the size of the plotted data points. The uncertainty associated with individual slitlets accounts for both measurement errors and the contribution from lunar depolarization, and is propagated through the slitlet averaging procedure. Errors for each spectrum and calculated quantity are provided in the public database (see Sec. 6.8). For the simulations, error bars are similarly small, within the thickness of the plotted points. A more detailed discussion of the simulation uncertainties is available in Roccetti et al. (2025a).

Although a comparison between observed and simulated reflectance spectra would be informative, well-calibrated reflectance data are not available for this Earthshine catalog. Nevertheless, as discussed in Roccetti et al. (2025a,b), polarization spectra and phase curves are more sensitive to surface and cloud properties. For example, the implementation of the 3D Cloud Generator (3D CG) affects the spectral slope in polarization but causes minimal changes in reflectance. In reflectance, the main effect is a shift in the continuum level, which requires high-precision calibration, unavailable in this dataset.

6.5.1 Phase curves to distinguish between an ocean and mixed surface scenario

In Fig. 6.2, we present the phase curves from both our observations and simulations as a function of different metrics: the spectral slope γ in the visible (first row), the B–R broadband filter difference (second row), and the reflectance and polarization at single wavelengths (500 and 700 nm; third and fourth rows, respectively). Comparing the diagnostic power of these approaches helps to identify the most effective observational strategies for retrieving information about different surface viewing geometries of the Earth seen as an exoplanet and to understand the sensitivity of different metrics to the various surface scenarios.

Analyzing the spectral slope in the VIS reflectance, we find that the Atlantic (mixed surface) configurations, indicated by red stars, tend to cluster with shallower slopes compared to the Pacific (ocean-dominated) geometries. This trend holds until phase angles exceed 130°, where the reflectance spectra flatten due to the strong contribution of ocean glint. A clear distinction between ocean and mixed surface compositions is evident in the spectral slopes at phase angles smaller than quadrature. Beyond quadrature, the differences become less significant. It is important to note that we simulate 53 specific geometries corresponding to the observations, and Earth does not perfectly represent a pure ocean or

land surface planet. In particular, for the Atlantic case, the land–ocean fraction plays a key role in shaping the spectral slope, especially depending on whether the sunglint falls over ocean or land.

A similar but opposite trend appears in polarization: Atlantic (mixed) configurations display steeper polarization slopes than Pacific (ocean) ones at comparable phase angles. This difference is more pronounced at phase angles below quadrature than in reflectance. At larger phase angles over the Pacific, the ocean glint substantially enhances polarization, resulting in a flatter slope. In this polarization panel (top right in Fig. 6.2), both the simulations (stars) and Earthshine observations (dots) are included, with observed slopes broadly matching the simulated values. As explained in Section 6.4, we consistently exclude the epochs from A.1 to C.2 in subsequent analyses, and these epochs are shown in opaque colors.

In the second row of Fig. 6.2, we examine the sensitivity of the B-R broadband index to distinguish between Pacific and Atlantic configurations. In reflectance, the B–R value tends to be smaller for Atlantic cases relative to Pacific ones at the same phase angle, though the clustering is less distinct than for the spectral slope. A similar trend is observed in polarization, where Atlantic epochs exhibit larger B–R values than Pacific ones, though again without clear separation between the two groups.

The third and fourth rows show the phase curves of reflectance and polarization at single wavelengths: 500 and 700 nm. For these plots, we overlay the set of reference phase curves for an ocean (Pacific) and a mixed (Atlantic) surface, as presented in Roccetti et al. (2025a,b), corresponding to the 3D CG EXP-RAN x3 scenario. While Earth never fully resembles a pure ocean planet and its surface composition varies with viewing geometry, these models guide interpretation and highlight existing trends. The shaded regions indicate the 1σ spread due to cloud variability, calculated from averaging phase curves with different cloud fields from different days of the year (Roccetti et al., 2025a). Comparing the simulations for each Earthshine epoch (stars) with the model phase curves allows us to assess how representative these models are across the Earthshine catalog.

All reflectance simulations fall within the 1σ cloud variability range, while some polarization simulations extend beyond it. This suggests that while disk-integrated reflectance is relatively well constrained, polarization is more complex to model, but also richer in diagnostic information about surface, atmospheric, and cloud characteristics.

Reflectance phase curves at 500 and 700 nm show similar behavior, with higher values at 500 nm due to Rayleigh scattering. However, the differences between the two model phase curves fall within the cloud variability, making it difficult to distinguish surface properties from reflectance at a single wavelength in the VIS. At 500 nm in polarization, the phase curves for the ocean and mixed cases are also similar and within the cloud variability spread. Observed and simulated Atlantic epochs are slightly below the reference model predictions, occasionally falling outside the 1σ range. However, at 700 nm, beyond the Rayleigh scattering regime, we observe a pronounced separation between the ocean and mixed model phase curves, far exceeding the 1σ cloud variability. This diagnostic power was previously highlighted in Roccetti et al. (2025a). Overlaying the individual simulations and observations, we find broad agreement with this trend, reinforcing the value of polariza-

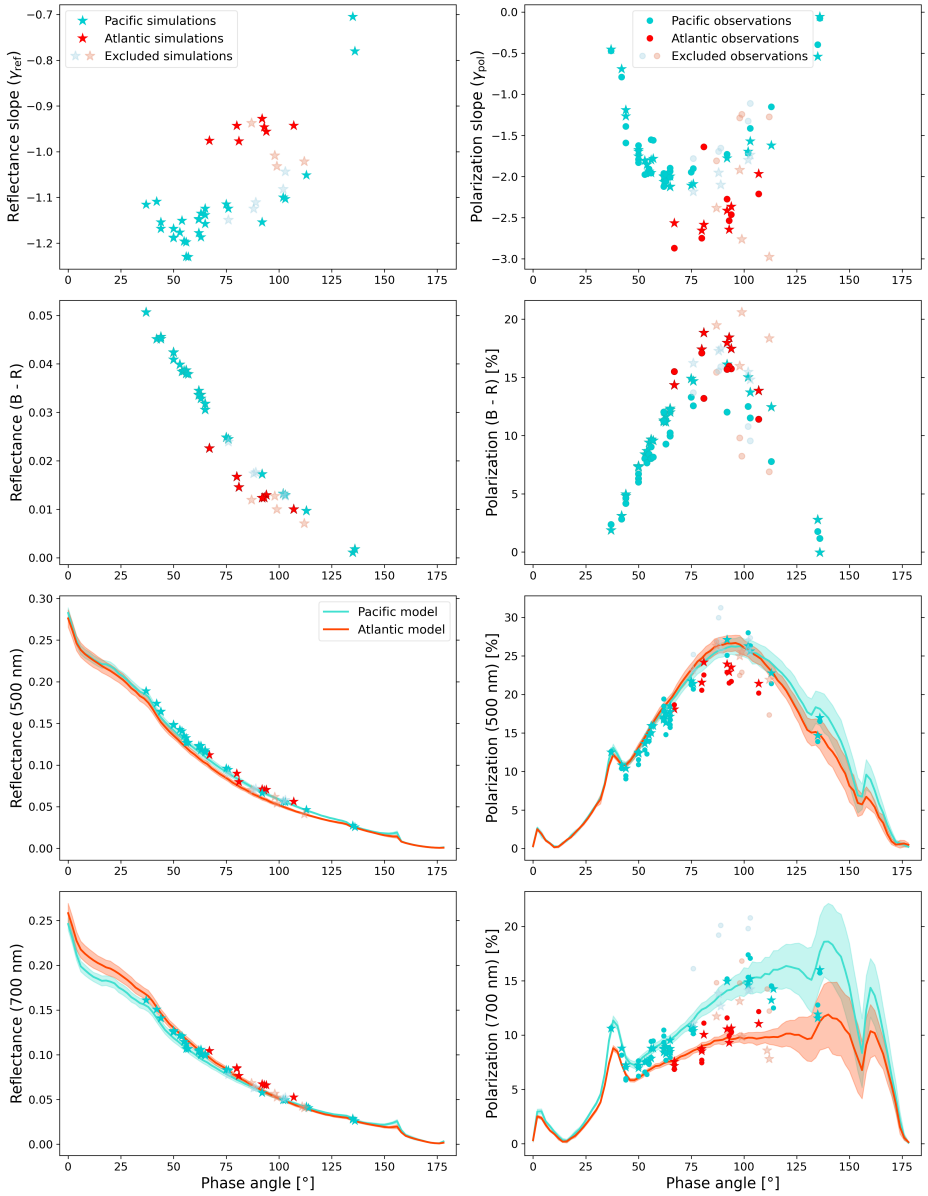

Figure 6.2: Reflectance simulations (first column) and polarized observations and simulations (second column) from our Earthshine catalog. We examine different diagnostic metrics: the spectral slope in the visible range (first row), the B–R broadband difference (second row), and the continuum reflectance or polarization at single wavelengths ($\lambda = 500$ nm and 700 nm; third and fourth rows, respectively), to assess whether we can reliably distinguish between Pacific (ocean-dominated) and Atlantic (mixed land–ocean) viewing geometries. The simulated values at single wavelengths in both reflected and polarized light are derived from the reference phase curves presented in Roccetti et al. (2025a), with the shaded regions indicating the 1σ cloud variability spread.

tion in distinguishing surface types. In particular, the presence of ocean glint significantly increases polarization when the sunglint is over water, while it contributes little when the glint is hidden over land. Some intermediate epochs fall between the two model curves, representing the scenes not fully described by either a pure ocean or a glint-obscured mixed surface. This behavior is consistent with earlier findings, including preliminary simulations of ocean planets with horizontally inhomogeneous clouds with varying cloud fractions by Trees & Stam (2019), as well as indications of ocean presence in Earthshine polarization observations in the NIR reported by Takahashi et al. (2021).

6.5.2 Cloud properties

After evaluating the sensitivity to various surface conditions, we now focus on cloud properties. Specifically, we examine the averaged cloud optical thickness τ and cloud cover (cc) for the different viewing geometries of our Earthshine catalog. The true values of τ and cc are derived from the ERA5 reanalysis product for the cloud field used in the simulations (the closest in time), as described in Roccetti et al. (2025a), and are reported in Table 6.9. These values are calculated only for the illuminated side of the planet, as seen from the Moon in the corresponding geometry. In Fig. 6.3, we explore the correlation between cloud optical thickness and both the VIS spectral slope (γ from Eq. 6.4) and the B-R broadband differences in both reflectance and polarization. We also tested the single wavelength cases, as in 6.5.1, but we did not find any significant trends. To evaluate whether any linear correlation exists between the simulations and/or observations, we use the Pearson correlation coefficient (R-value), which is reported in each panel. For reflectance, we report only the R-value for simulations ($R_{\rm sim}$), while for polarization, the Pearson correlation coefficient is calculated for both simulations and observations ($R_{\rm obs}$). From the R-values, we conclude that there is no significant correlation between either the reflectance slope or the B-R difference and the cloud optical thickness. However, a moderate linear correlation is observed for the polarization slope, which becomes moderately strong in the case of the B-R difference. This can be understood physically as increasing cloud optical thickness enhances multiple scattering within the cloud layer, which generally reduces the degree of polarization. At the same time, the relative contribution of Rayleigh scattering (which has strong wavelength dependence) decreases compared to Mie scattering (which varies weakly with wavelength in this spectral range), resulting in a flatter polarization slope. This suggests that a steeper VIS slope or a larger broadband B-R difference in polarization corresponds to a smaller cloud optical thickness in the corresponding viewing geometry. Additionally, we observe a clustering of the Atlantic (mixed) epochs in the lower optical thickness range, consistent with τ predictions for a mixture of land and ocean sceneries, as previously reported by the statistical analysis of ERA5 cloud fields in Roccetti et al. (2025a).

Next, we examine the same trends, but with cloud cover instead of optical thickness (Fig. 6.4). Cloud cover values are calculated for the illuminated viewing geometry of each Earthshine epoch and range from 55% to more than 69%, as obtained from the ERA5 cloud fields. With cloud cover, we find a weak correlation with the polarization slope. Instead, we see a

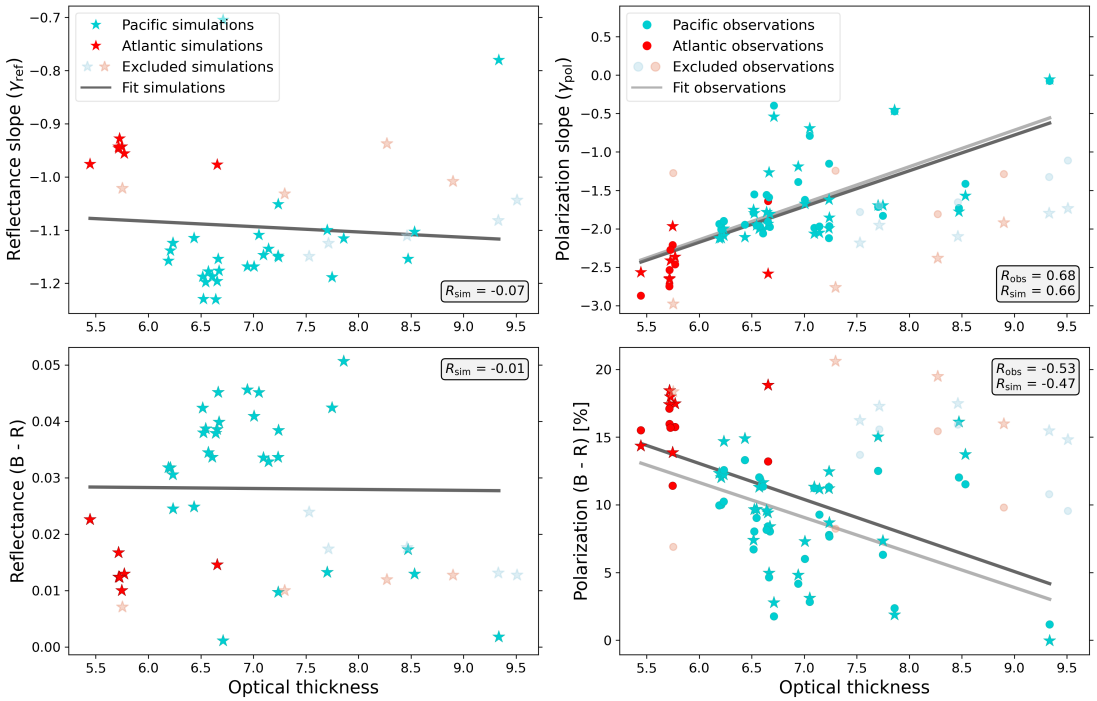

Figure 6.3: Correlations between the cloud optical thickness and the VIS spectral slopes (first row) and the B-R broadband filter differences (second row) for reflectance simulations (first column) and polarized simulations and observations (second column). We provide the Pearson correlation coefficient (R) values and the linear fits for the simulations (black) and observations (gray).

moderate linear correlation with the polarization B-R differences, with an R-value around -0.5 for both simulations and observations. This negative correlation indicates that a larger cloud cover is associated with a flatter spectrum from the B to the R filter. For cloud cover, we observe larger R-values in reflectance, suggesting that this is a better diagnostic metric for assessing cloud cover, particularly through the B-R coefficient. In contrast, the best diagnostic metric for optical thickness was found to be the VIS spectral slope in polarization. In reflectance, we observe a moderate anticorrelation between the spectral slope and cloud cover, while the B-R difference exhibits a moderately strong linear correlation with an R-value of 0.67.

Thus, we find that polarization is more sensitive to the cloud optical thickness, while reflectance is more sensitive to cloud cover. Furthermore, the spectral slope provides more diagnostic information on optical thickness in polarization, whereas the B-R difference contains more sensitivity in reflectance. Moreover, it is important to note that assessing cloud properties is challenging due to the degeneracy of various parameters such as optical thickness, cloud cover, cloud deck height, and cloud droplet size. Thus, these moderately strong linear correlations with optical thickness and cloud cover are highly relevant and may pave the way for novel methods of discriminating cloud properties on exoplanets. Our

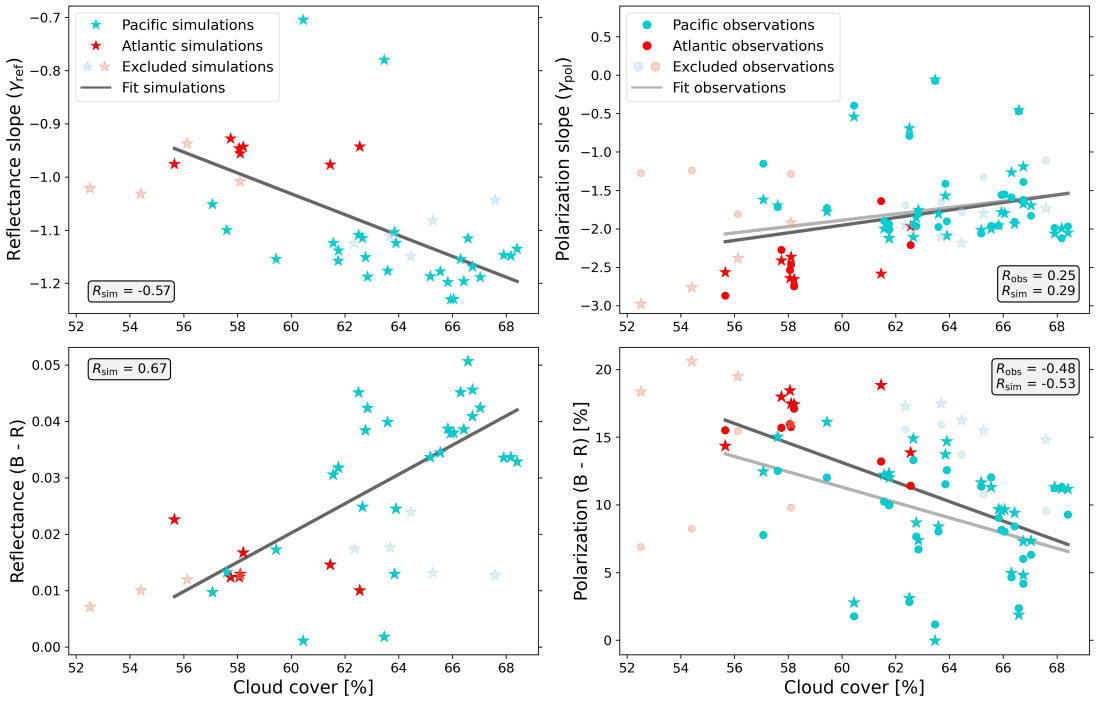

Figure 6.4: Correlations between the cloud cover and the VIS spectral slopes (first row) and the B-R broadband filter differences (second row) for reflectance simulations (first column) and polarized simulations and observations (second column). We provide the Pearson correlation coefficient (R) values and the linear fits for the simulations (black) and observations (gray).

findings suggest that combining reflected and polarized light could be a promising avenue for such investigations.

6.5.3 Vegetation red edge

As a final feature, we examine the detection of the VRE in both the simulated reflectance spectra and the observed and simulated spectra in polarization. The VRE is characterized by an increase in reflectivity (and a decrease in polarization) between 700 and 800 nm due to chlorophyll. In reflectance, the VRE is quantified using the NDVI, defined as

$$\mathrm{NDVI} = \frac{\mathrm{NIR} - \mathrm{R}}{\mathrm{NIR} + \mathrm{R}}, \tag{6.6}$$

where the NDVI is calculated from the continuum in the NIR range (748–758 nm and 769-778 nm in order to exclude the O_2-A band feature) and the red spectral range (R) between 675 and 685 nm, normalized by their sum. In polarization, the VRE is observed as a decrease in the spectral continuum in the same wavelength range. We calculate the (PDVI) as

$$\mathrm{PDVI} = \mathrm{NIR} - \mathrm{R}. \tag{6.7}$$

Following Sterzik et al. (2019), we apply a normalization procedure to estimate the PDVI from both observed and simulated polarization spectra. Specifically, we fit a fourth-order polynomial to the spectra in the 530–890 nm range, excluding regions affected by O_2 and H_2O absorption features. We then subtract this fit from the original spectra. Unlike the NDVI, the PDVI is not normalized by the term NIR + R, in order to avoid unphysical behavior when the denominator approaches zero. The resulting PDVI values are consistent with those reported in Sterzik et al. (2019).

The fractional vegetation coverage for each viewing geometry is calculated using the MODIS surface type maps. We consider all pixels containing grass or vegetation percentages and sum their vegetation fractions, accounting also for cloudy pixels. The results are reported in Table 6.9, along with the percentage of land fraction, derived using a land-sea mask to distinguish between pixels over the ocean and those over land. Additionally, we account for the real dimensions of the pixels and correct for their projected area in our vegetation and land fraction estimations. For each pixel, we first compute its physical area by converting its latitude and longitude span into the area of the corresponding spherical quadrangle on Earth's surface. We then determine whether the pixel is illuminated by the Sun by calculating the dot product between the unit vector pointing toward the Sun and the surface normal vector of the pixel. If this dot product is negative, the pixel lies in shadow and is considered not illuminated. For the illuminated pixels, we project their area in the direction of the Moon by scaling the surface area by the dot product between the pixel's normal vector and the unit vector pointing toward the Moon. This projection accounts for viewing geometry, giving greater weight to pixels directly facing the Moon and diminishing the contribution of those observed at a slant angle.

In Fig. 6.5, we show the correlations between the NDVI (left panel) and PDVI (right panel) as a function of the vegetation fraction. We clearly observe that the Atlantic (mixed) geometry epochs cluster at larger vegetation fractions, while the Pacific (ocean) points form a compact cluster at very small vegetation fractions. Some Pacific epochs appear in transition between a nearly pure ocean configuration and one with a larger fraction of land and vegetation coverage. Calculating the Pearson correlation coefficients, we find a strong linear correlation between the NDVI and vegetation fraction, indicating a strong detection of the VRE in the reflectance spectra of Earth as an exoplanet. We obtain a maximum NDVI of around 0.07, consistent with previous studies such as Tinetti et al. (2006a). For reference, the NDVI values for a satellite image over a fully forested area are typically around 0.3, so a value of 0.07 for a vegetation cover fraction of 25% is in line with theoretical expectations.

For the PDVI, we also observe a moderately strong inverse correlation with the vegetation fraction, as expected due to the decrease in polarization slope. Thus, while polarization spectra are sensitive to the VRE, this feature is more prominent in reflectance.

Furthermore, we calculate the Pearson coefficients for the NDVI ($R_{\rm sim}$ = 0.88) and PDVI ($R_{\rm obs}$ = -0.67 and $R_{\rm sim}$ = -0.63) as a function of land fraction. This plot is not shown in the paper, but it is very similar to the vegetation fraction case (Fig. 6.5), and it displays slightly stronger correlations with the land fraction. This could be because the land fraction provides a more accurate reflection of the surface composition, whereas the vege-

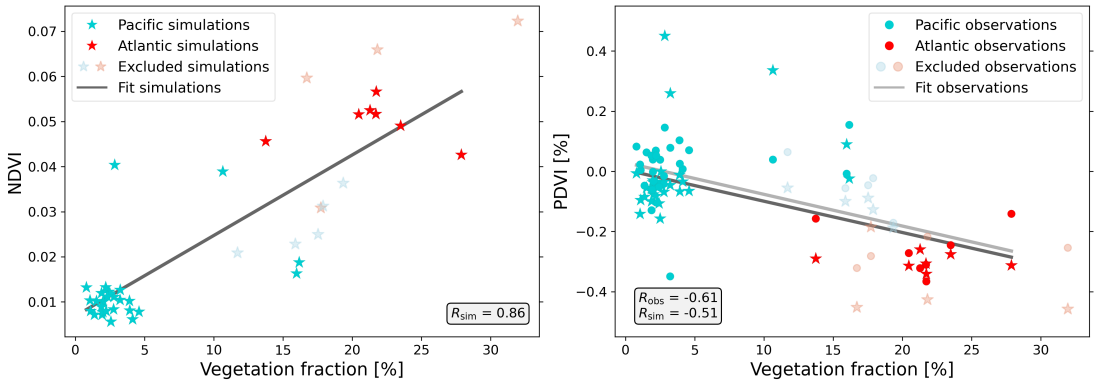

Figure 6.5: Correlation between the detection of the VRE feature and the vegetation fraction of the viewing geometry. The left panel shows the correlation with the NDVI, while the right panel shows the correlation with the PDVI. The Pearson correlation coefficients (R) and the linear fits for both simulations (black) and observations (gray) are provided.

tation coverage is based on simplistic assumptions about which pixels should be considered vegetated. Additionally, the MODIS surface type maps represent yearly averages, which may not accurately capture seasonal variations in vegetation, especially over savannas and mixed land cover regions.

6.6 Discussion

Through this catalog of Earthshine polarization observations, spanning phase angles from approximately 37° to 136°, we assess several key indicators of Earth's habitability as it would appear to a distant observer. Polarimetric Earthshine data reveal a wealth of information on both surface and atmospheric properties, crucial components in evaluating planetary habitability.

First, using observations focused on the Pacific (ocean-dominated) geometry, Sterzik et al. (2020) showed that the polarization cloudbow signature enables the retrieval of microphysical cloud properties. Specifically, the data allowed us to assess that Earth's clouds are composed of liquid water droplets with an effective radius of approximately 6 μm. This finding marked the first time such cloud microphysical properties were inferred from disk-integrated spectra, highlighting the unique diagnostic power of polarization.

Additionally, in this work, we demonstrate sensitivity to the ocean glint signature at large phase angles in the polarization continuum, evidenced by increased polarization levels in spectra that include specular reflection. The successful detection of ocean glint confirms the presence of surface liquid water and, together with the atmospheric clouds, supports the existence of an active hydrological cycle. Moreover, by analyzing both the spectral and temporal variability in the polarization VIS slope, building on the earlier work by Sterzik et al. (2019), we assess the coexistence of ocean and land surfaces. This further reinforces the idea that Earth's polarized signal encodes rich information about surface composition

and heterogeneity.
When combined with potential detections of atmospheric biosignature gases such as O_2, CH_4, and H_2O (though outside the scope of this paper), spectropolarimetry emerges as a powerful tool for assessing both planetary habitability and possible evidence of an active biosphere on the planet.
The diagnostic metrics introduced in this paper must, however, be interpreted in the context of degeneracies that may arise in exoplanet studies. For instance, although the VIS spectral slope shows sensitivity to surface composition, it is also influenced by cloud and aerosol properties (e.g., Powell et al., 2019; Ohno & Kawashima, 2020), making its interpretation non-trivial without prior knowledge of atmospheric conditions.
Nonetheless, our results reveal several spectral metrics with significant diagnostic power. These insights are essential for shaping the scientific requirements of future telescopes and instruments. For example, we find that broadband filters offer limited sensitivity to surface features, though they remain useful for assessing cloud cover. In contrast, polarization, especially at single wavelengths beyond the Rayleigh scattering regime, proves to be uniquely capable of distinguishing surface geometries, such as ocean-only versus mixed land-ocean configurations. Such distinctions are not achievable through reflectance alone. This work highlights the benefit of a complementary observational strategy that combines reflectance and polarization measurements. This dual approach offers a more comprehensive characterization of Earth-like planets and is likely to be valuable in future studies of habitable exoplanets.

6.7 Conclusions

In this work, we have presented the first effort to simulate a large catalog of 53 Earthshine polarization spectra, spanning a decade of observations from 2011 to 2020. The simulations were conducted using the advanced Monte Carlo radiative transfer model MYSTIC, incorporating a state-of-the-art treatment of 3D cloud properties and wavelength-dependent surface albedo maps. A physically consistent model for ocean specular reflection in both reflectance and polarization was also included (Roccetti et al., 2025a). In parallel, we significantly improved the quality of previously published Earthshine observations (Sterzik et al., 2012, 2019, 2020). This was achieved by refining the data reduction and slitlet averaging to reduce contamination from Moonshine and sky background, especially critical for high phase angle observations.
With this improved observational dataset, we robustly validated our modeling framework, demonstrating its ability to reproduce the polarization spectra of Earth as seen from afar. This represents a more stringent validation than reflectance comparisons alone, given the enhanced sensitivity of polarization to both surface and atmospheric properties, as further discussed in this paper and in earlier work of our paper series (Roccetti et al., 2025a,b).
Our model successfully reproduces the observed spectral slopes, polarization levels, and most of the absorption features, a substantial achievement considering the complexity involved in modeling Earthshine polarization (Emde et al., 2017; Gordon et al., 2023). This

success is primarily due to improved cloud representation, particularly through the 3D CG developed in Roccetti et al. (2025a). Accounting for sub-grid cloud variability and heterogeneity allows us to accurately simulate even the most challenging high phase angle spectra, which are dominated by a complex interplay between ocean glint and overlying 3D cloud structure.
We also accurately reproduce the Atlantic (mixed surface) viewing geometry spectra, thanks to the incorporation of HAMSTER wavelength-dependent albedo maps (Roccetti et al., 2024). These maps avoid overestimating the reflectivity of vegetated and soil-covered surfaces (Roccetti et al., 2025a), allowing us to match the continuum of the observations. However, our simulations were unable to reproduce the first eight observed spectra (from A.1 to C.2), which appear significantly flatter than later spectra acquired at similar phase angles and geometries. We did not find a definitive explanation, although possible causes include observational systematics or changes in the global atmospheric state, without clear supporting evidence.
We then used both the simulated and observed polarization spectra to assess the diagnostic potential of reflectance and polarization in probing surface viewing geometry, cloud properties, and the VRE. We evaluated the performance of various spectral metrics, including the VIS spectral slope, broadband B–R color differences, and single-wavelength values. Our main findings are:

- The VIS spectral slope in both reflectance and polarization effectively separates Pacific (ocean-dominated) and Atlantic (mixed surface) epochs. Atlantic observations show flatter slopes in reflectance and steeper slopes in polarization compared to the Pacific ones. The B–R color index shows limited diagnostic power.

- Polarization at wavelengths beyond the Rayleigh scattering regime effectively distinguishes surface types, confirming model predictions (Roccetti et al., 2025a). This result demonstrates the value of polarization for surface characterization in disk-integrated exoplanet spectra.

- For the first time, we demonstrate that Earthshine polarization spectra are sensitive to cloud properties. Specifically, the VIS polarization slope shows a moderately strong correlation with cloud optical thickness, while the B–R reflectance index better captures the cloud cover of the planet.

- We find a strong correlation between the NDVI and vegetation fraction, and a moderately strong anti-correlation between the PDVI and vegetation fraction. These results confirm the detectability of the VRE in disk-integrated spectra, especially in reflectance.

In conclusion, our model is now capable of reproducing the majority of the 53 Earthshine polarization spectra acquired with FORS2 at the VLT. This is a non-trivial accomplishment, considering that polarization signals are strongly influenced by viewing geometry, cloud and aerosol properties, surface composition, and solar illumination angle.

These results establish a critical benchmark for future modeling approaches and observational diagnostics for rocky exoplanet characterization. In particular, our advanced treatment of clouds and surfaces, introduced in Roccetti et al. (2025a), is the ground-truth framework for simulating Earthshine observations and can inform other modeling approaches for studying the Earth as an exoplanet. These results are instrumental in developing retrieval techniques for reflected light observations of rocky exoplanets, especially in the context of next-generation observatories such as the ELT and the mission concept HWO.

6.8 Data availability

The observational data and corresponding simulations are publicly available on GitHub[2]. The same repository also includes a Jupyter Notebook containing all plotting routines used to reproduce the figures in this work.

Acknowledgements

This paper is based on observations collected at the European Southern Observatory (ESO) under the P87.C-0040, P90.C-0096, and P104.C-0048 programmes. GR and JVS were supported by the Munich Institute for Astro-, Particle and BioPhysics (MIAPbP), which is funded by the Deutsche Forschungsgemeinschaft (DFG, German Research Foundation) under Germany´s Excellence Strategy – EXC-2094 – 390783311.

[2] https://github.com/giulia-roccetti/Earth_as_an_exoplanet_Part_III

6.9 Appendix A: Summary table of observed and simulated Earthshine spectra

Table 6.1: Overview of Earthshine observational epochs with dates, cloud and surface characteristics, and fitted parameters from observations and simulations.

								Observations				Simulations								
ID	date	α [°]	Geom.	Grism	τ	cc [%]	Land [%]	Veg. [%]	$\gamma_{\rm pol}$	$(B-R)_{\rm pol}$ [%]	P_{500} [%]	P_{700} [%]	PDVI	$\gamma_{\rm ref}$	$(B-R)_{\rm ref}$	R_{500}	R_{700}	NDVI	$\gamma_{\rm pol}$	$(B-R)_{\rm pol}$ [%]	P_{500} [%]	P_{700} [%]	PDVI
A.1	2011-04-24	99	A	300V	7.30	54.41	33.07	21.82	-1.08	8.23	22.87	16.82	-0.22	-1.03	0.01	0.05	0.05	0.07	-2.76	20.60	25.54	9.84	-0.43
A.2	2011-04-24	98	A	300V	8.90	58.10	20.86	17.74	-1.29	9.79	22.47	14.80	-0.28	-1.01	0.01	0.06	0.06	0.03	-1.92	15.98	24.98	13.13	-0.18
A.3	2011-04-25	87	A	300V	8.27	56.13	25.16	16.72	-1.81	15.42	26.79	14.83	-0.31	-0.94	0.01	0.07	0.07	0.06	-2.38	19.48	26.34	11.73	-0.45
B.1	2011-06-08	76	P	300V	7.53	64.46	17.15	15.89	-1.71	13.68	25.18	16.11	-0.06	-1.15	0.02	0.09	0.08	0.02	-2.18	16.23	23.12	11.06	-0.10
B.2	2011-06-08	88	P	300V	7.71	62.36	20.93	19.35	-1.64	15.56	29.96	19.20	-0.17	-1.12	0.02	0.07	0.06	0.04	-1.95	17.28	26.80	13.81	-0.19
B.3	2011-06-09	89	P	300V	8.46	63.69	18.81	17.53	-1.62	15.92	31.25	20.10	-0.05	-1.11	0.02	0.07	0.06	0.02	-2.10	17.48	25.69	12.65	-0.09
B.4	2011-06-10	102	P	300V	9.33	65.27	19.01	17.89	-1.27	10.78	27.03	19.80	-0.02	-1.08	0.01	0.06	0.05	0.03	-1.80	15.47	25.96	14.11	-0.13
B.5	2011-06-10	103	P	300V	9.51	67.59	12.44	11.71	-1.05	9.54	27.34	20.79	0.06	-1.04	0.01	0.06	0.05	0.02	-1.74	14.81	25.43	14.23	-0.05
C.1	2012-10-06	112	A	300V	5.75	52.52	49.97	31.96	-1.10	6.96	20.03	14.17	-0.30	-1.02	0.01	0.04	0.04	0.07	-2.98	18.35	21.92	7.80	-0.46
C.2	2012-10-06	111	A	600l	6.97	57.53	27.03	16.83	-	-	-	14.24	-	-1.03	0.01	0.04	0.04	0.05	-2.85	17.22	21.72	8.59	-0.29
D.1	2012-12-07	81	A	300V	6.66	61.46	33.80	21.74	-1.64	13.20	22.52	11.10	-0.37	-0.98	0.01	0.08	0.08	0.06	-2.59	18.84	24.18	10.04	-0.34
E.1	2012-12-17	50	P	300V	6.52	62.84	3.62	1.94	-1.81	6.74	12.55	7.59	-0.06	-1.19	0.04	0.15	0.13	0.01	-1.75	7.39	12.33	6.96	-0.06
E.2	2012-12-18	63	P	300V	6.61	65.18	3.82	2.57	-2.08	11.62	17.73	8.47	-0.05	-1.19	0.03	0.12	0.10	0.01	-2.02	11.65	17.51	8.94	-0.00
E.3	2012-12-18	63	P	600l	5.96	64.56	1.90	0.83	-	-	-	8.42	-	-1.17	0.03	0.12	0.10	0.01	-1.76	11.55	17.36	8.88	0.00
E.4	2012-12-19	75	P	300V	6.44	62.66	2.91	1.98	-1.96	13.30	21.23	10.49	0.04	-1.11	0.02	0.10	0.08	0.01	-2.11	14.89	21.73	10.73	-0.03
E.5	2012-12-19	76	P	600l	6.32	63.57	1.07	0.40	-	-	-	9.82	-	-1.13	0.02	0.10	0.08	0.01	-2.06	14.74	21.25	10.40	-0.06
E.6	2012-12-19	76	P	300V	6.24	63.90	1.47	0.80	-1.92	12.56	20.69	10.69	0.08	-1.12	0.02	0.09	0.08	0.01	-2.09	14.68	21.41	10.67	-0.01
F.1	2013-02-02	107	A	300V	5.75	62.55	42.18	27.88	-1.82	11.40	20.17	12.16	-0.14	-0.94	0.01	0.06	0.05	0.04	-1.97	13.86	21.41	11.05	-0.31
F.2	2013-02-03	94	A	300V	5.77	58.11	38.16	23.50	-2.49	15.74	21.68	10.23	-0.25	-0.96	0.01	0.07	0.07	0.05	-2.37	17.47	23.52	10.63	-0.28
F.3	2013-02-03	93	A	300V	5.72	58.06	34.71	20.47	-2.55	15.96	21.48	9.93	-0.27	-0.95	0.01	0.07	0.07	0.05	-2.64	18.44	22.90	9.30	-0.31
F.4	2013-02-03	92	A	300V	5.73	57.75	24.56	13.75	-2.28	15.69	22.87	11.58	-0.16	-0.93	0.01	0.07	0.07	0.05	-2.41	17.98	23.93	10.54	-0.29
F.5	2013-02-04	80	A	300V	5.72	58.22	36.39	21.71	-2.78	17.10	20.54	7.45	-0.31	-0.94	0.02	0.09	0.08	0.05	-2.66	17.41	21.56	8.74	-0.31
F.6	2013-02-04	80	A	600l	5.61	58.05	30.71	17.86	-	-	-	7.69	-	-0.95	0.02	0.09	0.09	0.05	-2.69	17.47	21.42	8.53	-0.34
F.7	2013-02-05	67	A	300V	5.45	55.66	35.74	21.29	-2.93	15.93	18.88	6.71	-0.33	-0.98	0.02	0.11	0.10	0.05	-2.57	14.34	18.08	7.57	-0.26
F.8	2013-02-05	67	A	600l	5.62	55.62	31.39	18.41	-	-	-	7.18	-	-0.98	0.02	0.11	0.10	0.05	-2.65	14.75	18.07	7.18	-0.29
G.1	2013-02-18	92	P	300V	8.47	59.44	3.41	3.23	-1.48	12.01	25.06	15.17	-0.35	-1.15	0.02	0.07	0.06	0.01	-1.78	16.12	27.12	14.95	-0.05
G.2	2013-02-19	102	P	300V	7.70	57.61	16.89	16.17	-1.36	12.50	28.00	17.39	0.15	-1.10	0.01	0.06	0.05	0.02	-1.70	15.02	26.29	14.89	-0.02
G.3	2013-02-19	102	P	600l	7.29	58.66	8.55	7.87	-	-	-	17.82	-	-1.11	0.01	0.06	0.05	0.02	-1.81	14.55	25.67	14.60	0.10
G.4	2013-02-19	103	P	300V	8.53	63.85	3.41	3.24	-1.41	11.51	26.31	17.07	0.08	-1.10	0.01	0.06	0.05	0.01	-1.57	13.72	25.62	15.17	0.26
G.5	2013-02-20	113	P	300V	7.24	57.07	16.79	15.98	-1.18	7.77	21.40	14.53	-0.01	-1.05	0.01	0.05	0.04	0.02	-1.62	12.45	22.76	13.22	0.09
G.6	2013-02-20	114	P	600l	8.06	59.64	4.80	4.48	-	-	-	12.49	-	-1.08	0.01	0.05	0.04	0.02	-1.78	11.04	22.88	14.25	0.15
G.7	2013-02-22	135	P	300V	6.71	60.45	11.74	10.65	-0.39	1.76	13.88	12.77	0.04	-0.70	0.00	0.03	0.03	0.04	-0.54	2.77	14.66	11.92	0.34
G.8	2013-02-22	135	P	600l	8.34	62.81	3.60	3.25	-	-	-	11.67	-	-0.76	0.00	0.03	0.03	0.04	-2.04	2.82	14.50	11.55	0.28
G.9	2013-02-22	136	P	300V	9.34	63.47	2.96	2.84	-0.08	1.16	16.49	15.72	0.15	-0.78	0.00	0.03	0.03	0.04	-0.06	-0.04	16.98	16.01	0.45
H.1	2019-10-30	37	P	300V	7.86	66.58	7.15	4.14	-0.49	2.36	12.60	10.66	0.01	-1.12	0.05	0.19	0.16	0.01	-0.45	1.87	12.49	10.61	-0.03
H.2	2019-10-31	50	P	300V	7.75	67.04	7.37	3.93	-1.83	6.31	10.88	6.21	0.03	-1.19	0.04	0.15	0.13	0.01	-1.70	7.34	12.44	7.19	-0.07
H.3	2019-11-01	50	P	300V	7.01	66.75	6.29	2.76	-1.60	6.00	11.53	7.15	-0.04	-1.17	0.04	0.15	0.13	0.01	-1.68	7.29	12.47	7.22	-0.04
H.4	2019-11-01	62	P	300V	6.57	65.55	7.76	3.91	-1.91	12.02	19.40	10.46	0.10	-1.18	0.03	0.12	0.10	0.01	-2.00	11.30	17.06	8.77	-0.01
H.5	2019-11-02	62	P	300V	7.24	68.18	5.94	2.03	-1.89	11.30	18.47	9.91	-0.03	-1.15	0.03	0.12	0.10	0.01	-1.99	11.20	16.88	8.70	-0.08
H.6	2019-11-02	62	P	300V	7.10	67.91	5.46	1.53	-1.96	11.23	17.86	9.32	0.06	-1.15	0.03	0.12	0.11	0.01	-2.06	11.31	16.72	8.43	-0.05
H.7	2019-11-02	63	P	300V	7.14	68.41	6.51	2.43	-1.97	9.27	14.78	7.68	-0.05	-1.14	0.03	0.12	0.11	0.01	-2.05	11.16	16.31	8.27	-0.11
I.1	2019-11-30	42	P	300V	7.05	62.51	6.35	2.78	-0.83	2.98	10.47	8.15	-0.03	-1.11	0.05	0.17	0.15	0.01	-0.69	3.11	10.82	8.78	-0.07
I.2	2019-12-01	53	P	300V	6.67	63.59	5.51	1.99	-2.01	8.23	12.97	6.57	0.00	-1.18	0.04	0.14	0.12	0.01	-1.81	8.39	13.60	7.51	-0.04
I.3	2019-12-01	54	P	300V	7.24	62.77	5.41	1.88	-2.02	7.82	12.33	6.24	0.06	-1.15	0.04	0.14	0.12	0.01	-1.86	8.68	14.00	7.58	-0.06
I.4	2019-12-02	65	P	300V	6.21	61.76	4.45	1.10	-2.07	10.20	15.64	7.59	0.02	-1.14	0.03	0.12	0.10	0.01	-2.12	12.01	17.13	8.47	-0.10
I.5	2019-12-02	65	P	300V	6.19	61.75	4.38	1.06	-1.97	10.06	15.95	8.14	0.03	-1.16	0.03	0.12	0.10	0.01	-2.13	12.33	17.75	8.75	-0.14
I.6	2019-12-02	65	P	300V	6.23	61.57	5.65	2.19	-1.93	10.35	16.66	8.47	0.06	-1.12	0.03	0.12	0.10	0.01	-2.00	12.22	18.51	9.52	-0.08
J.2	2019-12-30	44	P	300V	6.94	66.75	5.14	2.51	-1.41	4.34	9.25	5.94	0.04	-1.17	0.05	0.16	0.14	0.01	-1.19	4.81	10.40	7.25	-0.16
J.3	2019-12-30	44	P	300V	6.67	66.31	4.93	2.31	-1.61	4.82	9.69	6.04	-0.12	-1.15	0.05	0.16	0.14	0.01	-1.27	4.96	10.39	7.02	-0.05
J.4	2019-12-31	55	P	300V	6.65	66.42	3.50	1.38	-1.94	8.56	14.03	7.25	-0.04	-1.20	0.04	0.13	0.11	0.01	-1.94	9.41	14.67	7.70	-0.09
J.5	2019-12-31	56	P	300V	6.55	65.83	3.95	1.89	-1.96	9.32	15.36	8.03	-0.16	-1.20	0.04	0.13	0.11	0.01	-1.95	9.67	15.00	7.85	-0.10
K.2	2020-01-30	56	P	300V	6.52	66.05	5.48	4.60	-1.56	8.14	16.07	9.45	0.06	-1.23	0.04	0.13	0.11	0.01	-1.80	9.65	15.94	8.77	-0.07
K.3	2020-01-30	57	P	300V	6.64	65.93	3.01	2.22	-1.56	8.24	16.12	9.47	0.06	-1.23	0.04	0.13	0.11	0.01	-1.78	9.57	15.91	8.77	-0.03

6.10 Appendix B: Catalog of observations and simulations

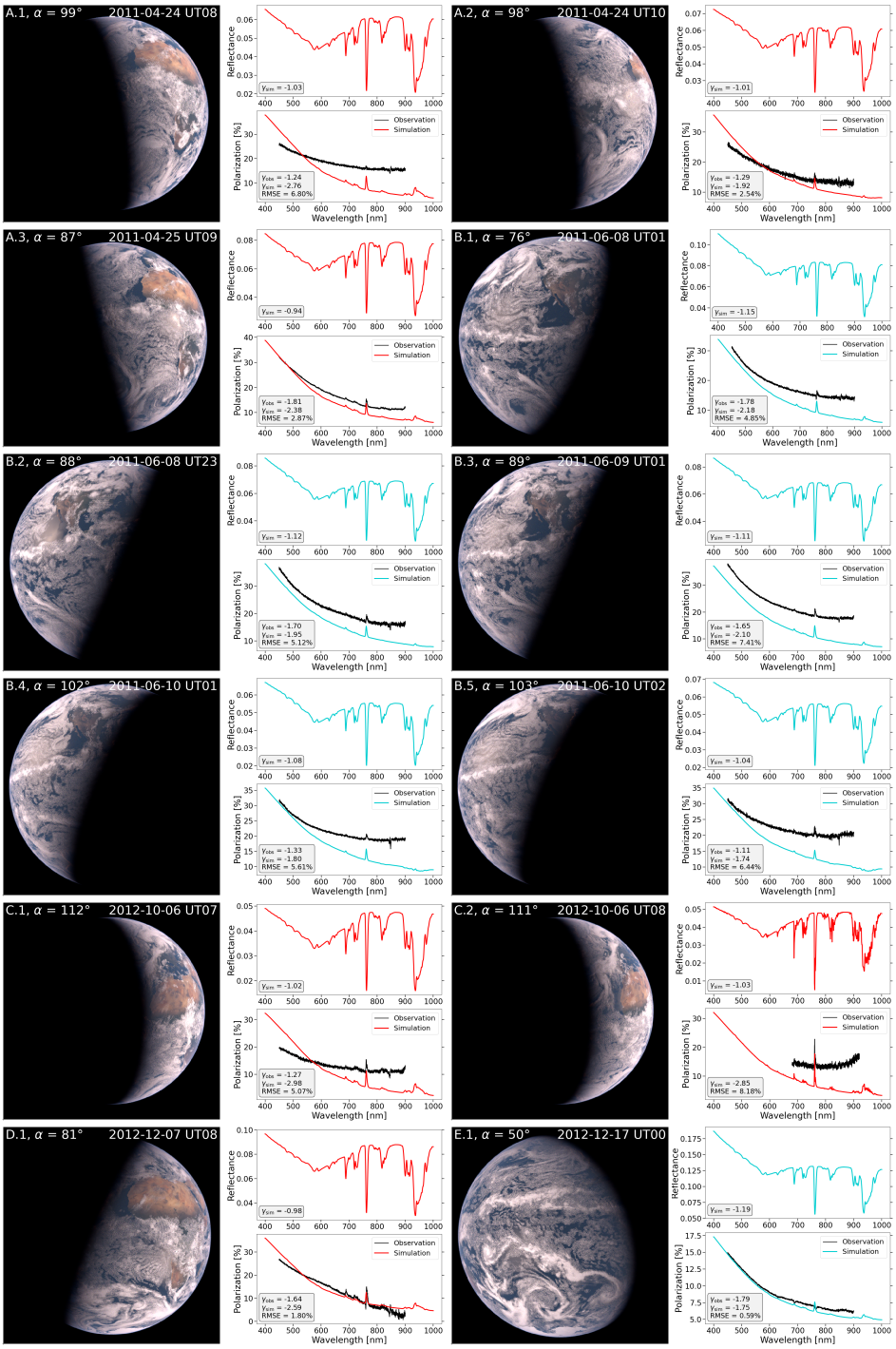

Figure 6.6: Catalog of observations and simulations from epochs A.1 to E.1.

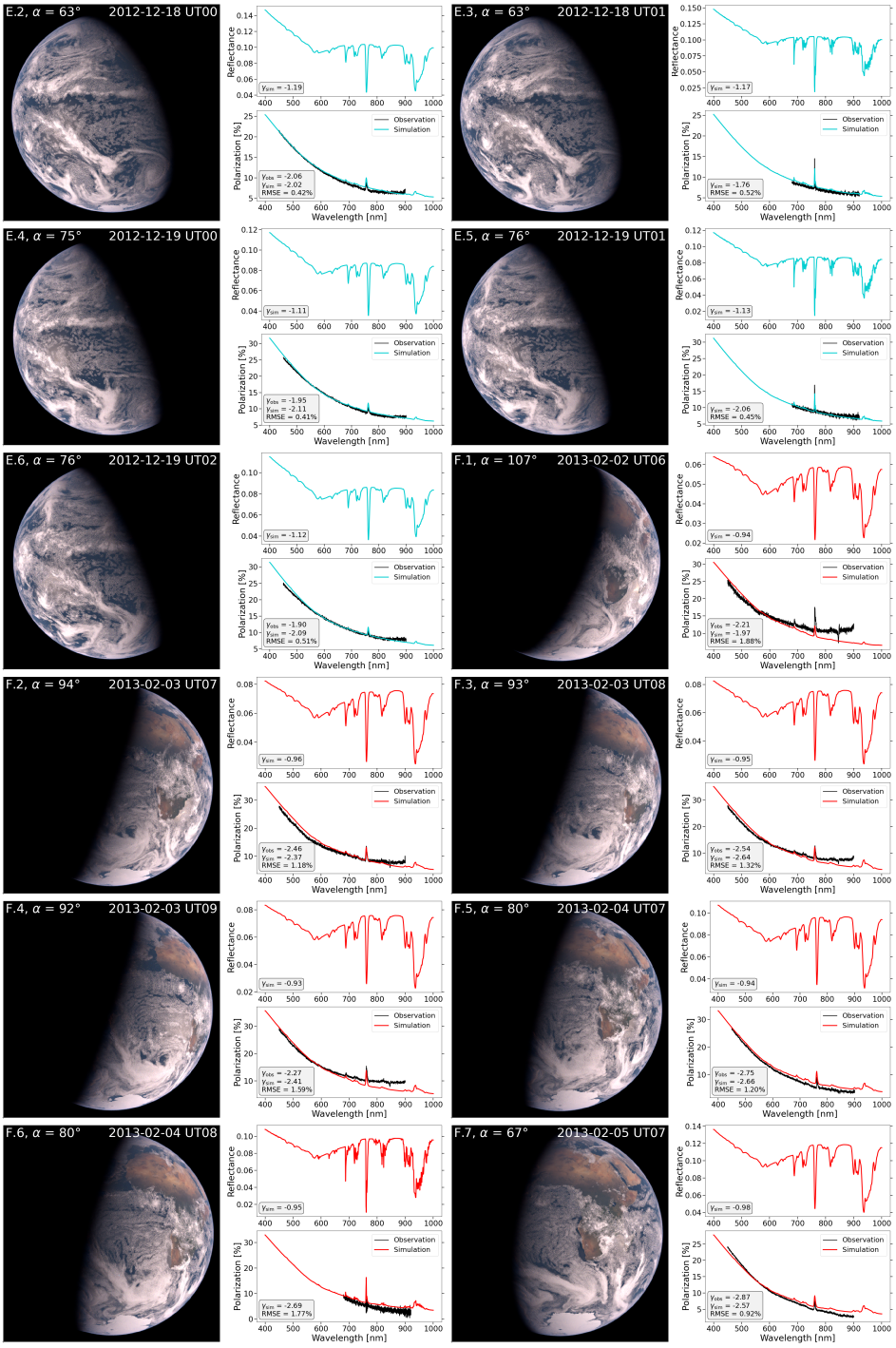

Figure 6.7: Catalog of observations and simulations from epochs E.2 to F.7.

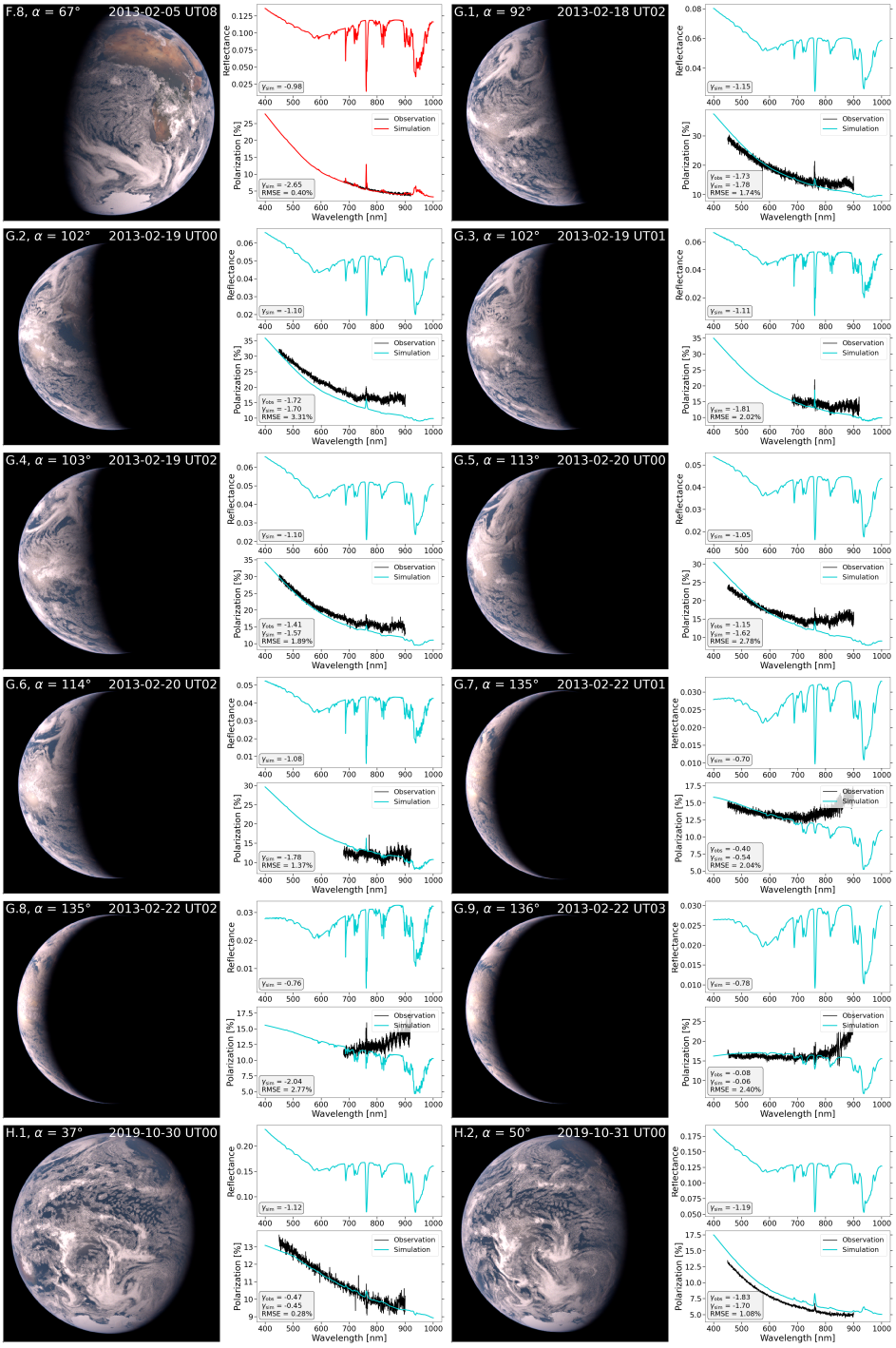

Figure 6.8: Catalog of observations and simulations from epochs F.8 to H.2.

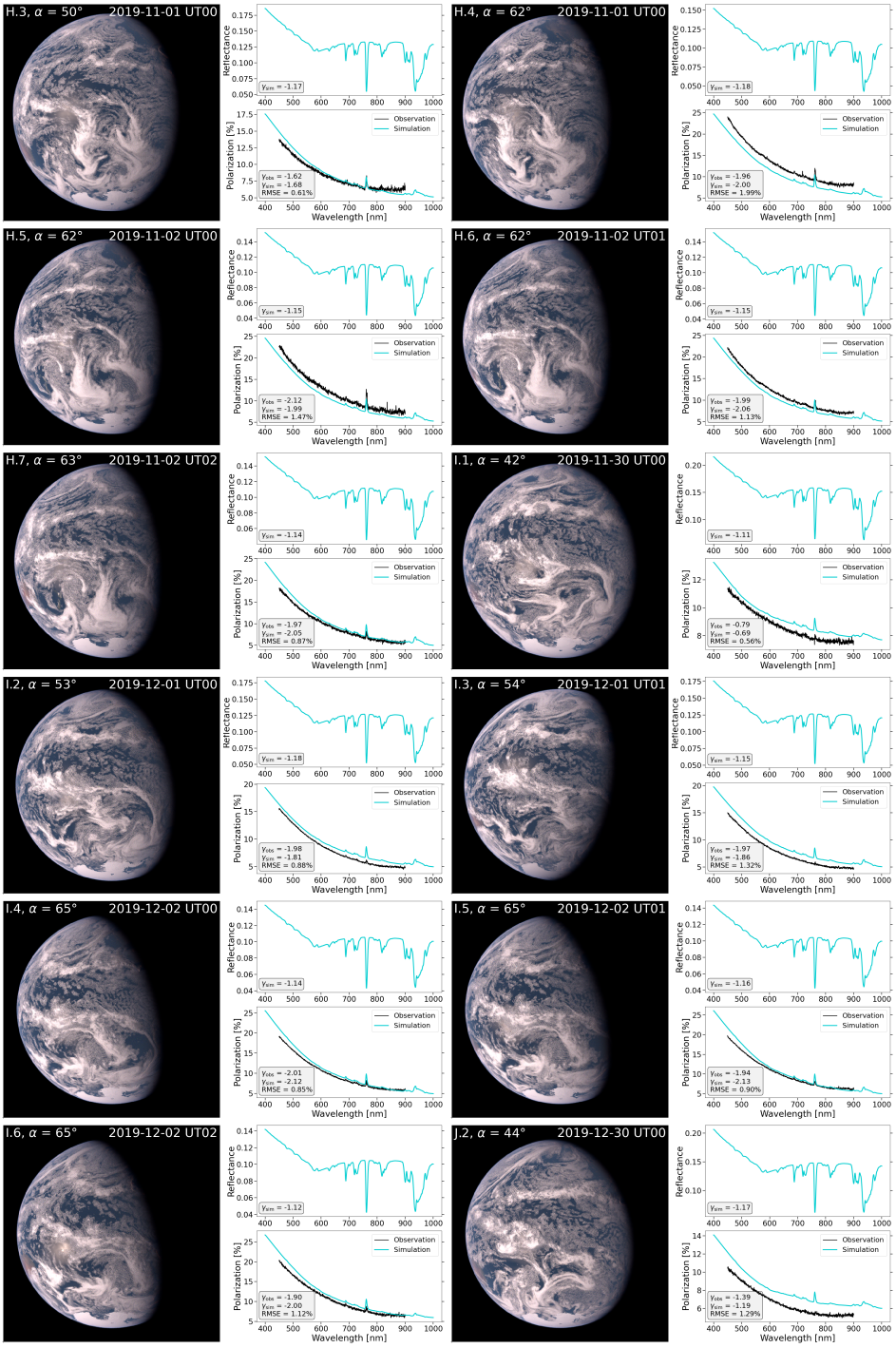

Figure 6.9: Catalog of observations and simulations from epochs H.3 to J.2.

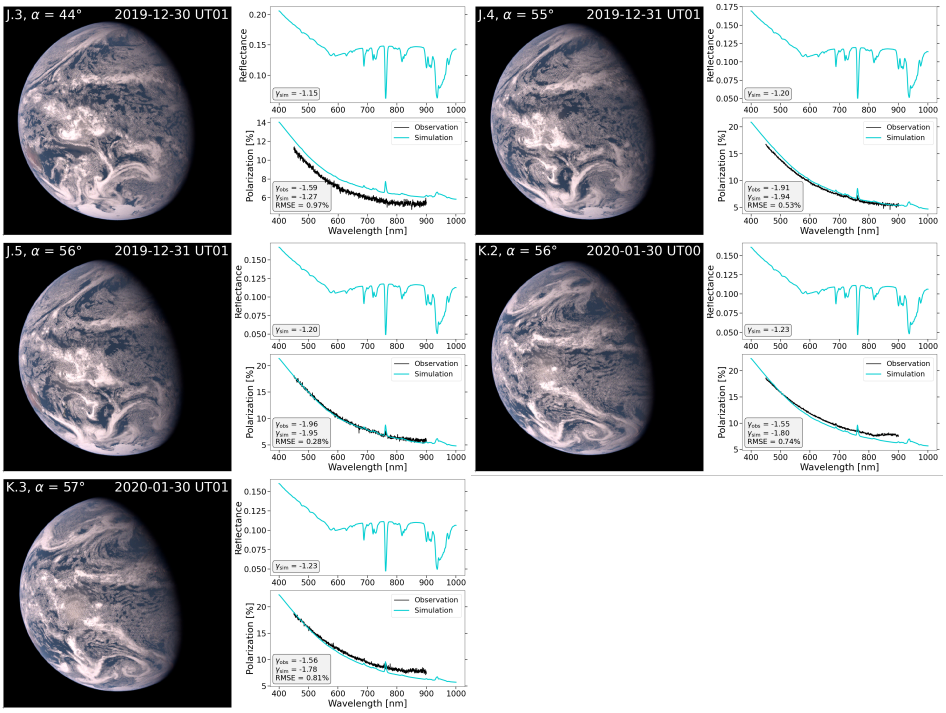

Figure 6.10: Catalog of observations and simulations from epochs J.3 to K.3.

7

Summary and Future Perspectives

7.1 Historical importance

Since ancient times, humans have been captivated by understanding our place in the Universe and whether we are alone. Thanks to technological advancement and the current development of the next generation of ground- and space-based telescopes, we will have the possibility, in the coming decades, to start addressing one of the most profound scientific questions: whether Earth is a truly unique planet or if other rocky exoplanets may also harbor life. In this pursuit, Earth has long been recognized as a crucial benchmark for evaluating the potential habitability of distant worlds (Sagan et al., 1993).
Earthshine, the faint glow visible on the darker portion of the visible Moon, had intrigued observers since the Renaissance, when it was first correctly identified as sunlight reflected by Earth. Galileo Galilei even invoked Earthshine to support the heliocentric model (Galilei, 1632). By the 20th century, the scientific value of Earthshine was being explored in two directions: as a tool for studying Earth's climate and albedo variability (Danjon, 1928), and as a proxy for understanding how Earth might appear to a distant observer (Dubois, 1947). This dual role laid the foundation for using Earthshine to study Earth's disk-integrated properties as an exoplanet, especially in preparation for future missions dedicated to exoplanet characterization (Woolf et al., 2002). Over the years, Earthshine observations have expanded in spectral coverage, phase angle range, and into the domain of polarization. Yet, despite this progress, no comprehensive model has succeeded in reproducing the full diversity of Earthshine spectra, particularly in polarization. Existing attempts often failed to capture key spectral features, such as the continuum polarization level and spectral slope (Emde et al., 2017; Gordon et al., 2023). This challenge marked the starting point of the investigation presented in this thesis.

7.2 Contribution of this work

The overarching question addressed in this thesis is how to develop a model capable of simulating Earth as an exoplanet, of growing importance given the upcoming generation of ground- and space-based telescopes, which will soon be able to observe rocky exoplanets in reflected light. As outlined in Chapter 1, Earthshine observations provide a unique opportunity to study Earth as a spatially unresolved exoplanet across different phase angles, effectively mimicking how rocky exoplanets will be observed with instruments such as ANDES and PCS at the ELT, or future missions like HWO. Importantly, Earthshine polarization measurements are self-calibrated compared to intensity-only observations, offering a benchmark for characterizing Earth-like planets.
In this thesis, I introduce novel modeling approaches for both the wavelength-dependent surface albedo (Chapter 3) and the representation of 3D cloud fields, accounting for subgrid cloud variability and heterogeneity (Chapter 4). In doing so, I revisit and extend questions raised nearly a century ago by Danjon (1928), who attributed the daily and seasonal variability of Earthshine to a combination of cloud properties, atmospheric conditions, and surface changes. These advancements were made possible by developing new algorithms based on extensive observational datasets and reanalysis products of Earth's surface and cloud properties. These innovative approaches are integrated into a Monte Carlo radiative transfer model capable of 3D simulations of Earth, including polarization. This framework is then validated against a comprehensive catalog of Earthshine observations in polarization (Chapter 6). In addition to supporting exoplanet studies, these improved surface and cloud modeling approaches could offer direct benefits for Earth System Modeling, enhancing simulations of Earth's climate system.
This achievement has two significant implications. First, a validated ground-truth model of Earth viewed as an exoplanet is essential for developing robust characterization strategies for exoplanets. As discussed in Chapter 1, accurate forward models are crucial for reliable atmospheric retrievals, particularly in the face of parameter degeneracies. This is especially important for upcoming observations of small, rocky exoplanets in reflected light, which are expected to exhibit greater diversity and surface heterogeneity than gas giants, factors intimately connected to their habitability. Second, Earthshine observations provide a unique source of disk-integrated data on Earth, which are typically inaccessible via satellite measurements. Using these observations to validate modeling approaches advances exoplanet models and contributes to refining Earth system models (ESMs) by incorporating more complete physical processes, helping to reduce uncertainties in climate predictions. The development of wavelength-dependent surface albedo maps and a fast 3D cloud generator is of further relevance for remote sensing and for minimizing radiative forcing biases associated with surface and cloud representations.
I can now address the central research questions of this thesis, as outlined in Chapter 1.

Q1: What is the threshold between overcomplexity and oversimplification in modeling Earth as an exoplanet? To accurately reproduce disk-integrated Earthshine polarization observations (Chapter 6), detailed surface and cloud modeling is essential.

This includes capturing the wavelength dependence of surface albedo to account for ocean glint features and their interaction with overlying clouds, as well as high-resolution representations of 3D cloud structure and microphysical properties. However, such detailed inputs are unattainable for exoplanets, highlighting that the complexity required to model Earth as an exoplanet exceeds the current capabilities of exoplanet modeling and retrieval frameworks. These findings should guide the exoplanet community toward developing more advanced modeling tools incorporating spatial resolution, 3D cloud structures, and sophisticated surface representations. In Chapter 5, I also investigate how increasing model complexity, ranging from spatially homogeneous planets to detailed Earth scene-based simulations, significantly affects reflected light spectra and phase curves, especially at small phase angles, and impacts polarization at larger phase angles. This emphasizes the limitations of 1D and overly simplified models.

Q2: What insights can be gained from studying Earthshine observations? In Chapter 6, I conduct a statistical analysis of a large sample of Earthshine polarization observations collected over a decade, encompassing a wide range of atmospheric, cloud, and surface conditions. I show that this dataset, comprising 53 spectra, can be used to identify signs of an active biosphere on Earth. Specifically, it enables the retrieval of the presence of liquid water clouds, the estimation of average cloud cover and optical thickness, and even the detection of vegetation. Moreover, the analysis allows me to infer that Earth's surface consists of both land and ocean. This conclusion is further supported by polarization measurements, as demonstrated in Chapter 5, where I show that polarization is particularly sensitive to surface features, mainly due to the strong linear polarization signal produced by the ocean glint. Chapter 5 also highlights that polarization is highly sensitive to cloud properties, as evident from the cloudbow features. However, observing polarized light from an exoplanet requires lower contrast than reflected light alone. Reaching lower contrast in polarized light is more feasible thanks to reduced speckle noise. Therefore, a complementary approach combining reflected and polarized light is likely the most effective, as the addition of polarization significantly aids in resolving retrieval degeneracies and distinguishing between different planetary characteristics.

Q3: Can this model validation with Earthshine observations also advance Earth system models? To achieve the goals of this thesis, I developed a dataset of wavelength-dependent surface albedo maps (Chapter 3), which are critical for interpreting reflected light observations. Neglecting this wavelength dependence has recently been shown to introduce significant biases in climate models, resulting in an average radiative forcing error of 3.55 $\mathrm{W\,m^{-2}}$ (Braghiere et al., 2023). Similar issues arise with clouds: Chapter 4 shows that omitting the 3D cloud generator leads to an overestimation of the total reflectance of the planet and an underestimation of its polarization. Clouds remain the largest source of uncertainty in climate projections, making their accurate representation and radiative impacts in models critically important. Thus, although the surface and cloud modeling approaches developed here were primarily intended for astrophysical applications, they hold significant potential for advancing Earth system modeling and remote sensing

efforts.

In conclusion, this thesis presents the first modeling framework capable of reproducing most Earthshine polarization observations. The surface albedo and cloud modeling techniques developed herein should be extended to exoplanet simulations to ensure accurate interpretation of reflected light data. Furthermore, these approaches offer substantial improvements for ESMs, particularly in reducing uncertainties in radiative forcing linked to surface and cloud representations.

7.3 Future perspectives

An immediate application of this work lies in its extension to the field of Earth sciences. In particular, HAMSTER could be integrated into climate models to evaluate the impact of the wavelength-dependent component of surface albedo on the prediction of climatological variables, similar to the approach adopted by Braghiere et al. (2023) using simplified wavelength-dependent albedo maps. As a further step, HAMSTER may also prove valuable in Earth remote sensing applications. Using albedo values that correspond precisely to the retrieval wavelength could reduce biases and improve atmospheric retrievals and abundance estimates. Moreover, HAMSTER could be enhanced by incorporating a BRDF. This extension would allow for modeling the directional reflectance properties of various surface types, which is essential in Earth remote sensing applications. Additionally, as shown in Chapter 3, HAMSTER can provide average spectral albedo values for specific surface types (e.g., forests, deserts) over defined geographic regions. These averages can be combined with precipitation and mean surface temperature maps to build an atlas of surface spectral albedos. This atlas could then be integrated into general circulation models (GCMs) for use in radiative transfer calculations.
While HAMSTER has already been validated against satellite observations, the 3D Cloud Generator has yet to undergo full validation. High-resolution observations of clouds and their top-of-atmosphere fluxes, such as those from MODIS or CALIPSO, could be used to improve the algorithm. The newly launched ESA's EarthCARE satellite offers unprecedented capability for assessing the 3D cloud structure and provides an even more promising validation. Potentially improving the representation of clouds in radiative transfer models, this work would provide significant insights into the cloud radiative effect.
Although applications in atmospheric physics are relatively straightforward, generalizing these methods for exoplanet characterization presents a substantial challenge. We will likely never have access to the exact surface properties, compositions, or detailed 3D cloud structures of exoplanets, including their microphysical characteristics. Nevertheless, this thesis has demonstrated the critical importance of including detailed modeling of surface albedo and clouds. It is, therefore, essential to generalize these models to account for the predicted diversity of physical and chemical conditions on rocky exoplanets.
All the abovementioned applications aim to extend these modeling approaches for both Earth and exoplanet studies. However, conclusively demonstrating that polarization is an

effective method for exoplanet characterization remains an open challenge. To address this, I am leading two observational proposals with ESO's VLT aimed at detecting polarized light scattered by an exoplanet using FORS2. The data have already been collected and are being analyzed. If successful, this would represent a first-time detection, though careful attention must be given to potential sources of instrumental noise and contamination. Concurrently, I lead an observational campaign to study Titan using CRIRES+ with spectropolarimetry. This program will allow for the detection of trace gases from the ground that would otherwise be obscured by telluric absorption and will serve as a test case for high-resolution spectropolarimetry.

While this thesis focused on the spectral continuum in Earthshine, spectral lines in polarization also offer strong diagnostic potential, particularly for surface characterization, as shown in Chapter 5. Although currently lacking observational data, high-resolution Earthshine spectra in the NIR could open a promising research path. Combined with the validated modeling framework developed here, such observations would support future high-resolution reflected-light studies of rocky exoplanets (e.g., with ANDES), aiding in retrieving surface and atmospheric properties and enhancing characterization when paired with polarization data.

This thesis makes a strong case for polarimetry for future instruments such as PCS at the ELT and HWO. Polarimetry offers a powerful advantage for exoplanet characterization, especially at small angular separations. Polarimetric differential imaging significantly improves sensitivity over intensity-only methods by suppressing speckle noise. Crucially, it enables unambiguous detection of atmospheres through Rayleigh scattering and breaks the radius–albedo degeneracy, a key limitation in reflected light studies. Polarimetry enhances atmospheric retrievals by being more sensitive to features such as ocean glint, cloud properties, and spectral slopes. It also helps overcome telluric contamination in spectroscopy, making it a vital tool for future exoplanet observations. In this thesis, I have shown that polarimetry is key to overcoming the current frontiers of exoplanet observation and that only through its lens can we detect the subtle glint of an ocean on the surface of a distant world.

Bibliography

Adam, J. A. 2002, Phys. Rep., 356, 229

Alei, E., Quanz, S. P., Konrad, B. S., et al. 2024, A&A, 689, A245

Allart, R., Lovis, C., Pino, L., et al. 2017, A&A, 606, A144

Anderson, G. P., Clough, S. A., Kneizys, F. X., Chetwynd, J. H., & Shettle, E. P. 1986, AFGL atmospheric constituent profiles (0.120km)

Appenzeller, I., Fricke, K., Fürtig, W., et al. 1998, The Messenger, 94, 1

Arnold, L., Gillet, S., Lardière, O., Riaud, P., & Schneider, J. 2002, A&A, 392, 231

Bagnulo, S., Landolfi, M., Landstreet, J. D., et al. 2009, PASP, 121, 993

Baldridge, A., Hook, S., Grove, C., & Rivera, G. 2009, Remote Sensing of Environment, 113, 711

Barstow, J. K., Changeat, Q., Garland, R., et al. 2020, MNRAS, 493, 4884

Bazzon, A., Schmid, H. M., & Gisler, D. 2013, A&A, 556, A117

Berdyugina, S. V., Berdyugin, A. V., Fluri, D. M., & Piirola, V. 2011, ApJ, 728, L6

Beuzit, J. L., Vigan, A., Mouillet, D., et al. 2019, A&A, 631, A155

Borsa, F., Rainer, M., Bonomo, A. S., et al. 2019, A&A, 631, A34

Bozdag, G. O., Szeinbaum, N., Conlin, P. L., et al. 2024, Astrobiology, 24, S

Braghiere, R. K., Wang, Y., Gagné-Landmann, A., et al. 2023, AGU Advances, 4, e2023AV000910

Breon, F.-M. & Maignan, F. 2017, Earth System Science Data, 9, 31

Brogi, M. & Line, M. R. 2019, AJ, 157, 114

Brown, A. J. 2014, J. Opt. Soc. Am. A, 31, 2789

Bréon, F.-M. & Goloub, P. 1998, Geophysical Research Letters, 25, 1879

Buchhorn, M., Lesiv, M., Tsendbazar, N.-E., et al. 2020, Remote Sensing, 12

Buehler, S., Eriksson, P., Kuhn, T., von Engeln, A., & Verdes, C. 2005, Journal of Quantitative Spectroscopy and Radiative Transfer, 91, 65

Buenzli, E. & Schmid, H. M. 2009, A&A, 504, 259

Bugatti, M., Lovis, C., Pepe, F., et al. 2024, arXiv e-prints, arXiv:2412.20879

Buras, R. & Mayer, B. 2011a, J. Quant. Spectr. Rad. Transf., 112, 434

Buras, R. & Mayer, B. 2011b, J. Quant. Spectr. Rad. Transf., 112, 434

Cadieux, C., Doyon, R., MacDonald, R. J., et al. 2024, ApJ, 970, L2

Carrer, D., Roujean, J.-L., & Meurey, C. 2010, IEEE Transactions on Geoscience and Remote Sensing, 48, 1714

Chahine, M. T., Pagano, T. S., Aumann, H. H., et al. 2006, Bulletin of the American Meteorological Society, 87, 911

Chandrasekhar, S. 1950, Quarterly Journal of the Royal Meteorological Society, 76, 498

Charbonneau, D., Brown, T. M., Noyes, R. W., & Gilliland, R. L. 2002, ApJ, 568, 377

Charbonneau, D., Noyes, R. W., Korzennik, S. G., et al. 1999, ApJ, 522, L145

Chauvin, G. 2024, Comptes Rendus Physique, 24, 139

Christensen, P. R. & Pearl, J. C. 1997, J. Geophys. Res., 102, 10875

Christiansen, J. L., Zink, J. K., Hardegree-Ullman, K. K., et al. 2023, AJ, 166, 248

Coddington, O., Schmidt, K. S., Pilewskie, P., et al. 2008, Journal of Geophysical Research: Atmospheres, 113

Collett, E. 1971, American Journal of Physics, 39, 517

Collier Cameron, A., Horne, K., Penny, A., & James, D. 1999, Nature, 402, 751

Collier Cameron, A., Horne, K., Penny, A., & Leigh, C. 2002, MNRAS, 330, 187

Costa Silva, A. R., Demangeon, O. D. S., Santos, N. C., et al. 2024, A&A, 689, A8

Cotton, D. V., Marshall, J. P., Bailey, J., et al. 2017, MNRAS, 467, 873

Cowan, N. B., Abbot, D. S., & Voigt, A. 2012, ApJ, 752, L3

Cowan, N. B., Robinson, T., Livengood, T. A., et al. 2011, ApJ, 731, 76

Cox, C. & Munk, W. 1954a, Journal of the Optical Society of America, 44, 838

Cox, C. & Munk, W. 1954b, Journal of Marine Research, 13, 198

Da Vinci, L. 1510, Codex Leicester

Damiano, M. & Hu, R. 2020, AJ, 159, 175

Dang, L., Bell, T. J., Shu, Y. Z., et al. 2025, AJ, 169, 32

Danjon, A. 1928, Ann. Obs. Strasbourg, 2, 165

Demangeon, O. D. S., Cubillos, P. E., Singh, V., et al. 2024, A&A, 684, A27

Denis, A., Vigan, A., Costes, J., et al. 2025, A&A, 696, A6

Des Marais, D. J., Harwit, M. O., Jucks, K. W., et al. 2002, Astrobiology, 2, 153

Dong, C., Jin, M., Lingam, M., et al. 2018, Proceedings of the National Academy of Science, 115, 260

Drossart, P., Rosenqvist, J., Encrenaz, T., et al. 1993, Planet. Space Sci., 41, 551

Dubois, J. 1947, Bulletin Astronomique, 13, 193

Dutta, S., Di Girolamo, L., Dey, S., et al. 2020, Geophysical Research Letters, 47, e2020GL090313

ECMWF. 2024, IFS Documentation CY49R1 - Part IV: Physical Processes (ECMWF)

Edwards, B. & Tinetti, G. 2022, AJ, 164, 15

Ehrenreich, D., Lovis, C., Allart, R., et al. 2020, Nature, 580, 597

Emde, C., Barlakas, V., Cornet, C., et al. 2015, J. Quant. Spectr. Rad. Transf., 164, 8

Emde, C., Barlakas, V., Cornet, C., et al. 2018, Journal of Quantitative Spectroscopy and Radiative Transfer, 209, 19

Emde, C., Buras, R., & Mayer, B. 2011, J. Quant. Spectr. Rad. Transf., 112, 1622

Emde, C., Buras, R., Mayer, B., & Blumthaler, M. 2010, Atmospheric Chemistry and Physics, 10, 383

Emde, C., Buras-Schnell, R., Kylling, A., et al. 2016, Geoscientific Model Development, 9, 1647

Emde, C., Buras-Schnell, R., Sterzik, M., & Bagnulo, S. 2017, A&A, 605, A2

Eriksson, P., Buehler, S., Davis, C., Emde, C., & Lemke, O. 2011, Journal of Quantitative Spectroscopy and Radiative Transfer, 112, 1551

Fan, S., Li, C., Li, J.-Z., et al. 2019, ApJ, 882, L1

Feng, Y. K., Robinson, T. D., Fortney, J. J., et al. 2018, AJ, 155, 200

Ford, E. B., Seager, S., & Turner, E. L. 2001, Nature, 412, 885

Fujii, Y., Kawahara, H., Suto, Y., et al. 2011, ApJ, 738, 184

Fulton, B. J., Petigura, E. A., Howard, A. W., et al. 2017, AJ, 154, 109

Galilei, G. 1632, Dialogue Concerning the Two Chief Worlds Systems (Giovanni Battista Landini)

Gao, P., Piette, A. A. A., Steinrueck, M. E., et al. 2023, ApJ, 951, 96

García Muñoz, A. 2015, International Journal of Astrobiology, 14, 379

García Muñoz, A., Zapatero Osorio, M. R., Barrena, R., et al. 2012, ApJ, 755, 103

Gasteiger, J., Emde, C., Mayer, B., et al. 2014, Journal of Quantitative Spectroscopy and Radiative Transfer, 148, 99

Geiger, B., Carrer, D., Franchisteguy, L., Roujean, J.-L., & Meurey, C. 2008, IEEE Transactions on Geoscience and Remote Sensing, 46, 3841

Gibson, N. P., Merritt, S., Nugroho, S. K., et al. 2020, MNRAS, 493, 2215

Gomez Barrientos, J., MacDonald, R. J., Lewis, N. K., & Kaltenegger, L. 2023, ApJ, 946, 96

González Hernández, J. I., Suárez Mascareño, A., Silva, A. M., et al. 2024, A&A, 690, A79

Goode, P. R., Qiu, J., Yurchyshyn, V., et al. 2001, Geophys. Res. Lett., 28, 1671

Goodis Gordon, K. E., Karalidi, T., Bott, K. M., et al. 2025, ApJ, 983, 168

Gordon, K. E., Karalidi, T., Bott, K. M., et al. 2023, ApJ, 945, 166

Govaerts, Y. & Lattanzio, A. 2008, Global and Planetary Change, 64, 139

Greene, T. P., Bell, T. J., Ducrot, E., et al. 2023, Nature, 618, 39

Groot, A., Rossi, L., Trees, V. J. H., Cheung, J. C. Y., & Stam, D. M. 2020, A&A, 640, A121

Gu, L., Fan, S., Li, J., et al. 2021, AJ, 161, 122

Halko, N., Martinsson, P. G., & Tropp, J. A. 2011, SIAM Review, 53, 217

Hall, R. D., Thompson, S. J., Handley, W., & Queloz, D. 2018, MNRAS, 479, 2968

Hansen, J. E. 1971, Journal of Atmospheric Sciences, 28, 1400

Hansen, J. E. & Hovenier, J. W. 1974, Journal of the Atmospheric Sciences, 31, 1137

Hansen, J. E. & Travis, L. D. 1974, Space Sci. Rev., 16, 527

Harman, C. E., Felton, R., Hu, R., et al. 2018, ApJ, 866, 56

Harrison, T. M. 2009, Annual Review of Earth and Planetary Sciences, 37, 479

He, T., Liang, S., & Song, D.-X. 2014, Journal of Geophysical Research (Atmospheres), 119, 10,281

He, T., Liang, S., Yu, Y., et al. 2013, Environmental Research Letters, 8, 044043

Hearty, T., Song, I., Kim, S., & Tinetti, G. 2009, ApJ, 693, 1763

Hersbach, H., Bell, B., Berrisford, P., et al. 2020, Quarterly Journal of the Royal Meteorological Society, 146, 1999

Hoeijmakers, H. J., Snellen, I. A. G., & van Terwisga, S. E. 2018, A&A, 610, A47

Hogan, R. J. & Bozzo, A. 2018, Journal of Advances in Modeling Earth Systems, 10, 1990

Hogan, R. J. & Illingworth, A. J. 2000, Quarterly Journal of the Royal Meteorological Society, 126, 2903

Hohmann-Marriott, M. F. & Blankenship, R. E. 2011, Annual Review of Plant Biology, 62, 515

Hu, R., Bello-Arufe, A., Zhang, M., et al. 2024, Nature, 630, 609

Hunziker, S., Schmid, H. M., Mouillet, D., et al. 2020, A&A, 634, A69

ICRAF-ISRIC. 2021, ICRAF-ISRIC Soil VNIR Spectral Library

Ingersoll, A. P. 1969, Journal of the Atmospheric Sciences, 26, 1191

Intergovernmental Panel on Climate Change (IPCC). 2023, Climate Change 2021 – The Physical Science Basis: Working Group I Contribution to the Sixth Assessment Report of the Intergovernmental Panel on Climate Change (Cambridge University Press)

Jakosky, B. M., Brain, D., Chaffin, M., et al. 2018, Icarus, 315, 146

Jiang, C. & Fang, H. 2019, International Journal of Applied Earth Observation and Geoinformation, 83, 101932

Johnson, T. V., Yeates, C. M., & Young, R. 1992, Space Sci. Rev., 60, 3

Juncu, D., Ceamanos, X., Trigo, I. F., Gomes, S., & Freitas, S. C. 2022, Geoscientific Instrumentation, Methods and Data Systems, 11, 389

Kaltenegger, L., Traub, W. A., & Jucks, K. W. 2007, ApJ, 658, 598

Karalidi, T. & Stam, D. M. 2012, A&A, 546, A56

Karalidi, T., Stam, D. M., & Hovenier, J. W. 2012, A&A, 548, A90

Kasper, M., Cerpa Urra, N., Pathak, P., et al. 2021, The Messenger, 182, 38

Kasting, J. F. 1988, Icarus, 74, 472

Kasting, J. F. 2004, Scientific American, 291, 78

Kasting, J. F., Whitmire, D. P., & Reynolds, R. T. 1993, Icarus, 101, 108

Kawahara, H. & Fujii, Y. 2010, ApJ, 720, 1333

Kemp, J. C., Henson, G. D., Steiner, C. T., & Powell, E. R. 1987, Nature, 326, 270

Khurana, K. K., Kivelson, M. G., Stevenson, D. J., et al. 1998, Nature, 395, 777

Kitzmann, D., Patzer, A. B. C., von Paris, P., Godolt, M., & Rauer, H. 2011, A&A, 534, A63

Knoll, A. H. 2015, Cold Spring Harbor Perspectives in Biology, 7, a018093

Kofman, V., Villanueva, G. L., Fauchez, T. J., et al. 2024, , 5, 197

Kopparapu, R. K., Ramirez, R., Kasting, J. F., et al. 2013, ApJ, 765, 131

Kopparapu, R. k., Wolf, E. T., Arney, G., et al. 2017, ApJ, 845, 5

Kopparla, P., Natraj, V., Crisp, D., et al. 2018, AJ, 156, 143

Korkin, S., Yang, E.-S., Spurr, R., et al. 2022, J. Quant. Spectr. Rad. Transf., 287, 108194

Kratz, D. P., Mlynczak, M. G., Mertens, C. J., et al. 2005, J. Quant. Spectr. Rad. Transf., 90, 323

Kreidberg, L. & Loeb, A. 2016, ApJ, 832, L12

Kurucz, R. L. 1992, in Infrared Solar Physics: Proceedings of the 154th Symposium of the International Astronomical Union, Tucson, Arizona, U.S.A., March 2-6 1992, ed. D. M. Rabin, J. T. Jefferies, & C. Lindsey, Vol. 154 (Kluwer Academic Publishers, Dordrecht), 523

Lagrange, A. M. 2014, Philosophical Transactions of the Royal Society of London Series A, 372, 20130090

Lawrence, D. M., Fisher, R. A., Koven, C. D., et al. 2019, Journal of Advances in Modeling Earth Systems, 11, 4245

Leconte, J., Forget, F., Charnay, B., Wordsworth, R., & Pottier, A. 2013, Nature, 504, 268

Li, S. & Yang, J. 2024, Remote Sensing of Environment, 311, 114272

Liang, S., Wang, K., Zhang, X., & Wild, M. 2010, IEEE Journal of Selected Topics in Applied Earth Observations and Remote Sensing, 3, 225

Lin, Z. & Kaltenegger, L. 2020, MNRAS, 491, 2845

Line, M. R., Wolf, A. S., Zhang, X., et al. 2013, ApJ, 775, 137

Liou, K.-N. 1973, Journal of the Atmospheric Sciences, 30, 1303

Liou, K.-N. 2002, An introduction to atmospheric radiation

Liu, B., Guo, B., Zhuo, R., Dai, F., & Chi, H. 2023, Soil and Water Research, 18, 43

Liu, N. F., Liu, Q., Wang, L. Z., et al. 2013, Hydrology and Earth System Sciences, 17, 2121

Livengood, T. A., Deming, L. D., A'Hearn, M. F., et al. 2011, Astrobiology, 11, 907

Loarie, S. R., Lobell, D. B., Asner, G. P., Mu, Q., & Field, C. B. 2011, Nature Climate Change, 1, 105

Lovis, C., Blind, N., Chazelas, B., et al. 2022, in Society of Photo-Optical Instrumentation Engineers (SPIE) Conference Series, Vol. 12184, Ground-based and Airborne Instrumentation for Astronomy IX, ed. C. J. Evans, J. J. Bryant, & K. Motohara, 121841Q

Luger, R. & Barnes, R. 2015, Astrobiology, 15, 119

Lupu, R. E., Marley, M. S., Lewis, N., et al. 2016, AJ, 152, 217

Lustig-Yaeger, J., Meadows, V. S., Tovar Mendoza, G., et al. 2018, AJ, 156, 301

Lyapustin, A., Wang, Y., Korkin, S., & Huang, D. 2018, Atmospheric Measurement Techniques, 11, 5741

Lyons, E. A., Jin, Y., & Randerson, J. T. 2008, Journal of Geophysical Research (Biogeosciences), 113, G02012

Madhusudhan, N. 2018, Atmospheric Retrieval of Exoplanets, ed. H. J. Deeg & J. A. Belmonte (Cham: Springer International Publishing), 2153–2182

Madhusudhan, N. 2019, ARA&A, 57, 617

Maignan, F., Bréon, F.-M., Fédèle, E., & Bouvier, M. 2009, Remote Sensing of Environment, 113, 2642

Manalo-Smith, N., Smith, G. L., Tiwari, S. N., & Staylor, W. F. 1998, J. Geophys. Res., 103, 733

Marchuk, G. I., Mikhailov, G. A., & Nazaraliev, M. A. 1980, The Monte Carlo methods in atmospheric optics

Marley, M. S., Gelino, C., Stephens, D., Lunine, J. I., & Freedman, R. 1999, ApJ, 513, 879

Marshak, A. & Davis, A. 2005, 3D Radiative Transfer in Cloudy Atmospheres

Marshak, A., Herman, J., Adam, S., et al. 2018, Bulletin of the American Meteorological Society, 99, 1829

Martin, G. M., Johnson, D. W., & Spice, A. 1994, Journal of Atmospheric Sciences, 51, 1823

Martin-Torres, F. J. & Mlynczak, M. G. 2005, in AAS/Division for Planetary Sciences Meeting Abstracts, Vol. 37, AAS/Division for Planetary Sciences Meeting Abstracts #37, 31.15

Martins, J. H. C., Santos, N. C., Figueira, P., et al. 2015, A&A, 576, A134

Mayer, B. 2009, in European Physical Journal Web of Conferences, Vol. 1, European Physical Journal Web of Conferences, 75

Mayer, B. & Kylling, A. 2005a, Atmospheric Chemistry and Physics, 5, 1855

Mayer, B. & Kylling, A. 2005b, Atmospheric Chemistry and Physics, 5, 1855

Mayor, M. & Queloz, D. 1995, Nature, 378, 355

Meadows, V. S., Reinhard, C. T., Arney, G. N., et al. 2018, Astrobiology, 18, 630

Meerdink, S. K., Hook, S. J., Roberts, D. A., & Abbott, E. A. 2019, Remote Sensing of Environment, 230, 111196

Mettler, J.-N., Quanz, S. P., & Helled, R. 2020, AJ, 160, 246

Mettler, J.-N., Quanz, S. P., Helled, R., Olson, S. L., & Schwieterman, E. W. 2023, ApJ, 946, 82

Miles-Páez, P. A., Pallé, E., & Zapatero Osorio, M. R. 2014, A&A, 562, L5

Mishchenko, M. I. & Travis, L. 1997, Journal of Geophysical Research, 102, 16989

Molaro, P. 2017, On the Earthshine depicted in Galileo's watercolors of the Moon

Montañés-Rodríguez, P., Pallé, E., Goode, P. R., & Martín-Torres, F. J. 2006, ApJ, 651, 544

Morcrette, J. & Jakob, C. 2000, Monthly Weather Review, 128, 1707

Mukherjee, S., Batalha, N. E., & Marley, M. S. 2021, ApJ, 910, 158

Nakajima, T. 1983, Journal of Quantitative Spectroscopy & Radiative Transfer, 29, 521

Nakajima, T. & King, M. D. 1990, Journal of Atmospheric Sciences, 47, 1878

National Academies of Sciences, E. & Medicine. 2021, Pathways to Discovery in Astronomy and Astrophysics for the 2020s

Noack, L., Rivoldini, A., & Van Hoolst, T. 2017, Physics of the Earth and Planetary Interiors, 269, 40

Noebauer, U. M. & Sim, S. A. 2019, Living Reviews in Computational Astrophysics, 5, 1

Nortmann, L., Lesjak, F., Yan, F., et al. 2025, A&A, 693, A213

Nutman, A. P., Bennett, V. C., Friend, C. R. L., van Kranendonk, M. J., & Chivas, A. R. 2016, Nature, 537, 535

Offerle, B., Jonsson, P., Eliasson, I., & Grimmond, C. S. B. 2005, Journal of Climate, 18, 3983

Ohno, K. & Kawashima, Y. 2020, ApJ, 895, L47

Orgiazzi, A., Ballabio, C., Panagos, P., Jones, A., & Fernández-Ugalde, O. 2018, European Journal of Soil Science, 69, 140

Pallé, E., Biazzo, K., Bolmont, E., et al. 2025, Experimental Astronomy, 59, 29

Pallé, E., Ford, E. B., Seager, S., Montañés-Rodríguez, P., & Vazquez, M. 2008, ApJ, 676, 1319

Pallé, E., Goode, P. R., & Montañés-Rodríguez, P. 2009a, Journal of Geophysical Research (Atmospheres), 114, D00D03

Pallé, E., Goode, P. R., Montañés-Rodríguez, P., et al. 2016, Geophys. Res. Lett., 43, 4531

Pallé, E., Goode, P. R., Yurchyshyn, V., et al. 2003, Journal of Geophysical Research (Atmospheres), 108, 4710

Pallé, E., Montañés Rodriguez, P., Goode, P. R., et al. 2004, Advances in Space Research, 34, 288

Pallé, E., Zapatero Osorio, M. R., Barrena, R., Montañés-Rodríguez, P., & Martín, E. L. 2009b, Nature, 459, 814

Pedregosa, F., Varoquaux, G., Gramfort, A., et al. 2011, Journal of Machine Learning Research, 12, 2825

Petty, G. W. 2004

Pino, L., Désert, J.-M., Brogi, M., et al. 2020, ApJ, 894, L27

Porco, C. C., Helfenstein, P., Thomas, P. C., et al. 2006, Science, 311, 1393

Poulet, F., Bibring, J. P., Mustard, J. F., et al. 2005, Nature, 438, 623

Powell, D., Louden, T., Kreidberg, L., et al. 2019, ApJ, 887, 170

Prinoth, B., Hoeijmakers, H. J., Morris, B. M., et al. 2024a, A&A, 685, A60

Prinoth, B., Sedaghati, E., Seidel, J. V., et al. 2024b, arXiv e-prints, arXiv:2406.08558

Pörtge, V., Kölling, T., Weber, A., et al. 2023, Atmospheric Measurement Techniques, 16, 645

Qu, Y., Liu, Q., Liang, S., et al. 2014, IEEE Transactions on Geoscience and Remote Sensing, 52, 907

Quanz, S. P., Ottiger, M., Fontanet, E., et al. 2022, A&A, 664, A21

Rauer, H., Aerts, C., Cabrera, J., et al. 2025, Experimental Astronomy, 59, 26

Robinson, T. D., Ennico, K., Meadows, V. S., et al. 2014, ApJ, 787, 171

Robinson, T. D., Meadows, V. S., & Crisp, D. 2010, ApJ, 721, L67

Robinson, T. D., Meadows, V. S., Crisp, D., et al. 2011, Astrobiology, 11, 393

Robinson, T. D. & Reinhard, C. T. 2018, arXiv e-prints, arXiv:1804.04138

Roccetti, G., Bugliaro, L., Gödde, F., et al. 2024, Atmospheric Measurement Techniques, 17, 6025

Roccetti, G., Emde, C., Sterzik, M. F., et al. 2025a, A&A, 697, A170

Roccetti, G., Sterzik, M. F., Seidel, J. V., et al. 2025b, A&A, 700, A62

Rodler, F., Kürster, M., López-Morales, M., & Ribas, I. 2013, Astronomische Nachrichten, 334, 188

Rogers, R. R. R. R. 1989, A short course in cloud physics

Rugheimer, S. & Kaltenegger, L. 2018, ApJ, 854, 19

Rugheimer, S., Kaltenegger, L., Zsom, A., Segura, A., & Sasselov, D. 2013, Astrobiology, 13, 251

Ryan, D. J. & Robinson, T. D. 2022, , 3, 33

Räisänen, P., Barker, H. W., Khairoutdinov, M. F., Li, J., & Randall, D. A. 2004, Quarterly Journal of the Royal Meteorological Society, 130, 2047

Sagan, C., Thompson, W. R., Carlson, R., Gurnett, D., & Hord, C. 1993, Nature, 365, 715

Salomonson, V., Barnes, W., Maymon, P., Montgomery, H., & Ostrow, H. 1989, IEEE Transactions on Geoscience and Remote Sensing, 27, 145

Sánchez-Zapero, J., Martínez-Sánchez, E., Camacho, F., et al. 2023, Remote Sensing, 15

Scandariato, G., Borsa, F., Sicilia, D., et al. 2021, A&A, 646, A159

Schaaf, C. & Wang, Z. 2021, MODIS/Terra+Aqua BRDF/Albedo Albedo Daily L3 Global 0.05Deg CMG V061

Schaaf, C. B., Gao, F., Strahler, A. H., et al. 2002, Remote Sensing of Environment, 83, 135, the Moderate Resolution Imaging Spectroradiometer (MODIS): a new generation of Land Surface Monitoring

Schiffer, R. A. & Rossow, W. B. 1983, Bulletin of the American Meteorological Society, 64, 779

Schmetz, J., Pili, P., Tjemkes, S., et al. 2002, Bulletin of the American Meteorological Society, 83, 977

Scott, D. 1992, Multivariate Density Estimation: Theory, Practice, and Visualization, A Wiley-interscience publication (Wiley)

Seager, S., Turner, E. L., Schafer, J., & Ford, E. B. 2005, Astrobiology, 5, 372

Seidel, J. V., Ehrenreich, D., Allart, R., et al. 2021, A&A, 653, A73

Seidel, J. V., Ehrenreich, D., Pino, L., et al. 2020a, A&A, 633, A86

Seidel, J. V., Lendl, M., Bourrier, V., et al. 2020b, A&A, 643, A45

Seidel, J. V., Lendl, M., Bourrier, V., et al. 2020c, A&A, 643, A45

Seidel, J. V., Otarola, A., & Théron, V. 2023, Atmosphere, 14, 1511

Seidel, J. V., Prinoth, B., Pino, L., et al. 2025, Nature, 639, 902

Sellers, P. J., Meeson, B. W., Hall, F. G., et al. 1995, Remote Sensing of Environment, 51, 3

Selsis, F., Kasting, J. F., Levrard, B., et al. 2007, A&A, 476, 1373

Shao, C., Shuai, Y., Tuerhanjiang, L., et al. 2021, Remote Sensing, 13

Shepherd, K. D., Palm, C. A., Gachengo, C. N., & Vanlauwe, B. 2003, Agronomy Journal, 95, 1314

Shonk, J. K. P., Hogan, R. J., Edwards, J. M., & Mace, G. G. 2010, Quarterly Journal of the Royal Meteorological Society, 136, 1191

Sing, D. K., Evans-Soma, T. M., Rustamkulov, Z., et al. 2024, AJ, 168, 231

Snellen, I. A. G., Albrecht, S., de Mooij, E. J. W., & Le Poole, R. S. 2008, A&A, 487, 357

Snellen, I. A. G., de Kok, R. J., de Mooij, E. J. W., & Albrecht, S. 2010, Nature, 465, 1049

Sousa-Silva, C., Seager, S., Ranjan, S., et al. 2020, Astrobiology, 20, 235

Spring, E. F., Birkby, J. L., Pino, L., et al. 2022, A&A, 659, A121

Stam, D. M. 2008, A&A, 482, 989

Sterzik, M. F., Bagnulo, S., Emde, C., & Manev, M. 2020, A&A, 639, A89

Sterzik, M. F., Bagnulo, S., & Palle, E. 2012, Nature, 483, 64

Sterzik, M. F., Bagnulo, S., Stam, D. M., Emde, C., & Manev, M. 2019, A&A, 622, A41

Stevenson, K. B., Line, M. R., Bean, J. L., et al. 2017, AJ, 153, 68

Sun, Z. 2001, Quarterly Journal of the Royal Meteorological Society, 127, 267

Sun, Z. & Rikus, L. 1999, Quarterly Journal of the Royal Meteorological Society, 125, 3037

Susemiehl, N., Mandell, A. M., Villanueva, G. L., et al. 2023, AJ, 166, 86

Takahashi, J., Itoh, Y., Akitaya, H., et al. 2013, PASJ, 65, 38

Takahashi, J., Itoh, Y., Matsuo, T., et al. 2021, A&A, 653, A99

Tilstra, L. G., de Graaf, M., Trees, V. J. H., et al. 2024, Atmospheric Measurement Techniques, 17, 2235

Tilstra, L. G., Tuinder, O. N. E., Wang, P., & Stammes, P. 2021, Atmospheric Measurement Techniques, 14, 4219

Tinetti, G., Drossart, P., Eccleston, P., et al. 2018, Experimental Astronomy, 46, 135

Tinetti, G., Meadows, V. S., Crisp, D., et al. 2006a, Astrobiology, 6, 34

Tinetti, G., Meadows, V. S., Crisp, D., et al. 2006b, Astrobiology, 6, 881

Toon, O. B., McKay, C. P., Ackerman, T. P., & Santhanam, K. 1989, J. Geophys. Res., 94, 16287

Traub, W. A. & Jucks, K. W. 2002, Geophysical Monograph Series, 130, 369

Trees, V. J. H. & Stam, D. M. 2019, A&A, 626, A129

Trees, V. J. H. & Stam, D. M. 2022, A&A, 664, A172

Trotta, R. 2008, Contemporary Physics, 49, 71

Tsang, L. & Li, Q. 1999, Microwave Remote Sensing Theory (John Wiley & Sons, Ltd)

Tucci, P. 2022, Quaderni di storia della fisica, 26

Turbet, M., Leconte, J., Selsis, F., et al. 2016, A&A, 596, A112

Turnbull, M. C., Traub, W. A., Jucks, K. W., et al. 2006, ApJ, 644, 551

Twomey, S. 1974, Atmospheric Environment (1967), 8, 1251

United States Committee on Extension to the Standard Atmosphere. 1976, U.S. Standard Atmosphere, 1976, NOAA - SIT 76-1562 (National Oceanic and Amospheric Administration)

Vaughan, S. R., Birkby, J. L., Thatte, N., et al. 2024, MNRAS, 528, 3509

Vaughan, S. R., Gebhard, T. D., Bott, K., et al. 2023, MNRAS, 524, 5477

Veach, E. 1998, PhD thesis, Stanford, CA, USA, aAI9837162

Velikodsky, Y. I., Opanasenko, N. V., Akimov, L. A., et al. 2011, Icarus, 214, 30

Vidot, J. & Borbás, É. 2014, Quarterly Journal of the Royal Meteorological Society, 140, 2186

Villanueva, G. L., Smith, M. D., Protopapa, S., Faggi, S., & Mandell, A. M. 2018, J. Quant. Spectr. Rad. Transf., 217, 86

Wagner, K., Boehle, A., Pathak, P., et al. 2021, Nature Communications, 12, 922

Wallace, J. & Hobbs, P. 2006, Atmospheric Science: An Introductory Survey, International Geophysics Series (Elsevier Academic Press)

Wang, F., Fujii, Y., & He, J. 2022, ApJ, 931, 48

Wang, F. & He, J. 2021, ApJ, 909, 9

Way, M. J., Aleinov, I., Amundsen, D. S., et al. 2017, ApJS, 231, 12

Welbanks, L., Madhusudhan, N., Allard, N. F., et al. 2019, ApJ, 887, L20

Williams, D. M. & Gaidos, E. 2008, Icarus, 195, 927

Wiscombe, W. J. 1980, Appl. Opt., 19, 1505

Wood, R. 2000, Quarterly Journal of the Royal Meteorological Society, 126, 3309

Woolf, N. J., Smith, P. S., Traub, W. A., & Jucks, K. W. 2002, ApJ, 574, 430

Wyttenbach, A., Ehrenreich, D., Lovis, C., Udry, S., & Pepe, F. 2015, A&A, 577, A62

Zhang, X., Liang, S., Wang, K., Li, L., & Gui, S. 2010, IEEE Journal of Selected Topics in Applied Earth Observations and Remote Sensing, 3, 296

Zhu, X., Liang, S., Pan, Y., & Zhang, X. 2011, IEEE Journal of Selected Topics in Applied Earth Observations and Remote Sensing, 4, 721

Zieba, S., Kreidberg, L., Ducrot, E., et al. 2023, Nature, 620, 746

Acknowledgements

Embarking on this PhD has been an incredibly challenging yet profoundly rewarding journey. I am deeply grateful for the many people I have met along the way, and for the experiences, travels, and opportunities that have allowed me to grow both as a scientist and as an individual. While it is impossible to thank everyone personally, please know that I truly appreciate each and every one of you.

First and foremost, I would like to express my sincere gratitude to Michael and Claudia for granting me the opportunity to pursue this PhD project, which so beautifully intertwines astrophysics and atmospheric physics. I learned immensely from working on this topic and deeply valued the flexibility to explore my own scientific questions. Meeting Julia V. S. at the beginning of this journey was a true blessing. Thank you for your constant support, mentorship, and the inspiring scientific discussions we have shared over the past three years. Mihail has been an endless source of ideas, greatly influencing my development in atmospheric physics. I am also grateful to all the people I have met through conferences and workshops; your insightful discussions and challenging questions have significantly enriched my scientific growth.

A heartfelt thank you to Barbara for being an exceptional role model and for always believing in me. A big thank you as well to Barbara's group, in particular to Tommaso and Karan, for supporting me since the beginning of my Master's journey. I am also thankful for the fruitful scientific discussions with Leonardo and for the support received during the final months of my PhD. I extend my appreciation to my committee members for taking the time to read and evaluate my thesis and exam.

This journey would have been significantly different without the vibrant community of students and fellows at ESO. To all my friends, thank you for your support, the fun we shared, the activities we organized together, and for being like family over the past three years. Aashish, you have been a fantastic officemate; thank you for all the adventures we shared, for introducing me to the richness of Indian culture, and especially for our unforgettable trip to India. Giuliana, thank you for your infinite support and encouragement during the most challenging times, and for always believing in me. Jens, for being a wonderful mentor and friend, for our scientific discussions, for organizing meetings and events together, and for always being there when I needed it. Marta, thank you for helping me grow as a person, for your advice, and for your constant encouragement. Luca, thank you for the fun, the Italian culture, and your positive spirit. Mari-Liis, my PhD twin, I am so glad we shared this journey and I am deeply grateful for our friendship and mutual support. Ivanna, thank you for your kindness, wise advice, and for being an amazing friend. Alice S., thank you for introducing me to ESO, for teaching me crochet, and for being a constant presence at ESO. Samuel, thank you for your community work, the New York trip, and for all the encouragement and confidence you gave me (and for teaching me new board games!). Claudia, for being a mentor and point of reference, and for your life advice. Alice C., thank you for your support and for believing in me even when I could not. Julia B., for all the roles we have shared as reps and co-supervisors; your kindness and friendship

have meant a lot, even from afar. Teresa, it was fantastic to share the last year with you, thank you for being so open, fun, and supportive. Nico, for everything you have taught me, for the inspiring discussions, and for advocating DEI causes with such strength and fearlessness. Natan, for being a sincere and sensitive friend, always present and fighting the right battles. Silvia, for the wonderful experiences we shared and for your courage. Domi, thank you for your encouragement and confidence boosts, and for being such a fantastic friend. Tommy, thank you for all the fun and for broadening my perspectives.
Thank you also to all the people who have been part of ESO during these years and with whom I have shared this journey, as well as to the entire IMPRS student community. Special thanks to Bibiana for taking the time to read my thesis and for always being present throughout my PhD journey, even though we never shared the same institute.
I am also grateful to those who contribute daily to making ESO a better place. To Anna, an inexhaustible source of encouragement, thank you for your infinite support and for never leaving me alone. I am also thankful to Nelma for our friendship, for always being present, and for making ESO a better place every day. To Francesca, for everything you have taught me and for sharing the organization of the EDI discussions with me. And to Elena, Marina, Amelia, Claudio, Paula, and all the others, thank you for your warmth and energy.
Questo percorso non sarebbe stato possibile senza l'aiuto e il sostegno dei miei amici e di tutte le persone che mi hanno vista crescere. Grazie a Sofia, Lorenza e Francesca per la vostra presenza costante, anche da lontano, e per aver mantenuto un legame profondo e autentico che mi ha sempre aiutata a crescere e a non dimenticare le mie origini. Le nostre conversazioni e riflessioni sono state per me una fonte preziosa di forza e ispirazione. Un grazie anche ai miei amici della Sapienza, in particolare a Maria Grazia, Gregorio, Ruggero e a tutti gli altri, per aver condiviso con me un pezzo importante del mio cammino. A Sara, Ilaria e Andrea, con cui sono cresciuta, e a tutti gli amici di Ostia e dintorni, grazie per aver mantenuto vivo quel legame che mi riporta sempre a casa.
Il ringraziamento più grande va però alla mia famiglia, per aver reso tutto questo possibile. Grazie ai miei genitori per avermi sempre sostenuta e per avermi lasciato la libertà di scegliere la mia strada, per avermi trasmesso fin da piccola la passione per la scienza e per avermi permesso di essere sempre me stessa. Un ringraziamento speciale a mio fratello, per essere sempre al mio fianco, compagno di avventure e di vita. Grazie anche a Sirya, per la tua presenza di spirito che mi ha insegnato tantissimo, a Nala, e in particolare a Louis, per essere stato inavvertitamente la mascotte di ESO e un vero e proprio meme vivente.
Infine, ma certamente non per importanza, grazie a Giovanni, il mio compagno di vita, con cui ho condiviso questo intero percorso. Grazie per rendermi una persona migliore, per credere sempre in me, per la tua pazienza e il tuo sostegno infinito, e per aver condiviso con me le gioie e le sfide di questo cammino.